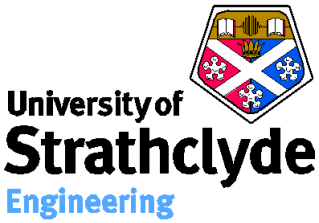

University of Strathclyde

Department of Mechanical Engineering

Development of 3D Erosion-corrosion Maps Using CFD Techniques

BY

SHEHAB EL-DIN ABDELRAHMAN MOHAMMED ABDELRAHMAN

A Thesis presented in fulfilment of
the requirements for the degree of
Doctor of Philosophy

Glasgow, UK
2010

Dedicated to

To my lovely wife, children, father and my mother

Development of 3D Erosion-corrosion Maps Using CFD Techniques

Shehab Abdelrahman

Submitted for the degree of Doctor of Philosophy
2010

Abstract

This work outlined a new methodology to extend the concept of erosion-corrosion maps from 2-Dimensional mapping to the wider 3-Dimensional mapping. The work has been carried out in the following phases:

Phase I: Development of three dimensional erosion-corrosion maps in popular applied geometry for a range of pure metals namely Fe, Ni, Cu and Al. The maps are constructed in two different forms: regime maps and wastage maps. In the Regime maps, the different apparent degradation mechanisms of erosion-corrosion are presented (e.g. pure erosion, pure dissolution or passivation, erosion domination areas over corrosion and corrosion domination regions over erosion) whereas the wastage maps represent the wear or metal loss levels regions in the form of high, medium and low regions. The methodology of constructing the 3-Dimensional maps is based on the use of the CFD (Computational Fluid Dynamics) to predict the erosion and corrosion rates then applying the erosion-corrosion mapping techniques to develop the maps in 3-Dimensional surfaces.

In the process of constructing these maps, various erosion models are inspected and compared to previous published experimental work to suitably choose the most model that well represent the erosion rates of this application. A considerably simple dissolution model is used to predict the corrosion rates in cases where the dissolution takes place. Meanwhile, a model to predict the re-passivation rates due to the oxide layer removal by the effect of solid particle impact has been developed to account for oblique impacts. The regime maps showed a significant difference from the wastage maps, this is apparently due to the target material response to erosion and corrosion processes. The advantage of including all the fluid parameters into consideration by using CFD analysis and data greatly enhanced the regime maps capability of capturing the erosion-corrosion interaction effect over the real surfaces.

Phase II: Development of the 2D and 3D erosion-corrosion maps for the Iron (Fe), as an example of a practical pure metal under a range of elevated temperature levels. To illustrate the capabilities of the new methodology of constructing the 3D erosion-corrosion maps and to investigate the effect of the operating temperature on the erosion-corrosion regimes, the same methodology is utilised with some modification to account for the complexity of the elevated temperature influence on both the erosion and corrosion process. For comparison reasons, the 2D erosion-corrosion maps are constructed as $V_p - E_{ap}$ diagrams but at a certain operating pH and temperature conditions. Finally, a comparison between the 2D and 3D erosion-corrosion maps is introduced to identify the differences, advantages, disadvantages, restrictions of use and benefits of each type over the other.

Declaration

The work in this thesis is based on research carried out at the department of mechanical engineering of the University of Strathclyde, Glasgow, Scotland; under the supervision of Professor Margaret Stack during the period from August 2007 to August 2010. No part of this thesis has been submitted elsewhere for any other degree or qualification and it is all my own work unless referenced to the contrary in the text. Some of the work has been published as listed in appendix C.

Acknowledgements

I take this opportunity to express my sincere gratitude to Professor Margaret Stack for her supervision, guidance and support throughout this period of study and in the preparation of this manuscript.

I am also thankful to Dr. Donald MacKenzie, Head of the department of Mechanical Engineering, University of Starthclyde for the assistance received during the course of this work.

I gratefully acknowledge the University of Strathclyde for giving me the opportunity to carry out this research, without which I would have been able to come to the UK where I have thoroughly enjoyed my international research experience.

I am also thankful to my friends and colleagues, especially Ghaith Abdulrahman, Muhammed Qurishi, and Wael Elmayyah for their help and encouragement during the period of this research.

Of course, this acknowledge would not be complete without expressing my sincerest gratitude to my wife who always supported me during the study. Without her encouragement and support, this work would not be completed. Thanks also must go to my family in Egypt who missed their son a lot during the course of this work. Special thanks to my father and mother who always pray for me to successfully finish this research on time.

Contents

List of Figures

List of Tables

Nomenclature

Latin letters:

Symbol	Description	Value	Unit (SI)
A_a	Affected area.		$[m^2]$
a	Constant, .		
a_o	Activity of a species.		
b	Empirical constant.		
b_a	Tafel slope at the anode.		
C'	Constant, Bitter model.		
C_D	Drag coefficient.		
C_f	Constant represents the fraction of particles that cut material in an idealised manner, Finnie model.	0.5	
$\bar{C_f}$	Skin friction coefficient..	0.5	
C_k	Cutting characteristic velocity, Forder model.		$[m\,s^{-1}]$
C_p	Specific heat capacity.		$[J\,kg^{-1}K^{-1}]$
c	concentration of a species.		
c_p	concentration of a particles.		
D	Empirical constant.		
d	diameter.		$[m]$
d_c	Crater depth.		$[m]$
D_k	Modified deformation characteristic velocity, Forder model.		$[m\,s^{-1}]$

Symbol	Description	Value	Unit (SI)
E	Electric potential.		$[V]\,SCE$
$\bar{E}$	Modulus of elasticity.		$[Pa]$
E_{ap}	Applied electric potential.		$[V]\,SCE$
E^o	Standard electrode potential.		$[V]\,SCE$
E_p	potential in passive mecahanism.		$[V]\,SCE$
E_{pas}	Passivation potential boundary value.		$[V]\,SCE$
E_X	Erosion rate, (X) represents scientist's name abbreviation (see in subscripts).		$[kg\,m^{-2}s^{-1}]$
e_n	Normal coefficient of restitution.		
e_t	Tangential coefficient of restitution.		
F	Faraday	96485	$[C\,mol^{-1}]$
F_D	Drag force.		$[kg\,m\,s^{-2}]$
f_a	Mechanically affected corrosion component of the synergism coefficient.		
f_t	Numerical constant.	0.025	
ΔG^o	Standard Gibbs free energy.		$[J\,mol^{-1}]$
g	Gravitational acceleration.	-9.81	$[m\,s^{-2}]$
H	Hardness.		$[Pa]$
H_s	Material hardness.		$[Pa]$
h	Radial distance from the inner wall of the pipe.		$[m]$
$\overline{h}$	Thickness of the oxide layer.		$[m]$
$\bar{I}$	unit tensor.		
I	Impact frequency.		$[imp\,m^{-2}s^{-1}]$
i_a	Affected current density of a metal.		$[A\,m^{-2}]$
i_{anet}	Net anodic current density of a metal.		$[A\,m^{-2}]$
i_o	Exchange current density of a metal.		$[A\,m^{-2}]$
i_{th}	Threshold current density of a metal.		$[A\,m^{-2}]$
i_u	Unaffected current density of a metal.		$[A\,m^{-2}]$
K	Ratio of vertical to horizontal (frictional) force.	2.0	
K_c	Total corrosion rate.		$[kg\,m^{-2}s^{-1}]$

Symbol	Description	Value	Unit (SI)
ΔK_c	Erosion enhanced corrosion rate.		$[kg\,m^{-2}s^{-1}]$
K_{ce}	Total erosion-corrosion rate.		$[kg\,m^{-2}s^{-1}]$
K_{co}	Pure corrosion rate.		$[kg\,m^{-2}s^{-1}]$
K_e	Total erosion rate.		$[kg\,m^{-2}s^{-1}]$
ΔK_e	Corrosion enhanced erosion rate.		$[kg\,m^{-2}s^{-1}]$
K_{eo}	Pure erosion rate.		$[kg\,m^{-2}s^{-1}]$
K_{eq}	Reaction equilibrium constant.		
K_t	Empirical erosion constant.		
K_1	Constant, Bitter model.		
k	Turbulence kinetic energy per unit mass.		$[m^2\,s^{-2}]$
$\overline{k}$	Constant.		
k_m	Constant.		
m_p	particle mass.		$[kg]$
M_t	Mass removed from the passive layer per impact.		$[kg\,imp^{-1}]$
n	Empirical constant; velocity exponent.		
n_c	Strain hardening coefficient.	0.3	
P_H	Eroding surface flow stress, Finnie model.		$[Pa]$
Q	reaction quotient.		
q	Poisson ratio.		
R	Gas constant.	8.314	$[J\,K^{-1}mol^{-1}]$
R_c	Elbow core radius.		$[m]$
Re	Reynolds number..		
R_Ω	Ohmic resistance of a cell..		$[\Omega]$
RAM	Molecular weight of the metal.		$[g\,mol^{-1}]$
Sc	Schmidt number.		
$S^{\check{o}}, S^o$	Absolute and standard Entropy.		$[J\,K^{-1}mol^{-1}]$
r_p	Particle radius.		$[m]$
T	Temperature.		$[K]$
T_m	Material melting temperature point.		$[K]$
$\overline{U}$	Crater volume.		$[m^3]$
U_b	Fluid bulk velocity.		$[m\,s^{-1}]$

Symbol	Description	Value	Unit (SI)
$\overline{U}_f$	Crater volume after relaxation.		$[m^3]$
U_T	Material toughness.		$[J\,m^{-3}]$
U_τ	Frictional velocity.		$[m\,s^{-1}]$
$\vec{V}$	Velocity component (vector).		$[m\,s^{-1}]$
V_{el}	Normal threshold velocity limit.		$[m\,s^{-1}]$
V_p	Particle velocity.		$[m\,s^{-1}]$
V_t	Parallel threshold velocity limit.		$[m\,s^{-1}]$
W	crater width.		$[m]$
x	Mass fraction of the silica contained in an ash sample.		
Y	Material yield stress.		$[Pa]$
y^+	Dimensionless wall distance.		
y, y_{n1}	First node near-to-wall distance.		$[m]$
Z	Constant.		
z_m	Number of electrons participating in a reaction.		

Greek letters:

Symbol	Description	Value	Unit, (SI)
α	Impact angle.		$[deg^o]$
β	Symmetric factor.		
γ_o	Activity coefficient.		
Δ	Difference between two points, change.		
ε_b	Material deformation factor.		$[J\,m^{-3}]$
ε_c	Critical strain.		
ε_f	Fatigue or fracture strain.		
ε_U	Uniform strain to necking in a tensile test.		
ϵ	Rate of dissipation of the turbulence kinetic energy.		$[m^2\,s^{-3}]$

Symbol	Description	Value	Unit, (SI)
η	Over-potential.		$[V]$
λ	Particle shape factor.	0.0	
μ	Molecular viscosity.		$[m^2\,s^{-1}]$
μ_f	Tangential friction coefficient.	0.1	
μ_{fc}	Critical tangential friction coefficient.		
μ_t	Turbulent or eddy viscosity.		$[m^2\,s^{-1}]$
ρ_f	Oxide layer density.		$[kg\,m^{-3}]$
ρ_p	Particle density.		$[kg\,m^{-3}]$
ρ_t	Target material density.		$[kg\,m^{-3}]$
ϕ_c	Material cutting factor.		$[J\,m^{-3}]$
σ	Plastic flow stress.		$[Pa]$
τ	The recovery time.		$[s]$
$\overline{\overline{\tau}}$	Stress tensor.		$[s]$
ψ	ratio of the depth of contact to the depth of cut, Finnie model.		

Subscripts:

Symbol	Description
a	affected area, anode
ap	applied
b	Bulk flow.
$C-B$	Cutting model of Bitter.
$C-F$	Cutting model of Finnie.
$C-S$	Cutting part of the 2^{nd}Sundararajan model.
$D-B$	Deformation model of Bitter.
$D-S$	Deformation part of the 2^{nd} Sundararajan model.
eq	Equilibrium.
o	initial, standard.
ox	Oxidised, products.

Symbol	Description
l	liquid.
p	Particle.
pas	Passive.
m	Melting point.
$N-G$	Neilson-Gilchrist model.
red	reduction, reduced, reactants.
$S1$	First model of Sundararajan.
s	Substrate material.
t	Target material.
th	Threshold.
$tran$	transition.

Abbreviation:

Abbreviation	Description
$ASTM$	American Society for Testing of Materials.
CFD	Computational Fluid Dynamics.
FAC	Flow Affected Corrosion.
LDV	Laser Doppler Velocimeter.
SEM	Scanning Electron Microscope.

Chapter 1

INTRODUCTION

Erosion-corrosion is a type of wear process involving both synergistic and antagonistic effect of both erosion on corrosion, and corrosion on erosion [1]. Although they are different phenomena; as erosion is due to mechanical impact of solid particles on the target material, while corrosion is mainly an electrochemical action taking place on the target material surface; they act together as a combined wastage process. Erosion-corrosion practically takes place in many wide range of environments, from mining and mineral processing to offshore applications [2].

Erosion modelling has been proposed and investigated extensively over several decades and there are very big advances in predicting and analysing this phenomenon. Actually, erosion mechanisms have attracted both of material and fluid dynamics researchers and lots of investigations and data have been developed over this short period of time [1, 3]. Corrosion also has attracted very wide sector of electrochemical and mechanical experts because of its electrochemical and mechanical nature on the material surfaces [4, 5].

The need for investigating the combined effect of both erosion and corrosion phenomena; or what so called erosion-corrosion, has recently arisen as most of practical cases encounter both processes acting together and the contribution of both of them in the total metal degradation is yet more complex to understand or to assume simple summation of erosion rate and corrosion rate [6]. In this system, material degradation depends on several parameters that affect the whole process. These parameters are target material, impacting particles and environment properties [7].

Erosion may enhance corrosion due to removal of a passive film, which is termed as the “Additive effect” [8]. Corrosion may enhance erosion through the dissolution of the target material surface and its consequences of lowering the hardness and micro-structure deformation of the grain bonds [9]. This enhancement sometimes referred as “Synergistic effect”. Corrosion also may inhibit erosion through the rapid formation of the passive film which overcomes the rate of passive film removal by particles impact; what so called “Antagonistic effect” [1]. These complex interaction processes between erosion and corrosion have made the erosion-corrosion system process very difficult to explore, but yet gives very attractive aspects for endeavour researchers.

Therefore, it is very hard for researchers to investigate the whole system parameters in one model. Furthermore, the models developed to study each individual process; (i.e. erosion models and corrosion models), are not capable of capturing all features of the erosion-corrosion process[10]. One big advance in investigating erosion-corrosion was the development of erosion-corrosion mapping techniques which have been constructed to visually illustrate the degradation mechanisms and wastage rates of erosion-corrosion process [11, 12].

Historically, the first wear map was generated in 1987 by Lim and Ashby [13] to investigate the sliding wear of mild steel. Since then, various investigation were made to develop wear maps to other metals wear types such as erosion and corrosion. In recent years, erosion-corrosion maps have attracted many researchers and more sophisticated and organised maps have been constructed for not only pure materials, but also for polymers, composites and coatings [14, 15, 16].

These erosion-corrosion maps become very useful tools to identify the regions where the erosion-corrosion mechanisms occur and the transition boundaries related to each mechanism [8]. It is also used to predict the total wastage of the material under investigation [8, 15]. The construction of these maps is related to the behaviour of the material under specific severe conditions, thus is dependent mainly of the selection of erosion and corrosion models that describe the wear rates and is also dependent of the corrosion trends determined by the Pourbaix diagram [17] for this material.

The basic idea behind is to relate one parameter affecting erosion rates (such as impact velocity, impact angle, particle concentration, etc..) and one parameter affecting the corrosion rates (pH, applied potential, temperature, etc...) to the corrosion-erosion rate ratio [18]. By this relation, the effect of these parameters on erosion-corrosion maps and how they influence the total wastage of the material under investigation can be revealed. The transition between the erosion-corrosion regimes can be identified and determined accordingly [19].

One limitation to this approach is that the erosion-corrosion process is dependent of all these parameters together. Although the big leap of relating the erosion-corrosion mechanisms to specific two variables, it yet does not provide the effect of all the parameters that influence the erosion and corrosion rates at the same time [20].

Another important limitation of 2D erosion-corrosion maps, is that cannot monitor the influence of the parameters that affect both erosion and corrosion process together. One example of these parameters is the environment temperature. Increasing temperature affects erosion by decreasing the mechanical properties of the target material [21]. An increase in temperature will decrease the hardness of the material and hence increase the brittleness which leads to changing in material response to the impact angles or velocities [22]. Meanwhile, increasing the temperature will also decrease the viscosity of the carrier fluid which increases the impact velocities and consequently erosion.

On the other hand; in active environment, temperature rise will also increase the dissolution rates of the target metal. Furthermore, changing the environment temperature will accelerate the rate of passive film formation and as a result; it will affect the ability of the material to create the protective layer that helps prevent more wastage due to dissolution [23].

Computational Fluid Dynamics (CFD) recently becomes one of the most economical facilities used to predict erosion and fluid affected corrosion (FAC) rates [24]. However, no one to date has introduced a methodology to predict the erosion-corrosion regimes regions of domination or the total wastage transition regimes of the erosion-corrosion process on practical surfaces such as pipes and slurry pumps blades.

In this study, a new methodology has been developed to combine the computational fluid dynamics techniques with the concept of erosion-corrosion maps. A case study is used to validate and simulate the erosion rates on the interior surfaces of a pipe bend carrying a slurry fluid flow. The erosion and corrosion rates at different conditions are then predicted and the methodology for constructing the 3D erosion-corrosion maps is introduced. The effects of the common parameters that influence erosion-corrosion process and their influences on the 3D maps are investigated and evaluated. The elevated temperature levels to values near boiling point of water are studied and 2D erosion-corrosion maps are constructed to monitor the temperature effect on the erosion-corrosion transitions. Three dimensional maps are constructed and compared to 2D erosion-corrosion maps for the same temperature range.

Chapter 2

LITERATURE REVIEW

2.1 General

Wastage as a result of the combined effects of the erosion-corrosion by solid particles is a major factor of many industrial economic costs and damages. There is an interaction between the two processes, which results in the presence of residual effect. This influence may be additive, synergistic, or antagonistic [1]. The synergistic effect of both erosion and corrosion may cause rapid metal wastage of many industrial species such as pipelines and internal parts of engines, while erosion-corrosion rates decrease in the case of antagonistic effect [25, 6].

In erosion model selection for any engineering application, one must consider the type of multiphase flow under investigation. Coupling between the erosion modelling and fluid mechanics was found very important in predicting the erosion rate on the target material surfaces [26]. Thus, a comprehensive study for the types of particulate flow is necessary to understand the bonds between the fluid flow mechanics and the suspended particles within.

In this chapter, a broad literature review is presented to cover the major investigations carried out in erosion, corrosion, and interaction between them in the erosion-corrosion process. the review will concentrate on the following aspects:

(i) Erosion and corrosion in aqueous slurry flow.

(ii) Erosion of ductile and brittle materials.

(iii) Aqueous corrosion of metals and its modelling techniques.

(iv) Methods used to simulate the erosion rate process specifically CFD methods.

(v) Interactions of erosion and corrosion in the erosion-corrosion systems.

2.2 Dispersed flow

A very earlier study for particulate flow was found in the 19^{th} century, when Boussinesq in 1877 [27] studied the sediment transport in open channel. Since this date, numerous studies have addressed the analysis of different particulate flows regimes,

for example [7, 28]. The purpose of this section is to provide a brief introduction for the particulate flow and its applications from the erosion and corrosion point of view. A special focus in the slurry flow will be given to investigate the strong connection between the slurry flow and the degradation of metals due to erosion-corrosion process.

2.2.1 Classification of dispersed flows

Considering two-phase flow, particulate flow can be classified according to the phase couplings to the following [29]:

(i) *Gas-solid flow.*

(ii) *Gas-liquid flow.*

(iii) *Liquid-gas flow.*

(iv) *Liquid-solid flow.*

The latter is referred to slurry flow which represents the flow of solid particles in a carrier liquid. Particulate flow in aqueous conditions has been the subject of much research in recent years concentrating on a very wide range of materials and conditions [30, 31, 32]. Transport of slurries has a wide spread in industries such as coal, minerals, crude oil, mines, and food industries. Such wide applications make the slurry flow one of the most important type of flow that attracts most of the erosion-corrosion researches during the past three decades [33].

2.2.2 Aqueous slurry flow and erosion-corrosion

In their study to the sand-oil flow in slurry pumps, Llewellyn et al. [34] reported that slurry pump impeller experienced extremely high wear as illustrated in Figure 2.1. Therefore, large number of researches have been carried out to investigate the effect of the erosion-corrosion process in aqueous slurry flow. These studies have been done by experimental and modelling programs [35, 3, 36, 37].

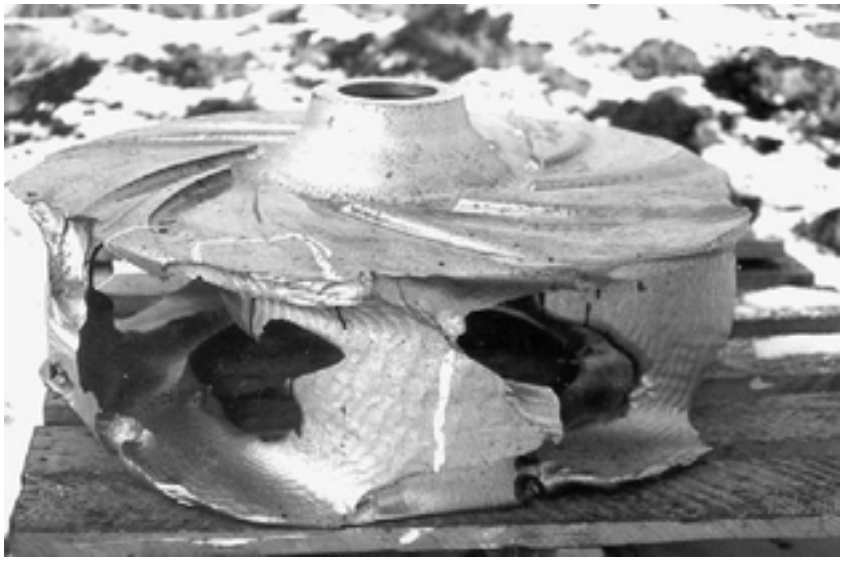

Figure 2.1: Worn 1m diameter, high Cr white iron impeller after 3 months use in an oil-sand slurry pump [34].

Variety of test rigs have been developed to achieve better understanding of the erosion-corrosion process in aqueous environment. Zu et al. [38] designed a slurry impingement jet type test rig. Another type of test rig have been designed by Tsai et al. [39] which is well known as slurry pot tester. According to their literature review, Desale et al. [40] reported that slurry pot testers comparably gives better results in pipeline wear. Clark and Hartwich [41] listed the advantages and disadvantages of the jet test rig and slurry pot tester, from which table 2.1 have been constructed to compare between the two types of test rigs.

There are many researches listed and investigated the parameters that affect the slurry erosion-corrosion process. Clark [32] studied the effect of several parameters including slurry flow speed and particle size on the erosion in slurries using a slurry pot device. The results indicate the importance of isolating the corrosion process parameters in any erosion analysing experiments to get qualitative results. Stack and Pungwiwat [42] experimentally revealed a threshold value for the slurry flow velocity below which, no erosion occurs. In general, the parameters that affect the erosion-corrosion process can be summarised as [19, 32]:

(i) *Solid particle parameters:* such as particle hardness, particle size, particle size distribution, particle impact velocity, particle impact angle, and particle shape

Table 2.1: Comparison between Slurry jet and pot testers based on [41].

	Slurry jet tester	Slurry pot tester
particle-particle interaction	high even in low particle concentration	depending on the particle concentration
impact velocity	can be varied due to particle-particle interaction	homogeneous distribution of particles make it dependant of the stirring speed
impact angle	can be varied due to particle-particle interaction	can be adjusted easily by pre-adjustment of specimen or by the profilometry of the specimen
Adjusting and calibration	calibrated to a nominal test conditions	referenced to predetermined operating conditions.
Effect of particle size	can be determined	very complex to be estimated
Corrosion parameters evaluation	can be included during testing	can not be included
Slurry refreshing	provide fresh slurry flow (self recirculating device)	the slurry must be replaced after a limited test time

factor.

(ii) *Slurry flow parameters:* such as liquid flow velocity, turbulence, squeeze film effect, temperature of the carrier fluid, and pH value.

(iii) *Target material parameters:* hardness, elasticity, toughness, wall smoothness, applied potential on the surface, temperature of the target material surface, and Tafel slope value.

The need to understand each process (erosion, corrosion, erosion-corrosion) and explore the recent advances in every distinct field is important to determine the future directions and requirements.

2.3 Erosion by solid particle impact

Historically, the word erosion derives from the Latin verb "rodene", which means to wear away gradually [43]. The study of surface degradation by the impact of small solid particles has been carried out for many years, when an erosion model was proposed by Finnie in 1958 [44]. Since then, great attention has been given to the study of the material wear due to the impact of solid particles to ductile and brittle materials. Several models were proposed to predict the erosion rates accompanied by some experimental tests to validate these models [45, 46, 47, 48].

In order to understand the erosion process and its nature, a brief study of the modelling research that have been done up to date will be introduced. The classification of the types of these models and the difference between each erosion mechanisms are discussed in the following subsections.

2.3.1 Erosion models classifications

Erosion models have been classified according to several categories. In their extensive statistical study, Meng and Ludema [7] classified erosion models according to their proportionality to the erosion parameters to:

(i) *Empirical erosion models:* these models were very common in the period between 1947-1970 and they were constructed directly from the experimental tests taken under specific conditions. Typically empirical equations are valid only within the range of the test and usually fail outside these ranges. Example of these kinds of developed models are found in [49] and [50].

(ii) *Contact-mechanics-based erosion models:* Many of these equations are based on the assumption that the mechanical material properties; usually Young modulus (E) or hardness (H), will be important in the wear process. They introduced Archad's model [51] as an example of these kinds of models. These models appear between 1970-1980.

(iii) *Failure mechanism erosion models:* The use of the Scanning Electron Microscope (SEM)technology revealed that in the microscopic scale, the material response to the impact of solid particle differs. Therefore, scientists recognised these differences in the material failure, and they found that not only the mechanical properties that control the erosion process, but also the fatigue propagation parameters such as the toughness factor and fracture strain rate are also important. This leads to the evolution of another type of erosion models that distinguished between the erosion mechanisms. One example of these kinds of models is one developed by Challen [52] and Sundararajan first and second model [53, 54].

From another point of view, Lyczkowski et al. [28] classified the erosion models according to their applicability to:

(i) *Single-particle (dilute phase) models:* these models assume the erosion process as aresult of a single particle impacting a flat surface. The material removal mechanism may be ductile, brittle or combination of both modes. These kinds of erosion models are more applicable for the dilute two-phase flow (gas-solid or liquid solid) and the particle-particle interaction is neglected. Most industrial applications involve dilute flow and these erosion models are used widely to describe the erosion rates in two phase flow. Finnie's first model [44], Bitter's model [45, 46], and Neilson-Gilchrist model [47] are considered three examples of the single particle erosion models.

(ii) *Dense phase models:* when the solid phase volume fraction considered higher than 10% of the bulk flow, the flow is said to be dense flow, and the single particle models are not applicable. The dense flow models consider the repeated impact of the solid phase bulk on these walls, which makes a repeated cycles of fatigue failure on the wall surfaces. These models were used to predict the erosion rates in applications like the fluidization beds and food production lines such as sugar and salt packing industries. One example of these erosion models is the one developed by Soo [55].

(iii) *Power and energy dissipation models:* The main trend in these models is to treat the solid flow as a continuum like the fluid flow and calculate the material removal as a result of the solid phase shear stress on the contacted walls. One example of these models is the one developed by Bouillard and Lyczkowski [56].

The erosion-corrosion in aqueous slurry flow for most applications is characterised by its low particle concentration. Because of its severe consequences, several filtration systems and controls are designed to reduce the material degradation. Therefore, aqueous slurry flow is always considered a dilute particulate flow. For this reason, it is not the scope of this study to provide a detailed literature for every erosion models type. This study will concentrate on the single particle type erosion models which used to simulate the erosion due to dilute slurry flow.

2.4 Single particle erosion models

The single particle erosion models handle the erosion process as a cumulative removal of target material by repeated impact of individual particles. They usually used in cases where the particle-particle interaction is ignored. The solid phase is treated as a discrete phase. Thus, the Newtonian equations of motion can be applied to identify the trajectories of each particle and the impact characteristics [28]. All famous and pioneer works in erosion modelling are based on the single particle interaction with the target material.

2.4.1 Finnie's erosion models

The first model reported for predicting the erosion rate due to a single particle impact is by Finnie [44]. The model based in studying the removal of ductile target material by impact. The model assumes that the particle cuts a small amount of the target material equal to the cross-sectional part of the particle immersed in the target material surface, and related to the length of contact between them.

Analysing the equation of motion of the solid particle, Finnie [44] came up with a model to predict the erosion rate in ductile materials by solid particles impact. To simplify the problem, Finnie [44] has made some assumptions. For example, he assumed that the ratio between the vertical and horizontal force components on the particle during the impact is constant; which practically is unmeasurable value, but can be adjusted to experimental data [28]. The final formulation for the volume removed per impact is given as:

$$E_{C-F} = C_f \frac{V_p^2}{P_H \psi K} f(\alpha) \tag{2.1}$$

where

$$f(\alpha) = \begin{cases} \sin(2\alpha) - 4\sin(\alpha) & \tan(\alpha) \leq \frac{K}{6} \\ \frac{1}{4}\cos^2(\alpha) & \tan(\alpha) > \frac{K}{6} \end{cases} \tag{2.2}$$

Finnie [57] recommended values of 1 and 2 for (ψ) and (K) respectively. Figure 2.2 shows the experimental work by Finnie and the model prediction of erosion rate

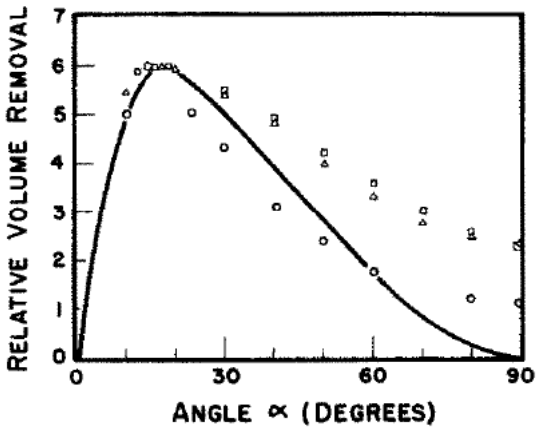

Figure 2.2: Predicted variation of volume removal with angle for a single abrasive grain compared with Experimental points for erosion by many grains (a) copper [△], (b) SAE 1020 steel [□], (c) aluminium [○]) are plotted so that the maximum erosion is the same in all cases by Finnie [57].

varied with impact angles for several grains.

The model was capable of predicting the impact angle at which the erosion is maximum. The disadvantage of this model is that it under-predicts the erosion rates above impact angle of 45^o, while it gives zero erosion at normal impact angle [28]. Another disadvantage is that, the particle shape factor is not included as an erosion parameter. This means that round particles may give the same erosion rate as the sharp ones, which practically is not true.

To overcome this disadvantage, Finnie modified his original model and inserted the moment of inertia of the particle to account for the particle shape [58]. The results of this modified model showed slight difference from that of the original one. Finnie concluded that the impact velocity is considered the main parameter that affects the erosion process [59].

In 1966, Sheldon and Finnie introduced their brittle erosion model [60]. Unlike the ductile erosion mechanisms, the model described the erosion mechanism in brittle materials as a result of cracks propagation and chipping. The wear at normal impact was investigated to relate the velocity exponent to the coefficient of friction between the target material and solid particle during the impact.

Although Finnie's models are considered now as a historic interest [28], they have

been used in recent researches in combination with the what so called the kinetic theory erosion models to predict the erosion rate in dense types of flow like fluidised-bed inside heat exchangers [61]. They are also used in numerical investigations of some industrial applications [62, 63].

2.4.2 Bitter's erosion models

Extending Finnie's original work, Bitter [45, 46] assumed that the ductile and brittle erosion mechanisms (namely: cutting and deformation mechanisms) are acting at the same time. Bitter applied some corrections and modifications to Finnie's work by introducing the concept of the threshold energy needed for erosion initiation [45]. The threshold energy was represented in the model by applying the threshold velocity. The threshold velocity can be related to the elastic limit of the target material above which the material begins to deform plastically. The model is introduced in two equations as follows, for the brittle erosion (deformation mechanism) [45]:

$$E_{D-B} = \begin{cases} \frac{m_p \left[V_p \sin(\alpha) - V_{el}\right]^2}{2\,\varepsilon_b} & for\ V_p \sin(\alpha) > V_{el} \\ 0 & for\ V_p \sin(\alpha) \leq V_{el} \end{cases} \tag{2.3}$$

and for ductile erosion model (cutting mechanism) [46]:

$$E_{C-B} = \begin{cases} \frac{2\,m_p\,C'\left[V_p \sin(\alpha) - V_{el}^2\right] V_p \cos(\alpha)}{\left[V_p \sin(\alpha)\right]^{0.5}} - \frac{C'\left[V_p \sin(\alpha) - V_{el}\right]^2}{\left[V_p \sin(\alpha)\right]^{0.5}} \phi_c & \alpha \leq \alpha_o \\ \frac{m_p \left[V_p^2 \cos^2(\alpha) - K_1 \left(V_p \sin(\alpha) - V_{el}\right)^{1.5}\right]}{2\,\phi_c} & \alpha > \alpha_o \end{cases} \tag{2.4}$$

Bitter corrected the inefficiency in Finnies models. In ductile materials [46], it is observed that the erosion at normal impact is not zero as in Finnie's model. The maximum erosion rate in the case of brittle erosion was observed at normal impact, which is consistent with the experimental findings [45]. The involvement of the threshold velocity also overcomes some of the experimental contrasting with the Finnie's models [57]. The substantial advance was the inclusion of more target material and particle properties than that of Finnie's model. The shortcoming in

the Bitter's erosion model is that, it contains some material factors that are semi-empirical factors, which must be defined through experimental work [28].

2.4.3 Neilson-Gilchrist erosion model

Neilson and Gilchrist [47] continued the work of Bitter and introduced their model; which is similar to Bitter model, but differs in some points. First, they included another threshold velocity term which account for the parallel velocity component of the particle (V_t), which is dependant of an empirical constant (n). The brittle expression is the same while the ductile expression is more simple than that of Bitter [45, 46]. They proposed an easy procedure to get the material properties factors by the mean of the empirical constant (n). The model is in good agreement with the experimental results, but again it depends on the empirical constant determination and the same semi-empirical factors in Bitter's model. The only material that was investigated to determine its factors was the Aluminium. No further detail for any other material is found.

The model is proposed in two expressions; the total erosion is simply the addition of two parts; one account for the cutting erosion mechanism and the other represents the deformation erosion mechanism. The two parts have different expressions depending on (α_o), which defined as the impact angle at which the first expression gives the same erosion rate as the second expression. The formulations are given as [47]:

$$E_{N-G} = \begin{cases} \frac{m_p \left[V_p^2 \cos^2(\alpha) - V_t^2\right]}{2\,\phi_c} + \frac{m_p \left[V_p \sin(\alpha) - V_{el}\right]^2}{2\,\varepsilon_b} & \alpha \leq \alpha_o \\ \\ \frac{m_p \left[V_p^2 \cos^2(\alpha)\right]}{2\,\phi_c} + \frac{m_p \left[V_p \sin(\alpha) - V_{el}\right]^2}{2\,\varepsilon_b} & \alpha > \alpha_o \end{cases} \tag{2.5}$$

Unfortunately, there is no evidence of continuing Neilson-Gilchrist work to determine the material cutting and deformation parameters. Although some publications suggested these parameters values for stainless steel [64] and later these parameters values used successfully to predict erosion rates by [65] and [66], but no experimental efforts have been done to identify the values of these parameters for further materials, which is thought the main reason for the restriction on the use of this model

widely.

2.4.4 Hutchings' erosion model

Hutchings introduced his normal impact erosion model in 1979 [67] with a new concept of erosion as a low cycle fatigue process, which means serial of plastic and failure deformation occurs after less than $(10^4 - 10^5)$ cycles of strain. By using the approach of Coffin-Manson, he extracted a simple relation between the erosion rates of ductile materials at normal incidents. He argued that the low cycle fatigue erosion mechanism can be used to explain the erosion at normal impacts [67]. Using others experimental results, he concluded that the effect of transient pressure during impacts may not affect the erosion process.

Hutchings [67] assumed that the amount of energy required to create a fixed indentation in the metal target must equal the kinetic energy of the solid particle. By this assumption, Hutchings ignored the effect of elastic range of material on absorbing some of the particle energy, nor the energy reserved for the rebound process [67]. Although the model includes three target material dependent factors, these factors are not responsive to direct measurement. Finally, the model introduced was not congruent with the experimental results, but it gives an indication of the importance of the inclusion of more material properties that may affect the erosion process, even in a special case like the normal impact condition.

In 1981, Hutchings [68] revised his earlier investigation by including the critical strain as an erosion process parameter. The model proposed (the critical strain model) still contain unmeasurable values like(α/ε_c^2) and dynamic hardness, but he assumed a constant value for the former (0.7) and related the latter to the Vickers micro-hardness and static hardness of the target material.

2.4.5 Sundararajan's erosion models

Introducing a new criteria; a what so called critical plastic strain, Sundararajan and Shewmon [53] proposed their normal impact erosion model in 1983. Similar to Hutchings critical strain erosion model [68], Sundararajan's first model was based on

the idea of the localisation of deformation. When a particle collides with the target material surface, the indentation occurred forms an expelled lip on the crater edge. This lip is removed by the subsequent impact of the other particles in the form of thin platelets [53].

The difference between the two models was in the way how the critical strain is derived. Sundararajan and Shewmon related the removal of the material during normal impact to cumulative strain within the area of impact when it exceeds the critical strain needed for material separation. The erosion rate may be given by [53]:

$$E_{S1} = \frac{6.5 \times 10^{-3}\, \rho_p^{025}\, V_p^{2.5}}{C_p\, T_m^{0.75}\, H_s^{0.25}} \tag{2.6}$$

The other notable advantage of the localisation model is its capability of capturing the experimental results better than the fatigue model by Hutchings [68]. The inclusion of the thermodynamical and mechanical properties results in a model that account for the thermo-physical nature of the erosion process which enhanced the model predictiveness. Comparing with the experimental data taken from several resources; the localisation model was able to explain the essential features such as the velocity exponent, and correlated well with the erosion rate results [53].

Later, Sundararajan has introduced his second erosion model for oblique impacts [54]. The model based on the combination between the concept of the localisation of plastic deformation and the work of Brach [69], who introduced a new analytical model to equate impulse and momentum for an arbitrarily shaped rigid body striking a flat massive surface at any impact angle.

The model makes use of the normal coefficient of restitution (e_n), and tangential friction coefficient (μ_f), which is defined as the coefficient of friction at the contact surface between the colliding particle and the target material [54]. In the deformation equation, the effect of energy absorption for high impact angles is considered by the use of the normal coefficient of restitution (e_n), while the energy absorbed by shear in oblique angles is regraded by the coefficients of friction (μ_f, μ_{fc}). The model is introduced through two equations; one considers the localised deformation at the impact region which may be removed by the subsequent impacts and is given

by [54]:

$$E_{D-S} = \frac{5.5 \times 10^{-2}}{(T_m - 436)^{0.75}} \frac{2^{n_c} f_t \ (V_p \, sin \, \alpha)^2 \, (1 - e_n^2)}{n_c \, C_p} \tag{2.7}$$

The inclusion of the coefficient of friction in the model accounts for the energy absorbed in the shear associated by the impact process. In the deformation erosion equation, (f_t) is a numerical factor accounts for the fact that multiple impacts are required to gain the needed critical strain to remove a chip from the material surface. This factor is not found in the ductile erosion equation where one impact can effectively remove an amount of the target material [54].

The other equation referred to the ductile cutting mechanism during the impact and is given as [54]:

$$E_{C-S} = \frac{5.5 \times 10^{-2}}{(T_m - 436)^{0.75}} \frac{(n_c + 1) \left(\frac{\mu_f}{\mu_{fc}}\right) \left(2 - \frac{\mu_f}{\mu_{fc}}\right) (V_p \, cos \, \alpha)^2}{2^{(2-n_c)} \ (1 + \lambda) \ n_c \, C_p} \tag{2.8}$$

Another factor is also included to account for the particle shape (λ), which takes values from [0] for mass-less particle to [3] for sharp particles [69, 54]. The target material properties are indirectly implemented in the model by the inclusion of the normal coefficient of restitution (e_n), which was related to the static hardness and modulus of elasticity for collision in various publications [70]. The temperature effect is not included, but in the other hand, the material heat capacity and the melting point indicate the thermo-physical properties that are superior for the critical strain erosion modelling [54].

Although the second model of Sundararajan has an attractive potential to be one of the best models developed so far, as it includes a variety of variables that affect the erosion process, it is not used extensively in erosion applications and researches. The only shortcoming for this model is that it does not relate the use of Equations 2.7 and 2.8 to any angle ranges. Sundararajan [54] suggested using Equation 2.8 up to impact angle of 30^o, and Equation 2.7 for angles higher than 60^o, while summing both equations for the region in between, but this must be decided by experimental tests.

2.4.6 Other erosion models

As mentioned before, there are many erosion models have been developed by researchers. In 1995, Meng and Ludema [7] counted more than 300 equations from only the wear journal and wear of materials conferences from 1957-1991. Since then, several models have proposed most of them are empirically developed. In this section, a review of some of these models will be introduced within the period from 1995 to present.

Forder et al [48] developed an erosion model to predict erosion rates in computational fluid dynamics applications. The model based on a combined deformation and cutting erosion models. The model assumes that the ductile (cutting) and the brittle (deformation) occur simultaneously at any impact angle. A stress field is produced within the contact surfaces between the particle and the target material, causing a plastically deformed sub-layer beneath the surface. When the stress is greater than the yield strength of the target material, erosion by separation of the micro-cracks takes place. The formulation of this model is given as [48]:

$$E_{Forder} = \frac{100}{2\sqrt{29}}\, r_p^3 \left(\frac{V_p}{C_k}\right)^n \sin(2\alpha)\ \sqrt{\sin(\alpha)} + \frac{m_p\ (V_p \sin(\alpha) - D_k)^2}{2\,\varepsilon_b} \qquad (2.9)$$

where (C_k) and (D_k) are the cutting and modified deformation characteristic velocities respectively. The model was in good agreement with the experimental work and was hooked easily to the CFD commercial program (CFX). Forder gave a value of 2.54 for the velocity ratio exponent (n) in case of carbon steel target material and some other alloys [48]. The model has been considerably used in CFD erosion simulation [71, 72].

O'Flynn et al. [73] introduced their erosion model which based on the correlation of the impact angle function to the experimental work done for a series of test materials at elevated temperature. They presented a new material parameter that thought to influence the erosion process, namely the target material toughness and uniform strain. The model well predicts the erosion rate at the temperature range from $(200^oC - 300^oC)$ but gives unsatisfactory results at room temperature. They

suggested that this behaviour results from the model dependency of the localised heating during impact and the high strain-strain rate deformation during the erosion process [73]. The model formulation is as follows [73]:

$$E_{O'Flynn} = \frac{V_p^2}{\varepsilon_U U_T} \left(a \cos^4(\alpha) + b \sin^2(\alpha) \right) \tag{2.10}$$

where a, b are empirical constants determined by curve fitting the experimental test results. The material toughness can be related to the temperature difference to the room temperature; assuming adiabatic process, by [73]:

$$U_T = \rho_t C_p \Delta T \tag{2.11}$$

where (ρ_t) is the density of the target material and (C_p) is its specific heat capacity. The idea of superimposing the temperature effect through the material properties can be also used in the fluid properties, such as the density and viscosity. The model assumes; by contrast to the Sundararajan's second model [54], that upward strain flow around the impacting particle does not need prior work hardening for lip separation [73].

In their investigation of the erosion due to fly ash impingement on the internal surfaces of the boiler furnaces in coal-fired power stations, Mbabazi and coworkers [74] developed an erosion model that included the properties of the ash particles and the target metal surface, along with the characteristics of the ash particle motion in the form of the impact velocity and angle. When compared using the experimental results in their study, the model deviated by less than 15%, which considered fairly accepted. The model assumes erosion by cutting and deformation mechanisms, and the final total erosion is given by [74]:

$$E_{Mbabazi} = \frac{K_t \, x^{4.95} \, \rho_t \, \rho_p^{0.5} \, V_p^3 \, \sin^3(\alpha)}{Y^{1.5}} \tag{2.12}$$

One important result from this research is that the silica content of the ash particles has a large influence on the erosion rate for mild steel, which gives another factor that influence the erosion process [74]. Using the idea of superimposing the effect of the operating temperature that had been applied by [73], Das et al. [75] used

Mbabazi's model to simulate the erosion rate for several materials and alloys. The model predictions have been found to be in good agreement with the published data [75].

In 2008, a very sophisticated erosion model has been developed by Nandakumar et al. [76]. The erosion model was described as a phenomenological model which captures most of the particle, fluid, and target material parameters that affect the erosion process. Unlike any other models that usually investigate the energy dissipated through the impact process, they examined the forces acting on the particle during the impact process and its relation to the cutting and deformation erosion mechanisms. The simplified form of this model is introduced as [76]:

$$E_{Nandak} = D\,\rho_p^{0.1875}\,d_p^{0.5}\,V_p^{2.375}\,\left(\cos\left(\alpha\right)\right)^2\,\left(\sin\left(\alpha\right)\right)^{0.375} \tag{2.13}$$

For deformation mechanisms, the model revealed that the exponent of the particle's mass is independent on the target material, while the exponents of particle's impingement angle, velocity and density depend on the properties of target material. In the cutting case, the model suggested that the range of the exponent of impingement velocity is 2-2.75 which is consistent with the experimental findings. Moreover, the cutting removal also pointed out that erosion rate has little dependence on particle size [76].

All the listed models are not the only models that have been created in the literature, but are likely examples of them during the last 15 years. Most of these models are characterised by the implementation of some empirical constants that are curve fitted or correlated to attached experimental work [73, 74]. Although some recent erosion models have good agreements with the experimental tests [73], they still need to be more quantitatively tested by applying them to more experimental tests or industrial applications.

The most useful point from the former models [73, 75], is that it is possible to modify any erosion model parameter to account for the effect of the elevated temperature if the suitable relation between this parameter and the operating temperature can be found. This concept has proved promising results in tracking the influence of the operating temperature on the erosion rate prediction.

2.4.7 Erosion and CFD

The erosion modelling is categorised by its engagement to the computational fluid dynamics techniques. The nature of the two phase flow governs the selection process of the erosion model and how it is implemented into the CFD solver. Multiphase flows are numerically investigated using two different methods. The first method is using Lagrangian-Eulerian approach where the suspending fluid is simulated using Navier-Stokes equations, and the dispersed or the secondary phase is studied by applying the equation of motion for the solid bodies [77, 63].

The second method utilises the Eulerian-Eulerian approach where the two phases are treated as two continuum; therefore, it requires applying the effect of the phase volume fraction for each phase. The first method (L-E) is suitable for investigating the dilute multiphase flows as they assume no collisions between particles and the trajectories of every particle can be modelled [64, 78, 66]. On the other hand, dense flows are studied by using the second method (E-E) because the particle-particle interaction affects the particles trajectories; thus, the correct impact properties (locations, velocity and angle of impact) of the particles are very hard to estimate [79, 80].

2.5 Corrosion in aqueous flow

Briefly, Corrosion is the deteriorate attack of a material by chemical or electrochemical reaction with its environment [81]. In practical applications, the term aqueous corrosion referred to the corrosion process in aqueous medium. In aqueous medium, corrosion is an electrochemical process where any reaction consists of two partial reactions, namely the anodic partial reaction and the cathodic partial reaction. The electrochemical reaction is characterised by the release of free electrons. As a result of the electrons release, the metal ions are evolved from the metal surface in contact with the aqueous solution (electrolyte), and the metal is said to be dissolved. For the reaction process to complete, it is necessary the two partial reactions are activated [82].

For example the dissolution of iron in an acidic solution; which is illustrated in Figure

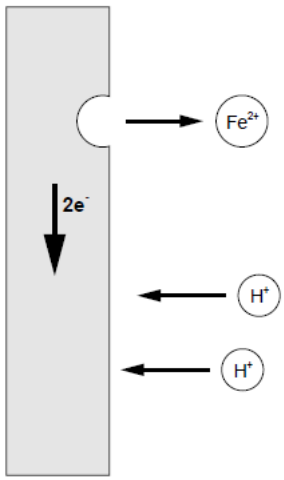

Figure 2.3: Simple model describing the electrochemical nature of corrosion processes [81].

2.3, is governed by the following overall reaction [81]:

$$Fe + 2H^+ \rightarrow Fe^{2+} + H_2 \tag{2.14}$$

this overall reaction can be divided to the following anodic and cathodic partial reactions respectively

$$Fe \rightarrow Fe^{2+} + 2e^- \tag{2.15}$$

and

$$H^+ + 2e^- \rightarrow H_2 \tag{2.16}$$

The corrosion rate is dependent of the electric current that produced from the migration of the released electron from the anode to the cathode through the metal or the corrosion circuit. If this current is known, the dissolution rate of one molecule of corroded metal can be computed by using Faraday Law [8]:

$$K_c = \frac{RAM\, i_{anet}}{z_m\, F} \tag{2.17}$$

where $(RAM)$is the molecular weight of the metal, (i_{anet}) is the partial anodic current density in $[A\, m^{-2}]$, $(z_m)$is the number of electrons released or exchanged during the

dissolution reaction per atom of the dissolved metal, and (F) is the Faraday number.

A detailed study is taken to understand corrosion process and the parameters that influence this process in aqueous conditions. In his review, Kritzer [23] classified these factors according to the target material parameters, and electrolyte parameters. The electrolyte corrosion determining factors can be summarised as:

(i) Ionic reactions and oxide film stability,

(ii) Temperature.

(iii) Electrolyte pH-value.

(iv) The electrochemical potential and the solubility of gases.

(v) Influence of anions.

while the material corrosion parameters can be listed as:

(i) Alloy composition.

(ii) Heat treatment and surface conditions.

Studying the thermodynamics of the corrosion reactions is fundamental to understand the corrosion process. In the following subsection, a presentation of the thermodynamics of the electrochemical corrosion reaction is introduced to illustrate how these basics are important in corrosion modelling.

2.5.1 Corrosion thermodynamics

Pourbaix [17] constructed the E-pH diagrams for several metals. Pourbaix diagram is a graphical illustration of the possible corrosion phases or products at equilibrium for a metal/H_2O system at any operating temperature. Some interesting benefits of these diagrams are [81]:

(i) To estimate whether or not corrosion can occur at certain circumstances (pH, applied potential, and operating temperature).

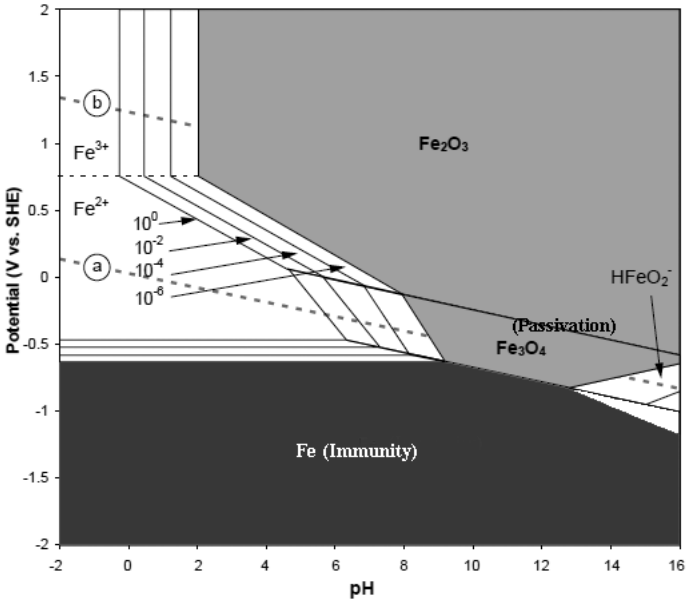

Figure 2.4: E-pH equilibrium diagram for the iron-water system at 25°C [81].

(ii) To identify the corrosion products formed and its nature (pure substances or soluble ions).

(iii) To predict the environmental changes to reduce the corrosion impact.

Pourbaix diagrams become the bases for many researches in the field of corrosion and erosion-corrosion. It was an essential tool to construct the erosion-corrosion maps [83]; which considered one of the best tools to identify the erosion-corrosion regimes and wear rate. Figure 2.4 illustrates the Pourbaix diagram for (Fe) as an example of the E-pH diagrams. In the regions between the upper and lower dotted lines (lines a, b), H_2O, H^+, $and\, OH^-$ are stable where in the regions below and above the dotted line,H_2, O_2 are stable.

Pourbaix [17] defined three regions of corrosion activities. The immunity region (dark area) where the corrosion is theoretically impossible from the thermodynamics point of view, the passivation region (shadowed area) where the oxide products of the metal are formed, and the active region (white area) where the metallic ions are released. The figure shows the variation of each region as the concentration of the soluble species changes from $(1 - 10^{-6})$. It was assumed that no corrosion is taken place if the concentration of the metal ions is lower than (10^{-6}), but in practical,

corrosion does occur, but has a negligible rate.

2.5.2 Corrosion kinetics

One fundamental characteristic of the electrode kinetics is the exchange current (I_o). The exchange current is dependent of many variables and cannot be measured. Instead, the exchange current is normalised by the interface area between the electrode and the electrolyte, which is known as the current density and has the unit $[A\,m^{-2}]$. According to Butler-Volmer expression, the net current density can be calculated as [84]:

$$i = i_o \left[\exp\left(\frac{\beta\, z_m\, F\, \eta}{R\, T} \right) - \exp\left(\frac{-\left(1-\beta\right)\, z_m\, F\, \eta}{R\, T} \right) \right] \tag{2.18}$$

The term (η) is the over-potential or the polarisation of the reaction. it is defined as the difference between the resultant or applied potential (E_{ap}), and the equilibrium potential of the reaction (E_{rev}). There are three types of polarisation and they are additive; namely: activation polarisation, concentration polarisation, and ohmic polarisation. They can be expressed as:

$$\eta_{total} = \eta_{active} + \eta_{conc} + i\, R_\Omega \tag{2.19}$$

Activation polarisation is usually the controlling factor during corrosion in strong acids. On the other hand, for example, in dilute acids where the active component (dissolved oxygen) is at very low levels, the concentration polarisation controls the corrosion process. If there is a considerable seperation between the anode and cathodic sites; as in the case of crevise corrosion, the ohmic drop will become an important part. [81].

2.5.3 Corrosion modelling

There are numerous models in the literature to simulate the corrosion in both active and passive metals. In this section, only a brief introduction to some of the corrosion models found in the literature. Walton et al. [85] introduced a transient

mathematical and numerical model for crevice corrosion. The model is generalised and applicable to a variety of metallic and electrolyte systems to simulate crevice corrosion. The model was compared to previous experimental data and found to be satisfactory.

Based on the laws of physical chemistry, Botte et al. [86] presented a numerical simulation approach of iron dissolution in a corrosion process. The proposed model describes the development of the corrosion current and the concentration of each ionic species involved in the redox reactions, then it allows the evaluation of the corrosion rate of a sample. The drawback of this model is represented; as stated by the authors [86], by the discredited system of equations whose numerical solution is quite demanding, partly due to the exponential behaviour of the boundary values.

Recently, Guo et al. [87] proved experimentally that corrosion-enhanced erosion may occur as a result of corrosion-induced surface hardness degradation. As a consequence, reduction of the resistance of materials against erosion is experienced. Based on these findings, a correlation model was developed to predict the rate of corrosion-enhanced erosion of the anodic current density, as follows [88]:

$$\frac{\Delta K_e}{K_{eo}} = Z \log\left(\frac{i}{i_{th}}\right) \tag{2.20}$$

where (i_{th}) is the threshold anodic current density to cause the corrosion-enhanced erosion and (Z) is a constant. Correlating the above equation with the theoretical models of mechanical erosion enables prediction of the erosion behaviour of metals in corrosive slurries. Lu et al. [89] hinted that this model can be used in predicting the erosion-enhanced corrosion (additive effect), even accurately, by taking the effect of corrosion-enhanced erosion into account.

2.6 Erosion-corrosion

The American Society for Testing of Materials (ASTM) defines erosion-corrosion as: " the synergistic process; involving both erosion and corrosion, in which one process is affected by the simultaneous action of the other". This synergism may be positive; in this case, the wear rate is highly accelerated. In some other cases; it has a neg-

ative sign, in which the wear is decelerated. Stack et al. [1, 90] observed negative synergism in their researches, which may occur in the erosion-corrosion process at elevated temperature [1]. Because of its very complicated nature, the interaction between the erosion and corrosion process has been investigated by many researchers and the erosion-corrosion theory has several scientific description and identifications [91, 92, 93].

The erosion-corrosion mechanisms are classified according to the interaction between the erosion and corrosion process as follows [1]:

(i) *The additive effect:* which refers to the erosion enhancement of the corrosion rate during the wear process.

(ii) *The synergistic effect:* which represents the contribution of corrosion process on the erosion rate.

(iii) *The antagonistic effect:* in which the corrosion obstructs the erosion process.

Mathematically, this can be represented by the total wear rate equation below [36]:

$$K_{ce} = K_{eo} + K_{co} + \Delta K_{ec} \tag{2.21}$$

where (K_{ce}) is the total wear rate, (K_{eo}) is the pure erosion rate in the absence of any corrosion, (K_{co}) is the pure corrosion rate in the absence of erosion, and (ΔK_{ce}) represents the overall interaction between the two processes, which can be given by:

$$\Delta K_{ce} = \Delta K_c + \Delta K_e \tag{2.22}$$

where (ΔK_c) is the additive effect in which the erosion process enhances the corrosion process, and (ΔK_e) is the synergistic effect by which the corrosion contributes to the erosion process. From these distinct types of erosion-corrosion mechanisms, Stack et al. [94, 1] identified the erosion-corrosion regimes boundaries as follows:

$$Erosion\,Dominated: \qquad \frac{K_c}{K_e} < 0.1 \tag{2.23}$$

$$Erosion - corrosion: \qquad 0.1 \leq \frac{K_c}{K_e} < 1 \tag{2.24}$$

$$Corrosion - erosion: \qquad 1 \leq \frac{K_c}{K_e} < 10 \tag{2.25}$$

$$Corrosion\, dominated: \qquad \frac{K_c}{K_e} \geq 10 \tag{2.26}$$

The aim of this section is to provide a brief review of the literature available on the erosion-corrosion interaction. The basic advances in monitoring this effect are introduced, and the science contributions that have been made specifically in analysing the additive and synergistic effects are interviewed.

2.6.1 The additive effect

The additive effect is the term that describes the process of erosion accelerated corrosion and has been studied widely in the past. As a result, number of synopsis have been presumed. Wang and Postlethwaite [95] used the low Reynolds number $(k - \epsilon)$ turbulence mode1 to investigate the effect of mass transfer on corrosion rate. The surface concentration of dissolved metal ions decreases with rising Reynolds number and increases when the corrosion is active controlled. In case of the concentration controlled corrosion, however, the surface concentration of dissolved metal ions and surface pH do not vary with Reynolds number. The Reynolds number is an important parameter in any fluid flow and is used as a scale for the fluid flow turbulence. On this spot, the conclusion that the corrosion is strongly related proportionally to the turbulence level and shear stress of the fluid flow.

Erosion enhanced corrosion for carbon steel was also analysed by using Mott-Schottky analysis and the point defect model (PDM) by Guo et al. [96]. They found that although the polarisation curves suggested that carbon steel showed comparable passive behaviour in solutions with different solutions concentrations, the erosion-enhanced corrosion resistance increases with solution concentration significantly.

In a recent study, Liu et al. [97] investigated the effect of the flow enhanced corrosion of carbon steel in seawater flow. On driving a corrosion model for laminar and turbulent flow cases, they found that the corrosion rate is strongly dependent on the oxygen concentration, fluid velocity, and the corrosiveness of the seawater.

A direct proportionality of the corrosion rate with wall shear stress, mass transfer coefficient was made [97]. However, in the case where a cathodic protection current is implemented to the carbon steel specimens, the damage rates of the carbon steel decreased substantially and the degree of cathodic protection of carbon steel flow enhanced corrosion at velocity range from 0-18 $[m\,s^{-1}]$ was greater than 95% [97].

Stack et al. [94, 12] stated that the additive effect and the synergistic effect appearance in an erosion-corrosion system depends on the erosion parameters; specifically the velocity of the slurry, and the corrosion parameters (potential). In addition, they can occur in both the active and passive conditions.

The continuous removal of passive layer was found the result of 15-42 % of the total wear rate at different impact angle for Co-steel alloys [92]. In a recent study, Niu et al. [98] studied the synergistic effects of fluid flow and sand particles on erosion–corrosion of 3003 aluminium (Al) alloy in ethylene glycol–water solution to simulate the automotive engine coolant through a rotating disk electrode by electrochemical measurements. It was apparent from their experimental results; when the sand particles were added, that there was a competition between the electrode oxidation and de-stabilisation, which means the exposure of fresh (oxide-free) surface; leading to increased corrosion.

2.6.2 The synergistic and antagonistic effect

In the literature, there are some postulations of the mechanisms by which corrosion may enhance the erosion rate. Postlethwaite [99] suggested an increase in the erosion rate due to the surface roughening during the corrosion process. In addition to the surface roughness effect, Matsumara et al. [100] also suggested that erosion is accelerated by corrosion through the removal of the passive film by particle impact, followed by dissolution of the surface, leading to the elimination of the work-hardened layer.

Li et al. [101] disagreed with Matsumara's work-hardening theory; based on his experimental results, and proposed another mechanism for the effect of corrosion on slurry erosion, in which localised attack at interruptions of the surface oxide (caused by the particle impacts) induces the rate of crack growth by which the flakes sep-

arated and results in a higher erosion rate. Lu et al. [88] proved experimentally that the rate of material loss produced by the corrosion enhanced erosion increases with anodic current density while the pure mechanical erosion rate increases with decreasing hardness, indicating that the hardness degradation caused by the anodic dissolution is a synergistic mechanism in slurry erosion process.

Stack et al. [94] reported that there is a small effect of the corrosion induced erosion at the transition potential between active and passive corrosion regions in mild steel. Later, the same group [102] explained this observation as environment induced fracture process. It is accepted; in some cases, that the synergistic effect is a small amount which can be safely excluded from the total erosion-corrosion wastage[83, 8].

In contrast to their findings, but using in-situ, localised, electrochemical experimental conditions,Malka et al. [2] observed that the dominant process was the effect of corrosion on erosion in the total synergistic contribution of the wear process. However, Addis [103] doubted Malka's results and repeated his experimental work when he found that under the same conditions there was no significant synergy and the summation of pure erosion and pure corrosion weight loss rate was equal to the erosion-corrosion weight loss rate. He suggested that an inhibition might be presented in Malka's system [2], which led to significant synergy that developed between erosion and corrosion.

In other point of view, the synergistic effect was reported in some publications as a negative value. Li et al. [101] observed negative synergistic effect in $Na_2\,CO_3$ slurry (equivalent pH=11.7) except at intermediate impact angles for pure Aluminium target material. This was contrary to the same experiments made by slurry with pH= 4.4 and 7; where the synergistic effect was positive. The negative sign of synergistic effect can be refered to two possible mechanisms:

(i) The increase in solubility of Al_2O_3, compared with that in lower pH (acidic) slurries would remove the tendency for passivation and the whole surface dissolution would occur, leading to blunting of the crack tips by lateral dissolution, and thus hindering the crack spreading.

(ii) The possibility that the silica erodent particles used in their experiments suffered some dissolution and hence were blunted and its erosion efficiency is

reduced.

It is acknowledged that the synergistic effect is very important and can not be neglected in some circumstances where severe corrosion experienced. In these cases, the synergistic effect must be considered as a main factor in the erosion-corrosion process.

2.6.3 Erosion-corrosion modelling

Erosion-corrosion modelling is found very difficult because of its complexity and number of factors ivolved in the erosion-corrosion process [104]. Furthermore, erosion-corrosion modelling was always subjected to specific applied conditions, and assumptions. Therefore, there were few modelling methods in the literature where they are all based on the combination between the erosion modelling, and corrosion modelling in some way or another. The erosion-corrosion modelling techniques were different as the research groups evolved these techniques are [105, 8, 106, 6]. Accordingly, in monitoring these techniques, the erosion-corrosion modelling were referred to the scientific groups who investigated and developed these models.

The model derived by Nesic and Postlethwaite [105] studied the concentration controlled corrosion. the model were developed by relating the corrosion rate to the mass transfer of dissolved oxygen through the turbulent boundary layer by using the following correlation:

$$K_c = 4923\, c_{Ob} \left(\frac{D_{O_2}}{d_{pipe}}\right) Re^{0.86}\, Sc^{0.33} \tag{2.27}$$

where (c_{Ob}) is the oxygen concentration at the bulk flow, and (D_{O_2}) is the diffusion coefficient for oxygen in the liquid (usually water). Later, Keating and Nesic [107] investigated the erosion-corrosion wear by using a numerical particle-tracking code in a commercially CFD software (PHOENICS) to predict erosion, and the same corrosion model of Nesic [108] in calculating the corrosion rate assuming concentration controlled flow in a 180^o rectangular cross sectional pipe bend:

$$K_c = \frac{2\, k_m\, c_{Ob}\, RAM}{\rho_t}\, 86400 \times 365 \times 10^3 \tag{2.28}$$

The same corrosion model was used recently by Davis and Frawley [37] who re-simulate the experimental work of Postlethwaite [105] of a sudden expansion piping flow. By modification of the above equation, they indicated that in order to predict erosion-corrosion in practical geometries successfully, the computational mesh must be Sherwood number independent.

The models that have been developed by this group were derived for erosion-corrosion in the disturbed two phase flow and was subjected to these applications. Although disturbed internal two phase flow have a wide range of applications, these models are not suitable for identifying the erosion-corrosion regimes or erosion-corrosion mechanisms. They are suitable of determining the erosion-corrosion total wear rate.

Bozzini et al. [3] proposed a corrosion model to simulate the synergistic and additive effects using CFD. This model is suitable for evaluating both for passivating and actively corroding materials. The so called recovering target model states that each particle impact gives a rise in corrosion current density. This was in agreement with the observation made earlier by Burstein and Sasaki [109] who studied the electrochemical transients generated during solid particle erosion–corrosion. It was observed when a particle impacts a target material surface there is an increase in the current transient, accompanied with the removal of oxide film on the target material surface. Since not all the sample's area on the metal surface is affected by the particle impact, the effective corrosion current density at a given electrode potential is given by [3]:

$$i_{corr} = f_a \, i_a + (1 - f_a) \, i_u \tag{2.29}$$

where ($i_a \, and \, i_u$) are the affected and unaffected corrosion current density (referred unaffected and the affected areas) respectively, and (f_a) is the coefficient of the mechanically affected corrosion component of the synergistic damage which can be obtained by

$$f_a = I \, A_a \, \tau \tag{2.30}$$

where (I) is the impact frequency, (A_a) is the affected area, and (τ) is the recovery time. This model was implemented later to a generalised semi-empirical model

to predict erosion–corrosion [110, 6]. The disadvantage of semi-empirical models is that they are dependent of specific empirical parameters, which must be determined experimentally according to the operating conditions and materials used.

Starting from the idea that erosion-corrosion process is dependent on the applied condition, Stack et al. [12, 83, 111, 8] developed a new technique based on graphically relates the erosion-corrosion rate to the parameters influencing the erosion and corrosion processes. One parameter affects corrosion in the x-axis is plotted to another that affects erosion in the y-axis. By this method, it was able to identify the erosion-corrosion regimes and wastage boundaries and monitor the influence of every parameter in the erosion-corrosion process. Furthermore, Stack et al. [111, 8] suggested that these maps can be used for material optimisation and selection in the design stage of any application.

In addition, these maps can be theoretically constructed as well as experimentally using the available experimental data [16, 112]. In its modelling versions, Stack used various models available for pure erosion, while using the Butler-Volmer equation to calculate the pure corrosion rate with ignoring the additive and synergistic effects in the active corrosion conditions. In passive corrosion conditions, the additive effect is accounted for. Stack developed four types of erosion-corrosion maps, namely: the regime maps, wastage maps, material selection maps and synergism maps. Various parameters were investigated using these maps to evaluate the effect of these parameters on the erosion-corrosion process [84, 113] and [91, 104].

However, a limitation of the erosion-corrosion maps application to erosion-corrosion in flowing conditions is that they do not incorporate any fluid flow parameters [20]. This is in contrast with the fact that the erosion-corrosion process is influenced by the combined effect of all erosion, corrosion, fluid flow parameters simultaneously [19]. In studies of erosion–corrosion, there are no models available which attempt to combine the effects of particle erosion, corrosion and fluid flow with mapping tribo-corrosion methodologies. This has limited the characterisation of tribo-corrosion phenomena in real life environments to date.

In addition, the erosion-corrosion mapping techniques are not able to map some parameters that affect the erosion and corrosion processes at the same time like the

effect of elevated temperature. The 2D erosion-corrosion maps were constructed on the basic concept of referring the erosion-corrosion regimes and wastage boundaries to one parameter affecting the erosion rate, and another affecting the corrosion rate [19]. Since the temperature affecting both erosion and corrosion rates, it is not possible to build temperature based maps explicitly.

Although the 2D erosion-corrosion maps are particularly useful tools in the design stage for an application to predict the most optimised operating conditions for every parameter affecting the erosion-corrosion process or in material selection [20], these maps are not practical in the design enhancement or service stages. In these stages, the need for a tool to predict the combined effect of the erosion, corrosion and fluid flow parameters is preferred. This has also limited the applicability of the 2D erosion-corrosion maps to cover a wide range of applications in realistic service life period.

2.7 Thesis objective and layout

According to the previous literature study, a list of conclusions can be summarised as follows:

(i) Erosion models vary significantly according to the application under investigation. For slurry flows with velocities lower than 10 $[m\,s^{-1}]$ and adiabatic erosion process, the second model of Sundararajan was found suitable.

(ii) Active corrosion modelling depends on the Butler-Volmer formulation in calculating the dissolution rate. If active controlled-corrosion is assumed, the effect of mass flow rate of the electrolyte is very small and is assumed to be ignored.

(iii) The additive effect is very important in passivation environment in the erosion-corrosion process, while in the active corrosive environments, the synergistic effect can be ignored.

(iv) A model for calculating the additive effect for oblique impacts is important for erosion-corrosion maps developing.

(v) The 2D erosion-corrosion maps are not able to monitor the integrated effect of all the parameters influencing the erosion-corrosion process, nor can monitor the effect of some factors that influence both erosion and corrosion processes at the same time. It can not also be used in the service stage of any application.

The objective of this thesis is to provide a new tool for constructing a new types of erosion-corrosion maps that are capable of:

(i) Including the fluid flowing conditions and parameters that influence the erosion-corrosion process.

(ii) Monitoring the combined effect of all the parameters influencing the erosion-corrosion process. Hence, they can be used in the service life stage of any industrial application.

(iii) Identifying the effect of the parameters that influence both the erosion and corrosion processes.

On achieving these goals, a new methodology is proposed based on combining the concept of the erosion-corrosion mapping and the CFD techniques, to construct the erosion-corrosion maps on the surfaces of the real application. In other words, extending the erosion-corrosion maps from the limited 2-dimensional maps to what is so called "3D erosion-corrosion maps". A case study was chosen from the literature; namely a 90^o pipe bend, to simulate the slurry flow within. The CFD simulation and validation is introduced in the next chapter (chapter 3). The methodology is explained in chapter 4 at standard room temperature or nominal condition for a range of pure materials. The effect of the elevated temperature in the 2D and 3D erosion-corrosion maps is investigated for (Fe) as an example of the parameters that influence both erosion and corrosion process in chapter 5. The conclusions and future directions are introduced in chapter 6.

Chapter 3

CFD SIMULATION AND VALIDATION

3.1 Introduction

Many engineering applications, such as the oil and gas offshore wells and power plants stations involve the transportation of fluid; mostly slurries, which contain two or multiphase flows [114]. Even smaller scale applications such as cooling systems in the internal combustion engines and generators used in the power plants, they involve the transportation of the sea water which is usually mixed with sand particles into a net of piping systems. These piping systems are exposed to severe attack of the sand particles as well as the corrosive media of the suspending fluid.

The prediction of erosion-corrosion wear enables us to evaluate the service life of the application under investigation, and areas where severe wear rates occur. Experimental investigation techniques are very useful tool to quantify the erosion and corrosion rates. However, it still a time and cost consuming. Computational Fluid Dynamics (CFD) instead becomes important to tackle erosion problems because of it economically can predict the erosion rates in real fluid flow applications. The CFD erosion prediction procedure has three major steps: flow modelling step, particle tracking step, and erosion prediction step [114].

Considerable efforts have been carried out by investigators to study the erosion problems and many erosion prediction models have been developed. On the other hand, few attempts have been taken to simulate the erosion-corrosion using CFD. Keating and Nesic [107] used the CFD simulation to study the erosion– corrosion problems in U-bends, assuming oxygen or mass transfer controlled corrosion. Bozzini et al. [3] also proposed a numerical simulation methodology of erosion–corrosion in four-phase flows comprising two immiscible liquids, gas and particulate solid, in a pipe bend flow.

The purpose of this chapter is to select an application to develop the 3D erosion-corrosion maps on its surfaces. The application must be then well known and numerically and experimentally validated in the literature. Moreover, it must have been investigated before regards to erosion rates prediction numerically and experimentally. Elbow pipebend slurry flow was investigated extensively by several authors. It has been investigated by Enayet et al. [115, 116] using the "Laser Doppler Velocimeter" measurement technique (LDV) which gives high accurate measurements for fluid flow. Therefore, this publication was referenced by several investigators, to validate

their experimental [117] or numerical simulation of erosion works [31]. Wood et al. [71, 72] also studied the erosion rate prediction in elbow pipe bend slurry flow and validated their erosion simulation by their own experimental work.

Based on this introduction; and following the CFD erosion prediction procedure of [114], the simulation work in this study will involve the following steps:

(i) The fluid flow in 90^o pipe bend is simulated based on the experimental and numerical work of [115] and [31] respectively.

(ii) The erosion simulation will be validated by the work of Wood et al. [71, 72].

3.2 Modelling description

The simulation commenced here is divided to three stages as mentioned above:

(i) Fluid flow modelling and validation. In this stage, an evaluation of the turbulence model and mesh carried out by comparing the numerical results with the experimental work of Enayet et al. [115]. The elbow pipe and fluid flow configuration used by [115] is simulated in this stage.

(ii) Erosion prediction using the available erosion models and validation. In this stage, the validated mesh and turbulence model in the first stage will be used to simulate the elbow pipe configuration and erosion rate are compared to the experimental work done by Wood et al. [71, 72].

In a recent study, Wang and Shirazi [118] used the same technique above to validate a CFD based mass transfer coefficient model in elbows as a function of its (R_c/D) ratio. The same validation methodology was also used by Edwards et al. [31], who validate the fluid flow scheme using Enayet experimental work, and the erosion prediction using Eyler work [30].

The simulation presented in this study is carried out using the commercial software FLUENT [119]. FLUENT is a finite volume software that can simulate a variety of fluid flow under several operating conditions. The following subsection will outline the governing equations for the fluid flow, followed by another subsection that describe the equations governs the particle motion.

3.2.1 Fluid flow modelling

Numerical 3D predictions have been carried out with the FLUENT V6.3 using the standard $k-\epsilon$ model for turbulence. For steady, incompressible and viscous fluid flow; Navier-Stokes equations for the continuity and momentum are solved. The continuity equation is given as [119]:

$$\nabla \cdot \left(\vec{V}\right) = 0 \tag{3.1}$$

while the momentum conservation equations can be described in tensor form as [119]:

$$\nabla \cdot \left(\rho \vec{V}\vec{V}\right) = -\nabla p + \nabla \cdot \left(\bar{\bar{\tau}}\right) + \rho g \tag{3.2}$$

where (p) is the static pressure, (ρg) is the gravitational body force, and $\left(\bar{\bar{\tau}}\right)$ is the stress tensor which may be expressed as [119]:

$$\bar{\bar{\tau}} = \mu \left[\left(\nabla\vec{V} + \nabla\vec{V}^T\right)\right] \tag{3.3}$$

where (μ) is the molecular viscosity, (I) is the unit tensor. The standard $k-\epsilon$ model with standard wall function and zero roughness proposed by Launder and Spalding [120] is used for turbulence modelling for its robustness, economy, and reasonable accuracy. The transport equation for the turbulence kinetic energy (k) is given as [119]:

$$\frac{\partial}{\partial x_i}\left(\rho\, k\, u_i\right) = \frac{\partial}{\partial x_j}\left[\left(\mu + \frac{\mu_t}{\sigma_k}\right)\frac{\partial k}{\partial x_j}\right] + G_k + G_b - \rho\epsilon \tag{3.4}$$

$$\frac{\partial}{\partial x_i}\left(\rho\, \epsilon\, u_i\right) = \frac{\partial}{\partial x_j}\left[\left(\mu + \frac{\mu_t}{\sigma_\epsilon}\right)\frac{\partial \epsilon}{\partial x_j}\right] + C_{1\epsilon}\frac{\epsilon}{k}\left(G_k + C_{3\epsilon}\, G_b\right) - C_{2\epsilon}\,\rho\frac{\epsilon^2}{k} \tag{3.5}$$

, and (μ_t) is the turbulent or eddy viscosity and is calculated as [119]:

$$\mu_t = \rho\, C_\mu \frac{k^2}{\epsilon} \tag{3.6}$$

where (G_k) represents the production of turbulence kinetic energy due to the mean velocity gradients, (G_b) is the production of turbulence kinetic energy due to buoy-

Table 3.1: The closure coefficients of the $k-\epsilon$ turbulence model [119].

σ_k	σ_ϵ	$C_{\epsilon 1}$	$C_{\epsilon 2}$	C_μ
1.0	1.3	1.44	1.92	0.09

ancy, σ_k, and σ_ϵ are the turbulent Prandtl numbers for k and ϵ respectively, and ($C_{\epsilon 1}$, $C_{\epsilon 2}$, *and* C_μ) are constants listed in table 3.1 [119]. The constant ($C_{\epsilon 3} = 1$) for buoyant shear layers which the main flow direction is aligned with the direction of gravity, while has a zero value for buoyant shear layers that are perpendicular to the gravitational vector. The simulation commenced in this study uses a standard wall function for near wall treatment [120].

The turbulent kinetic energy at the wall boundaries are characterised by the following equation:

$$\frac{\partial k}{\partial n} = 0 \tag{3.7}$$

where n is a normal vector to the wall. The dissipation rate can be then calculated after as:

$$\epsilon = \frac{C_\mu^{3/4} k^{3/2}}{\kappa\, y} \tag{3.8}$$

where y is the distance to the wall.

To validate the turbulence model and mesh used in this study, the experimental work of Enayet et al. [115] is simulated here with the same physical configuration. The results were compared to the experiments to select the best mesh that gives the minimum deviation from the experimental data. Figure 3.1 illustrates the physical dimensions of the elbow pipe used in [115], while table 3.2 lists the flow conditions for the simulation.

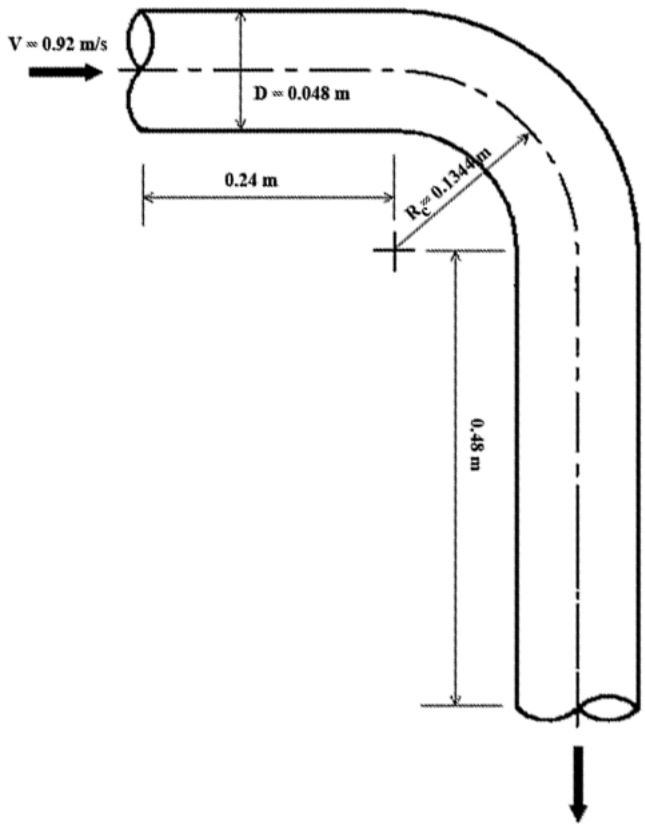

Figure 3.1: A schematic drawing of the case study by Enayet et al. [115].

Table 3.2: Flow conditions for Enayet et al. [115].

Parameter	Value [SI]
Pipe diameter, D	0.048 $[m]$
elbow bend ratio, R_c/D	2.8
Fluid bulk velocity, V	0.92 $[m\,s^{-1}]$
Kinematic viscosity, ν	1.027 $[m^2\,s^{-1}]$
Reynolds number, Re	43000

3.2.2 Particle tracking and erosion simulation

The dispersed secondary phase (solid particles) is simulated using the Discrete Phase Model (DPM) in FLUENT. It is based on tracking the trajectory of every particle ingested from the inlet surface following the Eulerian-Lagrangian approach, where the fluid phase is treated as a continuum by solving the Navier-Stokes equations in the previous section. Assuming one way coupling, FLUENT predicts the trajectory of each particle by integrating the Lagrangian equation of motion for a particle suspended by the fluid flow which may be represented as [119]:

$$\frac{d\,\vec{V_p}}{dt} = F_D\,\left(\vec{V} - \vec{V_p}\right) + \frac{\vec{g}\,(\rho_p - \rho)}{\rho_p} \tag{3.9}$$

The first term in the right hand side represents the drag force exerted on the surface of the particle per unit mass, while the second term represents the body force on particle per unit mass due to the gravitational effect. (F_D) is given as [119]:

$$F_D = \frac{18\,\mu}{\rho_p\,d_p^2}\,\frac{C_D\,Re_p}{24} \tag{3.10}$$

Here, $\left(\vec{V}\right)$ is the fluid phase velocity, $\left(\vec{V_p}\right)$ is the particle velocity, (μ) is the molecular viscosity of the fluid, (ρ) is the fluid density, (ρ_p) is the density of the particle, and (d_p) is the particle diameter. (Re) is the relative Reynolds number, which is defined as [119]:

$$Re_p = \frac{\rho\,d_p\,|V_p - V|}{\mu} \tag{3.11}$$

The drag coefficient (C_D) is calculated according to [121] in the following piece-wise continuous formulae for spherical particles

$$C_D = 24\,Re_p^{-1} \qquad 0 < Re_p \leq 0.1 \tag{3.12}$$

$$C_D = 22.73\,Re_p^{-1} + 0.903\,Re_p^{-2} + 3.69 \qquad 0.1 < Re_p \leq 1 \tag{3.13}$$

$$C_D = 38.8\,Re_p^{-1} - 12.65\,Re_p^{-2} + 0.36 \qquad 1 < Re_p \leq 10 \tag{3.14}$$

$$C_D = 46.5\, Re_p^{-1} - 116.667\, Re_p^{-2} + 0.61667 \qquad 10 < Re_p \leq 100 \tag{3.15}$$

$$C_D = 98.33\, Re_p^{-1} - 2778\, Re_p^{-2} + 0.3644 \qquad 100 < Re_p \leq 1000 \tag{3.16}$$

$$C_D = 148.67\, Re_p^{-1} - 47500\, Re_p^{-2} + 0.35713 \qquad 1000 < Re_p \leq 5000 \tag{3.17}$$

The erosion rate prediction is based on the accurate estimation of the particle trajectories and where the particle is hitting the target surface. Forder et al. [48] introduced the parallel and perpendicular coefficient of restitution as a polynomial function of the impact angle respectively for steel as [48]:

$$e_{per} = 0.988 - 0.78\,\alpha + 0.19\,\alpha^2 - 0.024\,\alpha^3 + 0.0027\,\alpha^4 \tag{3.18}$$

$$e_{par} = 1 - 0.78\,\alpha + 0.84\,\alpha^2 - 0.21\,\alpha^3 + 0.028 \tag{3.19}$$

A 90^o horizontal pipe bend with bore diameter of 0.078 $[m]$ and (R_c/D) ratio of 1.2 is simulated as in [71]. Figure 3.2 shows a schematic drawing for the pipe and its dimension. The liquid phase is water with standard properties for water at room temperature. The material of the pipe is also chosen as stainless steel SS 304. Straight pipe extensions from both sides of the elbow were added with length of 0.2 $[m]$. The solid phase density was chosen equal to alumina particles with value = 2670 $[kg\, m^{-3}]$ and with a uniform size set to 1.0 $[mm]$. Both liquid and solid phase inlet velocity was set to a uniform velocity value equal to 3.0 $[m\, s^{-1}]$. The parameters of the Forder erosion model that used by [71] are summarised in table 3.3.

3.2.3 Grid generation

For the standard $k - \epsilon$ model, the grid was constructed in a way that the y^+ value for the first grid point near to the wall was in the range of 30-100. According

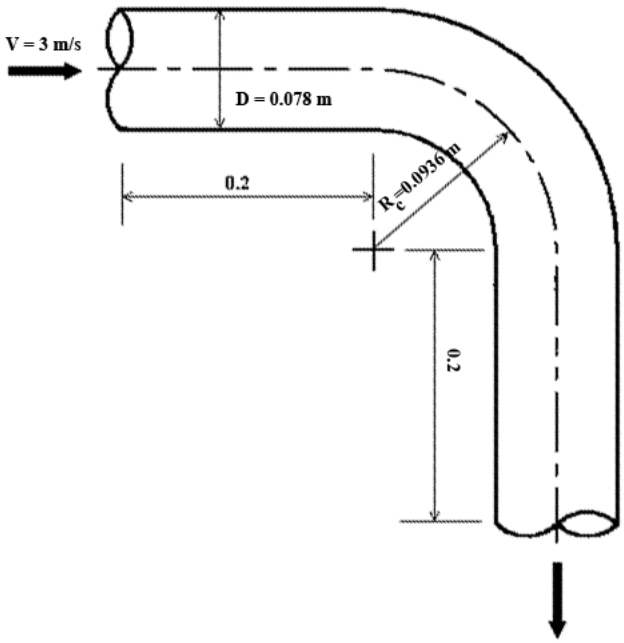

Figure 3.2: Schematic configuration of the pipe bend physical domain [71].

Table 3.3: Parameters values used in Forder erosion model by [71].

Parameters	**Value**
Volume flow rate, Q_v $\left[m^3\, s^{-1}\right]$	0.01
Pipe bore, D $[m]$	0.078
Particle density, ρ_p $\left[kg\, m^{-3}\right]$	2670
Roundness factor, R_f	0.5
Plastic flow stress, σ $[Pa]$	1×10^9
Yield stress of target material, Y $[Pa]$	3.2×10^8
Target material density, ρ_t $\left[kg\, m^{-3}\right]$	7850
Target Poisson ratio, q_t	0.3
Particle Poisson ratio, q_p	0.23
Particle Young's modulus, E_p $[Pa]$	5.9×10^{10}
Target Young's modulus, E_t $[Pa]$	2.07×10^{11}
Deformation erosion factor, E_f $\left[J\, m^{-3}\right]$	1.9×10^{10}
Particle radius, r_p $[\mu m]$	500
velocity ratio exponent, n	2..54
Particle velocity on entry, V_p $\left[m\, s^{-1}\right]$	3.0
Particle mass, m_p $[kg]$	1.4×10^{-6}

to FLUENT manual [119], there is no methodology to calculate the near-wall first node distance accurately prior to the simulation. On the other hand, the guide for evaluating the near-wall node distance (y_{n1}) value is dependent of the wall shear stress. The calculation begins by estimating the skin friction coefficient $\left(\overline{C}_f\right)$ from the following empirical correlation for flow in a duct [119]:

$$\overline{C}_f \approx \frac{0.078}{Re^{0.25}} \tag{3.20}$$

then calculating the friction velocity (U_τ) as[119]:

$$U_\tau = U_b \sqrt{\frac{\overline{C}_f}{2}} \tag{3.21}$$

for standard wall function, (y^+) must lie between 30-100 to avoid the buffer sublayer. Thus, (y_{n1}) can be estimated by using the following formula [119]:

$$y_{n1} = \frac{y^+ \nu}{U_\tau} \tag{3.22}$$

Another approach is also proposed by Glockner and Naterer [122] to evaluate the friction velocity as a function of dimensionless distance from wall (y^+) as follows [122]:

$$U^+ = \frac{1}{\kappa} \ln\left(1 + \kappa\, y^+\right) + 7.8 \left[1 - \exp\left(\frac{-y^+}{11}\right) - \frac{y^+}{11} \exp\left(\frac{-y^+}{3}\right)\right] \tag{3.23}$$

where (κ) is the Von Karman constant = 0.41. Then, getting U_τ from

$$U_\tau = \frac{U_b}{U^+} \tag{3.24}$$

where (U_b) is the fluid bulk velocity. Then, equation 3.22 can be used for (y_{n1}) evaluation.

It is worth noting that these methods are only guidance for estimating the first node to the wall distance order of magnitude, and the mesh must be evaluated for the fluid flow accuracy against experimental or pre-approved numerical results. Therefore, for this turbulence model, a grid refinement study was performed using

Table 3.4: Comparison between the first node-to-wall distance evaluation methods

Case study	Parameter	FLUENT [119]	Glockner and Naterer [122]	mesh name and size
Enayet et al.[115]	y^+	30-100	30-100	**name=size**
	$U_\tau\ [m\,s^{-1}]$	0.048	0.068-0.054	A1=1.0
	Re	43000	-	B1=1.2
	$y_{n1}\ [mm]$	0.64-2.15	0.45-1.89	C1=1.4
Wood et al.[71]	y^+	30-100	30-100	**name=size**
	$U_\tau\ [m\,s^{-1}]$	2.244×10^{-4}	0.22-0.314	A2=0.6
	Re	2.328×10^{5}	-	B2=0.8
	$y_{n1}\ [mm]$	0.134-0.45	0.09-0.3	C2=1.0

Table 3.5: Grid configuration for both case studies [71, 115].

Configuration	Enayet case study [115]	Wood case study [71]
First node-to-wall distance	1.0, 1.2, 1.4 mm	0.6, 0.8, 1.0 mm
Number of nodes in radial direction	72	40
Number of nodes in pipe axis direction	300	120
Number of nodes on the inlet surface	1163, 1153, 1149	1849, 1655, 1539
Total number of nodes	361200, 358190, 356986	228690, 205216, 191180

the standard $k-\epsilon$ model. This is done by increasing the first node distance near to the wall (y_{n1}) from 1.0-1.4 $[mm]$ with 0.2 $[mm]$ increment in the case of Enayet work comparison (mesh A1, B1, and C1 respectively). In the case study of Wood et al., the (y_{n1}) values varied from 0.6-1.0 $[mm]$ with the same increment step (mesh A2, B2, and C2 respectively).

The solutions at zero horizontal level for the velocity profiles at cross-sections with angles ($30^o\,and\,75^o$) of the elbow bend, and at a distance $\left(\frac{x}{D}=1\right)$ after the bend were investigated in order to choose the best mesh for the rest of the study. Table 3.4 compares between the two methods and the chosen grid distance investigated for both cases under study while table 3.5 lists the mesh configuration for both cases (Enayet and Wood).

3.2.4 Discretisation method

FLUENT solves the governing integral equations for the conservation of mass and momentum using the pressure-based solver method and turbulence. A control-volume-based technique is used that consists of [119]:

(i) Division of the domain into discrete control volumes using a computational grid.

(ii) Integration of the governing equations on the individual control volumes to construct algebraic equations for the discrete dependent variables such as velocities, pressure, and other conserved scalars.

(iii) Linearization of the discritized equations and solution of the resultant linear equation system to yield updated values of the dependent variables.

The pressure-based solver uses the pressure correction technique which satisfy the constraint of mass conservation (continuity) of the velocity field by solving a pressure correction equation. Since the governing equations are nonlinear and are coupled to one another, the solution process involves several iterations until the solution converges [119].

FLUENT uses a control-volume-based method to convert the scalar transport equations to algebraic equations that can be solved numerically. The governing equations for the fluid flow are divided into two sections, namely: the convection term which is discritised here in this study using the second order upwind technique and the diffusion term which is discritised using central-differenced second-order scheme [119]. The gradient of any variable is computed using the Least Squares Cell-Based method [119]. The convergence criteria were chosen so that the difference between the fluid mass flow rate at the inlet and the outlet is neglected (in the order of 1.0×10^{-5} $[kg\,s^{-1}]$ at least. The convergence residuals for continuity, velosity components and turbulence parameters were chosen to be lower than 0.001.

3.3 Results

All simulations were executed using a PC with windows XP operating system, Intel Core 2 Duo CPU 6600, with 2.4GHz and 3GB Ram memory. All simulations

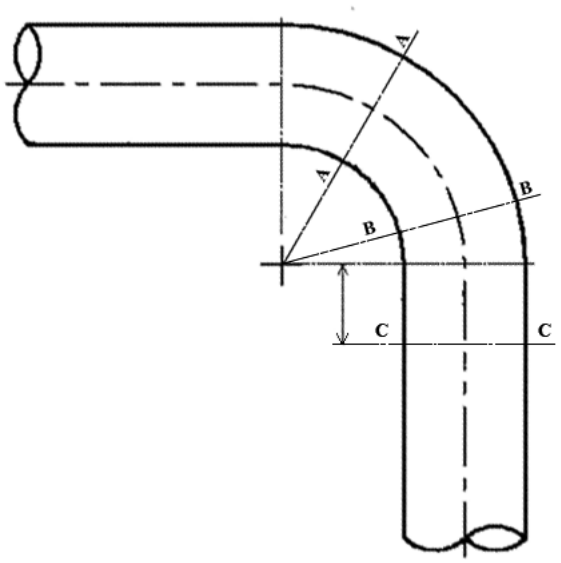

Figure 3.3: Cross-sections positions used for the validation

converged after from 120-170 iterations. Appendix B lists all the simulation configurations and preferences.

3.3.1 Fluid flow validation and results

To investigate the fluid flow results and in order to verify the flow modelling capabilities, several comparisons between predicted velocity profiles with experimental data at various locations inside the elbow were commensed. Figure 3.3 shows the positions of the zero horizontal (i.e. at y-coordinate=0.0) cross-sectional at bend angle 30^o (line A-A), bend angle 75^o (line B-B), and at downstream position $x = D$ (line C-C) that will be considered for the comparison of the numerical results in this study with the experimental results for Enayet et al [115].

Figure 3.4(a-c) shows the predictions and comparison with the experimental results where the velocity has been normalised with respect to the average bulk velocity of 0.92 $[m\,s^{-1}]$ and is plotted against the dimensionless distance from the inside wall (h/R) for line A, B and C respectively. In general, a good agreement with the experimental results is achieved specially in the outer surface regions (at $h/R = 2$) for all values of y_{n1}, with a consistency between the results related to y=1.2 and y= 1.4 mm in every cross-sectional position, which indicates that these two grids produced

are capable of capturing the fluid flow properties. The results also recorded better accuracy than those made by Edwards et al. [31], specially in the region of the inner wall of the bend (at $h/R = 0$), where the CFD results indicates poorer agreement with the experimental data.

With the same trend and at the same positions, the CFD results in the second case study are illustrated in Figure 3.5 (a-c). The velocity has been normalised to the average bulk velocity of 3.0 $[m\,s^{-1}]$ and is plotted against the dimensionless distance from the inside wall ($h/R = 0$) to the outside wall ($h/R = 2$). The same behaviour was found for the grids at y=0.8, 1.0$[mm]$ which are consistent to each other, indicating the good performance for both grids.

To demonstrate the y^+ value all over the outer surface, which expected to receive more erosion rate than the inner surface, Figure 3.6 shows the contours of y^+ profile on the outer surface at y_{n1} =0.6, 0.8, and 1.0 mm respectively. The results show lower than 30 values in the case at $y_{n1} = 0.6$ $[mm]$, Figure 3.6(a); which an indication of the poor quality of this grid from the turbulence parameters capturing point of view.

3.3.2 Erosion rates validation and predictions

After the grid evaluation for fluid flow accuracy, the erosion rate can be predicted by ingesting a sample of the solid particles into the fluid flow domain from the inlet boundary. The solid particle sample must have the same mass flow rate of the solid phase in the physical domain and should be distributed uniformly across the inlet plane. A sample of 1655 particles were ingested to the second case study with grid size near-to-wall = 0.8 [mm]. Each particle will represent a portion of the total mass flow rate, which is defined as the stream mass flow rate and it is automatically assigned by the FLUENT software for every stream. The particle size was set to 1.00 [mm].

To validate the erosion rate predictions in this study, results were compared to the original numerical and experimental work by [71]. The erosion rates were computed using different erosion models including the Forder erosion rate that was used in [71].

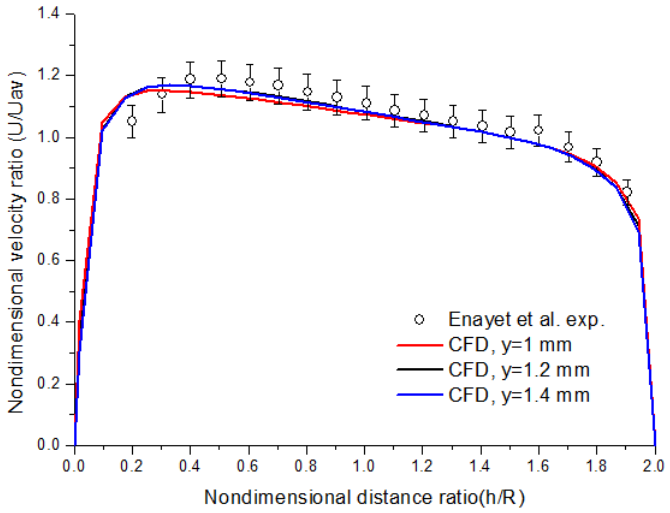

(a)

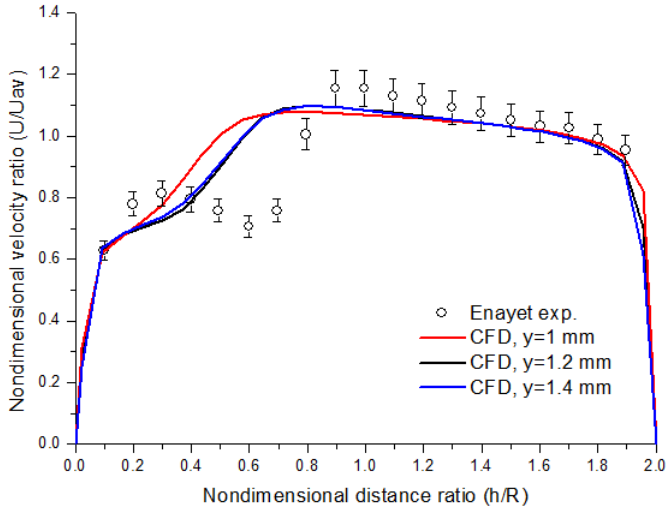

(b)

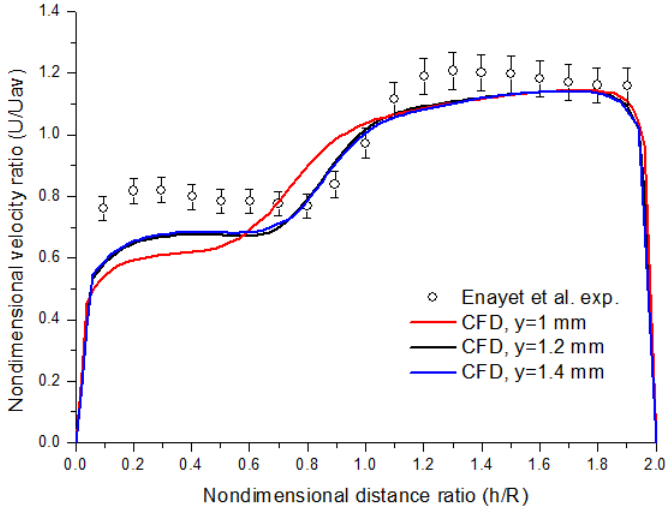

(c)

Figure 3.4: Comparison between the experimental results by Enayet et al. [115] and computation results for different first node near-to-wall distance values (y_{n1}) at cross-sectional positions: (a) A-A. (b) B-B. (c) C-C. (errors taken as $\pm 5\%$).

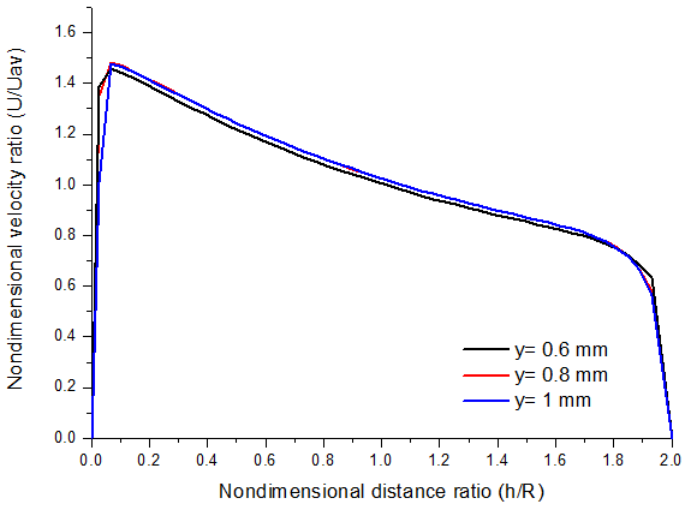

(a)

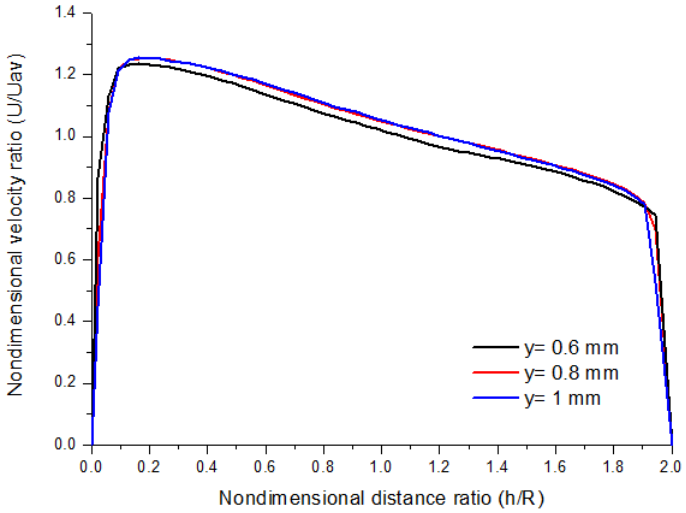

(b)

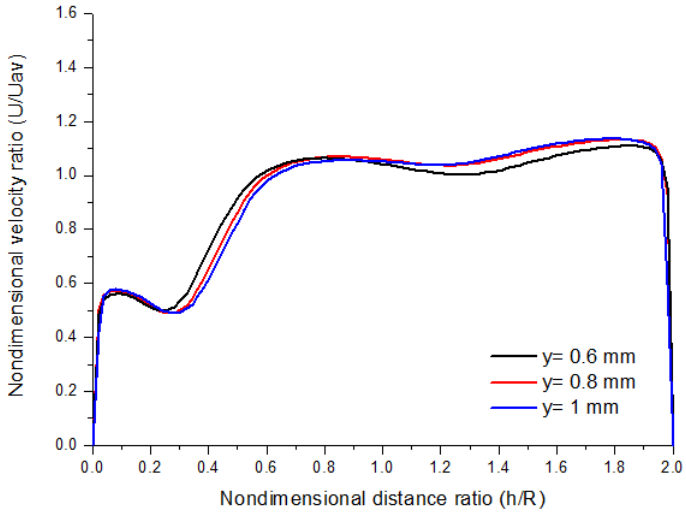

(c)

Figure 3.5: The velocity profile for different first node near-to-wall distance (y_{n1}) values at cross-sectional positions: (a) A-A. (b) B-B. (c) C-C.

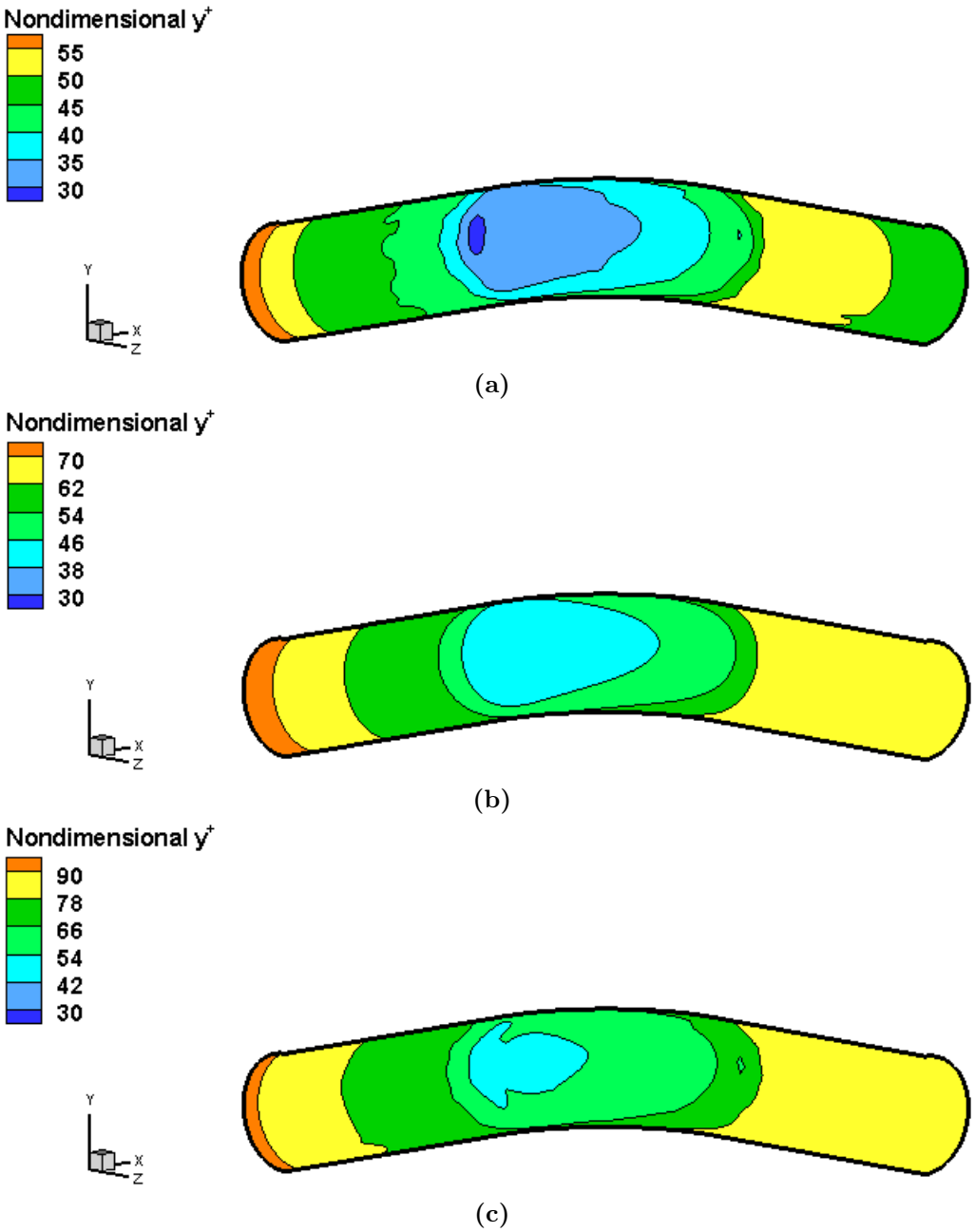

Figure 3.6: The contours of y^+ profiles on the outer surface first node near-to-wall distance (y_{n1}) values: (a) 0.6 (mesh A2) (b) 0.8 (mesh B2). (c) 1.0 mm (mesh C2).

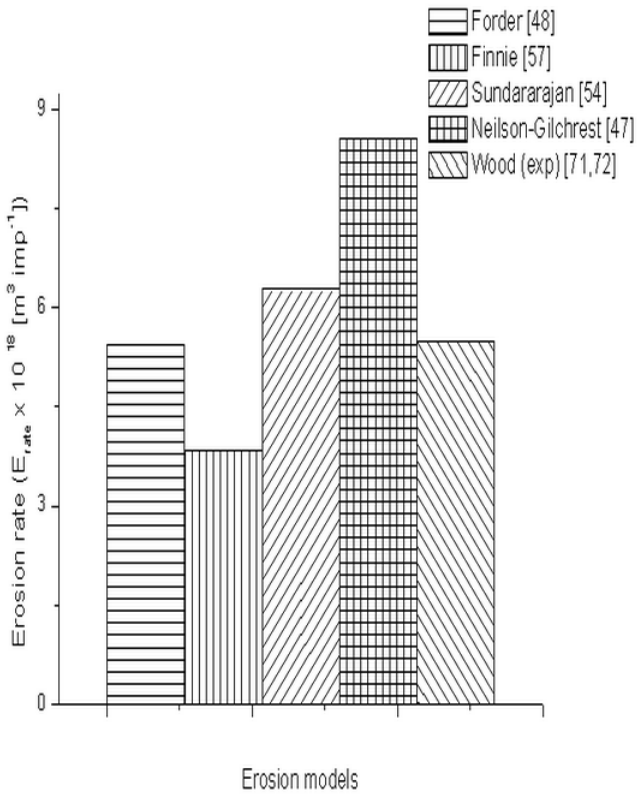

Figure 3.7: Prediction of various erosion models and comparison with experimental results in Wood et al. [71].

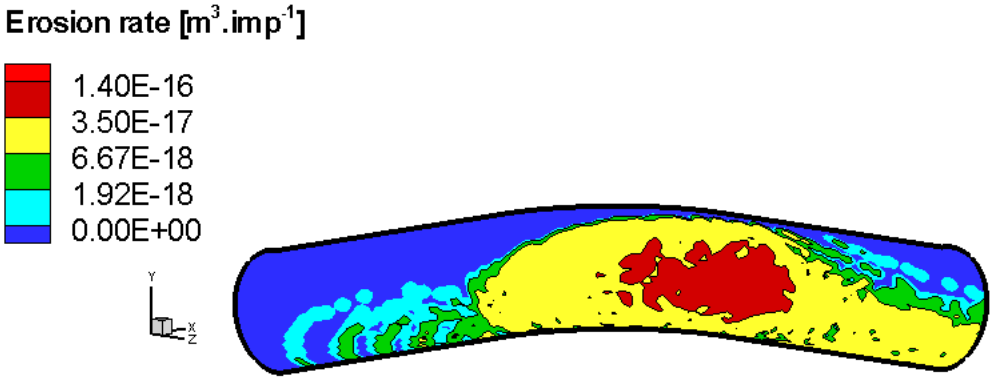

Figure 3.8: Erosion rates contours on the outer surface predicted by (DPM) Discrete Particle Method using Sundararajan second model [54].

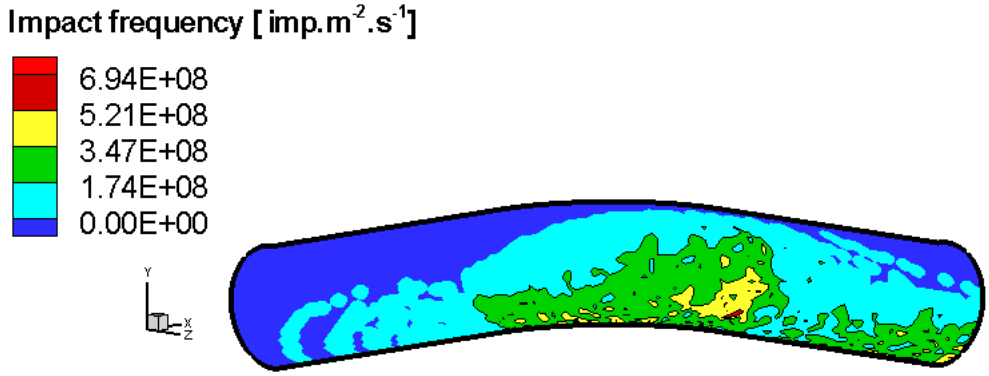

Figure 3.9: Impact frequency by (DPM) Discrete Particle Method.

Figure 3.7 indicates the various predictions of the erosion models and it can be seen that there are similarities between the erosion rates calculated and evaluated in the original work when the values in the earlier study were used. It is also noticed that there is an excellent consistency with the Forder erosion model with the Sundararajan erosion model, and hence this was a useful calibration exercise, to validate the erosion prediction.

The erosion rate predictions using the second model of Sundararajan on real outer surface are indicated in Figure 3.8 where the highest erosion rates were observed at the bend of the pipe. Analysis of the impact frequency; Figure 3.9 and the impact velocity profile; Figure 3.10 indicates the area around the bend experienced the highest impact frequency and velocities. These figures illustrate the impact locations and impact severity can be estimated by superimposing the impact frequency contours

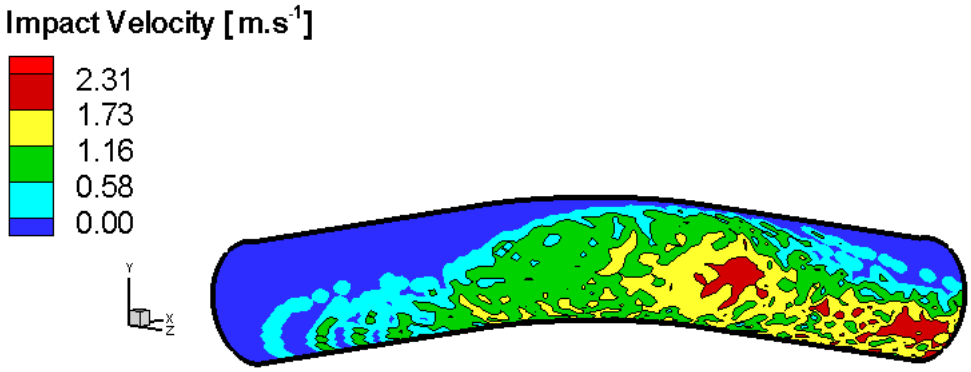

Figure 3.10: Average impact velocity distribution on the surface of the elbow-pipe.

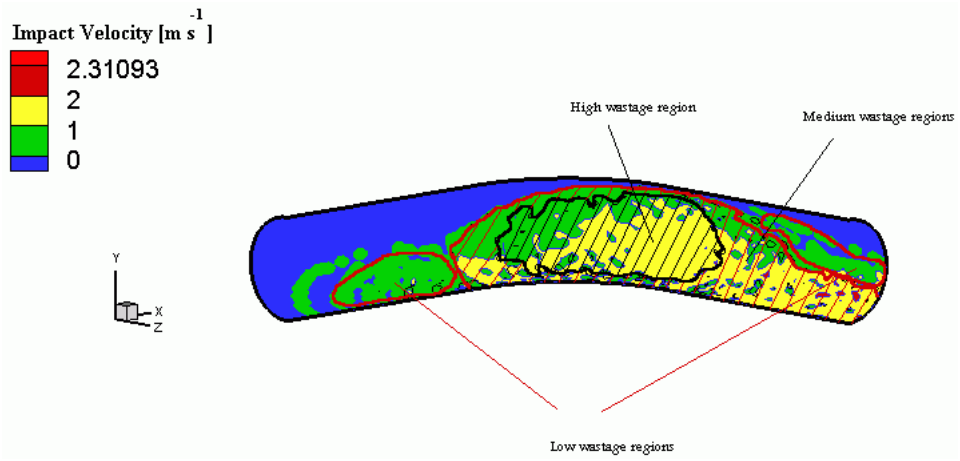

Figure 3.11: Superimposing impact frequency contours on the impact velocity contours reveals the wear levels.

into the impact velocity ones to indicate the regions of low, medium, and high wear on the outer surface of the pipe, Figure 3.11.

3.4 Discussion

The basic and essential rule in CFD simulation is to check the accuracy of the results by using the suitable grid or meshing. The criteria that control the gird selection is that this grid is capable of capturing the fluid flow properties as needed. Very fine mesh can give more details than coarser ones, but also is not economic or is time consuming. The optimisation between the grid refinement and the level of accuracy

requires examination of several grids sizes until reaching matching between two results from the upgraded meshes. Good estimation of the mesh size range at the start of the simulation process saves lots of efforts and time.

The two methods were used here to estimate the first mesh node near-to-wall distance proved good results in general, as in Figures 3.4 (a, b, and c) and Figure 3.5 (a, b, and c). The convergence between the three mesh types in every case study indicates the good estimation of both methods. The consistency in mesh (B1) and (C1) in the first case study; and (B2) and (C2) in the second case study, also indicates that both grids can be used in the simulation rather than mesh of type (A) in each case study.

For accuracy reasons, the mesh chosen to be used for the rest of this study is mesh (B2) in the second case study. This was validated by the y^+profiles on the outer surface for the three meshes (A2), (B2), and (C2) as in Figure 3.6 (a, b, and c) where the contours for mesh (B2) shows uniform distribution for the y^+ values which is far enough over the critical value ($y^+ = 5 - 30$).

Although the velocity profiles in Figure 3.5 (a, and b) shows lower velocity magnitude at the outer surface regions (i.e. $h/R > 1.0$) than that in the inner surface regions (i.e. $h/R \leq 1.0$), the erosion rates at the outer surface is found to be very much more than that of the inner surface. The reason behind is that the particles inertia keeps the projectile of the majority of the particles towards the outer surface until they hit this surface. After the first impact, every particles will make several impacts on the same surface until they enter the straight pipe domain after the pipe bend. The fluid velocity near the outer surface is higher than that in the inner surface, Figure 3.5 (c); which leads to more excessive erosion rate on the outer surface than in the inner surface. This is also supported by the fact that the low velocity range of impact through the pipe (from 1-2.4 $[m\,s^{-1}]$), Figure 3.10; prevents the majority of the particles from getting enough energy during the rebound to reach the inner surface.

The misalignment with the experimental results in the first case study towards the inner surface, Figures 3.4 (a, b, and c) is not of big importance. This assumption is supported by Edwards et al. [31] when they study the same case and compare it

to Enayet work [115]. Since the major erosion problems would exist on the outer surface of the bend, hence, accurate fluid velocity is required at this region where the particles trajectories will be influenced by the relative velocity between the fluid and the particles, regardless of the inaccuracy of the results in the other regions.

The erosion rates were computed for several erosion models; namely: Finnie erosion model [57], Neilson-Gilchrist erosion model [47], Sundararajan second model [54], and Forder model [48]. These erosion prediction results were compared to each other and against the experimental work done in [71]. The most compatible results with the experiments and Forder erosion model in [71] were that of Sundararajan second erosion model as illustrated in Figure 3.7.

Furthermore, In the case study [71], they reported that the erosion efficiency were from 8 – 20%, i.e. to account for the fact that not every particle hitting the walls in ideal manner to produce erosion, and / or to account for the particles that follow the fluid streams and don't hit the surfaces. It is found from the present work that 19% of the sample ingested didn't hit the surfaces. This indicates another validation to erosion rates predicted here.

There are several factors affecting the erosion rate. Among these factors, the impact velocity and impact frequency of the solid particles were found the most of them that have an explicit and direct influence on the erosion rate. These two parameters proved to promote their effect when they interfere on a surface. From Figure 3.11, the regions of high wear are consistent with the regions of high impact frequency and velocity, Figure 3.9 and 3.10. In accordance with the postulation above, the regions of low wear rates in Figure 3.11 were found where the impact frequency and velocity are minimum, Figures 3.9 and 3.10.

In investigating the CFD simulation accuracy, the grid size selection was found to be very important in decreasing the simulation efforts and giving the desired consistency. The erosion rate was found very sensitive to the accurate prediction of the fluid flow properties, specially the fluid flow velocity. On the other hand, the combined effect of the factors that affect the erosion process were well captured by the use of the CFD techniques such as the DPM method in monitoring the particles trajectories and hence predicting the erosion rates profiles on the real surfaces.

Furthermore, the implementation of the theoretical erosion models to predict the wear rates and sights on these surfaces were evaluated and validated showing excellent agreements with the literature experimental and numerical findings. Thus, these studies are flexible to be extended and include the effect of the corrosion process. By implementing the erosion-corrosion mapping techniques to the CFD, a promising new methodology to capture the erosion-corrosion combined effects on the degradation process can be introduced.

Chapter 4

DEVELOPMENT OF EROSION-CORROSION 3D MAPS

4.1 General

It has been shown in Chapter 2 that, the 2D erosion-corrosion maps are more applicable in the design stage of any engineering application because of their ability to record the change in every erosion-corrosion regime. Thus, the erosion-corrosion 2D maps enable the designer with a suitable tool for identifying the optimum operating conditions according to the covered parameters in the design stage of any component. However, limitation arising since using only two parameters to construct the 2D erosion-corrosion maps, make them less applicable in the improvement and the engineering service stages of any designed component. This leads to the need of development of another tool, to include the effects of all the parameters influencing both erosion and corrosion; or at least most of them, in one erosion-corrosion mapping.

In this Chapter, a new methodology is introduced to develop the erosion-corrosion maps on the real surfaces of a well-known case study (introduced in Chapter 3). The new approach is based on combining erosion-corrosion maps techniques with the CFD simulation, to produce the erosion-corrosion maps in a three-dimensional form (3D-maps). Applying erosion-corrosion maps in such practical case studies reveals the importance of these maps, as an essential tool for predicting and enhancing the engineering design in various applications. The results present a new technique for mapping erosion-corrosion on real pipes, thus, introducing an important step-forward in interpreting of erosion-corrosion mapping techniques so far.

The mathematical equations for the erosion-corrosion rates caused by dilute slurry flow are presented. These models are used to produce the erosion-corrosion maps for pure metals, namely: Iron (Fe), Nickel (Ni), Copper (Cu), and Aluminium (Al). The erosion model used to predict the erosion rates for these pure metals is the one developed by Sundararajan [54]. The model is classified to erosion by cutting (for small impact angles) and erosion by deformation (for large impact angles). Based on the applied potential and pH value, the corrosion may be active or passive. As a result, the corrosion models used can be classified into two categories:

(i) When the corrosion is determined by the kinetics of the charge transfer (dissolution mechanism). In this case, the Butler-Volmer equation is used and the

mechanism is said to be active corrosion [8].

(ii) When the pure metal is producing a passive layer, a new approach is derived to calculate the corrosion rate results from the repassivation, where the wear is because of the passive layer removal from the solid particle impacts.

4.1.1 Definitions

Erosion-corrosion regimes boundaries are defined by the ratio $\left(\frac{K_c}{K_e}\right)$. The total corrosion rate can be expressed as the summation of the pure corrosion rate (K_{co}) and the contribution of erosion in corrosion (ΔK_c), what is known as the additive effect. Meanwhile, the erosion rate can be presented as the summation of the pure erosion rate (K_{eo}) and the contribution of corrosion in the erosion (ΔK_e), which is called the synergistic effect. For this modelling approach, the synergistic effect is neglected and the additive effect was considered positive (no antagonism).

The total wastage (K_{ce}) is thus can be evaluated as:

$$K_{ce} = K_c + K_e \tag{4.1}$$

where

$$K_c = K_{co} + \Delta K_c \tag{4.2}$$

and

$$K_e = K_{eo} + \Delta K_e \tag{4.3}$$

4.1.2 Erosion-corrosion regimes and wastage boundaries

In the present study, results are introduced in the form of two types of mapping; namely the regime maps which identify the erosion-corrosion regimes domination and the wastage maps which indicate the total metal removal levels. Both regime and wastage maps are visualised on the outer surface (extrados) of the chosen case

study (90^o pipe bend) according to specified boundary conditions. These boundaries are determined by the value of the ratio $\left(\frac{K_c}{K_e}\right)$ in the regime maps while are related to the value of (K_{ce}) in the wastage maps. Stack et al. [12, 83] defined the boundaries of each erosion-corrosion regime as:

$$Erosion\,Dominated: \qquad \frac{K_c}{K_e} < 0.1 \tag{4.4}$$

$$Erosion - corrosion: \qquad 0.1 \leq \frac{K_c}{K_e} < 1 \tag{4.5}$$

$$Corrosion - erosion: \qquad 1 \leq \frac{K_c}{K_e} < 10 \tag{4.6}$$

$$Corrosion\,dominated: \qquad \frac{K_c}{K_e} \geq 10 \tag{4.7}$$

while in case of the wastage maps, they defined three levels of wastage; namely Low, Medium and High. These levels are identified to the wastage of metals in $[mm\ year^{-1}]$ as follows:

$$Low: \qquad K_{ce} < 1 \tag{4.8}$$

$$Medium: \qquad 1 \leq K_{ce} < 10 \tag{4.9}$$

$$High: \qquad K_{ce} \geq 10 \tag{4.10}$$

These boundaries are adopted throughout the work for constructing the regime and wastage maps. In addition, the term corrosion in the regime boundaries may be replaced with the specific corrosion mechanism applied (dissolution or passivation).

4.1.3 General assumptions

Several assumptions were adopted in constructing the 2D-erosion-corrosion maps in [8] to simplify the complexity of the erosion-corrosion interaction. These assumptions

were considered by dealing with the slurry flow as a quasi-static flow [8]. However, in 3D erosion-corrosion maps, the simulated slurry is fully dynamic and assumptions that related to the static slurry flow can be given away. Thus, the following assumptions were taken into consideration while developing of the 3D erosion-corrosion maps:

(i) The erosion rates are due to the impact of spherical particles on the surface of the metal and there are no other forces exerted on the metal surface except for the impact force.

(ii) The metal surface is assumed to be smooth at the beginning of the simulation.

(iii) The erosion and corrosion rates are assumed to be steady with time, i.e. both processes are independent of time. The mass flow rate of ingested particles is uniform at the inlet of the pipe. Moreover, the corrosion rate in Dissolution mechanism is assumed to be uniform along the metal surface area.

(iv) The crater created from individual impacts remains in its unrelaxed state and is considered to be a section of a sphere (hemisphere).

(v) From assumption (i), it is assumed that the erosion occurs due to the fluid shear stress is neglected.

(vi) The erosion-corrosion process is assumed to be additive in the corrosion passive mechanism, and the synergistic effect is assumed to be very small and neglected in the case of dissolution mechanism.

(vii) Following the deterioration of the passive film, there is no subsequent dissolution of the oxide film.

(viii) No adherent corrosion products are assumed to be existed on the metal surface after the impacts of the solid particles. It is assumed here that the shear stress of the fluid flow is high enough to sweep out all the corrosion products after impacts, but yet small enough not to remove the formed passive layer.

(ix) It is assumed that there is one-way-coupling between suspended particles and the carrier fluid flow. Moreover, there is no particle-particle interaction due to the low particle concentration (i.e. the volume fraction of the particles is lower than 0.1).

4.2 Methodology

The initial work involved evaluation of several erosion models against some laboratory erosion results [72]. A methodology was then developed to predict the combined effect of erosion and corrosion wastage, using the model of Sundararajan [54] to predict the erosion rates and a range of corrosion models to predict the corrosion rates. The total wastage was estimated by combining the erosion rates and the corrosion rates.

The modelling processes thus involved several steps i.e.:

(i) A single elbow- pipe with diameter ratio R_c/D of 1.2 with a bore diameter of 0.078 $[m]$ was used for the simulation.

(ii) A standard $k-\epsilon$ model, with standard wall function and zero roughness was employed to model the turbulence [120].

(iii) A Lagrangian-Eulerian simulation was used to model the multiphase flow of the particles trajectories to evaluate the erosion rate using the Discrete Phase Modelling (DPM) method [119]. The DPM method is based on the Lagrangian tracking of every particle using several discritizing methods for tracing the ingested particles (the method used here is Runge-Kutta method).

(iv) A user defined function (UDF) was developed to evaluate the erosion and corrosion rates based on the models of Sundararajan second model [54] and the famous Butler-Volmer equation to calculate the dissolution rate in case of active mechanism. In the case of passivation corrosion mechanisms, a simple approach is adopted to calculate the metal wastage due to removal of passive layer during impact.

The simulation commenced by using a single phase CFD run using FLUENT software and then injecting the particles uniformly at the inlet by using DPM method. A sample of 1655 particles of $10^{-3}[m]$ diameter was injected with total mass flow rate equal 3.847 $[kg\ s^{-1}]$ to represent 22.88 % particle concentration which corresponds to particle volume fraction of 0.09.

The work on 3D maps was based on earlier studies carried out by Stack and Jana [8],

where 2D erosion-corrosion maps for 1 $[mm]$ diameter particles were generated. The same particle size thus was chosen to be comparable with results in this earlier study. In their study [8], a value of 25.29% by mass (volume fraction = 0.101) was used. This value is marginally above the allowed limit for dilute slurries i.e. (0.1). Thus, a value of 22.88% was chosen which corresponds to a volume fraction of (0.091). This means that the value chosen is within the limit of using DPM in the FLUENT simulation. The walls were chosen as "no slip boundary conditions" and the initial flow velocity was 3.0 $[m\ s^{-1}]$ for both fluid and particles.

4.2.1 Erosion model for impact by solid particles

As mentioned in the literature, the slurry flow involves suspension of solid particles which can impact the target metal surfaces at any impact angles with any impact velocity. Therefore, there are several erosion mechanisms identified by the researchers. It was found from the literature that the erosion of ductile materials can be divided into main two mechanisms. The cutting mechanism is occurred at low impact angles, and the deformation mechanism which dominates at higher impact angles [45, 46, 47, 48].

One erosion model found in the literature in chapter 2 that describe the erosion of ductile materials according to these two main mechanisms was the one introduced by Sundararajan [54]. The second model of Sundararajan is divided into two expressions, one account for the localised deformation at the impact point, while the other accounts for the ductile cutting mechanism during the impact. The total erosion rate is the summation of these two mechanisms as mentioned above. The erosion due to deformation is given as [54]:

$$Er_{def} = \frac{5.5 \times 10^{-2}}{(T_m - 436)^{0.75}} \frac{2^{n_c}\, f_t\, (V_p\, sin\, \alpha)^2\, (1 - e_n^2)}{n_c\, C_p} \tag{4.11}$$

and the erosion by cutting is given as:

$$Er_{cut} = \frac{5.5 \times 10^{-2}}{(T_m - 436)^{0.75}} \frac{(n_c + 1)\left(\frac{\mu_f}{\mu_{fc}}\right)\left(2 - \frac{\mu_f}{\mu_{fc}}\right)(V_p\, cos\, \alpha)^2}{2^{(2-n_c)}\ (1 + \lambda)\ n_c\, C_p} \tag{4.12}$$

where

$$\mu_{fc} = \frac{1}{(1+\lambda)\ (1+e_n)\ tan\,\alpha} \tag{4.13}$$

Sunderarajan [54] suggested that most of pure ductile metals can exhibit cutting mechanisms at angles between $0^o - 30^o$ while pure deformation can be experienced at angles higher than 60^o. The impact angle ranged between $30^o - 60^o$ can be assumed to suffer from a combination of both cutting and deformation mechanisms and can be estimated by simply summation of both erosion rates together. Although, in practice, it is not likely the same behaviour can be expected for every pure metal but can be considered as a good assumption [54].

The normal coefficient of restitution can be estimated either by relating the energy dissipated during the impact with the mechanical properties of the target material and impact velocity [123]. This is valid only for normal impact and is given as:

$$e_n = \frac{1.36\, H_s^{0.625}}{E_e^{0.5}\, \rho_p^{0.125} V_p^{0.25}} \tag{4.14}$$

Or, it can be related to the impact angle through the semi-empirical relation [48]:

$$e_n = 0.988 - 0.78\,\alpha + 0.19\,\alpha^2 - 0.024\,\alpha^3 + 0.027\,\alpha^4 \tag{4.15}$$

and

$$e_t = 1.0 - 0.78\,\alpha + 0.84\,\alpha^2 - 0.21\,\alpha^3 + 0.028\,\alpha^4 - 0.022\,\alpha^5 \tag{4.16}$$

For unit consistency, erosion rates should be converted to $[kg\ m^{-2}\ s^{-1}]$ to be consistent with the computed corrosion rates in the following section.

4.2.2 Corrosion modelling

Corrosion may occurs in the form of dissolution of the metal surfaces contacted with the electrolyte (which is here the carrier water), or by forming a passive or protective oxide layer which eventually is removed partially or completely by the impact of the suspended solid particles. In either cases, corrosion mechanism performed on the metal surfaces is dependent on the pH value of the electrolyte and the applied potential between the metal and the electrolyte [17].

The corrosion process is controlled by the polarisation which is measured by the over-potential to a reference potential. There are three types of polarisation, namely: active polarisation, concentration polarisation and ohmic polarisation. We assume here in this work that the effect of the latter two types is not considered. This assumption maybe be valid in cases where the surface is active controlled by applying a certain potential to the component under investigation (pipe bend) [97].

While in passivation mechanism environments, in addition to the erosion rate, there is an additive effect, which must be considered from the continuous removal of the oxide layer during the solid particle impacts [89]. Thus, the corrosion contribution in the passivation mechanism is only considered and the pure corrosion rate is neglected. This is also dependent on the pH and the applied potential on the pipe surfaces [8].

4.2.2.1 Active corrosion model

Knowing that the pure corrosion rate in active environments is related to the current density, i.e. the current flowing per unit area of the electrode surfaces. According to Faraday's law the relationship between pure dissolution rate(K_{co}) and the anodic current density is expressed as [84]:

$$K_{co} = \frac{i\,RAM}{z_m\,F} \tag{4.17}$$

where the anodic current density can be calculated from the Butler-Volmer equation as [8]:

$$i_{anet} = i_o \left[\exp\left(\frac{2.303\,\eta}{b_a}\right) - \exp\left(\frac{-2.303\,\eta}{b_c}\right)\right] \tag{4.18}$$

the over-potential (ΔE)may be described by the following expression:

$$\eta = E_{ap} - E_{rev} \tag{4.19}$$

When (ΔE) is anodic (i.e. positive), the second term in equation 4.18 becomes very small and can be neglected and (i_{anet}) can be more simply expressed by:

$$i_{anet} = i_o \ \exp\left(\frac{2.303\,\Delta E}{b_a}\right) \tag{4.20}$$

where (b_a) is the Tafel coefficient that can be obtained from the slope of a plot of (ΔE)against ($\log i_{anet}$)and can be represented by the Tafel equation given as:

$$b_a = \frac{2.303\,R\,T}{\beta\,z_m\,F} \tag{4.21}$$

Similarly, when (ΔE) is cathodic (i.e. negative), the first term in equation 4.18 becomes very small and can be neglected and the cathodic current density can be given as:

$$i_c = i_o \ \left[-\exp\left(\frac{-2.303\,\eta}{b_c}\right)\right] \tag{4.22}$$

where (b_c) is again the Tafel coefficient and can be obtained by:

$$b_c = \frac{-2.303\,R\,T}{\beta\,z_m\,F} \tag{4.23}$$

Equation 2.18 is considered to be valid for any pure metal under activation controlled conditions. In this work, it will be used for investigating a range of pure metals namely, Iron (Fe), Nickel (Ni), Copper (Cu), and Aluminium (Al).

4.2.2.2 Passivation corrosion model

Dissolution corrosion continues until the surface of the anode (metal surface) exhibits conditions that lead to the formation of a protective oxide layer that prohibiting dissolution. It was assumed that the wear due to the repeated formation and removal of the passive layer is greater than the pure corrosion rate at same conditions [8]. Although it is found that this passive layer is dissolved instantaneously with its formation, the rate of formation of the oxide layer is much more than its dissolution. The corrosion rate may be derived from the additive effect of the erosion-affected

corrosion (ΔK_c). This can be represented by the following equations [8]:

$$K_c = K_{co}\,(\approx 0) + \Delta K_c \tag{4.24}$$

$$K_c = \Delta K_c \tag{4.25}$$

The need for developing an expression for the additive effect (ΔK_c) to suit the simulation study presented here is necessary. Meanwhile, in reaching the goal for developing such an expression, some simplifications to the case must be made. The formation of the oxide layer was found to be a very complicated process. Moreover, the removal of this oxide layer is modelled with some different assumptions that should be made to simplify the problem yet to express the removal process so effectively with acceptable errors.

Tirupataiah et al. [70] investigated the nature of the elastic rebound on ductile materials when impacted by spherical particles. In their work, an expression was developed for predicting the size of the crater diameter, by equating the kinetic energy of the particle impacting the surface with the energy needed to remove a crater volume from the oxide layer. The model assumed that all the energy of the impact is consumed in the erosion process. The basic assumption on which this model is based on all the relaxation of the crater shape occurs in the direction of the impacting particle [70].

Later, Roy et. al. [124] investigated the transition from the oxide erosion to substrate erosion and developed a similar expression for the crater diameter for a sharp edged or conical particles and for an oxide layer based on the same first assumption of Tirupataiah [70]. The derivation was applicable for both the substrate (ductile) and the oxide brittle layer. However, the model only considers normal impact and the assumption of the complete consumption of the particle energy in the erosion process ignores any energy expended in elastic work (i.e. in rebound process) [124].

Based on the work of Tirupataiah [70], Stack et al. [8] introduced an erosion model for passive layers of metals. The basic assumption was that the rebound velocity is explicitly small compared to the impact velocity, and the impact angle is normal. This erosion model was necessary in constructing the erosion-corrosion mapping for

various ranges of pure metals and low-carbon steel. However, these assumptions constrain the model applicability in dynamic slurry flow motions. In such environments, the target material is exposed to oblique impacts and the rebound characteristics of the impacting particles are considerable. Thus, it is necessary to adapt the model to account for oblique impacts or elastic rebound effects.

Based on this analysis, and according to the dynamic nature of the simulation carried out here; some assumption are made and listed below:

(i) It is assumed that the erosive action of the solid particles contained within the slurry repeatedly ruptures and subsequently removes the passive film.

(ii) For pure metals, it is assumed that the oxide formed consists of a mono-oxide layer.

(iii) The passivation process is immediate and instantaneous.

(iv) No passive film removal due to the shear stress of the flowing fluid on the metal surfaces.

(v) It is assumed that the energy involved in the erosion process is the difference between the initial impact energy, and the energy that causes the particle to rebound.

(vi) It is also assumed that the erosion process is adiabatic, thus discounting the amount of energy consumed during the erosion process due to friction and local melting of the material.

(vii) It is assumed that during the impact process, a crater is formed on the target surface by a single impact particle and this crater area under the passivation condition repassivate and is removed by the impacting action of subsequent particles.

(viii) Plastic deformation of the solid particles is avoided.

(ix) The inertial resistance of the target material is negligible compared to its resistance to plastic flow [125].

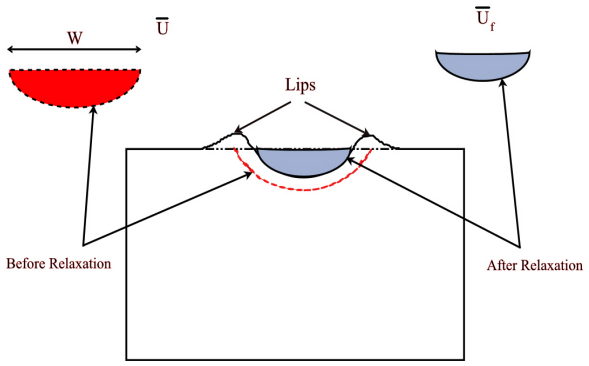

Figure 4.1: Particle indentation during impact shows the the crater volume before and after relaxation

In a present study, Sundararajan et.al. [125] have related the impact energy of the impact process to the crater volume of indentation after and before relaxation. The equation can be given as:

$$H\,\overline{U}\left(1-\frac{\Delta\overline{U}}{\overline{U}_f}\right)=\frac{1}{2}\,m_p\,\left(V_1^2-V_2^2\right) \tag{4.26}$$

where (m_p) is the particle mass, (V) is the particle velocity, (H) is the material hardness, $\left(\overline{U}\right)$ is the crater volume, $\left(\overline{U}_f\right)$is the final volume of the crater after fully relaxed, and the subscripts 1,2 are for the impact and rebound process respectively. $\left(\Delta\overline{U}\right)$ represents the decrease in indentation volume because of the elastic relaxation of the crater shape. Figure 4.1 illustrates the differences between these terms during the particle impact where:

$$\Delta\overline{U}=\overline{U}-\overline{U}_f \tag{4.27}$$

Knowing that in case of brittle materials, the change between unrelaxed and relaxed volume is very small and can be neglected. The value $\left(\Delta\overline{U}\approx 0\right)$, and equation 4.26 can be written as:

$$H\,\overline{U}=\frac{1}{2}\,m_p\,\left(V_1^2-V_2^2\right) \tag{4.28}$$

Assuming that the surface shear stresses due to oblique impact may be neglected in the case of brittle materials, Finnie [57] stated that the crater diameter of ring crack (d) is related to the vertical component of the velocity. Then, by default the energy balance in equation 4.28 will be:

$$H\,\overline{U} = \frac{1}{2}\,m_p\,\left(V_1^2\,\sin^2\alpha_1 - V_2^2\,\sin^2\alpha_2\right) \tag{4.29}$$

where (α_1) and (α_2) are the impact and rebound angles respectively. By definition, the normal impact velocity component is related to the normal rebound velocity component by the normal coefficient of restitution (e_n), thus and by rearranging:

$$H\,\overline{U} = \frac{1}{2}\,m_p\,V_1^2\,\sin^2\alpha_1\left(1 - e_n^2\right) \tag{4.30}$$

Using the approach of Tirupataiah [70], and assuming that the particle is a sphere, and the crater depth is comparably smaller than the particle diameter; i.e. at low particle velocities, the shape of the crater on the passive film (oxide) surface can be assumed as part of a sphere and $\left(\overline{U}\right)$ can be related to the crater diameter (W) by:

$$\overline{U} = \frac{\pi\,W^4}{32\,d_p} \tag{4.31}$$

where (d_p) is the particle diameter. Applying equation 4.31 into 4.30 gives:

$$W = 1.5023\,\left[\frac{m_p\,d_p\,\left(1 - e_n^2\right)}{H}\right]^{0.25}\,\left(V_1\,\sin\alpha_1\right)^{0.5} \tag{4.32}$$

The crater depth (d_c) is related to crater diameter using the same assumption above by:

$$d_c = \frac{W^2}{4\,d_p} \tag{4.33}$$

From [8], the mass of passivating oxide film removed per impact is given as:

$$M_t = \pi\,\overline{k}\,d_p\,d_c\,\overline{h}\,\rho_f \tag{4.34}$$

The constant $(\overline{k})$ is defined as the mass ratio between the metal and its oxide created during the corrosion reaction multiplied by the number of moles of metal involved in the reaction, and is related to (k_2) in [8]; by definition as: $(\overline{k} = k_2/2)$. $(\overline{h})$ is the passive layer thickness and ρ_f is the passive layer density. Substituting equation 4.32 into equation 4.33 and apply to equation 4.34 then we finally get:

$$M_t = 1.7726\,\overline{k}\,\overline{h}\,\rho_f \left[\frac{m_p\,d_p\,(1-e_n^2)}{H}\right]^{0.5} (V_1\,\sin\alpha_1) \tag{4.35}$$

Further simplification to the above equation can be made if we substitute (m_p) by:

$$m_p = \frac{\pi\,d_p^3\,\rho_p}{6} \tag{4.36}$$

A final formulation can be obtained as:

$$M_t = \pi\,\overline{k}\,h\,\rho_f\,d_p^2 \left[\frac{\rho_p\,(1-e_n^2)}{6\,H}\right]^{0.5} (V_1\,\sin\alpha_1) \tag{4.37}$$

The unit given for the erosion model by equation 4.37 is $[kg\ impact^{-1}]$. To convert to a useful unit $[kg\ m^{-2}\,s^{-1}]$, for example, one should multiply equation 4.37 by the particle impact flux as outlined in [8]. This can be varied according to the erosion-corrosion process being modelled. For example, if the flow is homogeneous (constant particle concentration), particle impact frequency may be given as mentioned in [89]:

$$I_p = \frac{c_p\,V_1\,\sin\alpha_1}{m_p} \tag{4.38}$$

For evaluation of properties of the pure metals and their passive films, the mechanical properties for Fe, Ni, Cu and Al are given below, in table 4.1.

The thickness of the passive layer $(\overline{h})$ can be assumed to be varied with the potential difference. Graham et al. [126] assumed that when the passive film initially and instantaneously forms, its thickness is $1\,[nm]$ and the thickness of the passive film is assumed to increase by $3\,[nm]$ per volt of over-potential. Thus $(\overline{h})$ follows a relationship as [8]:

$$\overline{h} = \overline{h}_o + 3\times10^{-9}\,(E_{ap} - E_{pas}) \tag{4.39}$$

Table 4.1: Properties for pure metals selected and their passive films from Stack et al. [8].

Metal Properties	Fe	Fe_2O_3	Ni	NiO	Cu	Cu_2O	Al	Al_2O_3	Solid Particle
$\rho\ [kg\ m^{-3}]$	7800	5240	8900	6720	8930	6400	2700	3970	2670
k_2		1.3989		1.5737		1.5977		1.0585	
$\overline{k}$		0.6995		0.7869		0.7989		0.5293	
$E\ [GPa]$	211		200		130		71		94
q_t	0.293		0.312		0.343		0.345		0.3
$H\ [GPa]$	0.820	8.012	0.862	6.561	0.495	2.736	0.260	20	

where $\left(\overline{h}_o = 1 \times 10^{-9}\right)\ [m]$.

All corrosion rates must be calculated in $[kg\ m^{-2}\ s^{-1}]$. The erosion rates from Sundararajan's model [54] must be converted from $\left[kg_{target}\ kg^{-1}_{particle}\right]$ accordingly as indicated above.

Equation 4.37 is a simple expression for estimating the erosion rates for the passive film on a substrate. It is valid for the impact of passive film formed during the erosion-corrosion process where the erosion footprint (i.e. the deformed surface) has a ring shape approximately (this is also assumed at oblique impact angles). It is also valid at low velocities (up to $10\,[m\ s^{-1}]$) as identified in [127, 125]. The equation is useful for CFD applications in which erosion occurs at a range of impact angles. If the particle fully penetrate the passive film and erode the substrate, another approach is considered; i.e. the use of a model for erosion of ductile materials.

To validate equation 4.37, experimental work in previous investigations was used to test the validity of the model. Oka et al. [128] investigated the erosion of the aluminium oxide scale at various impact angles. Later, Griffin et al. [129] used his experimental results to validate the results of a three dimensional finite element erosion model of alumina scale on MA956 alloy substrate. Figure 4.2 shows the experimental results of Oka as reported by Griffin and the prediction by equation 4.37 after multiplying by $[1/m_p\,\rho_f]$ for unit consistency. The experiment involved the impact of quartz particles with 325 $[\mu m]$ mean diameter and an impact velocity

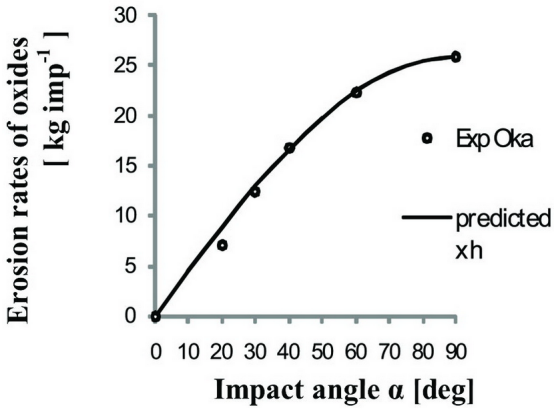

Figure 4.2: Comparison with the experiment results by Oka et al. [128].

of 100 $[m\ s^{-1}]$ on (Al_2O_3) scale.

The predicted solid line shown is a function of the scale thickness $(\overline{h})$ and thus the model agrees well with the experimental results. Although this agreement is sufficient for validating the model, further validation through a set of experimental work is necessary to investigate the effect of the oxide layer thickness on the model application. This was beyond the scope of this theoretical study and will be recommended in the future work.

To evaluate the oxide layer thickness, the passivation potential (E_{pas}) for every pure metal must be determined based on the Simplified Pourbaix diagrams shown in figure 4.3 (a-d) [17]. The passivation potential can be expressed as the potential value at which the passivating film (oxide layer) is thermodynamically stable and is represented in Pourbaix diagram for every metal as a boundary line between the dissolution and passivation region. The electrochemical reactions controlling the stabilisation process are presented in the following section.

4.2.3 Electrochemical reactions and Pourbaix diagrams

To explain the dissolution and passive regions of influence for every pure material selected in this study, Figure 4.3 illustrates the Pourbaix diagrams for Fe, Ni, Cu, and Al respectively [17]. These diagrams are the basis for constructing the erosion-corrosion maps below as they determine the corrosion mechanism which predominate

for each of the pure metals (i.e. dissolution, passivation and immunity) [83].

It is shown in figure 4.3 that every metal has its behaviour towards the applied conditions, namely applied potential and pH at the specified operating temperature. In the following four subsections, the electrochemical reactions involved in forming these Pourbaix diagrams for Fe, Ni, Cu, and Al are presented. All the passivation potential values for the mentioned pure metals are expressed in volts with respect to the standard hydrogen electrode (SHE). The activities of the dissolved metal ions are assumed to be equal to (10^{-6}).

4.2.3.1 Electrochemical reactions controlling passivation of Fe

Figure 4.3(a) shows the corrosion mechanisms of Fe in aqueous system. It is observed that Fe transition boundaries between the dissolution and passivation regions is categorised by both the applied potential and pH of the electrolyte. The metal is immune to corrosion at low applied potential and the transition between the immune and dissolution regions is independent of the pH value at the lower pH. Fe dissolves at lower pH values while passivates at higher values. At lower pH values, the dissolution mechanisms extend to higher applied potential values. The electrochemical reactions involved can be stated as [8]:

$$Fe_2O_3 + 6\,H^+ + 2\,e^- = 2\,Fe^{2+} + 3\,H_2O \tag{4.40}$$

From [8], this line boundary can be represented as a function of the potential and pH as:

$$E_{pas} = 1.08 - 0.1773\,pH \tag{4.41}$$

This expression is valid at room temperature for pH values up to (9.5) which is satisfied for the range of pH under investigation in this study.

4.2.3.2 Electrochemical reactions controlling passivation of Ni

As illustrated in figure 4.3(b), the transition boundary from immunity and the dissolution regions are slightly higher than that of Fe. Moreover, the dissolution region

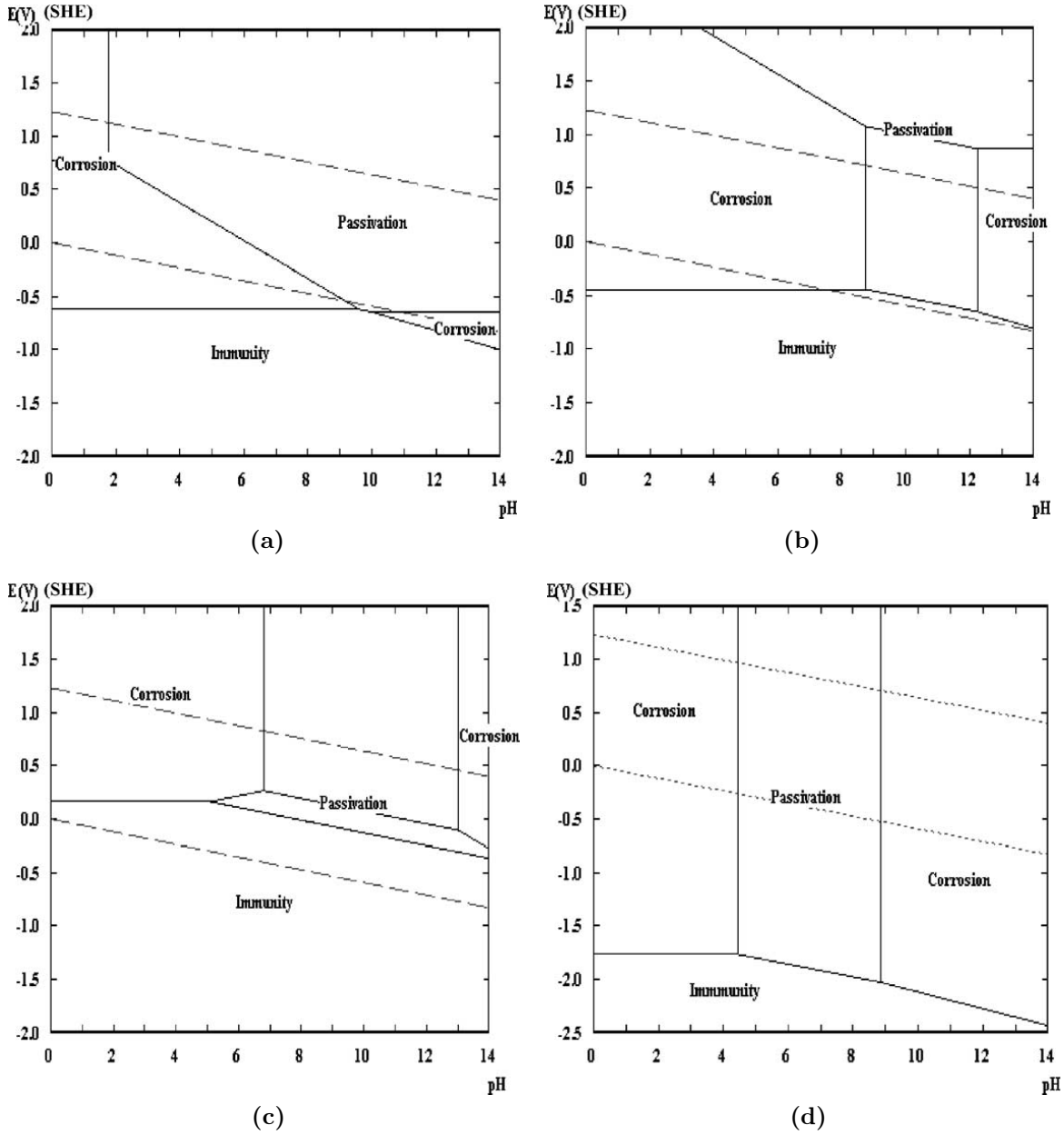

Figure 4.3: Simplified Pourbaix diagram at $T = 298\,[K]$ for (a) $Fe - H_2O$ system assuming passivation by formation of Fe_2O_3. (b) $Ni - H_2O$ system assuming passivation by formation of NiO. (c) $Cu - H_2O$ system assuming passivation by formation of Cu_2O. (d) $Al - H_2O$ system assuming passivation by formation of Al_2O_3.

extends more than Fe until pH value of 9.1, where the passive oxide layer begins to form in the surface of the metal. The transition between the immunity and passivity regions is function of both pH and potential. The electro-chemical reactions can be listed as follows

$$Ni + H_2O = NiO + 2\,H^+ + 2\,e^- \tag{4.42}$$

The line represent this reaction in the Pourbaix diagram can be formulated as [8]:

$$E_{pas} = 0.11 - 0.0592\,pH \tag{4.43}$$

4.2.3.3 Electrochemical reaction controlling passivation of Cu

It is noticed that Cu has no active passive transition at a constant pH like Ni. Cu is a noble metal, which can be indicated by the large immunity region. The passive region has a transition boundary with the immunity region at pH values from 6.9-12.8. The passivation reaction considered at this range is [8]:

$$Cu + H_2O = CuO + 2\,H^{2+} + 2\,e^- \tag{4.44}$$

and similarly, the line can be represented mathematically as [8]:

$$E_{pas} = 0.57 - 0.0592\,pH \tag{4.45}$$

4.2.3.4 Electrochemical reaction controlling passivation of Al

Al dissolves at low pH values. Although it behaves like Cu in the dissolution- passivation regions distribution, the transition boundary between immunity and dissolution occurs at very low potential compared to Cu and the other metals. The passivation region is bounded between pH 3.9-8.6. The passivation reaction can be given as [8]

$$2Al + 3\,H_2O = Al_2O_3 + 6\,H^+ + 6\,e^- \tag{4.46}$$

and hence can be represented by the mathematical formulation [8]:

$$E_{pas} = -1.55 - 0.0592\,pH \tag{4.47}$$

for pH values above the 8.6, Al suffers a dissolution mechanism which is characterised by the electro-chemical reaction [8]:

$$Al + 2\,H_2O = AlO_2^- + 4\,H^+ + 3\,e^- \tag{4.48}$$

the transition boundary line then can be represented by [8]:

$$E_{trans} = -1.38 - 0.079\,pH \tag{4.49}$$

4.3 Results

The results of the modelling work are illustrated in the form of 3-Dimensional erosion-corrosion maps. The maps constructed are divided into two different types:

(i) Regime maps: where the dominating degradation mechanisms are presented and identified as discussed according to the regime boundaries in subsection 4.1.2.

(ii) Wastage maps: where the total wear rates are presented and identified to identify the regions of critical wastage (high wastage) and also their boundaries are discussed and defined in subsection 4.1.2.

The maps are constructed for a range of pure metals, namely: Fe, Ni, Cu and Al. Based on the erosion and corrosion models introduced in the above sections, the erosion-corrosion 3-D maps include all the parameters affecting the erosion process, namely: particle parameters, hydrodynamic parameters, and the target material parameters. They also include some of the corrosion parameters, namely: pH, applied potential, particle concentration, passive layer properties. The results extracted from the simulation in this chapter will focus on the material change while keeping the operating temperature constant at standard room level (i.e. at 298 $[K]$).

The corrosion mechanism can be determined by using the Pourbaix diagrams for

each metal. Pourbaix diagrams [17] indicate whether the metal exhibits a dissolution or passivation process at specific pH and applied potential. For each metal, regime and wastage maps are generated for three different pH values, namely: at pH= 5, pH= 7, and pH = 9, to show the effect of the pH variation on the construction of these maps and its transition boundaries. The effect of the applied potential is investigated by assuming active controlled process. The effect of particle loading is also discussed by varying the mass flow rate in the pipe entrance assuming homogeneous distribution at the pipe inlet only. The effect of some of these parameters is discussed in details, in the discussion section.

4.3.1 Effect of pH on the erosion-corrosion maps for pure metals

The erosion-corrosion mapping results in Figure 4.4(a-d) show the change in erosion-corrosion regimes for the various pure metals at pH=5 and applied potential= -0.6 V (SCE). Numbers of erosion-corrosion regimes operating on the component, under nominally the same initial simulation conditions. It was shown that, there were significant differences between the regimes of erosion-corrosion behaviour observed, with dissolution and dissolution-erosion being dominant for Fe; Figure 4.4(a), a transition to erosion-dominated behaviour for Ni and Cu; Figure 4.4(b-c) and to erosion-passivation for Al; Figure 4.4(d).

At pH=7; Figure 4.5, and pH 5; Figure 4.4, only Fe; Figure 4.4(a) and 4.5(a), was affected by dissolution. All the other metals were in the erosion-dominated, except for Al; Figure 4.5(d), which exhibits passivation affected regimes. No change is observed in case of Fe, Ni, and Cu at pH=5 and pH=7, as the dissolution is dominating the corrosion process. According to the Butler-Volmer equation (equation 4.18), the only variable affecting the dissolution rate is the overpotential (ΔE), which in these two figures are kept constant. There is very slight change in the Al maps; Figure 4.5(d), compared to the map in Figure 4.4(d). The passivation-dominated regimes slightly extended at the beginning of the bend of the pipe, which indicates the transition boundary from dissolution to passivation regimes as in [8].

At pH=9; Figure 4.6, there was a transition to erosion-passivation and erosion-

dominated behaviour for the Fe; Figure 4.6(a). This is in contrast with the behaviour at lower pH values; Figure 4.4(a) and 4.5(a), in which dissolution affects the process. For the Ni and Cu, the erosion-corrosion processes were characterised by erosion-dominated behaviour; Figure 4.6(b-c). For Al; Figure 4.6(d), there was a transition to a new corrosion affected regime as dissolution dominated behaviour. This is contrast with the passivation dominated processes observed at the lower pH values; Figure 4.4(d) and Figure 4.5(d).

The results of erosion–corrosion wastage maps; Figures. 4.7, 4.8, and 4.9, indicate very significant differences for the pure metals at the various pHs. As in the case for the results above, a number of wastage regimes predominated on the component. At pH 5, the highest wastage was observed for the Fe; Figure 4.7(a), with the wastage decreasing for Ni and Cu; Figure 4.7(b and c). The high wastage regime had a greater presence for Al; Figure 4.7(d), than for the latter metals; Figure 4.7 (b and c). As the pH was increased to 7, the wastage profiles were similar for all metals; Figure 4.8(a–d), as in the case at pH 5; Figure 4.7. However, at pH 9, there was a change in the behaviour; Figure 4.9(a–d), with the high wastage regime predominant for the Al; Figure 4.9(d), to a greater extent than for the other metals.

It is shown, from the maps generated so far, that it is possible to identify erosion–corrosion mechanistic regimes on real components under nominally similar fluid flow conditions. Hence, the model developed provides a new tool for representing the transitions between erosion–corrosion regimes on real surfaces. The results indicate the variety of regimes possible over one single component. It can be applied to any pure metal and alloy, once we can capture the erosion and corrosion behaviour in terms of mathematical models.

Further investigation will be commenced to identify the effect of some parameters that influence the erosion and corrosion processes by focusing on these Iron (Fe) as the substrate metal. This is because of its wide applications in the industries and power stations units. The effect of applied potential, particle size, and particle concentration will be discussed in this chapter, while the effect of temperature will be investigated in the next chapter separately as mentioned before because of its influence in both erosion and corrosion.

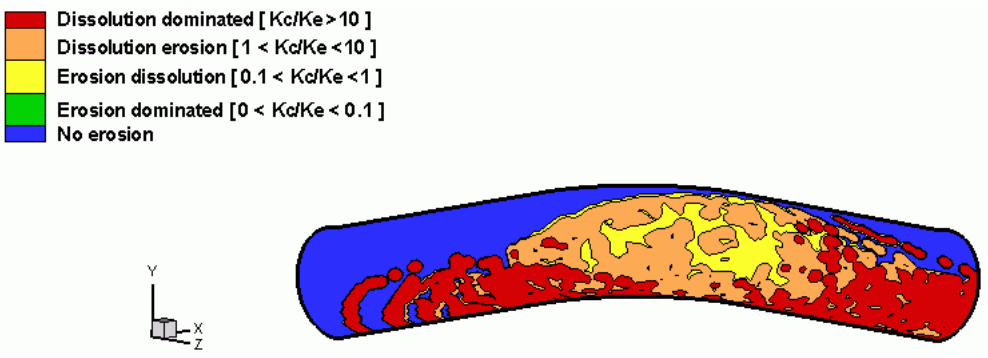

(a)

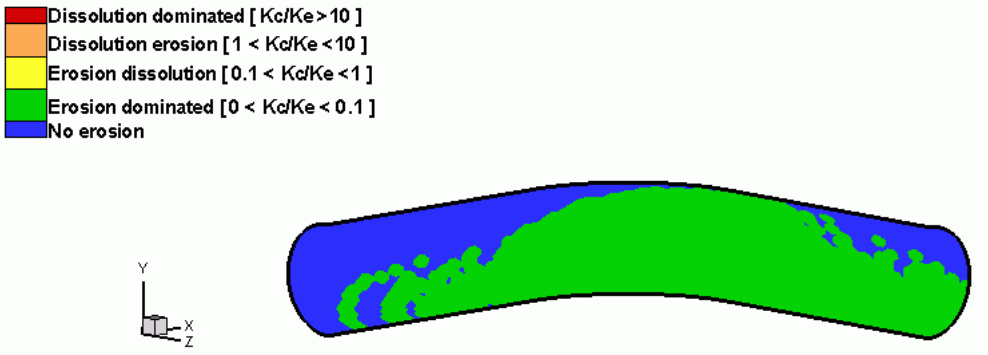

(b)

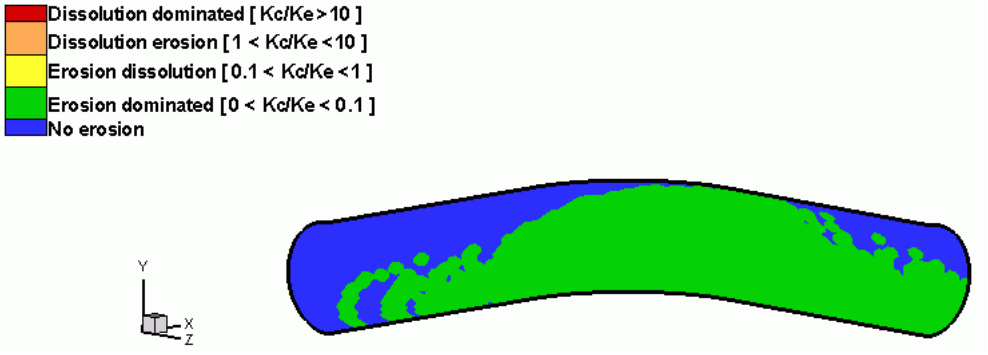

(c)

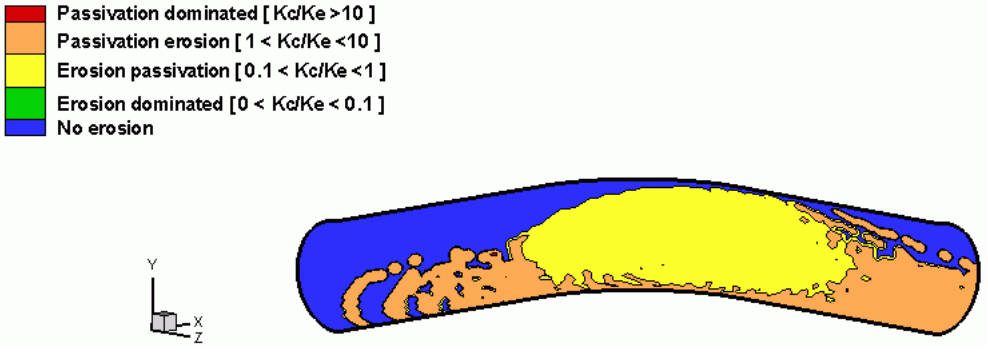

(d)

Figure 4.4: Erosion-corrosion maps for the outer surface of elbow-pipe at pH=5, E_{ap}=-0.6 V[SCE], particle size=1000 [µm] and concentration =22.88% (v_f = 0.1) for: (a) Fe. (b) Ni. (c) Cu. (d) Al.

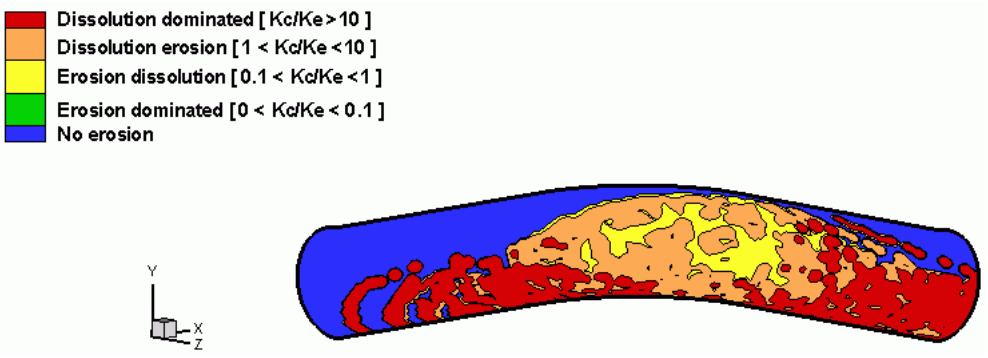

(a)

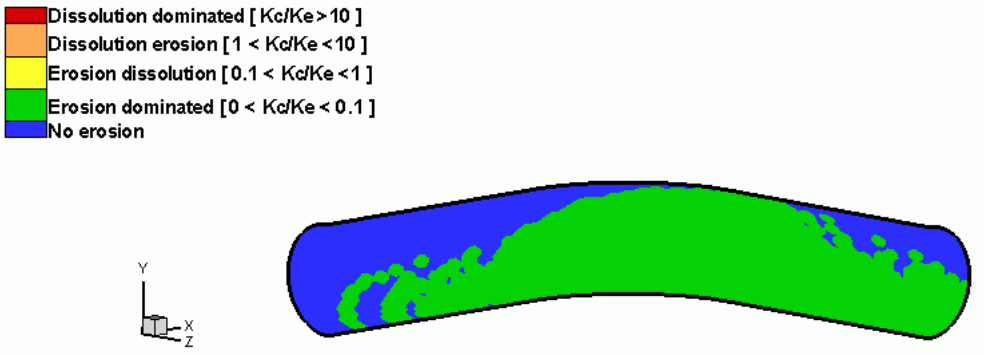

(b)

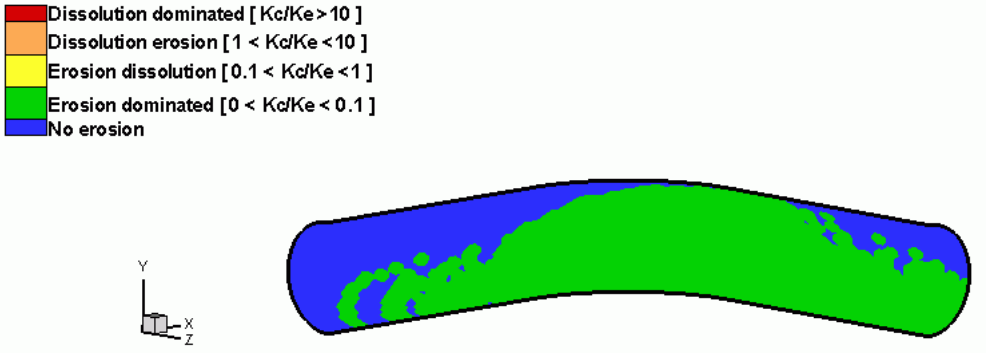

(c)

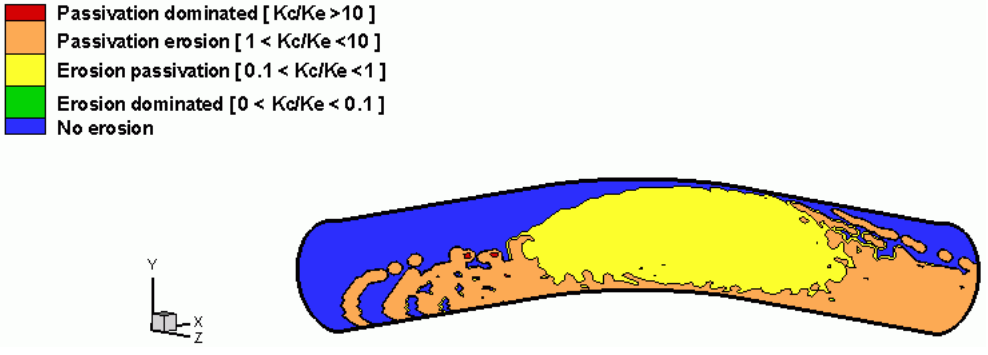

(d)

Figure 4.5: Erosion-corrosion maps for the outer surface of elbow-pipe at pH=7, E_{ap}=-0.6 V[SCE], particle size=1000 [µm] and concentration =22.88% (v_f = 0.1) for: (a) Fe. (b) Ni. (c) Cu. (d) Al.

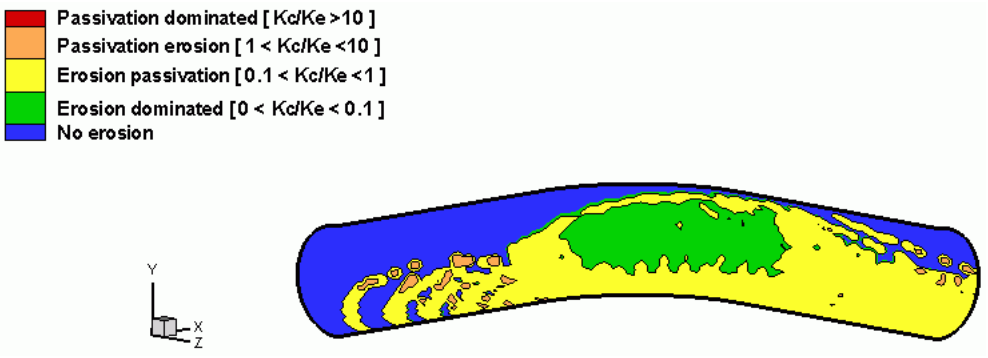

(a)

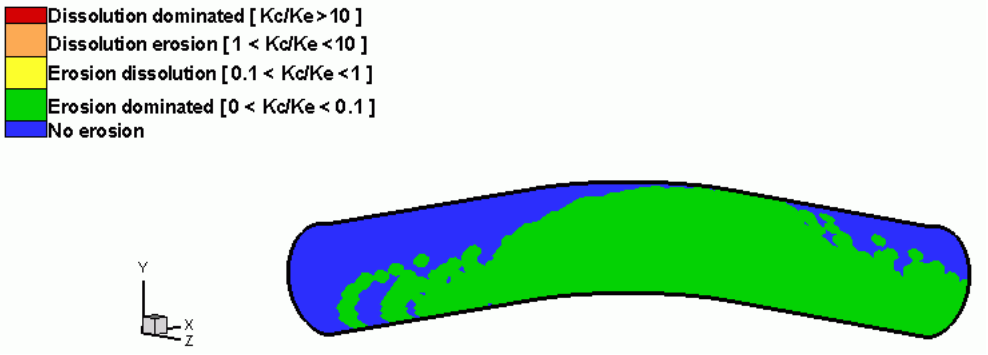

(b)

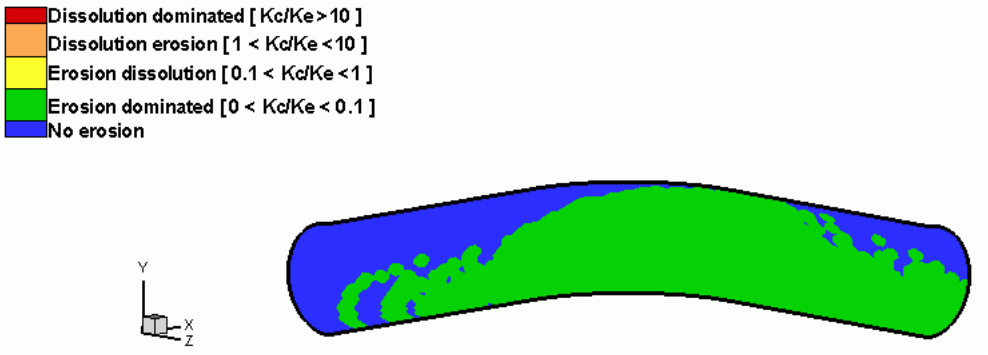

(c)

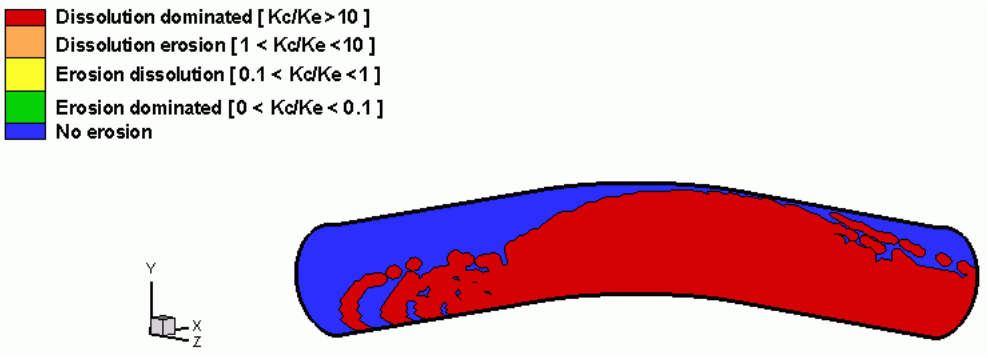

(d)

Figure 4.6: Erosion-corrosion maps for the outer surface of elbow-pipe at pH=9, E_{ap}=-0.6 V[SCE], particle size=1000 [µm] and concentration =22.88% (v_f = 0.1) for: (a) Fe. (b) Ni. (c) Cu. (d) Al.

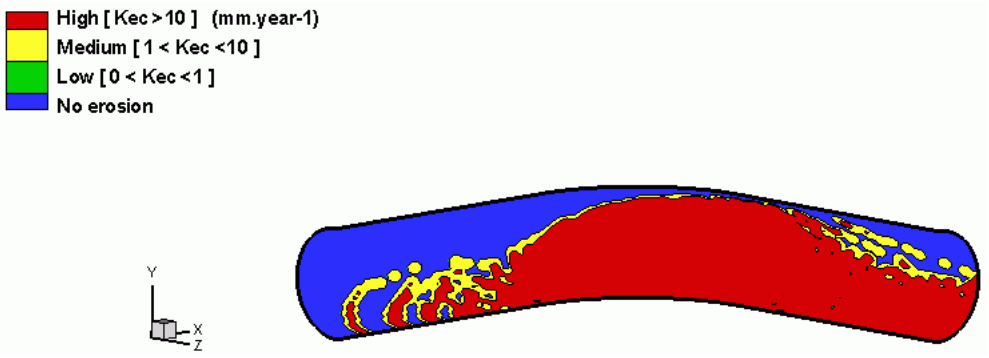

(a)

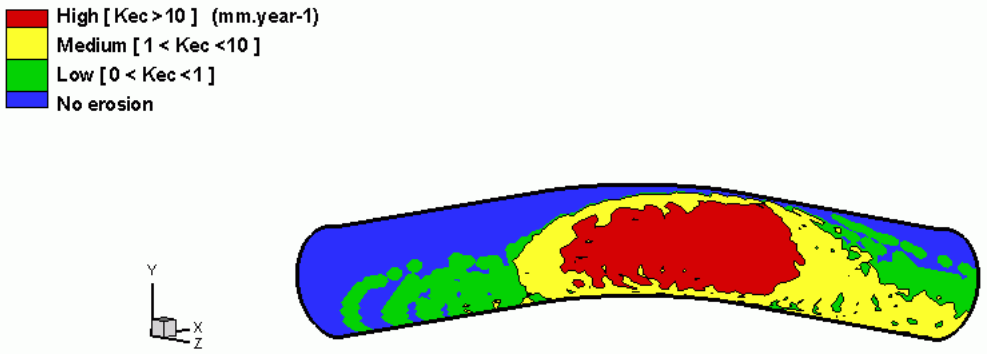

(b)

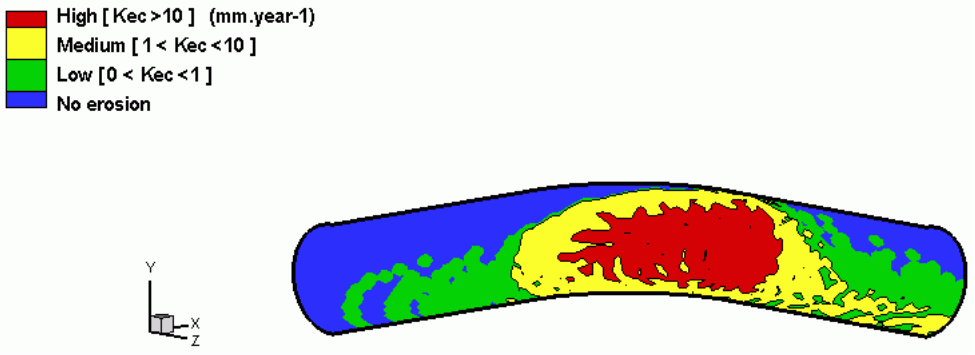

(c)

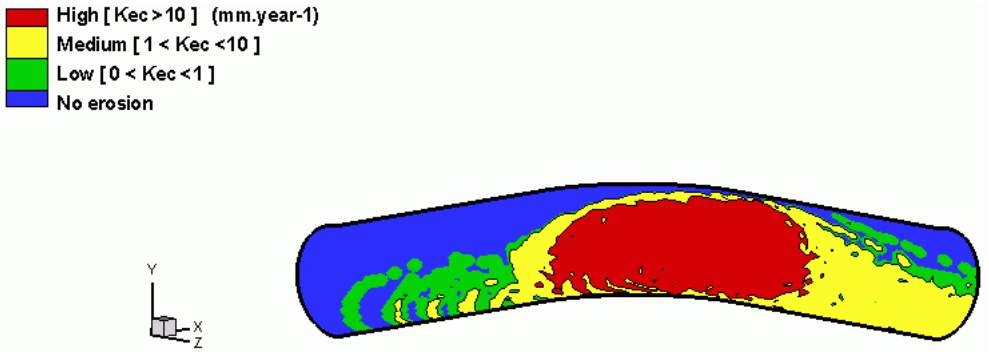

(d)

Figure 4.7: Erosion–corrosion wastage maps for the outer surface of elbow-pipe at pH 5, E_{ap}=−0.6 V(SCE), particle size = 1000 [μm] and concentration = 22.88% (v_f= 0.1) for: (a) Fe. (b) Ni. (c) Cu. (d) Al.

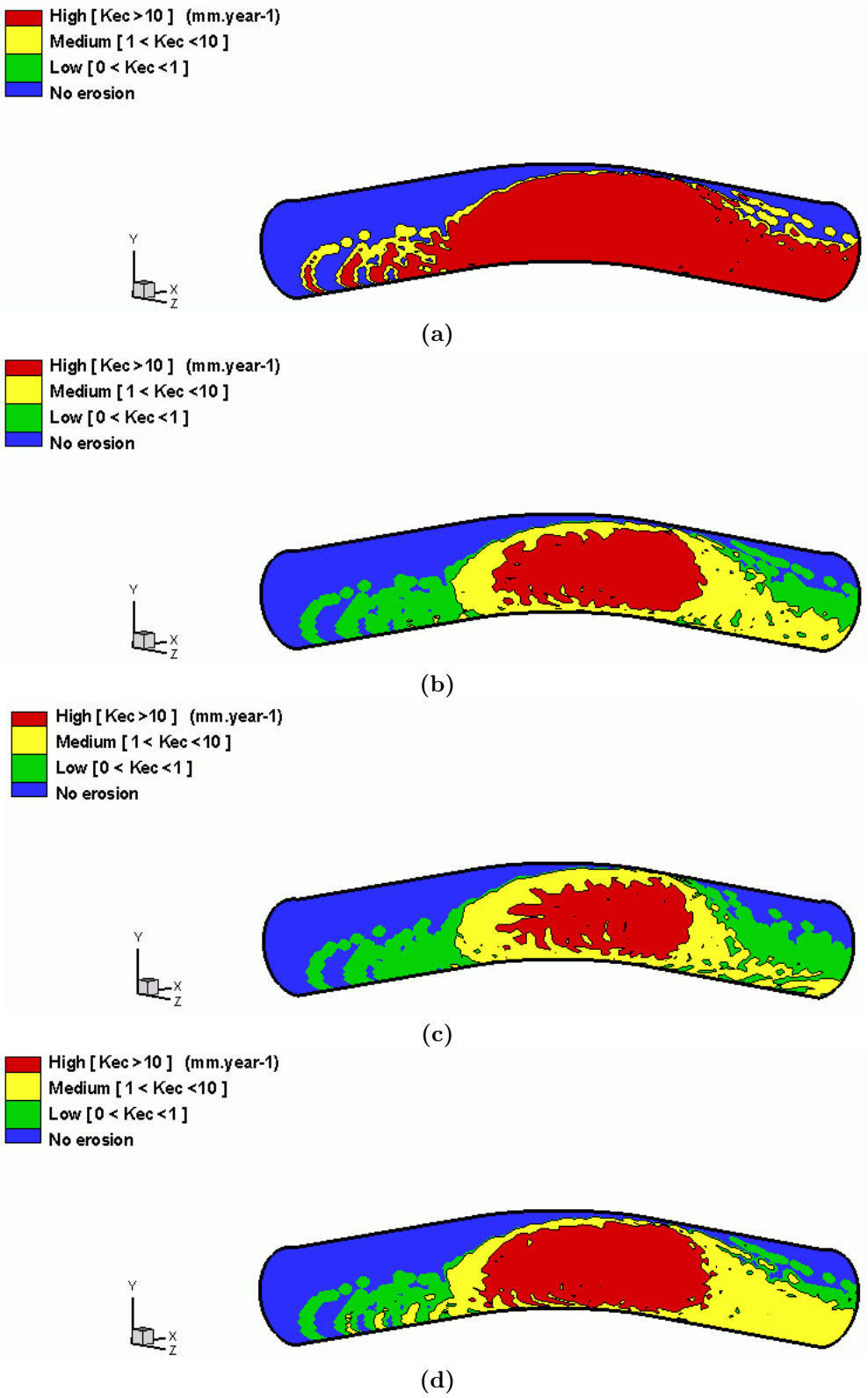

Figure 4.8: Erosion–corrosion wastage maps for the outer surface of elbow-pipe at pH 7, E_{ap}=−0.6 V(SCE), particle size = 1000 [μm] and concentration = 22.88% (v_f= 0.1) for: (a) Fe. (b) Ni. (c) Cu. (d) Al.

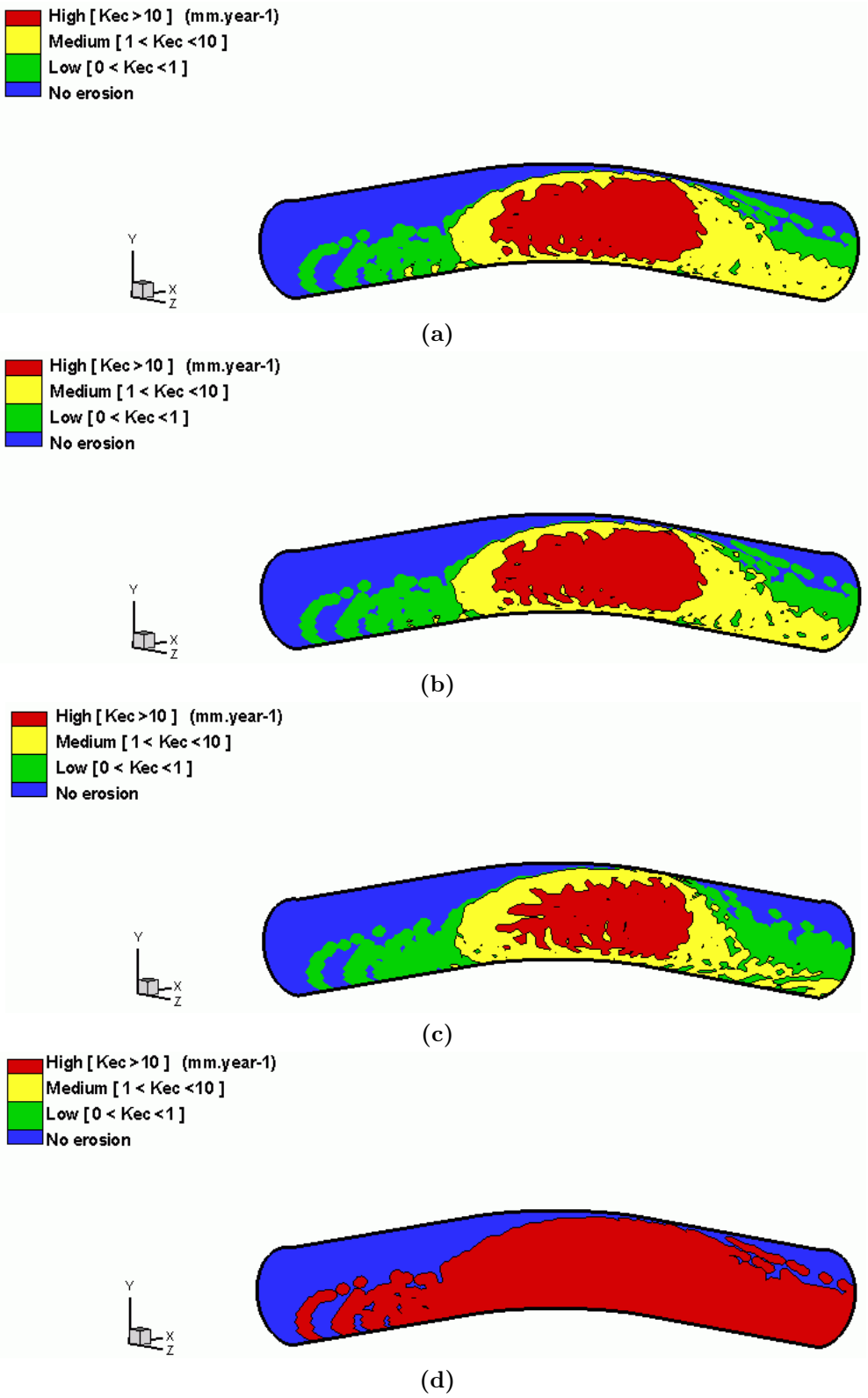

Figure 4.9: Erosion–corrosion wastage maps for the outer surface of elbow-pipe at pH 9, E_{ap}=−0.6 V(SCE), particle size = 1000 [μm] and concentration = 22.88% (v_f = 0.1) for: (a) Fe. (b) Ni. (c) Cu. (d) Al.

4.3.2 Effect of the applied potential on the erosion-corrosion maps

Increases in applied potential are introduced in Figure 4.10 for Fe at pH 7. The figure showed various significant transitions from mainly erosion dominated behaviour at −0.75 V(SCE), where the dissolution rate is apparently low; Figure 4.10(a), and gradually increasing the domination of the dissolution regimes at -0.6 V(SCE); Figure 4.10(b), to dissolution and mainly erosion–passivation dominated behaviour as the potential was increased from −0.5 to −0.25 V; Figure 4.10(c and d). The erosion-corrosion regime maps showed consistency with the Pourbaix diagram at operating environment, which indicates its reliability in predicting the erosion-corrosion regimes at the any operating conditions taking into consideration the assumption assumed at the methodology section.

4.3.3 Effect of the particle size on the erosion-corrosion maps

For the effect of particle size on Fe, an environment operating conditions at pH 9 and −0.6 V(SCE) were chosen. At these conditions, it was shown from the Pourbaix diagram; Figure 4.3(a), that Fe exhibits passivation corrosion mechanisms, which; according to equation4.37 is proved to be dependent of the particle size and density. Figure 4.11(a-d) shows increases in particle size by a factor of three; namely: at particle sizes 250, 500, 750, and 1000 [μm]. Figure 4.11(a–c) changed the erosion–corrosion processes from passivation dominated and passivation–erosion dominated behaviour, to a situation where erosion–passivation was the dominant degradation process.

4.3.4 Effect of the Tafel slope on the erosion-corrosion maps

All the results commenced so far were taken for a Tafel slope approximated to a value of 0.05 [8]. Figure 4.12 shows the dependency of the erosion-corrosion maps on the Tafel slope. The same conditions are investigated but the Tafel slope was taken by its calculated value according to Equation 4.21. The current density is known to be a function of the Tafel slope, which in turn affected by the solution temperature

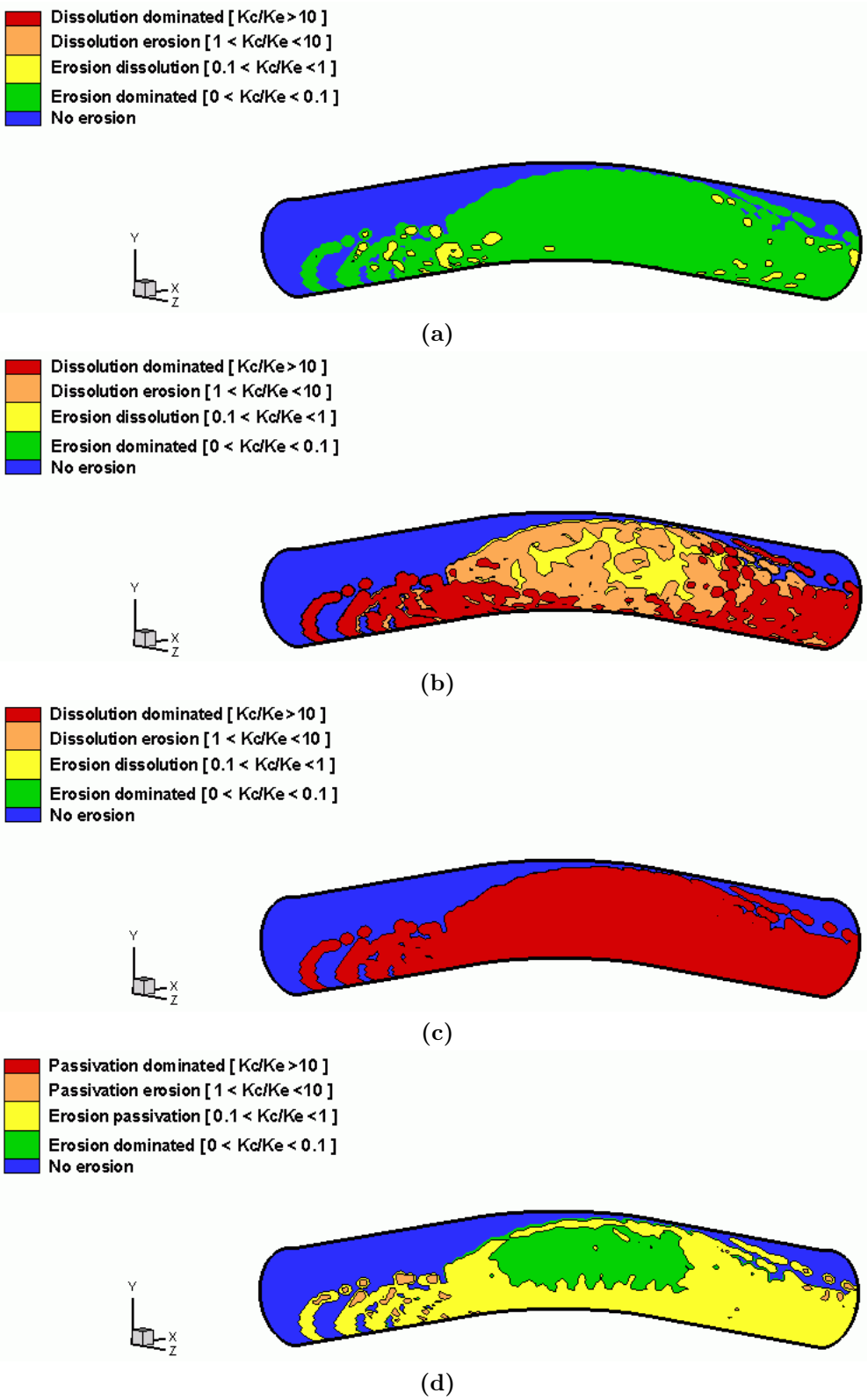

Figure 4.10: Erosion–corrosion maps for the outer surface of (Fe) elbow-pipe at pH 7, particle size = 1000 [μm] and concentration = 22.88% (v_f= 0.1) for E_{ap}: (a) −0.75, (b) −0.6 (c) -0.5 and (d) −0.25 V(SCE).

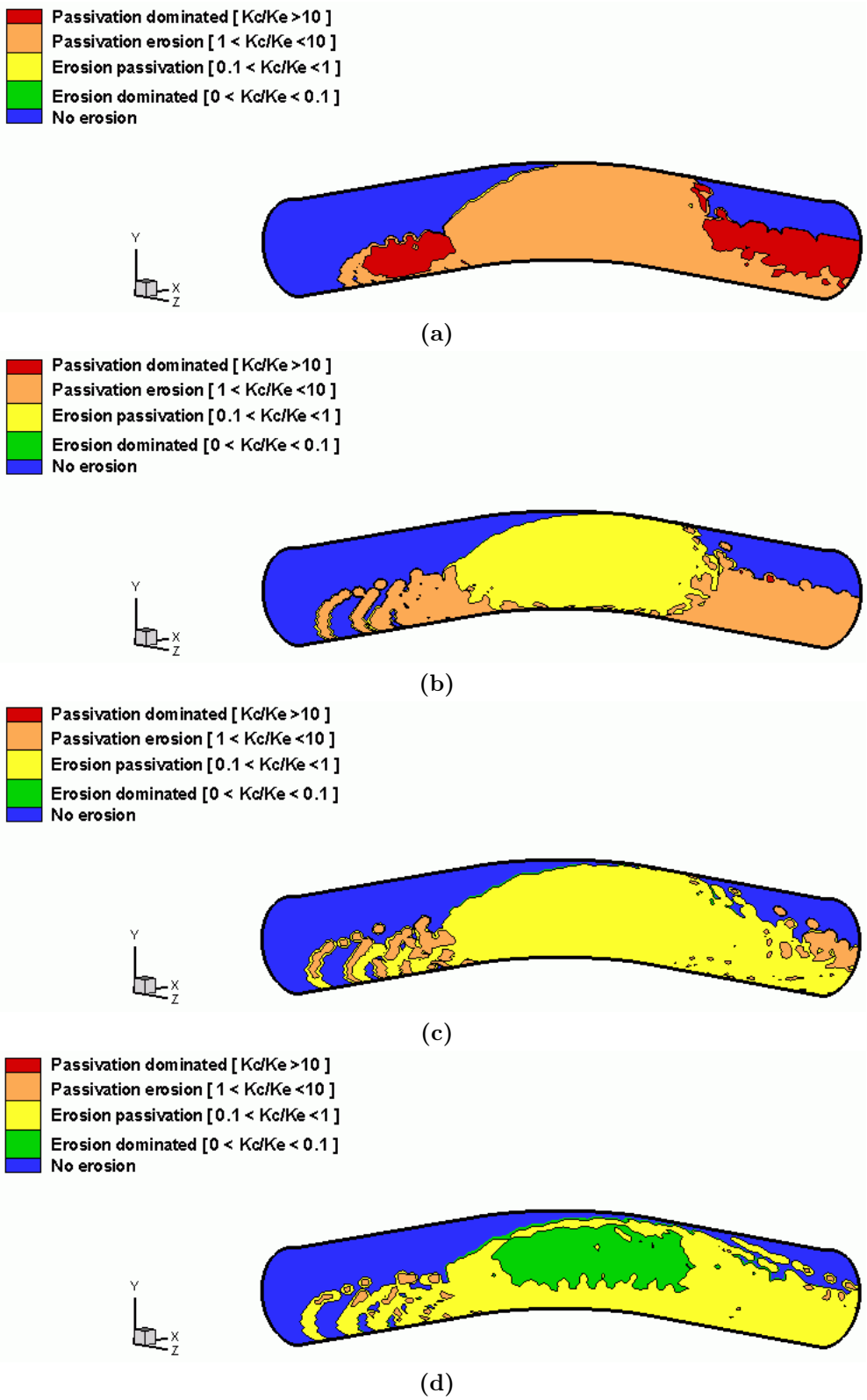

Figure 4.11: Erosion–corrosion maps for the outer surface of (Fe) elbow-pipe at pH 9, E_{ap}=−0.6 V(SCE) and concentration = 22.88% (v_f = 0.1) for particle size: (a) 250 [μm]. (b) 500 [μm]. (c) 750 [μm]. (d) 1000 [μm].

according to the Tafel equation. The results obtained in the dissolution affected regions at the same conditions show lower dissolution rate values for the dissolution regimes boundaries; Figure 4.12(b), than that obtained in Figure 4.12(a). The reason behind this change in the corrosion rates is the dependence of the dissolution rates on the symmetry factor, which is hard to be estimated [130]. It is important to note that the Tafel slope taken here as a function of the temperature which increasing the Tafel slope value to 0.059 at standard room temperature compared to 0.05 taken in the previous study [8], assuming constant symmetry factor $\beta = 0.5$.

The increase in Tafel slope causes lower predicted value for the corrosion rates, and when divided with the predicted erosion rate from the Sundararajan model, the predicted regimes boundary lines changed accordingly from dissolution-dominated and dissolution-erosion; Figure 4.12(a), to dissolution-erosion and erosion-dissolution domination. It is important to note that the Tafel slope is a very important parameter and must be calculated very carefully in predicting precise boundaries for the erosion-corrosion maps.

4.3.5 Effect of the particle concentration

To investigate the particle concentration effect, homogeneous particle distribution on the pipe at the inlet was assumed, and the particle concentration is thus related to the particle mass flow rate according to the relation:

$$\dot{m}_p = v_f \, \rho_p \, V_p \, A_{in} \tag{4.50}$$

Three more simulations were run to investigate the effect of particle concentration. The simulations run at different particle mass flow rates; namely: 0.957, 1.9169, 2.87 and 3.8276 [kg s-1], which are equivalent to particle inlet volume fraction of 0.025, 0.05, 0.075 and 0.0909 respectively. Figure 4.13(a-d) shows the regime maps at the outer extrados surface of the pipe bend at pH=7 and applied potential E=-0.6 [V] (SCE). The figure illustrates how the erosion-corrosion regimes alter as the particle volume fraction changes. As the particle volume fraction increases, the erosion rates increase linearly. As a result, the erosion-dissolution and erosion dominated regimes are spreading as the particle mass flow rate and volume fraction increases. This

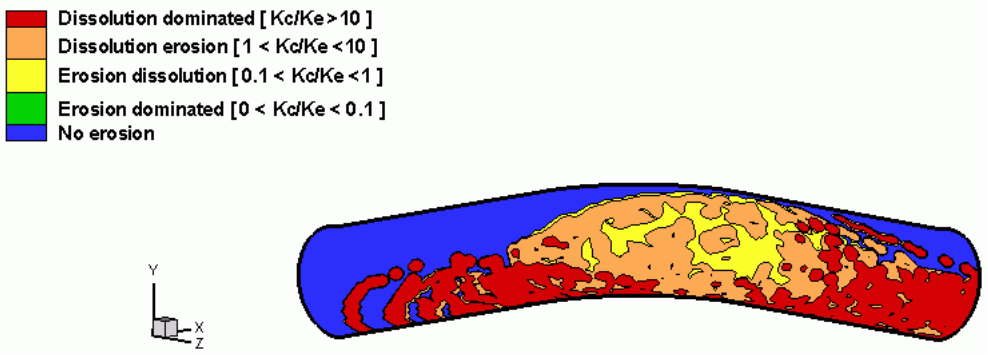

(a)

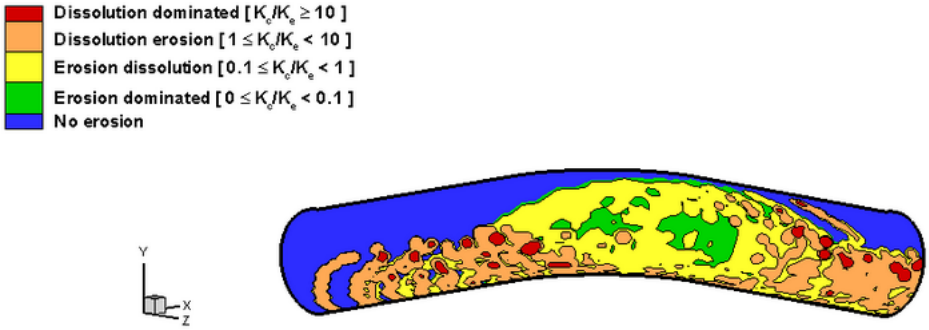

(b)

Figure 4.12: Regime maps on the outer surface of Fe pipe bend at pH=7 and E= -0.6 [V] (SCE) for Tafel coefficient: (a) 0.05 (Stack et al.2004b) (b) 0.059 (using equation 4.21).

indicates the importance of the volume fraction (or particle concentration) as a factor affecting the erosion-corrosion regimes.

4.4 Discussion

As in the two dimensional simulations for erosion–corrosion of pure metals [8], significant differences are found in the three-dimensional simulation between the regimes domination for the metals. Cu and Ni are more immune and less likely to be dominated by corrosion than Fe and Al; Figures 4.4, 4.5 and 4.6. However, it should be emphasised that, if the conditions differ, the results will change significantly. It is important to note that, various metals will exhibit different erosion–corrosion behaviour, and because of the changes of impact velocity and frequency over the component; Figs. 4 and 5, a variety of erosion–corrosion regimes are experienced on the surface of the component.

It is clear that a significant area of the component modelled will not experience any erosion or impact of flowing particles. These areas are indicated in all figures by the blue colouring. In practise, the un-eroded surfaces may experience corrosion through dissolution or passivation. These areas point out a regime where only corrosion exhibited on the surface of the material. This regime could not be indicated in the 2D erosion-corrosion maps [8].

The transition from passivation to dissolution dominated behaviour for Al, is illustrated in Figures 4.4(d) and 4.6(d). Here, at higher pH values, the Al dissolves, in contrast to that which occurs for the other pure metals at such pHs, Figure 4.6(a-c). This is a characteristic of Al which makes it unsuitable for use at such pH values.

The wastage maps for the pure metals at different pH values; Figures 4.7, 4.8 and 4.9, show very little differences between the pure metals at pH 5 and 7, at -0.6 V(SCE), which is surprising. However, at higher pH values; the wastage is significantly greater for the Al; Figure 4.9(d), than at lower pH values. This is possibly due to the high dissolution rate of this material.

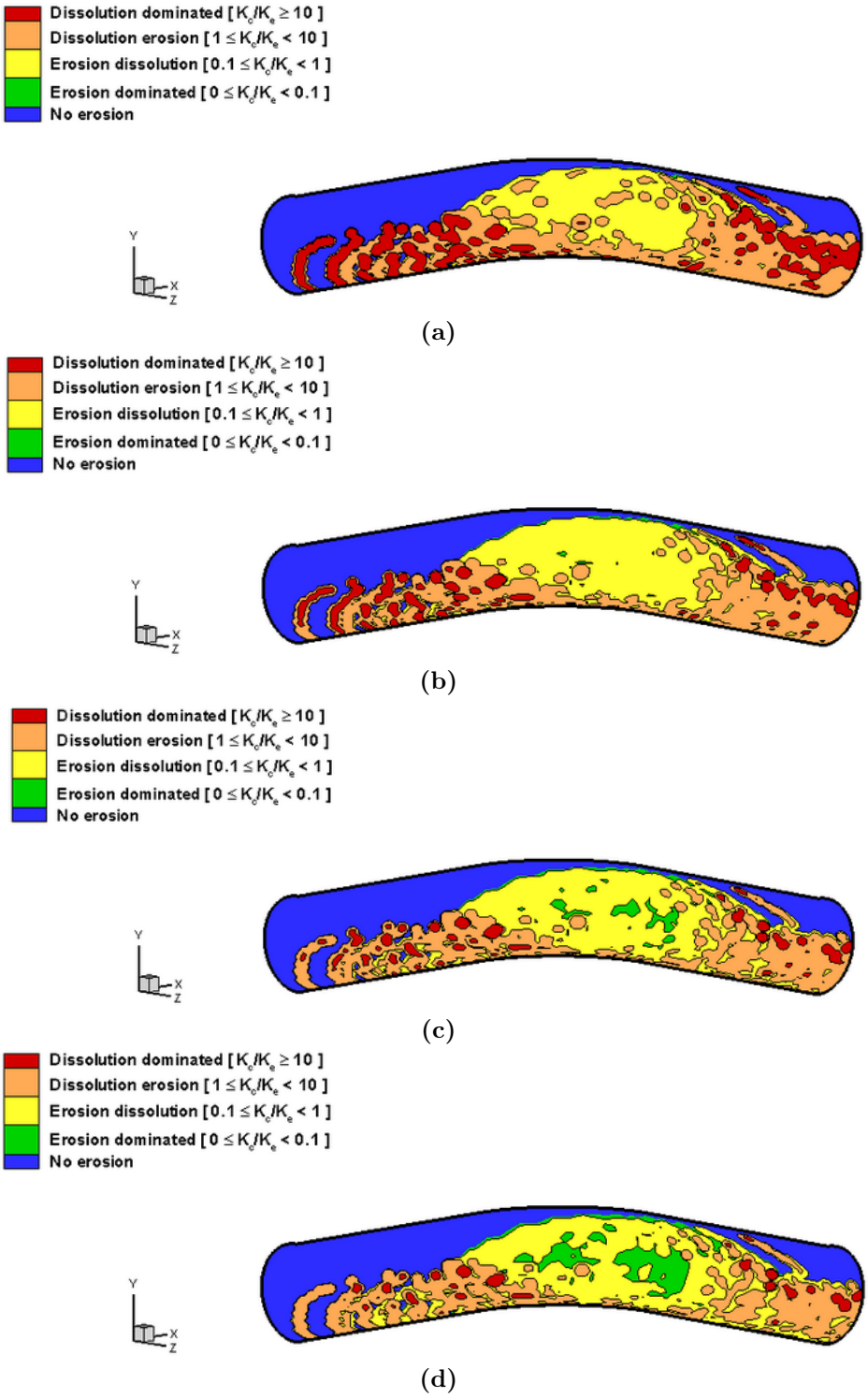

Figure 4.13: Regime maps on the outer surface of Fe pipe bend at pH=7 and E_{ap}= -0.6 [V] (SCE) for particle mass flow rates: (a) 0.957 (b) 1.9169 (c) 2.87 (d) 3.8276 $\left[kg\ s^{-1}\right]$.

Increases in particle size by a factor of three for the Fe reduces the passivation affected regimes on the component; Figure 4.11. The increase in erosion footprint results from the higher impact energy involved in the process. The three-dimensional results highlight the important influence that particle size has on the erosion–corrosion regime.

The effect of changing applied potential in the positive direction, i.e. from −0.75 to −0.25 V(SCE) has a very significant effect on the erosion–corrosion degradation mode for the Fe; Figure 4.10(a–d). Here, the regime is changed from dissolution, to predominately passivation affected behaviour over the component. This illustrates the importance of electrochemical potential on the stability of the corrosion regime as identified by the Pourbaix diagrams for the various pure metals and their influence on the erosion–corrosion two-dimensional maps [8].

Limited number of models developed to date that account for the interaction between erosion and corrosion i.e. the synergism or additive effect during the processes. However, the reasons for such effects are not well understood and can be material-specific [36][123][131]. This is why the initial work on mapping the component for the materials above has made such assumptions listed in the methodology section.

The 3D erosion-corrosion maps developed have advantages over the 2D erosion-corrosion maps in the service and enhancing design stages. It can provide a useful tool for predicting and identification of the erosion-corrosion regimes and wastage regions. In addition, the effect of all parameters that influence the erosion and corrosion process can be evaluated separately or in a combined manner. This is in contrast with the 2D maps, which are more applicable in the design stage where they can provide designers with the most optimum operating conditions; and even help choosing the suitable material for the application under design.

Chapter 5

TEMPERATURE EFFECT ON EROSION-CORROSION MAPS

5.1 General

The effect of environmental parameters on the wear process of metal surfaces is important to assess in evaluation of the erosion-corrosion mechanisms [132, 133, 84, 91]. In studies of erosion-corrosion regimes, even slight change of these parameters varies the material response to this change [134, 8]. 2D erosion-corrosion mapping is one step to theoretically understand and monitor the influence of these parameters on the metal degradation and the erosion-corrosion regimes.

The strategy of constructing the 2D erosion-corrosion maps was built in monitoring the erosion-corrosion regimes and wastage boundaries with respect to two parameters, one affecting the erosion process, and the other affecting the corrosion process [19]. One of the deficiencies to date of such approaches is that, in any environment in which erosion- corrosion occurs, more than two parameters can vary within that process. Furthermore, it cannot identify these variations in case of the parameters that affect both erosion and corrosion processes.

One example of these parameters is the environment temperature. The operating temperature is one of the most important parameters that affect both the erosion and corrosion processes [135, 136]. The temperature rise was found to cause a significant increase in the erosion by several authors [21, 137, 138]. On the other hand, high temperature differences also affect the mechanical properties of the target material; such as the yield strength, elasticity, heat capacity and hardness of the target material [22, 139]. This leads to the conclusion that, in investigating the erosion process, researchers must distinguish between the target material and the carrier fluid temperatures as distinct variables affecting the erosion process.

Suckling and Allen [138] found an increase in the erosion rate as the temperature of the carrier air rises, when measured at fixed fluid velocity and particles mass flow rate. Howes et al. [140] monitored the variation of the erosion rates of steel specimens with the metal surface temperature increase while keeping the fluid temperature constant at 500 $[^oC]$. The erosion rates first had increased until surface temperature reaches 300 $[^oC]$, then decreased to the lowest level at 500 $[^oC]$.

The corrosion process is also affected by the temperature rise. The current density

is a function of the Tafel coefficient, which in turn affected by the solution temperature [130, 122]. In the case of the passivation reaction, the effect of the temperature rise influences the thermodynamically stable region for the passive reaction. This can be revealed clearly in E-pH diagrams at various temperatures. Cubiccioti [141] had investigated the effect of the temperature rise on the E-pH diagram for stainless steel alloy, at standard room temperature and at 300 $[^oC]$. The results showed an increase in the passive reaction area along the diagram as the temperature increase and a decrease in the dissolution area accompanied by a decrease in the immunity region's area.

Using the same case study and applying the same methodology with some modifications, 3D erosion-corrosion maps were constructed and evaluated for iron (Fe) at a range of elevated temperature.

5.2 Erosion modelling

In the literature, we showed that there are many erosion models found, but few of them are accounting for the temperature rise. Chen et al. [142] developed a model to predict the erosion at elevated temperature for only normal impact. Although this erosion model accounts for the target material mechanical properties, such as the strain, it is not suitable in case of adiabatic processes.

O'Flynn et al. [73] developed a model that predicted the erosion as a function of the product of the toughness and uniform strain. This model gives reasonable results for temperatures between 200-300 $[^oC]$, but unsatisfied results in the room temperature. An empirical model was also proposed by Lee et al. [143] to predict the erosion rates as a function of seven accounted parameters affected the erosion process including the temperature of the target material. The results were in very good agreement with the experimental work, but the authors did not mention how the erosion constant in the empirical formula is given, which leads to the conclusion that it is adjustable constant depending on the erosion system.

5.2.1 Erosion model in 2D erosion-corrosion maps

In searching the literature to find a suitable erosion model which is simple, reliable and assumes adiabatic erosion process, the model of Sundararajan and Shewmon [53] was found suitable to be used in this work; with some adaptation to account for the effect of temperature rise on the surface of the material used (Fe). The Sundararajan and Shewmon model is based on the so called the localisation deformation during single impact. The model can predict the erosion rates at normal impacts. The effect of the target material mechanical properties are also included. The erosion rate is expressed in term of the mass removed from the target material per unit mass of ingested particle and is given as [53]:

$$E_r = \frac{6.5 \times 10^{-3}\, \rho_p^{0.25}\, V_p^{2.5}}{C_p\,(T)\; T_m^{0.75}\, H_s\,(T)^{0.25}} \tag{5.1}$$

To determine the erosion rate as a standard unit; i.e. $[g\,cm^{-2}\,s^{-1}]$, it is necessary to multiply equation 5.1 with the particle flux [8]in $[g\,cm^{-2}\,s^{-1}]$:

$$flux_p = 100\, c_p\, V_p \tag{5.2}$$

Thus, rearranging, an expression for the pure erosion rate (K_{eo}) in $[g\,cm^{-2}\,s^{-1}]$ is obtained:

$$K_{eo} = \frac{0.65\, c\, \rho_p^{0.25}\, V_p^{3.5}}{C_p\,(T)\; T_m^{0.75}\, H_s\,(T)^{0.25}} \tag{5.3}$$

The metal surface mechanical properties are affected by the temperature rise. Sheldon et al. [144] related the yield strength with the Vickers hardness number by the following empirical relation:

$$H_s\,(T) = 2.7\, Y\,(T) \tag{5.4}$$

Nho [139] listed the effect of elevated temperature on the hardness of various carbon and stainless steel alloys. Das et al. [75] used the data in Shida et al. [137] to propose polynomial relationships for various materials to accurately relate the yield strength and the material temperature. A correlation relation for the carbon steel is given, based in these data as follows [75]:

$$Y(T) = 9.81\left(2 \times 10^{-5}\, T^2 - 0.0353\, T + 30.871\right) \tag{5.5}$$

Thus, the target material hardness can be related to the operating temperature as

$$H_s(T) = 26.487\left(2 \times 10^{-5}\, T^2 - 0.0353\, T + 30.871\right) \tag{5.6}$$

The specific heat of the target material is also influenced by the temperature rise. From the available standard data for Fe [145], the following polynomial function can be created to represent this change:

$$\begin{aligned} C_p(T) \;=\; & 17.9\,(2.04 \times 10^{-12}\, T^5 - 4.66 \times 10^{-9}\, T^4 \\ & + 4.22 \times 10^{-6}\, T^3 - 1.87 \times 10^{-3}\, T^2 + 0.43\, T - 16.77) \end{aligned} \tag{5.7}$$

Therefore, we can use equations 5.6 and 5.7, to account for the temperature effect of the target material on its mechanical properties in the Sundararajan first model (equation 5.1).

As mentioned earlier, the effect of the fluid temperature rise can be estimated by its influence in the fluid viscosity and density. The effect of the temperature rise on the impact velocity of particles cannot be included in the 2D erosion-corrosion maps, but it is addressed in the 3D maps development.

5.2.2 Erosion model in 3D erosion-corrosion maps

In modelling the erosion rates at any impact angle, the second erosion model of Sundararajan [54] was found to be suitable for this new method, but also needs some adaption to account for the effect of temperature rise on the surface of the material used. Sundararajan's second model is based on the so called the localisation deformation during single impact. The model can predict the erosion rates at different impact angles and for different particle shape. It is split into two expressions; one is for the normal impact, and the other is for the oblique impact. The model discussed in details in section 2.4.5, and is summarised here as follows; for erosion by deformation [54]:

$$Er_{def} = \frac{5.5 \times 10^{-2}}{(T_m - 436)^{0.75}} \frac{2^{n_c} f_t \ (V_p \, sin \, \alpha)^2 \, (1 - e_n^2)}{n_c \, C_p} \tag{5.8}$$

for erosion by cutting:

$$Er_{cut} = \frac{5.5 \times 10^{-2}}{(T_m - 436)^{0.75}} \frac{(n_c + 1) \left(\frac{\mu_f}{\mu_{fc}}\right) \left(2 - \frac{\mu_f}{\mu_{fc}}\right) (V_p \, cos \, \alpha)^2}{2^{(2-n_c)} \ (1 + \lambda) \ n_c \, C_p} \tag{5.9}$$

where:

$$\mu_{fc} = \frac{1}{(1 + \lambda) \ (1 + e_n) \ tan \, \alpha} \tag{5.10}$$

The normal and tangential coefficient of restitution can be related to the impact angle through the semi-empirical relation [48]:

$$e_n = 0.988 - 0.78 \, \alpha + 0.19 \, \alpha^2 - 0.024 \, \alpha^3 + 0.027 \, \alpha^4 \tag{5.11}$$

and:

$$e_t = 1.0 - 0.78 \, \alpha + 0.84 \, \alpha^2 - 0.21 \, \alpha^3 + 0.028 \, \alpha^4 - 0.022 \, \alpha^5 \tag{5.12}$$

It can also be related to the target material properties as [8]:

$$e_n = \frac{1.36 \, H_s \, (T)^{0.625}}{E_e^{0.5} \, \rho_p^{0.125} V_p^{0.25}} \tag{5.13}$$

where the elastic modulus of collision (or reduced modulus of elasticity) (E_e) can be given by [123]:

$$E_e = \frac{E_t \, E_p}{E_p \ (1 - \nu_t^2) + E_t \ \left(1 - \nu_p^2\right)} \tag{5.14}$$

Eraslan and coworkers [146, 147, 148] have used experimental data of Noda [149]to model the dependency of the mechanical properties of steel on temperature. They used a nonlinear fitting formulae for the experimental data and assummed constant Poisson ratio in a temperature range from 0 – 400 [^oC]. This assumption was found to be hold for most of the engineering materials like steels. The modulus of elasticity is given as a function of temperature from [137, 139] as:

$$E_t = E_o \left[1 + \frac{(T - 273.16)}{T_1 \ln (T/T_2)}\right] \tag{5.15}$$

where: $E_o = 200[GPa]$, $T_1 = 2000[^oC]$ and $T_2 = 1100[^oC]$.

The effect of the fluid temperature rise can be estimated by its influence in the fluid viscosity and density. This was not explicitly included in the 2D erosion-corrosion maps, because the impact velocity is a variable parameter. However, changing the properties of the carrier fluid is very important in estimating the impact velocity of the particles in the case of the 3D simulation. Therefore, the change in the carrier fluid viscosity and density must be considered during the construction of the 3D erosion-corrosion maps. A curve fitting was used to fit the available data [150] for the density and viscosity change to account for their variation with the temperature rise in $[K]$. For the density of water:

$$\rho_l (T) = 1.65 \times 10^{-5} T^3 - 0.02 T^2 + 7.01 T + 207.51 \tag{5.16}$$

and for the water viscosity variation with temperature:

$$\mu_l (T) = 2.4 \times 10^{-5} \left[10^{\frac{247.8}{(T-140)}}\right] \tag{5.17}$$

Figure 5.1 and 5.2 show the variation of the viscosity and density of water with temperature and their curve fitting using the above two expressions.

5.3 Corrosion Modelling

Corrosion in steel is governed by several factors but mainly by the applied conditions of the solution alkalinity measured by pH scale and applied potential within the chemical reaction [17]. These are the factors that determine the corrosion process if it is in the dissolution or the passivation region, according to Eh-pH diagram for the Fe. Thus, to investigate the effect of the temperature rise on the corrosion rates, it is necessary to study the temperature rise effects on the Eh-pH diagram of the Fe.

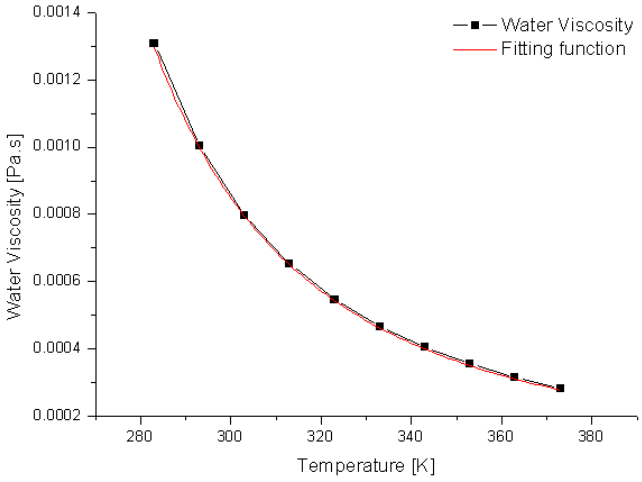

Figure 5.1: Variation of water viscosity with temperature and the curve fitting function with [150].

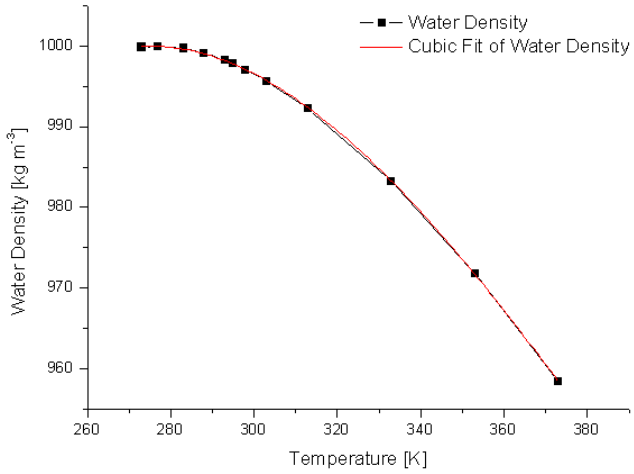

Figure 5.2: Variation of water density with temperature and the curve fitting function with [150].

Figure 5.3(a-d) shows the simplified E-pH diagrams for Fe at 298, 323, 343, and 363 [K] respectively. The figure illustrates how dissolution and passivation regions change with the temperature rise. The main electrochemical reactions equations involved are represented by the boundary lines numbered in Figure 5.3 (a), and are listed as follows [8]:

$$Line\,1: \qquad 2e^- + Fe^{2+} = Fe \tag{5.18}$$

$$Line\,2: \qquad e^- + Fe^{3+} = Fe^{2+} \tag{5.19}$$

$$Line\,3: \qquad Fe_2O_3 + 6H^+ + 2e^- = 2Fe^{2+} + 3H_2O \tag{5.20}$$

$$Line\,4: \qquad Fe_2O_3 + 6H^+ + 6e^- = 2Fe + 3H_2O \tag{5.21}$$

$$Line\,5: \qquad 2Fe^{3+} + 3H_2O = Fe_2O_3 + 6H^+ \tag{5.22}$$

In order to construct the 2D erosion-corrosion maps correctly, these lines must be represented mathematically as a function of the applied potential and pH variables. This can be done by using the thermodynamics relations that govern each electrochemical reaction. The equation of every line at the given temperature levels is listed in table 5.1. These lines represent the transition between dissolution, passivation and immunity regions. A full explanation of how these equations are discussed in Appendix A.

The corrosion rate is mainly characterised by the summation between the pure corrosion rates (K_{co}), which can be neglected; and the contribution of erosion to the corrosion process which denoted by (ΔK_c) (also known as erosion enhanced corrosion) in the passive regions. Corrosion rates in the dissolution region can be estimated by neglecting (ΔK_c) and calculating the net current density [$A\,cm^{-2}$] from the Butler-Volmer equation which is dependent on the temperature. Equation 4.18 can be formulated as a function of temperature by using Equation 4.21 and is given

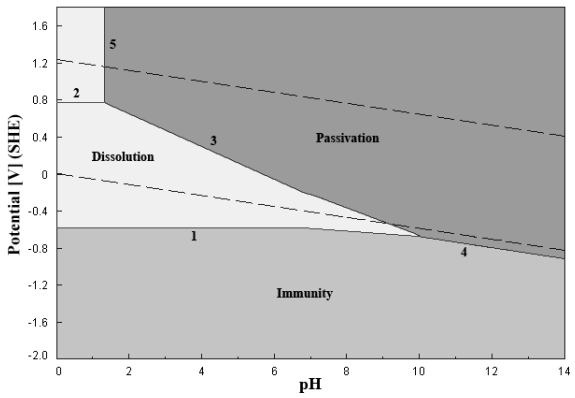

(a)

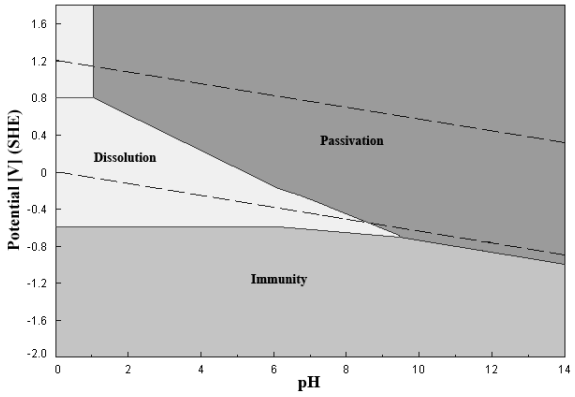

(b)

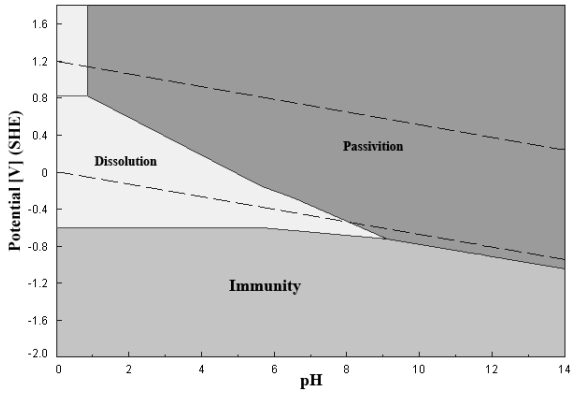

(c)

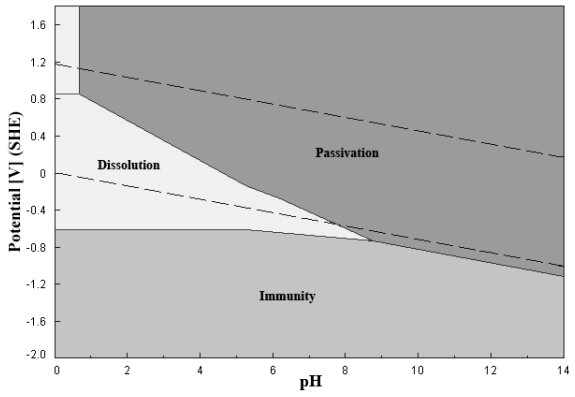

(d)

Figure 5.3: Simplified Pourbaix diagrams for the Fe-water system at : (a)298, (b)323 (c)343 (d)363 [K].

Table 5.1: The equations of boundary lines between the passive and dissolution regions see Figure 5.3(a).

Line	Temperature $[K]$	Equation
Line 1	298	E= -0.618
	323	E= -0.617
	343	E= -0.618
	363	E= -0.620
Line 2	298	E= 0.771
	323	E= 0.814
	343	E= 0.848
	363	E= 0.879
Line 3	298	E= 1.076 - 0.177 pH
	323	E= 1.097 - 0.192 pH
	343	E= 1.119 - 0.204 pH
	363	E= 1.144 - 0.216 pH
Line 4	298	E= -0.054 - 0.059 pH
	323	E= -0.046 - 0.064 pH
	343	E= -0.039 - 0.068 pH
	363	E= -0.032 - 0.072 pH
Line 5	298	pH = 1.72
	323	pH = 1.47
	343	pH = 1.33
	363	pH = 1.23

as:

$$i_{anet} = i_o \left[\exp\left(\frac{\beta\, z_m\, F \triangle E}{R\, T} \right) - \exp\left(\frac{-\left(1-\beta\right)\, z_m\, F \triangle E}{R\, T} \right) \right] \tag{5.23}$$

The pure dissolution rate can be expressed by the Faraday law:

$$K_c = K_{co} = \frac{i\, RAM_{Fe}}{z_m\, F} \tag{5.24}$$

the Butler-Volmer equation is used in modelling the dissolution corrosion rate in both 2D and 3D erosion-corrosion maps.

5.3.1 Passivation in 2D erosion-corrosion maps

In the case of passivation region, the passivation process prevents the pure corrosion from further occurring, and the total corrosion rate can be simplified to the amount of passive film removal (i.e. $K_{co} \approx 0$). Tirupataiah et al. [70] developed a simple expression for the crater diameter by equating the kinetic energy of the incident particle with the energy required to form a crater. Based on Tirupatiah's work, Stack et al. [83, 8] derived a formula for predicting the erosion rate in passive film, given its hardness and density and the passive film thickness at normal impacts, expressed in $[g\,cm^{-2}\,s^{-1}]$ and is given as:

$$K_c = \Delta K_c = \frac{86.0\,\rho_s\,\overline{h}\,c_p\,V_p^2}{r_p\,\rho_p^{0.5}\,H_s\,(T)^{0.5}} \tag{5.25}$$

Although the growth of the passive layer is dependent of the operating temperature, as discussed in [151, 19], the assumptions 3 and 7 in section 4.2.2.2 indicate that the formation of the oxide layer is instantaneously removed by the solid particle impact. Therefore, the time interval between impacts, which allow more oxide layer formation is very low. Moreover, assumption (3) in section 4.1.3 state that the erosion and corrosion process is assumed to be steady and independent of time. Thus, the oxide layer can be estimated as a linear function of over-potential only as mentioned in section 4.2.2.2, and as in [126]:

$$\overline{h} = \overline{h}_o + 3 \times 10^{-9}\,(E_{ap} - E_{pas}) \tag{5.26}$$

where: $\left(\overline{h}_o = 1 \times 10^{-9}\right)\,[m]$.

It is acknowledged that this is a simple model. Its use may be restricted at elevated temperature because of the increase in the rate of formation of the oxide layer at elevated temperatures. However, it is assumed here that the erosion and corrosion rates are steady, i.e. independent of time. This assumption discounts the effect of the time interval between impacts. The time interval between impacts is very important factor in the erosion-corrosion process, as in the passive region, it determines the film thickness and growth kinetics [151]. However, for this study, as the thickness of the passive film is assumed to be in the order of nanometres [126, 152], significant increase in film thickness is not considered for long intervals between impacts.

5.3.2 2D Erosion-corrosion regime boundaries

The 2D erosion-corrosion maps formed in this chapter are built as a map between the applied potential and particle impact velocity at specified pH and temperature levels. The regime boundaries are determined in terms of the ratio (K_c/K_e). Rearranging the equations 5.3, 5.24, and 5.25 and using equations 5.5, 5.6, and 5.7 to include the effect of increasing temperature, the transition velocity in the dissolution region is given as:

$$V = \frac{M_{Fe}\, i_{anet}^{0.28}\, T_m^{0.21}\, C_p\,(T)^{0.67}\; H_s\,(T)^{0.07}}{\rho_p^{0.07}\, c_p^{0.28}\; (K_c/K_e)^{0.28}} \tag{5.27}$$

While in case of the passive regions the transition velocity is:

$$V = \frac{k\, h^{0.67}\, \rho_f^{0.67}\, T_m^{0.5}\, C_p\,(T)^{0.67}}{r_p^{0.67}\, \rho_p^{0.5}\, H_s\,(T)^{0.17}\; (K_c/K_e)^{0.67}} \tag{5.28}$$

Equations 5.3, 5.27, and 5.28 are also used to produce the erosion-corrosion wastage maps:

$$K_{ce} = K_{eo} + K_{co} + \Delta K_e + \Delta K_c \tag{5.29}$$

The boundary conditions for both regime and wastage maps are the same as defined in section 4.1.2.

5.3.3 Passivation in 3D erosion-corrosion maps

The passivation model developed in section 4.2.2.2 is used to estimate the additive (ΔK_c). It must be noted that the effect of temperature is only apparent in reduction of the target material hardness. The formula used is summarised in this section; for comforting, the equation is re-listed here:

$$M_t = \pi\, \overline{k}\, \overline{h}\, \rho_f\, d_p^2 \left[\frac{\rho_p\; (1 - e_n^2)}{6\, H}\right]^{0.5} (V_1\, \sin\alpha_1) \tag{5.30}$$

Converting to $[kg\; m^{-2}\, s^{-1}]$ using equation 4.38; the passive layer erosion model will be:

$$\Delta K_c = \frac{\pi}{m_p}\, c\, \overline{k}\, \overline{h}\, \rho_f\, d_p^2 \left[\frac{\rho_p\ (1-e_n^2)}{6\, H_s\,(T)}\right]^{0.5} (V_1\ \sin\alpha_1)^2 \tag{5.31}$$

where (e_n)can be estimated as mentioned in section 5.2.2.

5.4 Results

The erosion-corrosion regime and wastage maps are developed as $V_p - E_{ap}$ diagrams at the given pH and temperature levels, Figure 5.3(a-d). These Pourbaix diagrams are very essential in construction of both 2D and 3D erosion-corrosion maps, as they categorise the behaviour of the metal under the specified corrosive conditions (temperature, pH and applied potential).

Figure 5.3 shows that, as the temperature increases, the areas indicate dissolution regions decrease while the passivation regions are increasing. This indicates unique behaviour for the Fe metal at this temperature range, and can be interpreted as the tendency of the Fe thermodynamically to passivate. The pH after which no dissolution occur is shifted to lower values as the temperature increases. This boundary is represented in Figure 5.3(a) by the vertical line (5). Assuming line 1, and 3 are straight lines (this is for the sake of simplification), the intersecting point between these two lines with line (4) is also found to be shifted to lower values as the temperature increases.

5.4.1 2D erosion-corrosion maps results

The effects of pH variation at elevated temperatures 298, 323, 343, and 363 $[K]$ are illustrated in Figures 5.4, 5.5 and 5.6 for the regime maps. The effects of the pH variation in the wastage maps are shown in Figures 5.7, 5.8 and 5.9.

In the regime maps, there are two boundary lines in each map. The left hand side vertical line represents the regions of applied potentials under which Fe is thermodynamically impossible to corrode; and is denoted by (E_o). In these regions, the total wastage of metals is considered to arise from the pure erosion as the corrosion at these regions is thermodynamically impossible. It is found from the erosion-corrosion

regime maps that this boundary is approximately constant at the studied temperature range while the dissolution regions exist. As the pH increases, the regions of passivation corrosion dominate, and no further dissolution occurs. This is accompanied by reduction of (E_o) to lower potential values.

The other boundary line represents the applied potential (E_{pas}) above which, the metal begins to develop a passive layer. The transition regimes may vary from passivation domination to erosion domination. In the passivation domination regime, the passive film continues to form and be removed because of the impact particles. Meanwhile, in the erosion domination regime, the rate of re-passivation is apparently much lower than the rate of metal erosion. Regions in between these two boundaries represent the dissolution regimes and its transitions. To illustrate the variation of (E_{pas}) boundary values with the temperature change, Figure 5.10(a-d) shows the difference in each pH level for passivity boundaries. From this figure, it can be concluded that (E_{pas}) value decreases as the temperature increases, and also decreases as the pH increases.

5.4.2 3D erosion-corrosion maps results

Figure 5.11 and 5.12 show the regime maps for Fe at constant applied potentials and different pH values. A low pH=5 and high pH=9 are chosen to reflect two extremes of the electrolyte characteristic, that represent common applications in industry and power plants. It is also selected for comparing with the 2D erosion-corrosion maps developed in [8].

Figure 5.11(a-d) shows the erosion-corrosion regime maps at pH 5 and applied potential V= -0.6 [V] (SCE). At these conditions, dissolution regimes are prevailed. Moreover, it is observed that; at the pipe bend, the erosion-dissolution and erosion-dominated regimes are dominant; Figure 5.11(a), and tend to increase as the temperature increase; Figure 5.11(b, c and d). This is consistent with the Pourbaix diagrams at these conditions. It can be referred to the high erosion rate values at the pipe bend location.

In contrast with the results at pH=5, Figure 5.12(a-d) shows the erosion-corrosion

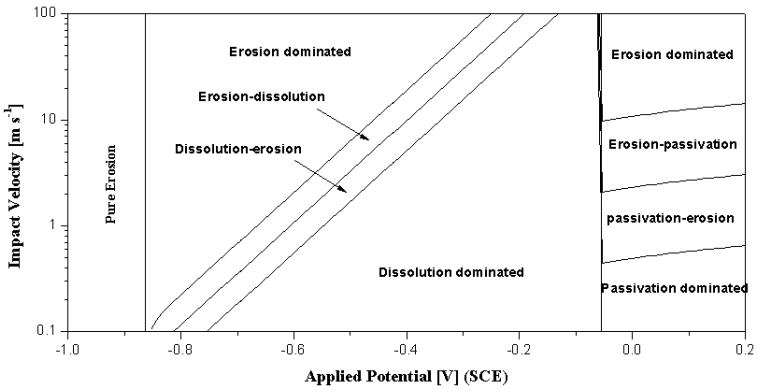

(a)

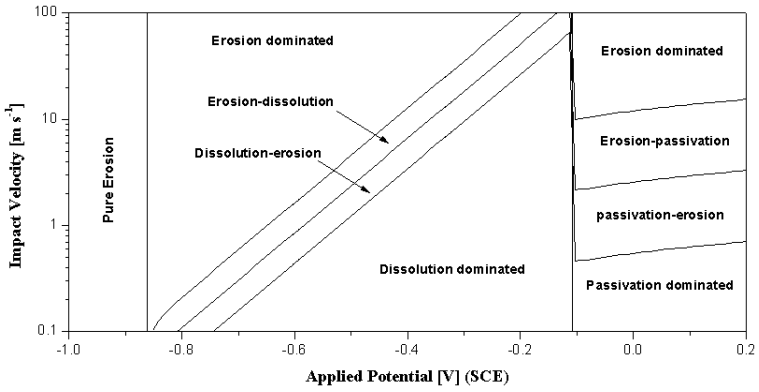

(b)

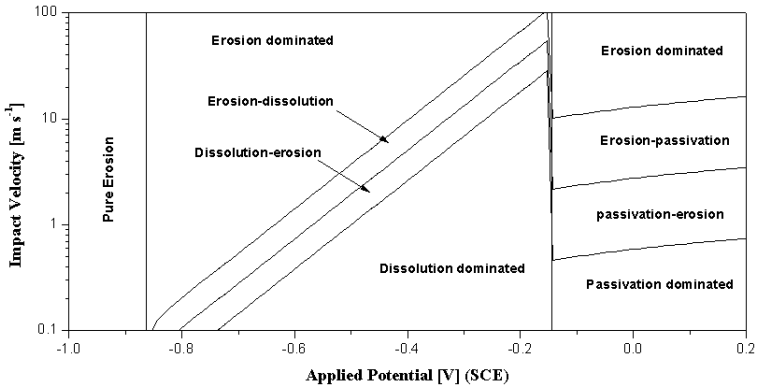

(c)

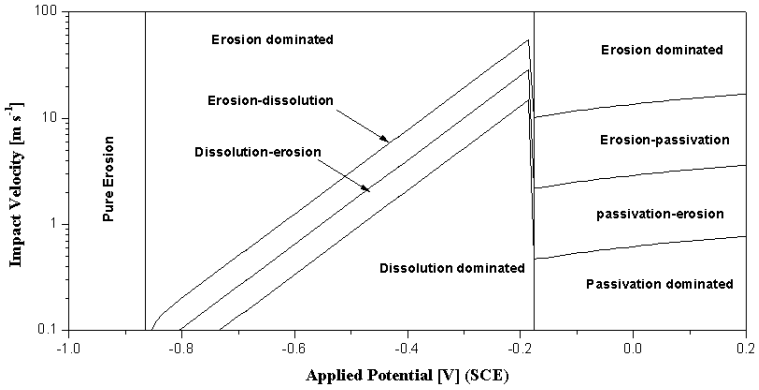

(d)

Figure 5.4: Regime maps for Fe at pH 5 and: (a) 298, (b) 323, (c) 343, and (d) 363 [K].

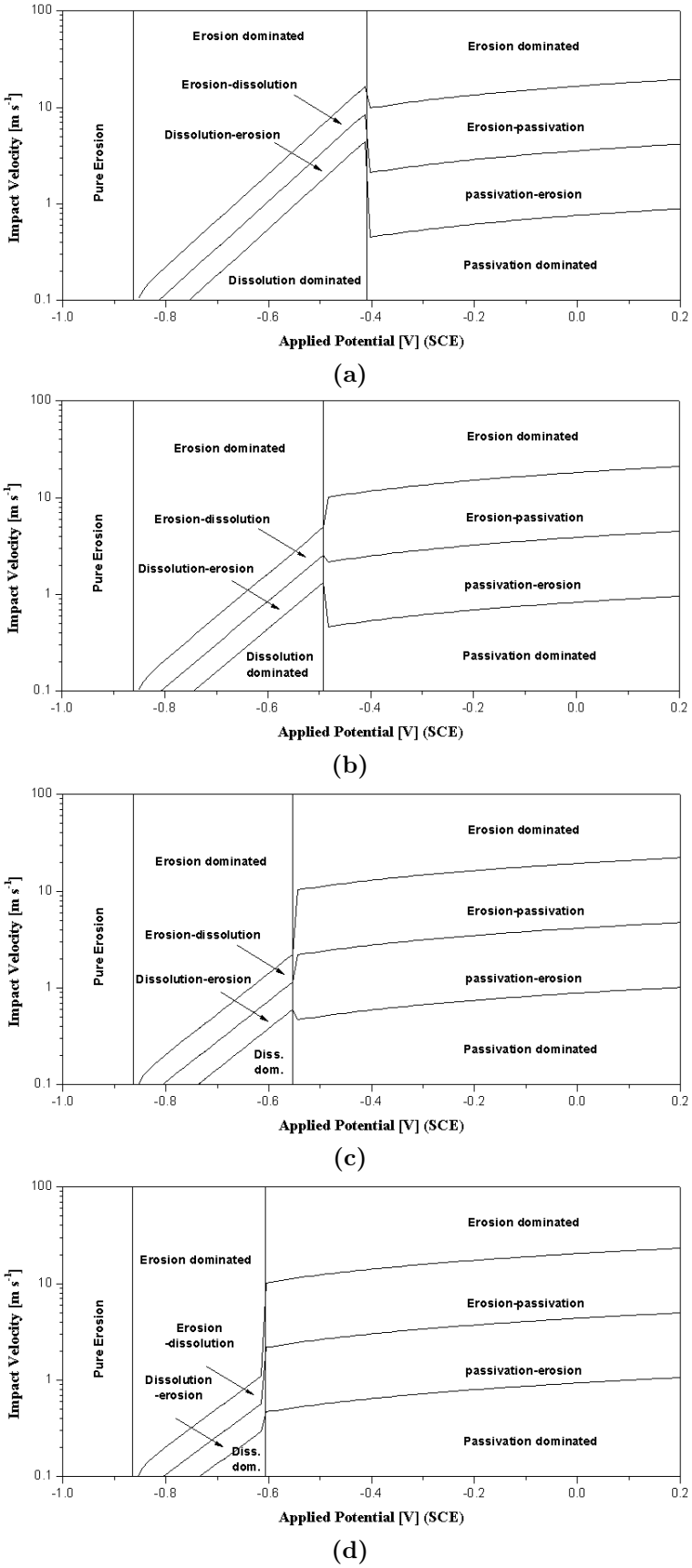

Figure 5.5: Regime maps for Fe at pH 7 and: (a) 298, (b) 323, (c) 343, and (d) 363 [K].

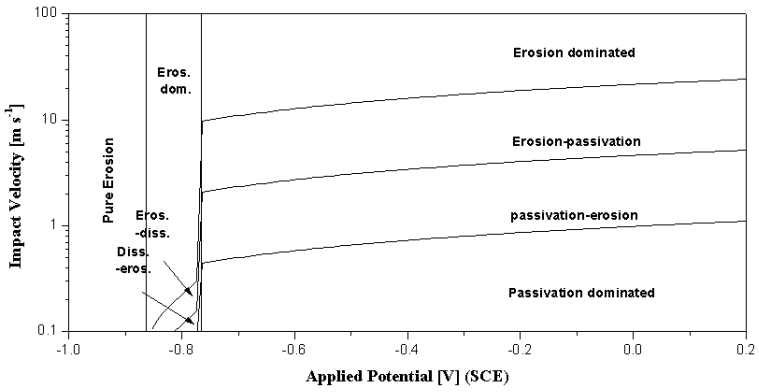

(a)

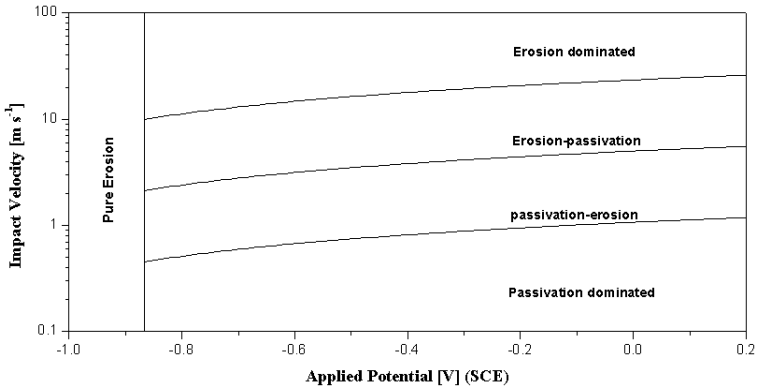

(b)

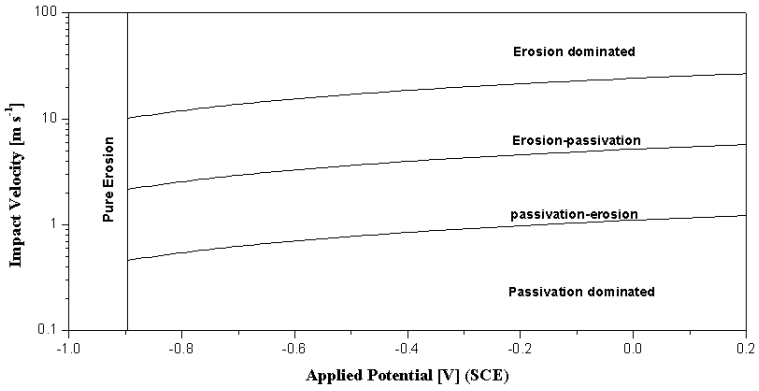

(c)

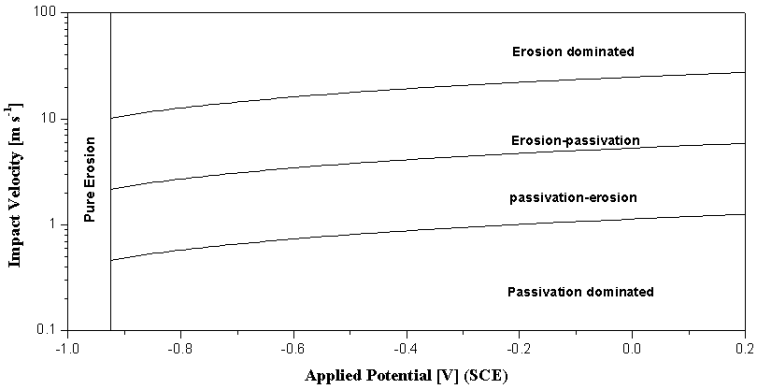

(d)

Figure 5.6: Regime maps for Fe at pH 9 and: (a) 298, (b) 323, (c) 343, and (d) 363 [K].

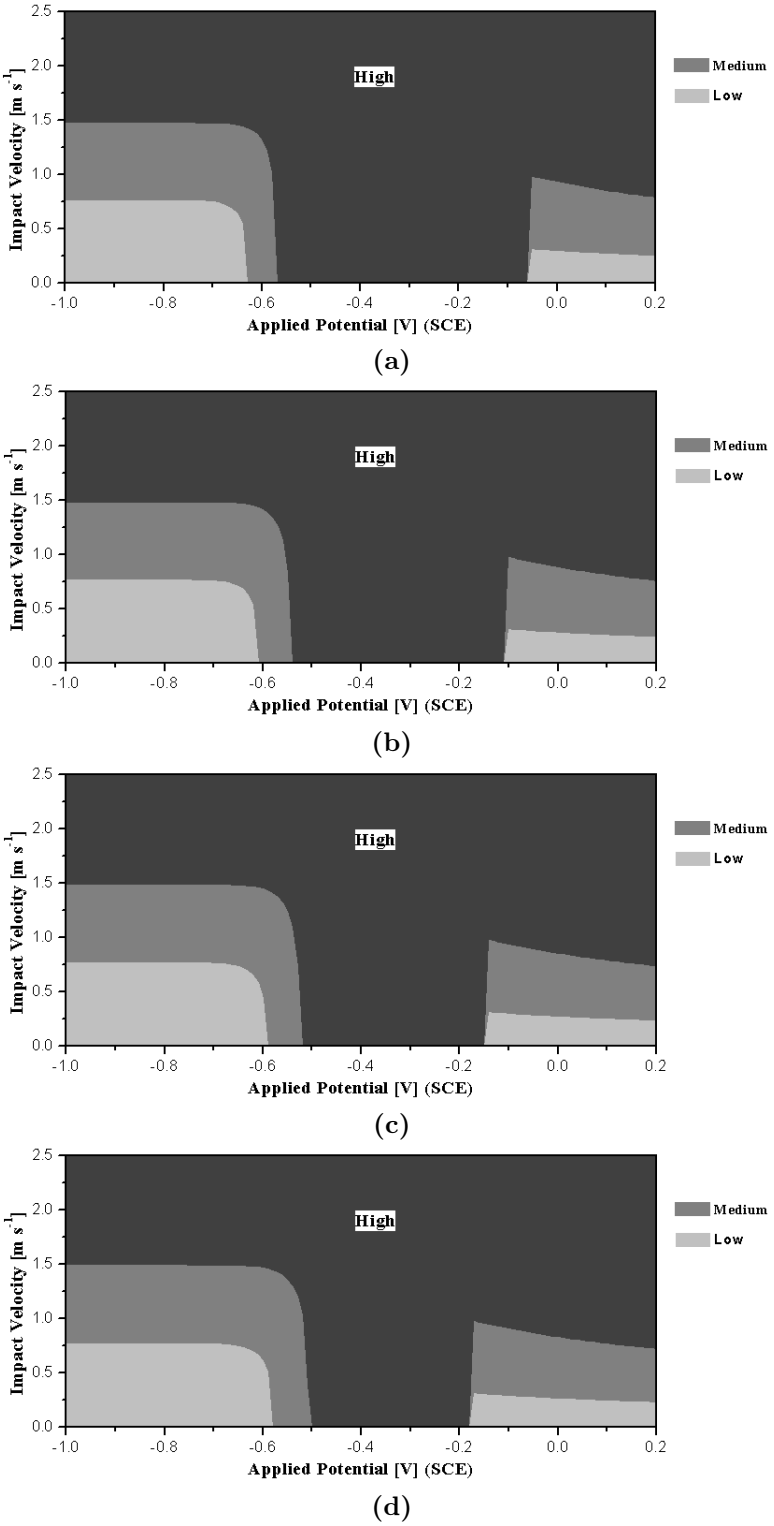

Figure 5.7: Wastage maps for Fe at pH 5 and: (a) 298, (b) 323, (c) 343, and (d) 363 [K].

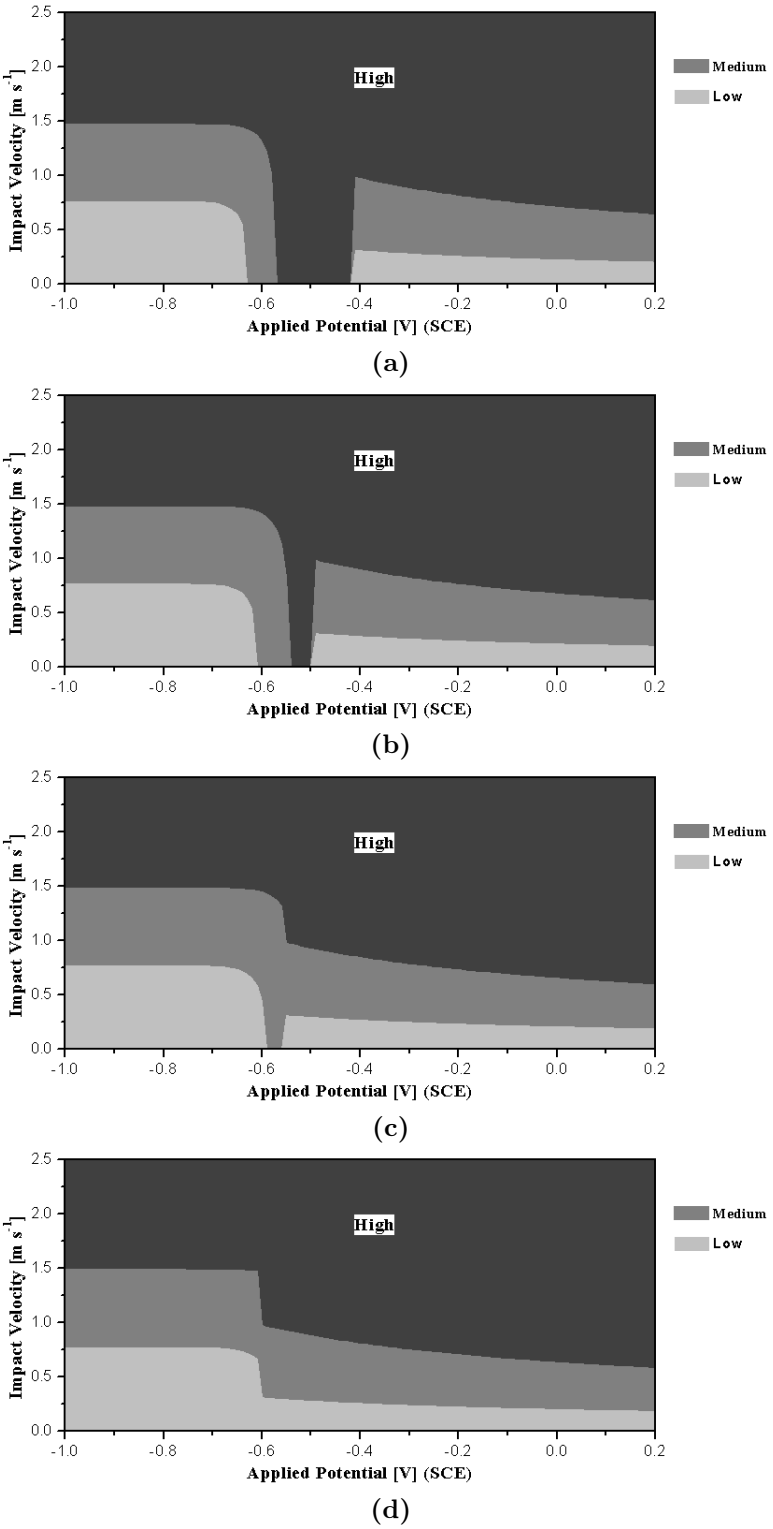

Figure 5.8: Wastage maps for Fe at pH 7 and: (a) 298, (b) 323, (c) 343, and (d) 363 [K].

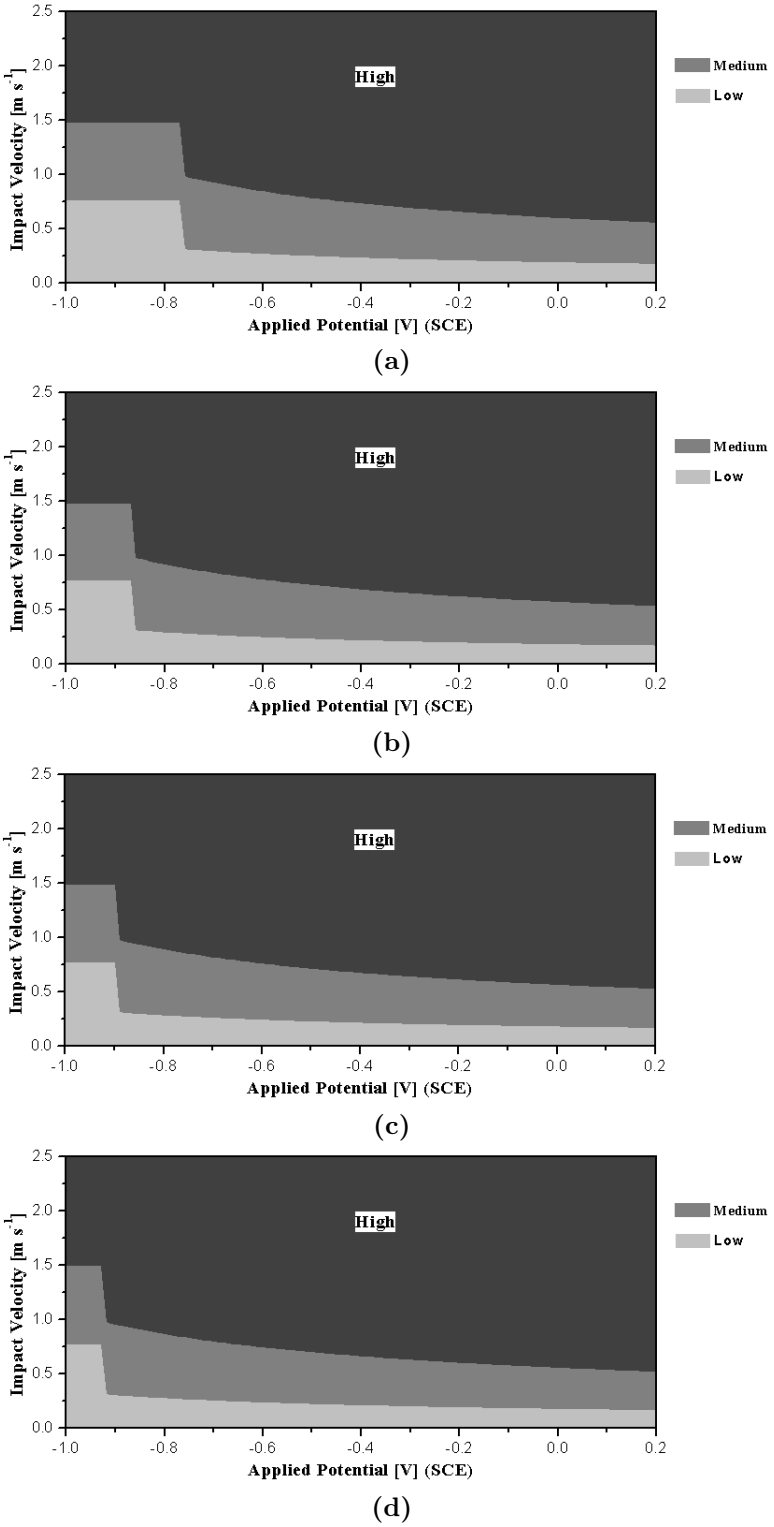

Figure 5.9: Wastage maps for Fe at pH 9 and: (a) 298, (b) 323, (c) 343, and (d) 363 [K].

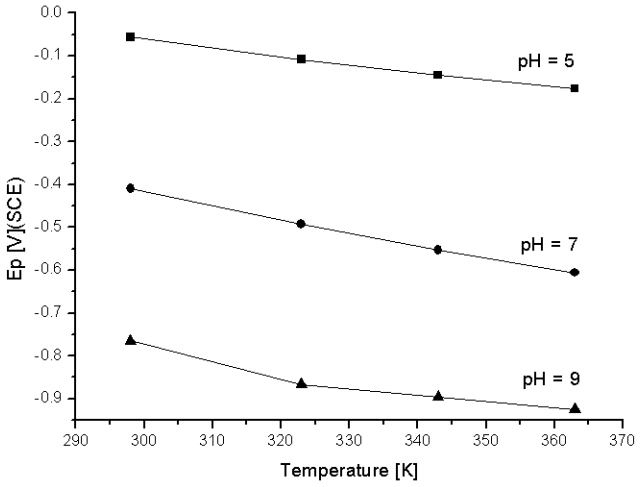

Figure 5.10: Variation of E_{pas} value with Temperature at different pH values.

regimes at pH=9 and applied potential V= -0.6 [V] (SCE). The dominant regime predicted at all temperature levels is the erosion-passivation regime. The reason behind this domination is that, at the passivation mechanism, the corrosion rate is decreased because of the formation of the thin oxide layer which prevents the metal from further dissolution.

The effect of applied potential variation is investigated in Figure 5.13 and 5.14, which show the regime maps for Fe at constant pH=7 at the same temperature levels. Two values also chosen here for the applied potentials. One value refers to low applied potential V= -0.6 [V] (SCE); Figure 5.13, where the corrosion mechanism is dissolution, while the other is corresponding to a higher potential V= -0.05 [V] (SCE); Figure 5.14, where passivation corrosion appears.

An identical mapping was found at pH=5; Figure 5.11(a-c), and pH=7; Figure 5.13(a-c), which indicates an identical behaviour for the metal in dissolution mechanism at the same applied potential regardless of the pH values. This is because of the dependence of the dissolution rate on the over-potential value.

On the contrary, Figure 5.14(a-d) shows similar but not identical maps on the pipe surface at every temperature level when comparing with the erosion-passivation maps

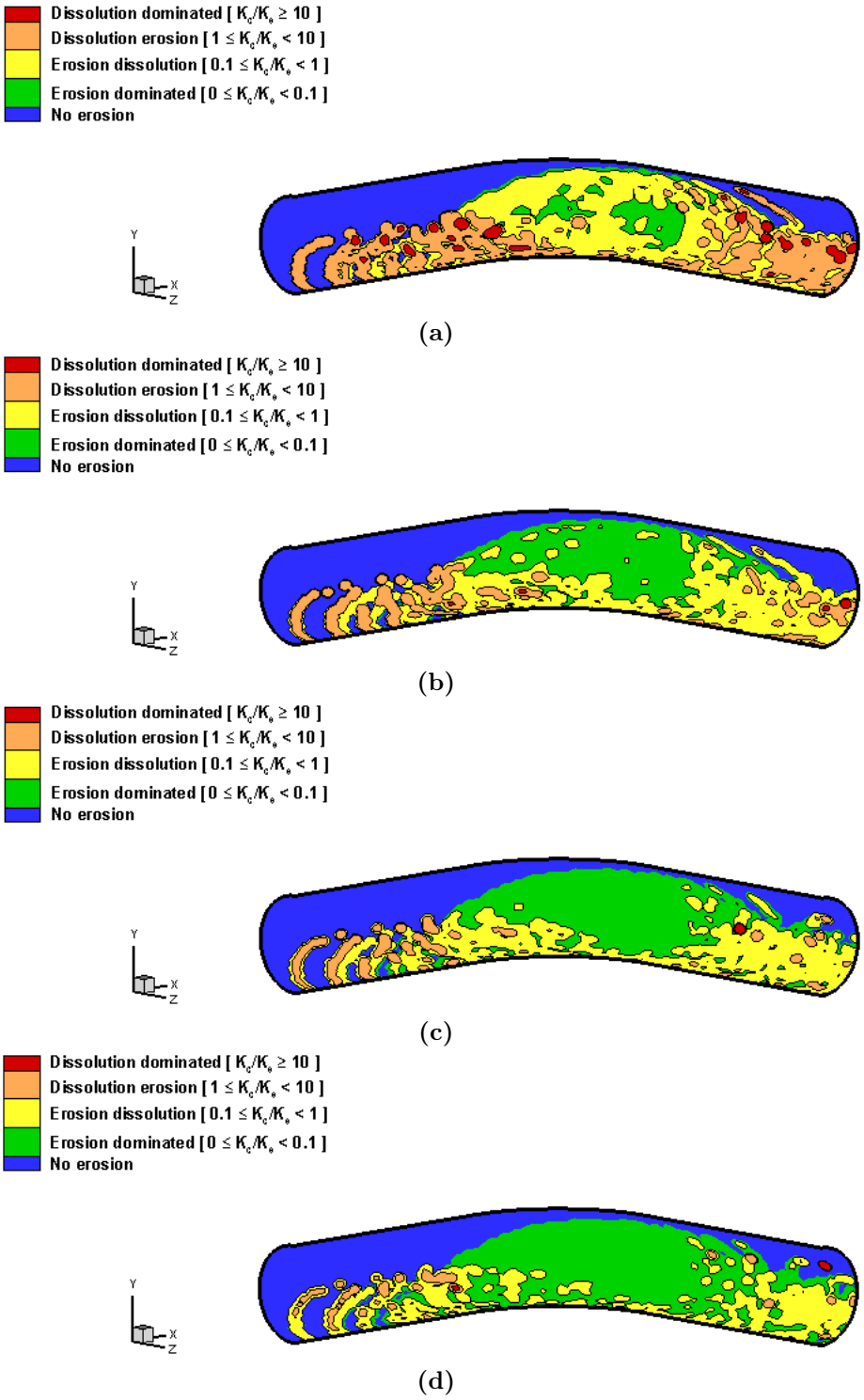

Figure 5.11: Regime maps for Fe at pH 5, V= -0.6 [V](SCE) at:(a) 298, (b) 323, (c) 343, (d) 363 [K].

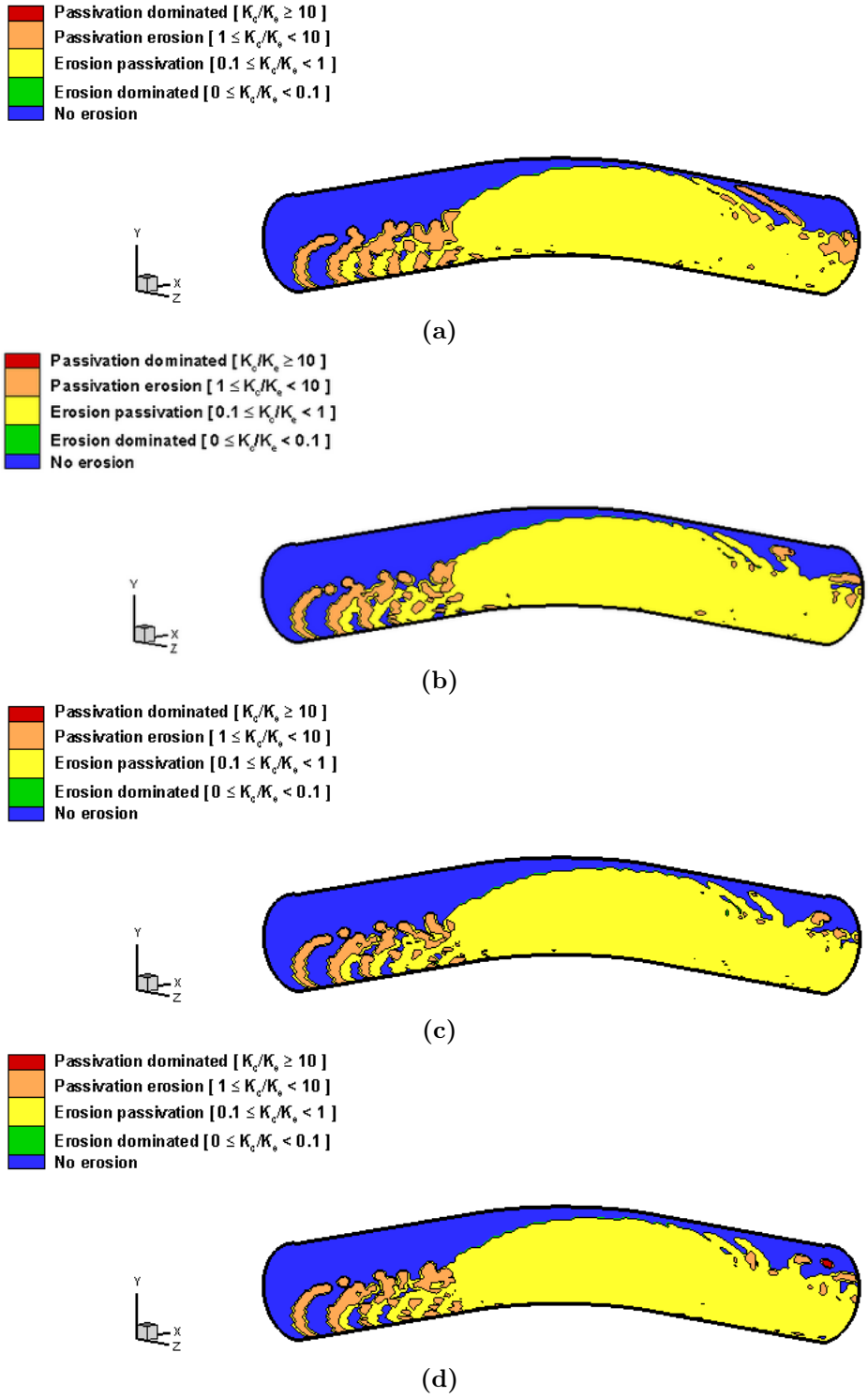

Figure 5.12: Regime maps for Fe at pH 9, V= -0.6 [V](SCE) at:(a) 298, (b) 323, (c) 343, (d) 363 [K].

in Figure 5.12(a-d)). The passivation-erosion regime is dominant on the straight ends of the pipe, while the erosion-passivation regime remains dominant in the pipe bend regions. This is because of the dependency of the (ΔK_c) on the passive layer thickness formation and removal mechanism. High overpotential gives higher rate of re-passivation in areas where the impact frequency is high (the pipe bend). On the other hand, a much more prevailing of the passivation-erosion regime is predicted on the regions where the solid particle impact frequency is low (pipe straight ends).

To illustrate the wastage maps dependency of the pH value, Figures 5.15 and 5.16 show the wastage maps for Fe at V= -0.6 [V] (SCE) and pH values 5 and 9 respectively. Although the erosion rate increases as the temperature increases; and consequently total wastage increases, the wastage maps in Figures 5.15(a-d)) show a decrease in the high wastage regimes as the temperature increases. This is a direct result of the corrosion rates reduction as the temperature increases.

However, this behaviour is reversed at pH=9; Figure 5.16(a-d). The passivation mechanism rules the corrosion rate, which is proportional to the particles impact frequency and velocity, that is why the wastage maps in Figures 5.16(a-d) exhibits an increase in the high wastage regime region. The additive effect between the erosion and corrosion at pH=9 is proportional to the increase in temperature level, and will cause an increase in the area suffers high wastage regime.

The applied potential effect on the wastage maps is investigated in Figures 5.17 and 5.18. The two figures illustrate the wastage maps for pH= 7 and at applied potentials -0.6 and -0.05 [V] (SCE) respectively. A similar behaviour in results is observed at applied potential V= -0.6 [V]; Figure 5.17(a-d), with that in Figure 5.15(a-d). This similarity in dissolution corrosion mechanism at any low pH value (5 and 7) can be referred to the independence of the corrosion rates on the pH value.

It is also observed that this similarity is seen at temperature T=363 [K], even it is considered following the passivation corrosion mechanism. This behaviour is an interpretation to the fact that the applied potential value (V=-0.6 [V]) is a transition point between dissolution and passivation mechanism in the Pourbaix diagram at T= 363 [K], as illustrated in the 2D erosion-corrosion maps; Figure 5.5(d). The

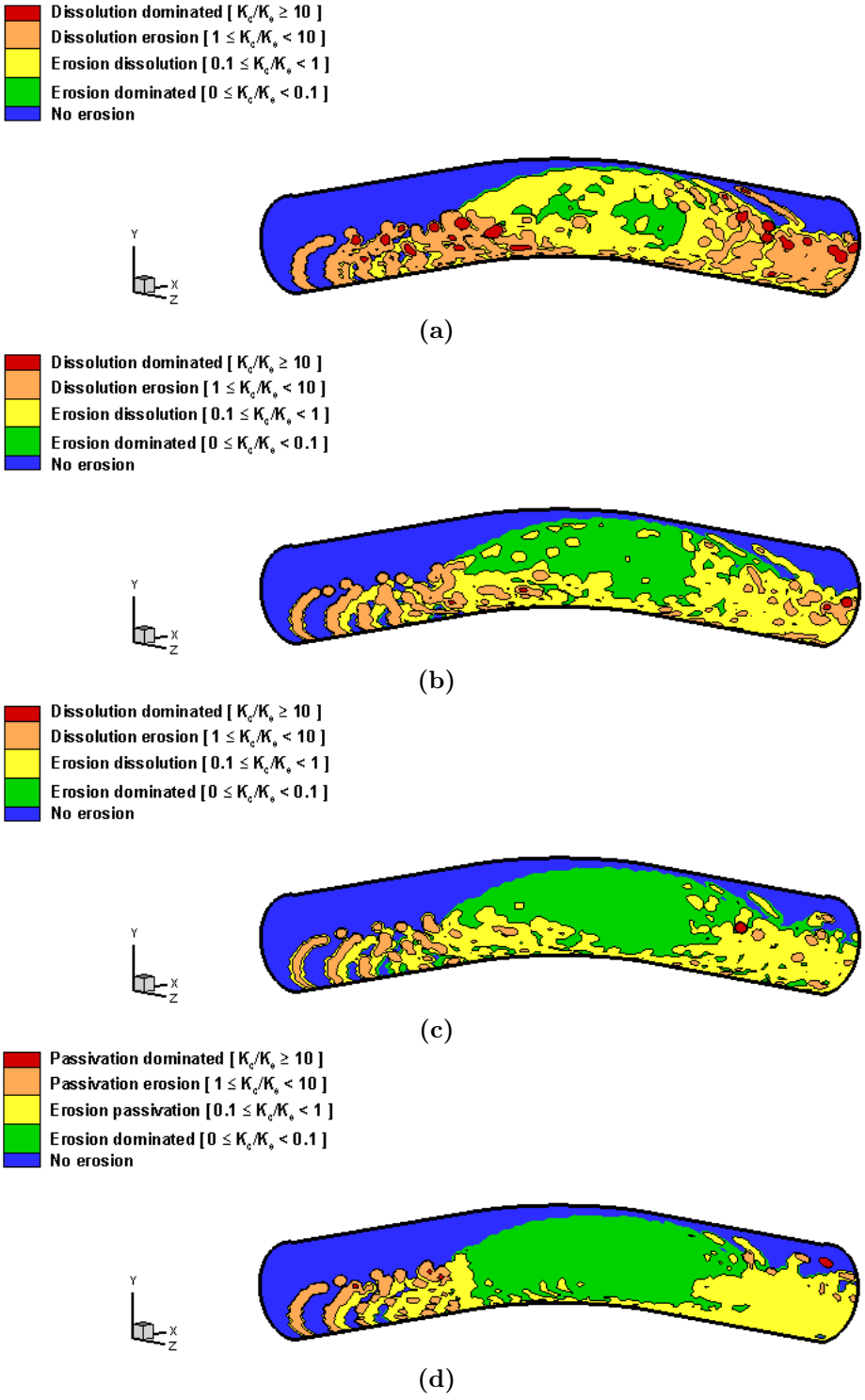

Figure 5.13: Regime maps for Fe at pH 7, V= -0.6 [V](SCE) at:(a) 298, (b) 323, (c) 343, (d) 363 [K].

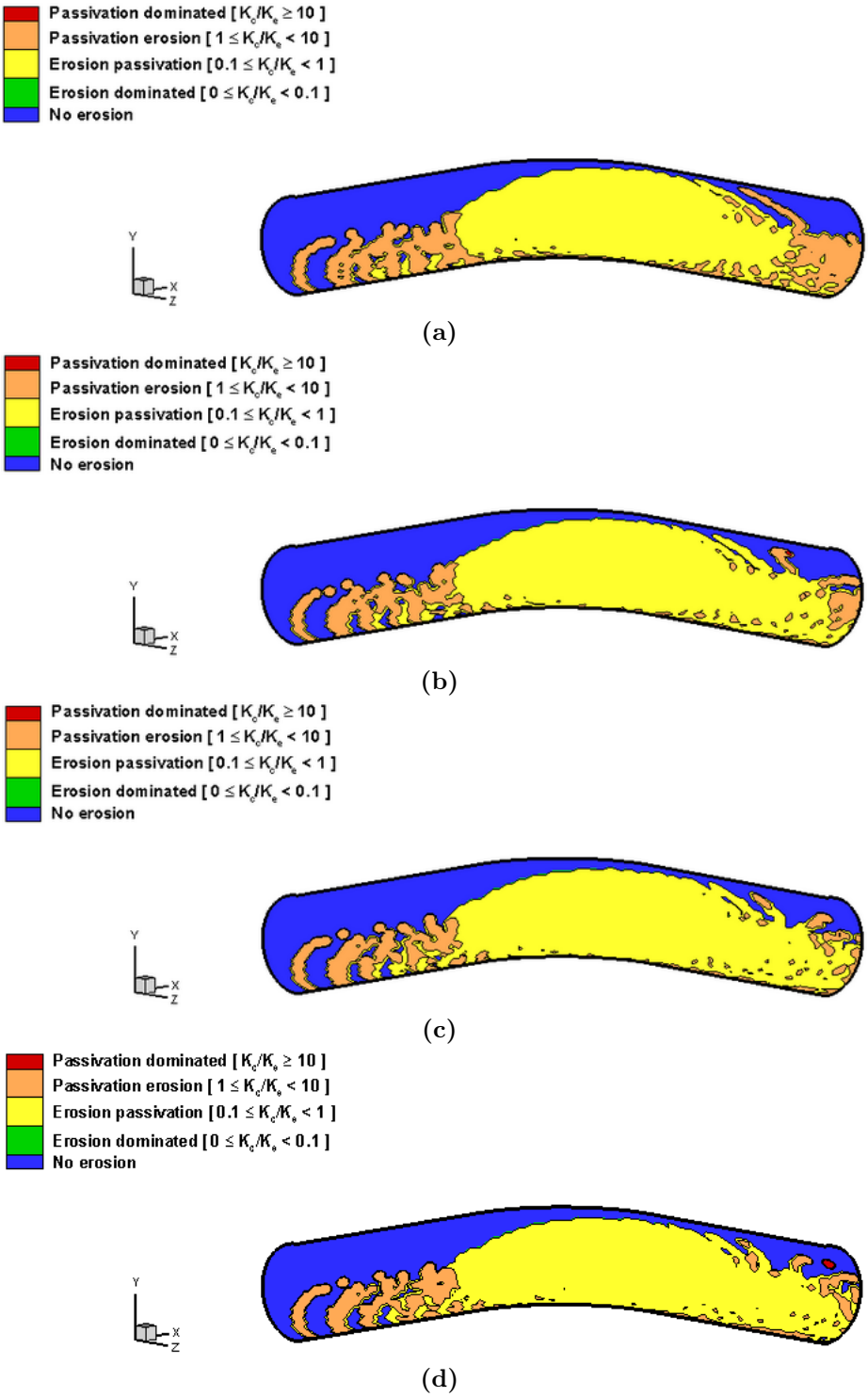

Figure 5.14: Regime maps for Fe at pH 7, V= -0.05 [V](SCE) at:(a) 298, (b) 323, (c) 343, (d) 363 [K].

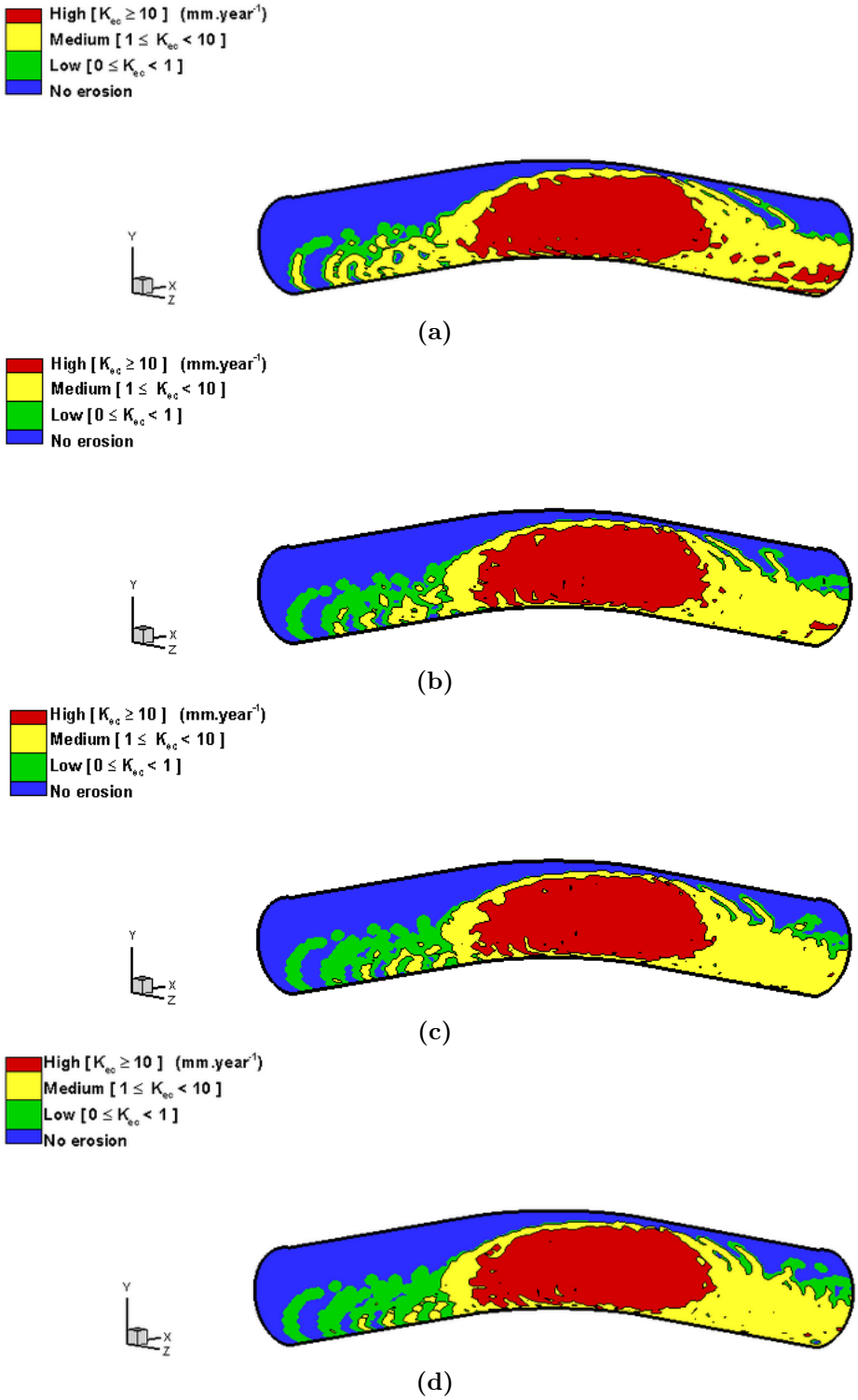

Figure 5.15: Wastage maps for Fe at pH 5, V= -0.6 [V](SCE) at:(a) 298, (b) 323, (c) 343, (d) 363 [K].

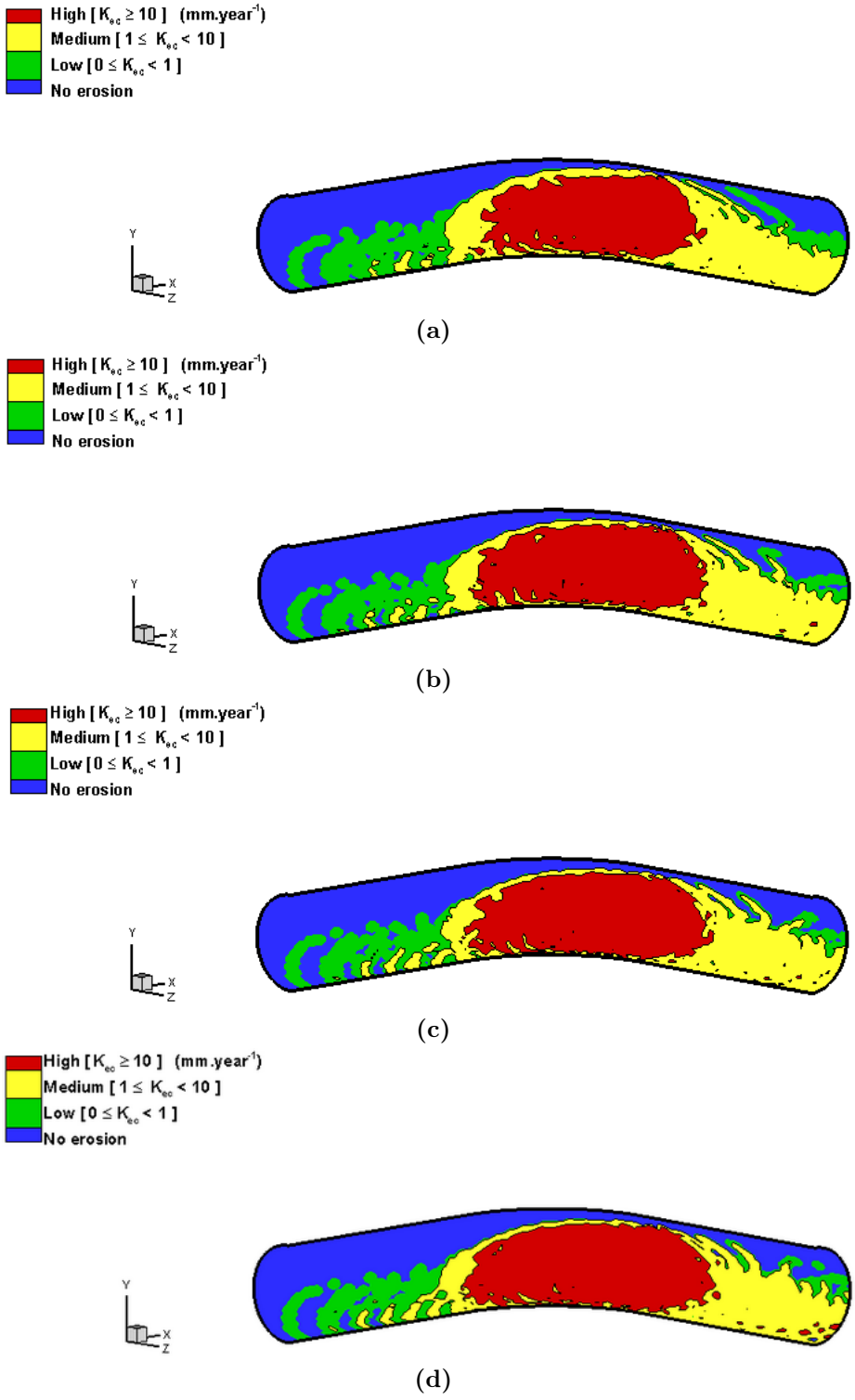

Figure 5.16: Wastage maps for Fe at pH 9, V= -0.6 [V](SCE) at:(a) 298, (b) 323, (c) 343, (d) 363 [K].

3D erosion-corrosion maps are capable of capturing the reflect of the metal at the transition boundary; while in the case of the 2D erosion-corrosion maps, the transition is represented as a discontinuity in the regime boundaries.

5.5 Discussion

It is worth noting that all the results for the erosion-corrosion regimes and wastage maps here are within the range of applied potentials that used in previous investigations of Stack group [8] for comparing reasons. The chosen pH levels are also taken to be consistent with the previous work for ease of comparison and for their use in several industrious and technological applications. The temperature range in this work is also taken to suit many applications that involve aqueous slurry flow.

5.5.1 2D erosion corrosion maps

The effect of elevated temperature is investigated to monitor and identify its influence on the erosion-corrosion regime and wastage maps. Comparing the erosion-corrosion regime maps in Figures 5.4, 5.5 and 5.6 with the wastage maps; Figures 5.7, 5.8, and 5.9, shows that, at dissolution regions, the total wastage of (Fe) is considerably higher than that in the passivation regions. This is because of the high corrosion rates in case of dissolution. The regime maps also show that, the dissolution regimes areas at pH=5; Figure 5.4(a-d), are wider than that at higher pH values; Figures 5.5(a-d) and 5.6(a-d), where the dissolution regimes regions reduce gradually and become less wider with the temperature increase.

As the temperature increase at pH=9; Figure 5.6(b-d), no dissolution regimes are observed, and the passivation regimes demonstrate the Fe behaviour at any given applied potential. This also affects the wastage maps at this pH value; Figure 5.9(b-d), where ascending wear rate from low to high regions are observed. This is in contrary to Figures 5.7 and 5.8(a, b), where the high wastage region is dominating specially at intermediate potentials due to dissolution corrosion.

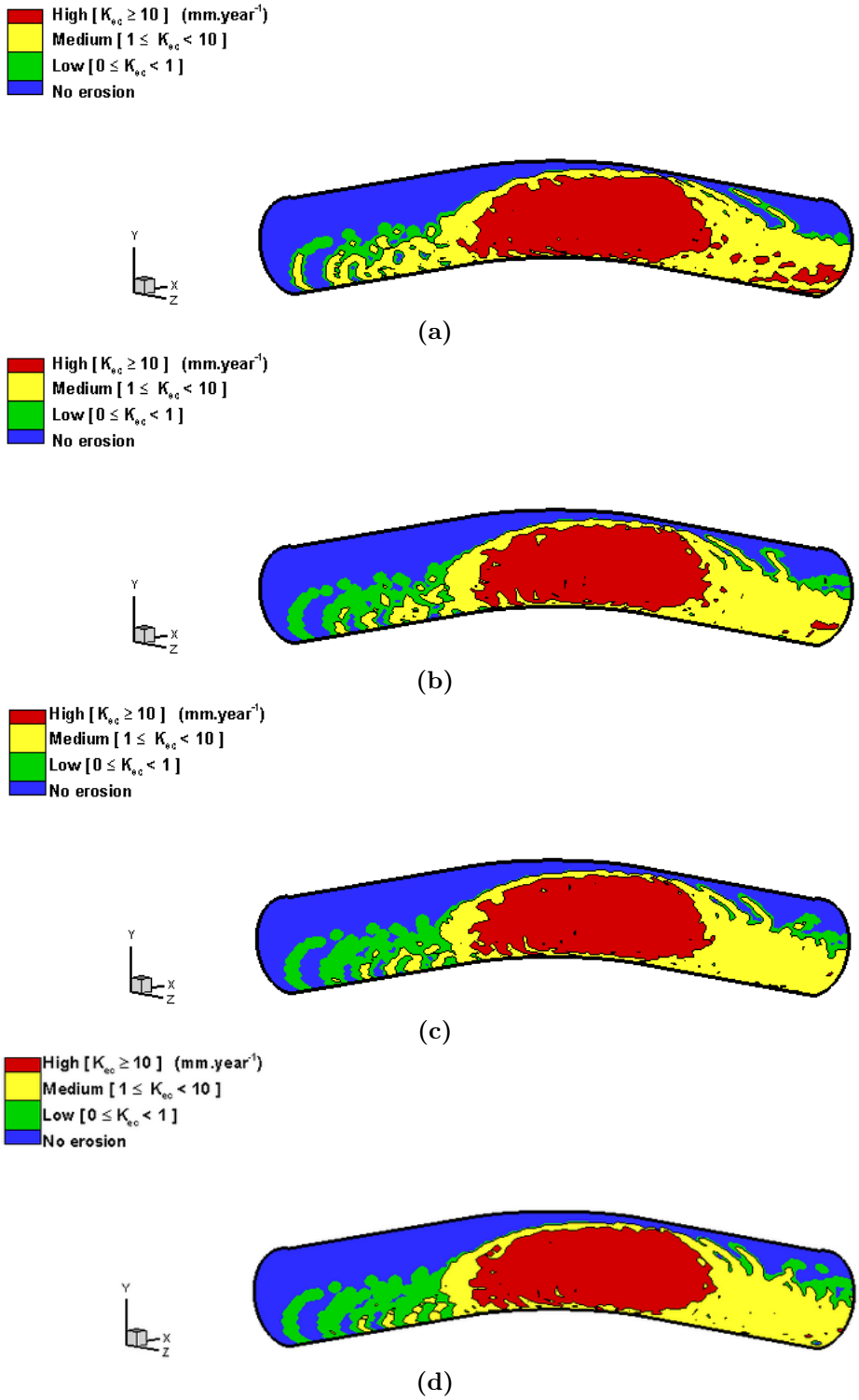

Figure 5.17: Wastage maps for Fe at pH 7, V= -0.6 [V](SCE) at:(a) 298, (b) 323, (c) 343, (d) 363 [K].

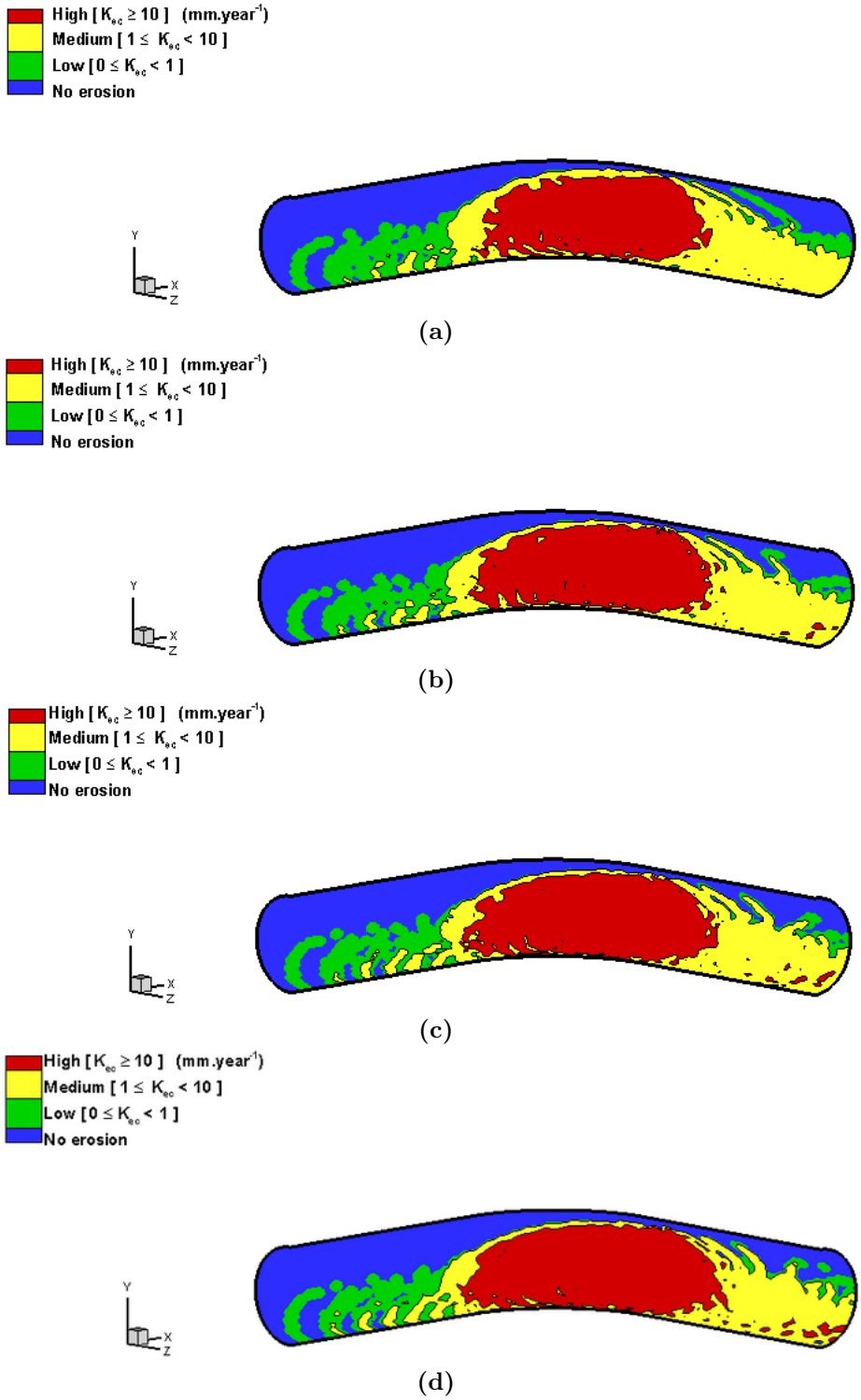

Figure 5.18: Wastage maps for Fe at pH 7, V= -0.05 [V](SCE) at:(a) 298, (b) 323, (c) 343, (d) 363 [K].

5.5.1.1 Comparison with the previous results [8] at 298 [K]

A qualitative comparison between the regime maps at standard room temperature; Figures 5.4(a), 5.5(a) and 5.6(a), and the maps in [8] indicates that the boundaries of the passivation affected regions are under-predicted. This is a result of using different hardness value in this study. Meanwhile, the passive film layer is assumed to be very thin and continuously removed by the impact particles and the erosion domination is likely to appear at lower impact velocities than the previously predicted. The erosion-passivation regime boundary in the passive region would not exceed 10 $[m\ s^{-1}]$ in aqueous flow according to the results in this study. This value considered very reasonable as a boundary for the erosion domination to reveal in aqueous slurries, compared to values of 12-15 $[m\,s^{-1}]$ [8].

The results obtained in the dissolution affected regions at the same figures above show lower slope value for the dissolution regimes boundaries, than that obtained in [8]. The reason behind this change in the slope is the dependence of the corrosion rates on the temperature level. It is important to note that, the Tafel slope; taken here as a function of the temperature, has a value equal to 0.059 at room temperature compared to 0.05 that assumed in [8]. The increase in Tafel slope causes lower predicted values for the corrosion rates. When the corrosion rates are divided by the predicted erosion rates, the slope of the dissolution affected regimes boundary lines decreases accordingly.

In accordance with the regime maps, wastage maps at the standard room temperatures show that, at lower potential values, the transition from medium to high wastage boundaries decreases when compared with the results in [8]. (from 2 to 1.5 $[m\ s^{-1}]$). This is also because of the use of a different hardness values to represent the carbon steel alloys family. Using different erosion model is considered another reason for this slight reduction in the boundary level. Nevertheless, it is considered a reasonable value and within the same range.

In contrast, the predicted transition velocities at higher potential regions (where passivation occurs) is slightly lower or identical of that in [8]. This similarity comes from the fact that the transition boundaries are existed at velocity levels where the passivation is dominated (passivation-dominated and passivation-erosion regions).

At these regions, the effect of erosion is negligible at the countered impact velocity values. As the potential increases, the total wear is increased because of the increase of the metal oxide removal (corrosion contribution to erosion ΔK_c). In fact, the formation and removal of the passive layer is very complicated process, which involves both mechanical and electrochemical interactions. We assume here that the passive layer is slowly formed and then removed simultaneously by the impact of the solid particles.

5.5.1.2 Effect of elevated temperature in the regime and wastage maps

At higher temperature levels, Fe tends to passivate, and the dissolution affected regions are shrunk over the pH range under investigation. The advantages from this behaviour can be indicated by the decrease of the total wear in dissolution affected regions along the potential range at a given pH. Figure 5.10 indicates a regular decrease in the passivation affected boundary value (E_{pas}), as the temperature increase at any given pH value; which is consistent with the Pourbaix diagrams; Figures 5.3(a-d).

The erosion-corrosion regime maps have the ability to monitor this shift in the boundary line as the temperature increases. It is worth noting that, regime maps are very useful tool to instruct the design engineers with the impact velocity limits to minimise the wastage rate, and to identify the applied regime at each impact velocity level for a given applied potential. On the other hand, the wastage maps are very useful to predict the wastage level and the regions of recommended applied potential for a given pH and temperature level. This will be useful in identifying the most optimised design condition for the application under design stage.

The wastage maps show a wide range of high metal removal rates at low temperature compared to higher temperatures. They indicate constant low to medium wear at applied potentials range from -1.0 to -0.8 [V](SCE), where pure erosion is the only regime acting on the material surfaces. As the dissolution affected regimes participate in the wear process, the wastage reaches its high levels which reveal the un-recommended range of applied potential. As the temperature increases, this range decreases to reach its narrowest width at pH =7 and 323[K]; Figure 5.8(b).

5.5.2 3D erosion-corrosion maps

The methodology introduced in chapter 4 has been modified to include the effect of the elevated temperature. It is important to note that (Fe) will exhibit different erosion-corrosion regimes because of the changes of velocity and particle frequency of impact over the component. The areas dominated by these regimes are also will change significantly as these parameters change.

The effect of the pH increase from 5 to 9; Figures 5.11 and 5.12, has an important influence on the corrosion mechanism that controls the degradation rate for the Fe. The same effect is also observed when changing the applied potential in the positive direction; Figures 5.13 and 5.14. The corrosion mechanism is changed from dissolution to passivation domination affected behaviour over the component. This illustrates the importance of environment alkalinity and applied electrochemical potential on the stability of the corrosion regime, as identified by the Pourbaix diagrams for the Fe or any pure metal, and their influence on the erosion-corrosion in both three-dimensional and two-dimensional maps.

Increases in temperature have also a significant effect on the erosion-corrosion regime maps. Comparing between low and high pH values; Figure 5.11 and 5.12, it is observed that, in low pH, Fe exhibits various erosion-corrosion regimes predominating. This is in contrast with the results at high pH value where a stable erosion-passivation regime is spread on the pipe surface.

In the case of passivation corrosion mechanisms, the corrosion rate is assumed to be dependant of the particles impact parameters such as the impact velocity and impact angle as mentioned above. On the other hand, dissolution corrosion mechanisms at low pH value, the corrosion rate is assumed to be independent of the erosion rate (no corrosion contribution to the erosion process).

This is for simplification only, but in reality, the contribution of corrosion in the erosion process is maybe because of weakening the bonds of the metal surface's grains and consequently reducing the hardness of the metals in the sites where the dissolution-dominated and dissolution-erosion exist. Another reason may be attributed to the sudden increase in current density during impacts.

Contrary to the erosion-corrosion regime maps, the effect of temperature increase in the wastage maps is considerably slight, even in low or high pH and applied potential values; Figures 5.15-5.18. This indicates that the erosion-corrosion wastage is affected only by its maximum value variation at the pipe bend region; where the high wastage regime is dominated. Another direct conclusion can be addressed as the temperature range investigated here, has a slight effect on the total wastage of the material. It is acknowledged that this behaviour will differ at higher temperature levels.

It is worth noting here at this stage that the production of erosion-corrosion 3D-maps is considered an important step to understand the complexity of erosion-corrosion mechanisms. The technique is capable of studying the influence of most of the parameters that acting together in the erosion-corrosion process. It can predict the regions of severe wear due to the additive effect of erosion and corrosion, as well as the rate of metal degradation. However, erosion-corrosion 3D maps are not produced to substitute for the 2D maps, but rather to give another tool to investigate and understand the erosion-corrosion process.

Chapter 6

CONCLUSIONS

6.1 Conclusions

In general, the following conclusions can be extracted from this study:

(i) The model for 2D erosion-corrosion mapping made by Stack et al. [8] has been extended to 3D erosion-corrosion mapping developed by a new methodology by combining the CFD methods; which involves fluid dynamics and multiphase flow parameters, and the concept of the 2D erosion-corrosion maps.

(ii) This new methodology have been used to model the erosion–corrosion behaviour of a range of pure metals systems on the real surfaces of a pipe bend case study, which indicates its potential to be applied in any industrial systems. Under similar assumptions of [8], erosion-corrosion regime and wastage maps have been constructed which showed how this new method can capture the additive effect of the erosion on the corrosion process.

(iii) In order to incorporate the dynamic effect of the solid particles during and after impact; which is needed for the 3D simulation, an erosion model was developed to predict the passive layer erosion rate by the solid particles impacts. This model was used to predict the additive or contribution effect of the erosion process in the corrosion rate.

(iv) The results indicate that it is possible to identify erosion–corrosion mechanistic regimes on 3D components under nominally similar fluid flow conditions. This methodology is capable of monitoring the combined effect of most of the erosion-corrosion process parameters in one map, which makes it a very important tool for predicting the life-time of any industrial component that suffers severe erosive-corrosive environments.

(v) The effects of erosion and corrosion parameters such as particle size and applied potential can also be monitored by this new methodology, showing significant differences on the three-dimensional erosion–corrosion regimes indicating the important effects of erosion–corrosion variables on the stability of such regimes observed on real life components.

(vi) The constrained applicability of the 2D erosion-corrosion maps in monitoring the effect of some parameters that influence both the erosion and corrosion pro-

cesses; such as temperature rise, has been excluded by using the new methodology. This can be done by using the CFD tools to simulate the flow under elevating temperature conditions. The results showed how iron (Fe) responded to the increase of temperature by its tendency to passivate where passivation regimes revealed over the dissolution ones. The effect of the elevated temperature was implicitly introduced to the 2D erosion-corrosion maps, assuming normal impact. This tendency to passivation decreases the total wastage rate compared with the standard room temperature maps.

(vii) The Tafel slope dependency on the environment temperature has an impact effect on the prediction of the corrosion rate and hence the total wastage at elevated temperature. Hence, an accurate determination of its value is very important to predict the erosion-corrosion rate and construct both 2D and 3D erosion-corrosion maps.

(viii) Notwithstanding the narrow range of temperature levels investigated here in this study, the temperature elevation effect has a very significant variation on the erosion-corrosion regime maps while it has a slight influence on the erosion-corrosion wastage maps. The 3D erosion-corrosion maps developed in this work are capable of capturing the nature of the transition regimes, even in the critical points where the corrosion mechanism changes from dissolution to passivation.

(ix) The methodology developed in this study makes the erosion-corrosion mapping techniques applicable to the service and enhancement design stage of any engineering application. These maps can be used at any engineering stage, namely: design, service and enhancement stages, to predict the erosion-corrosion regimes and total erosion-corrosion rates over the surface of any industrial application. It only requires an accurate description of the fluid flow properties, to produce an accurate fluid flow simulation using any CFD solver.

6.2 Future work

It is worth noting here that the methodology applied in this study is commenced using several simplification assumptions to keep the methodology as simple and well

presented as possible. However, the methodology can be extended to simulate more sophisticated applications and include more erosion-corrosion mechanisms. In this section, possible future research directions are proposed and are listed as follows:

(i) It was emphasised that no synergy or antagonism during the simulation is assumed. The reasons for such effects are not well manifested and is dependent of many parameters. Further work can be carried out to incorporate such effects in the model. This may be commenced by choosing a suitable erosion-corrosion models. Some of these models were listed in the literature review [3, 88]. In the case of the antagonestic effect, it can be assumed that the rate of the passive layer formation is higher than its removal rate by particles impacts. The antagonestic effect may occur when the particle concentration is very low. At this condition, the time interval between impacts is longer enough to form a thick passive layer and the passive layer formation becomes function of time [151]. If the critical time interval, after which the passive layer formation rate is higher than its removal rate is determined, the antagonestic effect can be calculated. This can be carried out by using the model proposed by Stack et al. [151] or the model in [19]. Another approach can be used is to determine the critical particle concentration below which the antagonestic effect occurs.

(ii) This study was applied to a range of pure metals as an example for target materials. Further work can be commenced to include more alloys and composite materials. This can be very complex, particularly in the case where they can be directly related to material properties i.e. for the erosion–corrosion of composites both in bulk and in coating form [15, 16, 112]. This study assumes mono-oxide layer formation in passivation corrosion, which is not the case for the composites or the metal alloys. The oxide layer may be formed as sub-multi oxide layers, each sub-layer contains different oxides compositions. At these situation, modelling the additive effect may require extensive experimental programs to verify the effect of these sub-layers on the erosion-corrosion process in a computational model.

(iii) The model used to calculate the additive effect is verified against some literature data. However, it is possible that very different results may be obtained for erosion of passive films of different density. To date, this has not been considered. Hence, future work may concentrate on the verification of this model

through a series of laboratory tests.

(iv) At the present study, the effect of corrosion on the mechanical properties; such as the hardness and surface roughness of the material, is not considered for simplicity in the existing model. However, it is acknowledged that this may be a very significant in the overall wastage rate. Further work will be to consider these factors in the three dimensional CFD simulations.

(v) In this study, the pipe bend is used to develop the 3D erosion-corrosion maps on the interior surfaces of the pipe. Further work can be carried out by using more sophisticated applications such as the interior surfaces of the slurry pumps. For the slurry pump, the fluid flow is considered very complicated and requires different frame of references as there are rotating and stationery components in the turbomachinery systems. This kind of flow requires also special techniques for the CFD simulation, as it involves high degree of swirling and turbulent flow, which has an essential influence in the erosion and corrosion processes. To date, no erosion-corrosion simulation has been performed to predict the erosion-corrosion rates or regime distribution on the turbomachines components.

(vi) The DPM method used here in this study assumes one way coupling between the fluid flow and the solid particle. However, this assumption may give errors due to the volume fraction used in this study. Further simulation can be enhanced by using two or four way coupling to get more accurate erosion rate predictions.

Bibliography

[1] M. M. Stack and N. Pungwiwat, "Erosion-corrosion mapping of Fe in aqueous slurries: some views on a new rationale for defining the erosion-corrosion interaction", *Wear* **256(5)**, 565 - 576, (2004).

[2] R. Malka, S. Nesic and D. A. Gulino, "Erosion-corrosion and synergistic effects in disturbed liquid-particle flow", *Wear* **262(7-8)**, 791-799, (2007).

[3] B. Bozzini, M. E. Ricotti, M. Boniardi and C. Mele, "Evaluation of erosion-corrosion in multiphase flow via CFD and experimental analysis", *Wear* **255**, 237-245, (2003).

[4] H. W. Wang and M. M. Stack, "Corrosion of PVD TiN coatings under simultaneous erosion in sodium carbonate bicarbonate buffered slurries", *Surface and Coatings Technology* **105(1-2)**, 141-146, (1998).

[5] R. E. Melchers and R. Jeffrey, "Early corrosion of mild steel in seawater", *Corrosion Science* **47(7)**, 1678-1693, (2005).

[6] S. S. Rajahram, T. J. Harvey and R. J. K. Wood, "Evaluation of a semi-empirical model in predicting erosion-corrosion", *Wear* **267(11)**, 1883-1893, (2009).

[7] H. C. Meng and K. C. Ludema, "Wear models and predictive equations: their form and content", *Wear* **181-183(Part 2)**, 443-457, (1995).

[8] M. M. Stack and B. D. Jana, "Modelling particulate erosion-corrosion in aqueous slurries: some views on the construction of erosion-corrosion maps for a range of pure metals", *Wear* **256(9-10)**, 986-1004, (2004).

[9] H. X. Guo, B. T. Lu and J. L. Luo, "Interaction of mechanical and electrochemical factors in erosion-corrosion of carbon steel", *Electrochimica Acta* **51(2)**, 315-323, (2005).

[10] M. M. Stack, S. Lekatos and F. H. Stott, "Erosion-corrosion regimes: Number, nomenclature and justification?", *Tribology International* **28(7)**, 445-451, (1995).

[11] M. M. Stack and F. H. Stott, "An approach to modeling erosion-corrosion of alloys using erosion-corrosion maps", *Corrosion Science* **35(5-8)**, 1027-1034, (1993).

[12] M. M. Stack, N. Corlett and S. Zhou, "Construction of erosion-corrosion maps for erosion in aqueous slurries", *Materials Science and Technology* **12(8)**, 662-672, (1996).

[13] S. C. Lim and M. F. Ashby, "Overview no. 55 Wear-Mechanism maps", *Acta Metallurgica* **35(1)**, 1-24, (1987).

[14] M. M. Stack, H. Jawan and M. T. Mathew, "On the construction of micro-abrasion maps for a steel/polymer couple in corrosive environments", *Tribology International* **38(9)**, 848-856, (2005).

[15] M. M. Stack and B. D. Jana, "Modelling particulate erosion-corrosion regime transitions for Al/Al2O3 and Cu/Al2O3 MMCs in aqueous conditions", *Tribology International* **38(11-12)**, 995-1006, (2005).

[16] M. M. Stack and T. M. Abd El Badia, "On the construction of erosion-corrosion maps for WC/Co-Cr-based coatings in aqueous conditions", *Wear* **261(11-12)**, 1181-1190, (2006).

[17] M. Pourbaix, *Atlas of Electrochemical Equilibria in Aqueous Solutions*, Pergamon Press, Oxford, New York, (1966).

[18] M. M. Stack, J. G. Chacon-Nava and F. H. Stott, "Relationship between the effects of velocity and alloy corrosion resistance in erosion-corrosion environments at elevated temperatures", *Wear* **180(1-2)**, 91-99, (1995).

[19] M. M. Stack and L. Bray, "Interpretation of wastage mechanisms of materials exposed to elevated temperature erosion-corrosion using erosion-corrosion maps and computer graphics", *Wear* **186(1)**, 273-283, (1995).

[20] M. M. Stack, N. Corlett and S. Turgoose, "Some recent advances in the development of theoretical approaches for the construction of erosion-corrosion maps in aqueous conditions", *Wear* **233**, 535-541, (1999).

[21] A. Levy, J. Yan and J. Patterson, "Elevated temperature erosion of steels", *Wear* **108**, 43-60, (1986).

[22] M. Yovanovich, "Micro and macro hardness measurements, correlations, and contact models.", *Proceedings of 44th AIAA Aerospace Sciences Meeting and Exhibition*, Reno, Nevada, USA., (2006), No. 979, .

[23] P. Kritzer, "Corrosion in high-temperature and supercritical water and aqueous solutions: a review", *The Journal of Supercritical Fluids* **29(1-2)**, 1 - 29, (2004).

[24] S. Nesic, "Using computational fluid dynamics in combating erosion-corrosion", *Chemical Engineering Science* **61(12)**, 4086-4097, (2006).

[25] B. Poulson, "Complexities in predicting erosion corrosion", *Wear* **233-235**, 497-504, (1999).

[26] G. Brown, "Erosion prediction in slurry pipeline tee-junctions", *Proceedings of the Second International Conference on CFD in the Minerals and Process Industries, CSIRO*, Melbourne, Australia, (1999), No. 052, pp. 237-242.

[27] J. Boussinesq, "Essai sur la theorie des eaux courantes, Memoires presentes par divers savants", *Acad. des Sci. Inst. Nat.* **XXIII**, 1-680, (1877).

[28] R. W. Lyczkowski and J. X. Bouillard, "State-of-the-art review of erosion modeling in fluid/solids systems", *Progress in Energy and Combustion Science* **28(6)**, 543-602, (2002).

[29] *Multi-phase Flow Handbook*, C. T. Crowe, , Taylor & Francis Group, LLC, (2006).

[30] R. Eyler, "Design and Analysis of a Pneumatic Flow Loop", *Master's Thesis,* West Virginia University, Morgantown, WV, USA, (1987).

[31] J. K. Edwards, B. S. McLaury and S. A. Shirazi, "Modeling Solid Particle Erosion in Elbows and Plugged Tees", *Journal of Energy Resources Technology* **123(4)**, 277-284, (2001).

[32] H. M. Clark, "Particle velocity and size effects in laboratory slurry erosion measurements OR... do you know what your particles are doing?", *Tribology International* **35(10)**, 617-624, (2002).

[33] P. Doron and D. Barnea, "Flow pattern maps for solid-liquid flow in pipes", *International Journal of Multiphase Flow* **22(2)**, 273 - 283, (1996).

[34] R. J. Llewellyn, S. K. Yick and K. F. Dolman, "Scouring erosion resistance of metallic materials used in slurry pump service", *Wear* **256(6)**, 592-599, (2004).

[35] G. T. Burstein and K. Sasaki, "Effect of impact angle on the slurry erosion-corrosion of 304L stainless steel", *Wear* **240(1-2)**, 80-94, (2000).

[36] M. M. Stack and T. M. Abd El-Badia, "Some comments on mapping the combined effects of slurry concentration, impact velocity and electrochemical potential on the erosion-corrosion of WC/Co-Cr coatings", *Wear* **264(9-10)**, 826-837, (2008).

[37] C. Davis and P. Frawley, "Modelling of erosion-corrosion in practical geometries", *Corrosion Science* **51**, 769-775, (2009).

[38] J. B. Zu, I. M. Hutchings and G. T. Burstein, "Design of a slurry erosion test rig", *Wear* **140(2)**, 331-344, (1990).

[39] W. Tsai, J. A. C. Humphrey, I. Cornet and A. V. Levy, "Experimental measurement of accelerated erosion in a slurry pot tester", *Wear* **68(3)**, 289-303, (1981).

[40] G. R. Desale, B. K. Gandhi and S. C. Jain, "Improvement in the design of a pot tester to simulate erosion wear due to solid-liquid mixture", *Wear* **259(1-6)**, 196-202, (2005).

[41] H. M. Clark and R. B. Hartwich, "A re-examination of the the particle size effect in slurry erosion", *Wear* **248(1-2)**, 147-161, (2001).

[42] M. M. Stack and N. Pungwiwat, "A note on the construction of materials performance maps for resistance to erosion in aqueous slurries", *Wear* **215(1-2)**, 67-76, (1998).

[43] A. Levy, *Solid Particle Erosion and Erosion-Corrosion of Materials*, second edition, ASM International, (1997).

[44] I. Finnie, "The mechanism of erosion of ductile metals", *In Proceedings of the Third National Congress on Applied Mechanics*, American Society of Mechanical Engineers, (1958), pp. 527-532.

[45] J. G. A. Bitter, "A study of erosion phenomena part I", *Wear* **6(1)**, 5-21, (1963).

[46] J. G. A. Bitter, "A study of erosion phenomena: Part II", *Wear* **6(3)**, 169-190, (1963).

[47] J. H. Neilson and A. Gilchrist, "Erosion by a stream of solid particles", *Wear* **11(2)**, 111-122, (1968).

[48] A. Forder, M. Thew and D. Harrison, "A numerical investigation of solid particle erosion experienced within oilfield control valves", *Wear* **216(2)**, 184-193, (1998).

[49] F. T. Barwell, "Wear of metals", *Wear* **1(4)**, 317-332, (1958).

[50] S. K. Rhee, "Wear equation for polymers sliding against metal surfaces", *Wear* **16(6)**, 431-445, (1970).

[51] J. F. Archard, "Contact and Rubbing of Flat Surfaces", *Journal of Applied Physics* **24(8)**, 981-988, (1953).

[52] J. M. Challen and P. L. B. Oxley, "An explanation of the different regimes of friction and wear using asperity deformation models", *Wear* **53(2)**, 229-243, (1979).

[53] G. Sundararajan and P. G. Shewmon, "A new model for the erosion of metals at normal incidence", *Wear* **84(2)**, 237-258, (1983).

[54] G. Sundararajan, "A comprehensive model for the solid particle erosion of ductile materials", *Wear* **149(1-2)**, 111 - 127, (1991).

[55] S. L. Soo, "A note on erosion by moving dust particles", *Powder Technology* **17(3)**, 259-263, (1977).

[56] J. X. Bouillard and R. W. Lyczkowski, "On the erosion of heat exchanger tube banks in fluidized-bed combustors", *Powder Technology* **68(1)**, 37-51, (1991).

[57] I. Finnie, "Erosion of surfaces by solid particles", *Wear* **3**, 87-103, (1960).

[58] I. Finnie, "Some Observations on Erosion of Ductile Metals", *Wear* **19(1)**, 81-&, (1972).

[59] I. Finnie and D. H. McFadden, "On the Velocity Dependance of Erosion of Ductile Metals by Solid Particles at Low Angles of Incidence", *Wear* **48(1)**, 181-190, (1978).

[60] G. L. Sheldon and I. Finnie, "The mechanism of material removal in the erosive cutting of brittle materials", *Journal of Engineering for Industry, Trans ASME* **88**, 393-400, (1966).

[61] J. Ding and R. W. Lyczkowski, "Three-dimensional kinetic theory modeling of hydrodynamics and erosion in fluidized beds", *Powder Technology* **73(2)**, 127-138, (1992).

[62] D. Achim, A. K. Easton, M. P. Schwarz, P. J. Witt and A. Zakhari, "Tube erosion modelling in a fluidised bed", *Applied Mathematical Modelling* **26(2)**, 191 - 201, (2002).

[63] Z. Mazur, R. Campos-Amezcua, G. Urquiza-Beltrn and A. Garca-Gutiérrez, "Numerical 3D simulation of the erosion due to solid particle impact in the main stop valve of a steam turbine", *Applied Thermal Engineering* **24(13)**, 1877 - 1891, (2004).

[64] M. S. Wallace, J. S. Peters, T. J. Scanlon, W. M. Dempster, S. McCulloch and J.B. Ogilvie, "CFD Based Erosion Modeling of Multi-orifice Choke Valves", *Proceedings of ASME Fluids Engineering Summer Meeting*, ASME, Boston, USA, (2000), No. FEDSM2000-11244., .

[65] Z. Mazur, L. M. Palacios and G. Urquiza, "Numerical modeling of gland seal erosion in a geothermal turbine", *Geothermics* **33(5)**, 599-614, (2004).

[66] J. I. Achebo, "Computational Analysis of Erosion Wear Rate in a Pipeline Using the Drift Flux Models based on Eulerian Continuum Equations", *Proceedings of the World Congress on Engineering, WCE-2009*, London, UK, (2009), .

[67] I. M. Hutchings, "Some comments on the theoretical treatment of erosive particle impacts", *In Proceedings of the 5th International conference on erosion by solid*

and liquid impact, Cavendish Laboratory, University of Cambridge, London, UK, (1979), No. paper 36, pp. 1-6.

[68] I. M. Hutchings, "A model for the erosion of metals by spherical particles at normal incidence", *Wear* **70(3)**, 269-281, (1981).

[69] R. M. Brach, "Impact dynamics with applications to solid particle erosion", *International Journal of Impact Engineering* **7(1)**, 37-53, (1988).

[70] Y. Tirupataiah, B. Venkataraman and G. Sundararajan, "The Nature of the Elastic Rebound of a Hard Ball Impacting on Ductile Metallic Target Materials", *Materials Science and Engineering a: Structural, Materials Properties, Microstructure, and Processing* **124(2)**, 133-140, (1990).

[71] R. J. K. Wood and T. F. Jones, "Investigations of sand-water induced erosive wear of AISI 304L stainless steel pipes by pilot-scale and laboratory-scale testing", *Wear* **255(1)**, 206-218, (2003).

[72] R. J. K. Wood, T. F. Jones, J. Ganeshalingam and N. J. Miles, "Comparison of predicted and experimental erosion estimates in slurry ducts", *Wear* **256(9-10)**, 937-947, (2004).

[73] D. J. O'Flynn, M. S. Bingley, M. S. A. Bradley and A. J. Burnett, "A model to predict the solid particle erosion rate of metals and its assessment using heat-treated steels", *Wear* **248(1-2)**, 162 - 177, (2001).

[74] J. G. Mbabazi, T. J. Sheer and R. Shandu, "A model to predict erosion on mild steel surfaces impacted by boiler fly ash particles", *Wear* **257(5-6)**, 612 - 624, (2004).

[75] S. K. Das, K. M. Godiwalla, S. Shubha, S. P. Mehrotra and P. K. Dey, "A mathematical model to characterize effect of silica content in the boiler fly ash on erosion behaviour of boiler grade steel", *Journal of Materials Processing Technology* **204(1-3)**, 239-247, (2008).

[76] K. Nandakumar, H. Cunkui, S. Chiovelli, P. Minev and L. Jingli, "A comprehensive phenomenological model for erosion of materials in jet flow", *Powder Technology* **187**, 273-279, (2008).

[77] M. A. Founti and A. Klipfel, "Experimental and computational investigations of nearly dense two-phase sudden expansion flows", *Experimental Thermal and Fluid Science* **17**, 27-36, (1998).

[78] Y. M. Ferng, J. H. Hsieh and C. D. Horng, "Computational fluid dynamics predicting the distributions of thinning locations on the shell wall of feedwater heaters", *Nuclear Technology* **153(2)**, 197-207, (2006).

[79] H. Enwald, E. Peirano and A. E. Almstedt, "Eulerian two-phase flow theory applied to fluidization", *International Journal of Multiphase Flow* **22(Supplement 1)**, 21 - 66, (1996).

[80] M. Gustavsson and A. E. Almstedt, "Two-fluid modelling of cooling-tube erosion in a fluidized bed", *Chemical Engineering Science* **55(4)**, 867 - 879, (2000).

[81] Pierre R. Roberge, *Corrosion Engineering: Principles and Practice*, Stephen M. Smith, , McGrow Hill, USA, (2008).

[82] *Corrosion Mechanisms in Theory and Practice*, 2nd edition, P. Marcus, and J. Oudar, , Marcel Dekker, Inc., NY, USA, (2002).

[83] M. M. Stack, N. Corlett and S. Zhou, "A methodology for the construction of the erosion-corrosion map in aqueous environments", *Wear* **203**, 474-488, (1997).

[84] M. M. Stack, N. Corlett and S. Zhou, "Impact angle effects on the transition boundaries of the aqueous erosion-corrosion map", *Wear* **225**, 190-198, (1999).

[85] J. C. Walton, G. Cragnolino and S. K. Kalandros, "A numerical model of crevice corrosion for passive and active metals", *Corrosion Science* **38(1)**, 1 - 18, (1996).

[86] V. Botte, D. Mansutti and A. Pascarelli, "Numerical modeling of iron corrosion due to an acidic aqueous solution", *Applied Numerical Mathematics* **55(3)**, 253 - 263, (2005).

[87] H. X. Guo, B. T. Lu and J. L. Luo, "Response of surface mechanical properties to electrochemical dissolution determined by in situ nanoindentation technique", *Electrochemistry Communications* **8(7)**, 1092-1098, (2006).

[88] B. T. Lu and J. L. Luo, "Synergism of Electrochemical and Mechanical Factors in Erosion-Corrosion", *Journal of Physical Chemistry B* **110 (9)**, 4217-4231, (2006).

[89] B. T. Lu, J. L. Luo, F. Mohammadi, K. Wang and X. M. Wan, "Correlation between repassivation kinetics and corrosion rate over a passive surface in flowing slurry", *Electrochimica Acta* **53(23)**, 7022-7031, (2008).

[90] M. M. Stack and G. H. Abdulrahman, "Mapping erosion-corrosion of carbon steel in oil exploration conditions: Some new approaches to characterizing mechanisms and synergies", *Tribology International* **In Press**(2010).

[91] M. M. Stack and N. Pungwiwat, "Particulate erosion-corrosion of Al in aqueous conditions: some perspectives on pH effects on the erosion-corrosion map", *Tribology International* **35**, 651-660, (2002).

[92] M. Reyes and A. Neville, "Mechanisms of erosion-corrosion on a cobalt-base alloy and stainless-steel UNS S17400 in aggressive slurries", *Journal of Materials Engineering and Performance* **10 (6)**, 723-730, (2001).

[93] R. J. K. Wood, "Erosion-corrosion interactions and their effect on marine and offshore materials", *Wear* **261(9)**, 1012-1023, (2006).

[94] M. M. Stack, S. Zhou and R. C. Newman, "Identification of Transitions in Erosion-corrosion Regimes in Aqueous Environments", *Wear* **186(2)**, 523-532, (1995).

[95] Y. Wang and J. Postlethwaite, "The application of low Reynolds number k-turbulence model to corrosion modelling in the mass transfer entrance region", *Corrosion Science* **39(7)**, 1265 - 1283, (1997).

[96] H. X. Guo, B. T. Lu and J. L. Luo, "Study on passivation and erosion-enhanced corrosion resistance by Mott-Schottky analysis", *Electrochimica Acta* **52(3)**, 1108-1116, (2006).

[97] J. J. Liu, Y. Z. Lin and X. Y. Li, "Numerical simulation for carbon steel flow-induced corrosion in hiqh-velocity flow seawater", *Anti-Corrosion Methods and Materials* **55(2)**, 66-72, (2008).

[98] L. Niu and Y. F. Cheng, "Synergistic effects of fluid flow and sand particles on erosion-corrosion of aluminum in ethylene glycol-water solutions", *Wear* **265(3-4)**, 367-374, (2008).

[99] J. Postlethwaite, "Effect of chromate inhibitor on the mechanical and electrochemical components of erosion-corrosion in aqueous slurries of sand", *Corrosion* **37 (1)**, 1-5, (1981).

[100] M. Matsumura, Y. Oka, H. Hiura and M. Yano, "The role of passivating film in preventing slurry erosion-corrosion of austenitic stainless steel", *ISIJ International* **31(2)**, 168-176, (1991).

[101] Y. Li, G. T. Burstein and I. M. Hutchings, "The influence of corrosion on the erosion of aluminium by aqueous silica slurries", *Wear* **186-187(Part 2)**, 515 - 522, (1995).

[102] S. Zhou, M. M. Stack and R. C. Newman, "Electrochemical studies of anodic dissolution of mild steel in a carbonate-bicarbonate buffer under erosion-corrosion conditions", *Corrosion Science* **38(7)**, 1071-1084, (1996).

[103] Joshua F. Addis, "Erosion-corrosion in disturbed liquid/particle flow", *Master's Thesis,* Russ College of Engineering and Technology, Ohio University, (2008).

[104] M. M. Stack, N. Corlett and S. Turgoose, "Some thoughts on modelling the effects of oxygen and particle concentration on the erosion-corrosion of steels in aqueous slurries", *Wear* **255(1-6)**, 225 - 236, (2003).

[105] J. Postlethwaite, S. Nesic, G. Adamopoulos and D. J. Bergstrom, "Predictive models for erosion-corrosion under disturbed flow conditions", *Corrosion Science* **35(1-4)**, 627-633, (1993).

[106] J. Jiang, M. M. Stack and A. Neville, "Modelling the tribo-corrosion interaction in aqueous sliding conditions", *Tribology International* **35(10)**, 669-679, (2002).

[107] A. Keating and S. Nesic, "Prediction of two-phase erosion-corrosion in bends", *Proceedings of 2nd International conference on CFD in the Minerals and Process Industries*, CSIRO, Melbourne, Australia, (1999), No. 035, pp. 229-236.

[108] S. Nesic, "Computation of localized erosion-corrosion in disturbed two-phase flow", PhD. Thesis, University of Saskatchewan, Canada, (1991).

[109] G. T. Burstein and K. Sasaki, "Detecting electrochemical transients generated by erosion-corrosion", *Electrochimica Acta* **46(24-25)**, 3675 - 3683, (2001).

[110] T. J. Harvey, J. A. Wharton and R. J. K. Wood, "Development of a synergy model for erosion-corrosion of carbon steel in a slurry pot", *Tribology - Materials, Surfaces & Interfaces* **1 (1)**, 33-47., (2007).

[111] M. M. Stack, "Some issues relating to the construction of materials selection maps for resistance to elevated temperature erosion", *Tribology International* **30(6)**, 435-444, (1997).

[112] M. M. Stack and T. M. Abd El Badia, "Mapping erosion-corrosion of WC/Co-Cr based composite coatings: Particle velocity and applied potential effects", *Surface & Coatings Technology* **201(3-4)**, 1335-1347, (2006).

[113] M. M. Stack, J. S. James and Q. Lu, "Erosion-corrosion of chromium steel in a rotating cylinder electrode system: some comments on particle size effects", *Wear* **256(5)**, 557-564, (2004).

[114] X. Chen, B. S. McLaury and S. A. Shirazi, "Application and experimental validation of a computational fluid dynamics (CFD)-based erosion prediction model in elbows and plugged tees", *Computers & Fluids* **33(10)**, 1251-1272, (2004).

[115] M. M. Enayet, M. M. Gibson, A. M. Taylor and M. Yianneskis, "Laser-Doppler measurements of laminar and turbulent flow in a pipe bend", *International Journal of Heat and Fluid Flow* **3(4)**, 213 - 219, (1982).

[116] M. M. Enayet, M. M. Gibson and M. Yianneskis, "Measurements of turbulent developing flow in a moderately curved square duct", *International Journal of Heat and Fluid Flow* **3(4)**, 221 - 224, (1982).

[117] N. M. Crawford, G. Cunningham and S. W. T. Spence, "An experimental investigation into the pressure drop for turbulent flow in 90° elbow bends", *Journal of Process Mechanical Engineering* **221(2)**, 77-88, (2007).

[118] J. Wang and S. A. Shirazi, "A CFD based correlation for mass transfer coefficient in elbows", *International Journal of Heat and Mass Transfer* **44(9)**, 1817 - 1822, (2001).

[119] "FLUENT user's guide, Version 6.3", FLUENT, Inc., (2006).

[120] B. E. Launder and D. B. Spalding, *Lectures in Mathematical Models of Turbulence*, Academic Press, London, (1972).

[121] S. A. Morsi and A. J. Alexander, "An investigation of particle trajectories in two-phase flow systems", *Journal of Fluid Mechanics Digital Archive* **55(02)**, 193-208, (1972).

[122] P. S. Glockner and G. F. Naterer, "Near-wall velocity profile with adaptive shape functions for turbulent forced convection", *International Communications in Heat and Mass Transfer* **32(1-2)**, 72 - 79, (2005).

[123] M. M. Stack, N. Corlett and S. Zhou, "Some thoughts on the effect of elastic rebounds on the boundaries of the aqueous erosion-corrosion map", *Wear* **214(2)**, 175-185, (1998).

[124] M. Roy, K. K. Ray and G. Sundararajan, "An analysis of the transition from metal erosion to oxide erosion", *Wear* **217(2)**, 312-320, (1998).

[125] G. Sundararajan and Y. Tirupataiah, "The localization of plastic flow under dynamic indentation conditions: I. Experimental results", *Acta Materialia* **54(3)**, 565 - 575, (2006).

[126] M. J. Graham, J. A. Bardwell, G. I. Sproule, D. F. Mitchell and B. R. MacDougall, "The growth and stability of passive films", *Corrosion Science* **35**, 13 - 18, (1993).

[127] Y. Tirupataiah and G. Sundararajan, "A dynamic indentation technique for the characterization of the high strain rate plastic flow behaviour of ductile metals and alloys", *Journal of the Mechanics and Physics of Solids* **39(2)**, 243 - 271, (1991).

[128] Y. I. Oka, H. Ohnogi, T. Hosokawa and M. Matsumura, "The impact angle dependence of erosion damage caused by solid particle impact", *Wear* **203**, 573-579, (1997).

[129] D. Griffin, A. Daadbin and S. Datta, "The development of a three-dimensional finite element model for solid particle erosion on an alumina scale/MA956 substrate", *Wear* **256(9-10)**, 900-906, (2004).

[130] E. Kirowa-Eisner E. Gileadi, "Some observations concerning the Tafel equation and its relevance to charge transfer in corrosion", *Corrosion Science* **47**, 3068-3085, (2005).

[131] M. M. Stack, M. M. Antonov and I. Hussainova, "Some views on the erosion-corrosion response of bulk chromium carbide based cermets", *Journal of Physics D-Applied Physics* **39(15)**, 3165-3174, (2006).

[132] M. M. Stack, S. Zhou and R. C. Newman, "Effects of particle velocity and applied potential on erosion of mild steel in carbonate/bicarbonate slurry", *Materials Science and Technology* **12(3)**, 261-268, (1996).

[133] M. M. Stack and N. Pungwiwat, "Slurry erosion of metallics, polymers, and ceramics: particle size effects", *Materials Science and Technology* **15(3)**, 337-344, (1999).

[134] M. M. Stack, Y. Purandare and P. Hovsepian, "Impact angle effects on the erosion-corrosion of superlattice CrN/NbN PVD coatings", *Surface & Coatings Technology* **188**, 556-565, (2004).

[135] M. M. Stack, F. H. Stott and G. C. Wood, "Review of Mechanisms of Erosion-corrosion of Alloys at Elevated Temperature", *Wear* **162**, 706-712, (1993).

[136] M. M. Stack, J. ChaconNava and M. P. Jordan, "Elevated temperature erosion of range of composite layers of Ni-Cr based functionally graded material", *Materials Science and Technology* **12(2)**, 171-177, (1996).

[137] Y. Shida and H. Fujikawa, "Particle Erosion Behavior of Boiler Tube Materials at Elevated Temperature", *Wear* **103(4)**, 281-296, (1985).

[138] M. Suckling and C. Allen, "Critical variables in high temperature erosive wear", *Wear* **203-204**, 528 - 536, (1997).

[139] K. M. Nho, "Experimental Investigation of Heat Flow Rate and Directional Effect on Contact Conductance of Anisotropic Ground/Lapped Interfaces", PhD. Thesis, University of Waterloo, Canada, (1990).

[140] T. E. Howes, P. M. Rogers, J. A. Little and I. M. Hutchings, "Erosion-corrosion of mild steel in a temperature gradient", *Wear* **186-187(Part 1)**, 316 - 324, (1995).

[141] D. Cubicciotti, "Potential pH Diagrams for Alloy Water-Systems Under LWR Conditions", *Journal of Nuclear Materials* **201**, 176-183, (1993).

[142] D. Chen, M. Sarumi, S. T. S. Al-Hassani, S. Gan and Z. Yin, "A model for erosion at normal impact", *Wear* **205(1-2)**, 32-39, (1997).

[143] B. E. Lee, C. A. J. Fletcher and M. Behnia, "Computational study of solid particle erosion for a single tube in cross flow", *Wear* **240(1-2)**, 95-99, (2000).

[144] G. L. Sheldon and A. Kanhere, "Investigation of Impingement Erosion Using Single Particle", *Wear* **21(1)**, 195-&, (1972).

[145] In *CRC Handbook of Chemistry and Physics*, 87thed., David R. Lide, , Taylor and Francis, Boca Raton, FL, USA, (2007), Properties of Solids, Ch.12, p. 195, , CD-ROM Version.

[146] Y. Orcan and A. N. Eraslan, "Thermal stresses in elastic-plastic tubes with temperature-dependent mechanical and thermal properties", *Journal of Thermal Stresses* **24(11)**, 1097-1113, (2001).

[147] A. N. Eraslan and Y. Orcan, "Computation of transient thermal stresses in elastic-plastic tubes: Effect of coupling and temperature-dependent physical properties", *Journal of Thermal Stresses* **25(6)**, 559-572, (2002).

[148] H. Argeso and A. N. Eraslan, "On the use of temperature-dependent physical properties in thermomechanical calculations for solid and hollow cylinders", *International Journal of Thermal Sciences* **47**, 136-146, (2008).

[149] N. Noda, "Thermal Stresses in Materials with Temperature Dependent Properties", *Proceedings of the NATO Advanced Research Workshop on Thermal Shockand Thermal Fatigue Behaviour of Advanced Ceramics*, MA, USA, (1993), pp. 15-26.

[150] In *CRC Handbook of Chemistry and Physics*, 87thed., David R. Lide, , Taylor and Francis, Boca Raton, FL, USA, (2007), Fluid Properties, Ch.6, p. 2, , CD-ROM Version.

[151] M. M. Stack, Q. Songroehrle, F. H. Stott and G. C. Wood, "Computer Simulation of Erosion-corrosion Interaction at Elevated Temperature", *Wear* **181**, 516-523, (1995).

[152] B. Stellwag, "The mechanism of oxide film formation on austenitic stainless steels in high temperature water", *Corrosion Science* **40(2-3)**, 337 - 370, (1998).

[153] C. M. Criss and J. W. Cobble, "The Thermodynamic Properties of High Temperature Aqueous Solutions. IV. Entropies of the Ions up to 200° and the Correspondence Principle", *Journal of the American Chemical Society* **86**, 5385-5390, (1964).

Appendix A

Electrochemical Reactions Thermodynamics: E-pH Diagrams for Iron

A.1 Basics

The tables and graphics in this appendix describe the thermodynamic behaviour of the following metals when exposed to pure water at a range of elevated temperatures; namely: 298, 323, 343, 363 $[K]$ for the iron. From which, the simplified E-pH (Pourbaix) diagrams are constructed respectively. Table A-1 contains the basic thermodynamic values for each species, solid or ionic, considered for the construction of the E-pH diagrams. The relations between the free energy of the species considered and the associated equations are evaluated with the data presented in Table A-1. The possible electrochemical reactions to construct these simplified E-pH diagrams are listed in table A-2.

The free energy (G^o)of a substance for which heat capacity data are available can be calculated as a function of temperature using Equation (A.1) [153]:

$$G^o_{T_2} = G^o_{T_1} - S^o_{T_1}\ (T_2 - T_1) - T_2 \int_{T_1}^{T_2} \frac{C^o_p}{T}\, dT\ + \int_{T_1}^{T_2} C^o_p\, dT \tag{A.1}$$

For pure substances, i.e., solids, liquids, and gases, the heat capacity $\left(C^o_p\right)$ is ex-

Table A.1: Pure species considered for the $Fe - H_2O$ system and their thermodynamic data [81].

Species	$G^o_{(298)}$ $\left[J\ mol^{-1}\right]$	$S^o_{(298)}$ $\left[J\ mol^{-1}\right]$	A	$B \times 10^3$	$C \times 10^{-5}$
H_2	0	131	27.28	3.263	0.502
H_2O	-237,000	69.9	75.27	0	0
Fe	0	27.1	12.72	31.71	-2.51
Fe_2O_3	-742,000	87.3	98.28	77.82	-14.85
			$\check{S}^o_{(298)}$ $\left[J\ mol^{-1}\right]$	a	b
H^+	0	0	-20.9	0.065	-0.005
Fe^{2+}	-92,200	-107	-149	0.13	-0.00166
Fe^{3+}	-17,800	-279	-342	0.13	-0.00166

Table A.2: The possible electrochemical reactions for the simplified $Fe - H_2O$ system [81].

Line	Reaction
Line 1	$2e^- + Fe^{2+} = Fe$
Line 2	$e^- + Fe^{3+} = Fe^{2+}$
Line 3	$Fe_2O_3 + 6H^+ + 2e^- = 2Fe^{2+} + 3H_2O$
Line 4	$Fe_2O_3 + 6H^+ + 6e^- = 2Fe + 3H_2O$
Line 5	$2Fe^{3+} + 3H_2O = Fe_2O_3 + 6H^+$

pressed as an empirical function of the absolute temperature:

$$C_p^o = A + B\,T + C\,T^{-2} \tag{A.2}$$

For ionic substances, one has to use another method, such as that proposed by Criss and Cobble [153] to obtain the heat capacity, provided that the temperature does not rise above 200 $[^oC]$. The expression of the ionic capacity makes use of absolute entropy values and the parameters (a) and (b) contained in Tables A-1 and is given as

$$C_p^o = \left(4.186\,a + b\,\check{S}_{(298)}^o\right)\,(T_2 - 298.16)\,/\,\ln\left(\frac{T_2}{298.16}\right) \tag{A.3}$$

By combining Equation (A.2) or (A.3) with Equation. (A.1), one can obtain the free energy at a given temperature by using the fundamental data contained in Tables A-1

$$G_{(T)}^o = G_{(298)}^o + \left(C_p^o - S_{(298)}^o\right)\,(T_2 - 298.16) - T_2\,\ln\left(\frac{T_2}{298.16}\right)\,C_p^o \tag{A.4}$$

An excel spreadsheet is generated to calculate these values accordingly with the data in table A-1. For any species O, the free energy of 1 mole can be obtained from (G^o) by

$$G_{(T)} = G_{(T)}^o + 2.303\,R\,T\,\log\left(a_o\right) \tag{A.5}$$

thus, for (x) mole of the species, the free energy is expressed by

$$x\,G_{(T)} = x\,\left(G_{(T)}^o + 2.303\,R\,T\,\log\left(a_o\right)\right) \tag{A.6}$$

where for pure substances such as solids, (a_o) is equal to 1. For soluble species, the activity of species (a_o), is the product of the activity coefficient of that species (γ_o) with its molar concentration $[O]$

$$a_o = \gamma_o\,[O] \tag{A.7}$$

The activity coefficient of a chemical species in solution is close to 1 at infinite dilution when there is no interference from other chemical species. For most other situations the activity coefficient is a complex function that varies with the concentration of the species and with the concentration of other species in solution. For the sake of simplicity the activity coefficient will be assumed to be of value 1; hence Equation. A-6 can be written as

$$x\,G_{(T)} = x\,\left(G^{o}_{(T)} + 2.303\,R\,T\,\log\left([O]\right)\right) \tag{A.8}$$

The (ΔG) of a cell can be calculated by subtracting the sum of the free energy values of the reactants from the sum values of the products.

$$\Delta G = \sum G^{o}_{(T)rectants} - \sum G^{o}_{(T)products} \tag{A.9}$$

To translate it into potential we substitute in

$$E = \frac{-\Delta G}{z_m\,F} \tag{A.10}$$

A.2 Potential-pH diagrams

Potential-pH (E-pH) diagrams, also called predominance or Pourbaix diagrams, have been adopted universally since their conception in the early 1950s. They have been repetitively proved to be an elegant way to represent the thermodynamic stability of chemical species in given aqueous environments. E-pH diagrams are typically plotted for various equilibria on normal Cartesian coordinates with potential (E) as the ordinate (y-axis) and pH as the abscissa (x-axis).

Conditions for equilibrium at a given constant temperature are derived from a form of the Van't Hoff reaction isotherm

$$\Delta G = \Delta G^{o} + R\,T\,\ln\left(J\right) \tag{A.11}$$

where (J) is the activity quotient corresponding to a free energy change, ΔG

$$J = \frac{a_{product1}\, a_{product2} \cdots a_{productn}}{a_{reactant1}\, a_{reactant2} \cdots a_{reactantn}} \tag{A.12}$$

substitute Equation. A.10 in Equation.A.11, This yields the $NernstEquation$

$$E = E^o - \frac{RT}{z_m F} \ln(Q) \tag{A.13}$$

In case of reactions that has no charge transfer, the activities are related simply by the normal equilibrium constant(K_{eq}) which can be also related to the free energy by

$$K_{eq} = \exp\left(\frac{-\Delta G}{RT}\right) \tag{A.14}$$

Also, K_{eq} can be related to the reaction quotient (Q). For a generalised equation of the form

$$aA + bB + \cdots \rightarrow mM + nN + \cdots \tag{A.15}$$

the reaction equilibrium constant(K_{eq}) and reaction quotient (Q) can be given by

$$K_{eq} = Q = \frac{a_M^m\, a_N^n \cdots}{a_A^a\, a_B^b \cdots} \tag{A.16}$$

To get the equations of the boundary lines illustrated in Figure A.1, the method above is used. Tables A.3 through A.7 list the calculation results which have been done using an excel spreadsheet. Table A.8 summarises these equations for each line according to the equivalent temperature.

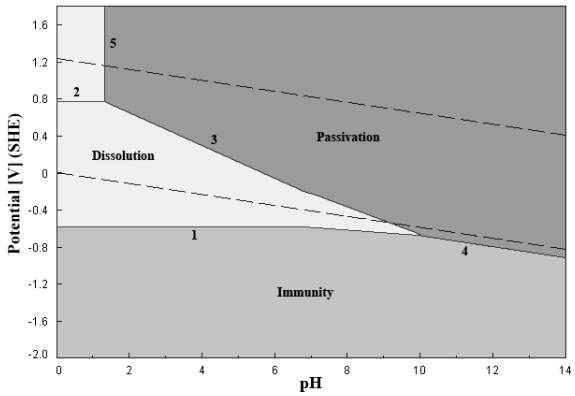

Figure A.1: Simplified Pourbaix diagram for Fe shows the transition lines 1-5 location.

Table A.3: Calculation for Line (1) represents the reaction: $2e^- + Fe^{2+} = Fe$.

T, $[K]$	**298**	**323**	**343**	**363**
$G^o(T)_{Fe^{2+}}$	-85099.77	-82689.34	-81116.19	-79880.29
$G^o(T)_{Fe}$	0	-699.031	-1299.153	-1932.207
$G^o(T)_{reaction}$	85099.77	81990.31	79817.04	77948.08
E^o	-0.441	-0.425	-0.414	-0.404
$RT\ln(Q)/zF$	0.1773	0.192	0.204	0.216
E	-0.618	-0.617	-0.618	-0.62

Table A.4: Calculation for Line (2) represents the reaction: $e^- + Fe^{3+} = Fe^{2+}$.

T, $[K]$	**298**	**323**	**343**	**363**
$G^o(T)_{Fe^{2+}}$	-85099.77	-82689.34	-81116.19	-79880.29
$G^o(T)_{Fe^{3+}}$	-10709.8	-4127	656.63	4966.6
$G^o(T)_{reaction}$	-74389.94	-78562.26	-81772.82	-84846.88
E^o	0.771	0.814	0.847	0.879
$RT\ln(Q)/zF$	0	0	0	0
E	0.771	0.814	0.847	0.879

Table A.5: Calculation for Line (3) represents the reaction: $Fe_2O_3 + 6H^+ + 2e^- = 2Fe^{2+} + 3H_2O$.

T, $[K]$	**298**	**323**	**343**	**363**
$G^o(T)_{Fe^{2+}}$	-85099.77	-82689.34	-81116.19	-79880.29
$G^o(T)_{H_2O}$	-237000	-238812.12	-240376.26	-242028.23
$G^o(T)_{H^+}$	0	0	0	0
$G^o(T)_{Fe_2O_3}$	-742000	-744278	-746275.6	-748419.9
$G^o(T)_{reaction}$	-139199.54	-137537.04	-137085.56	-137425.37
E^o	0.721	0.713	0.7104	0.712
$E = RT\ln(a_{Fe^{2+}})/zF$	0.355	0.385	0.408	0.432
Free parameter	1.076	1.097	1.12	1.14
pH parameter	-0.177	-0.192	-0.204	-0.216

Table A.6: Calculation for Line (4) represents the reaction: $Fe_2O_3 + 6H^+ + 6e^- = 2Fe + 3H_2O$.

T, $[K]$	**298**	**323**	**343**	**363**
$G^o(T)_{Fe}$	0	-699.031	-1299.153	-1932.207
$G^o(T)_{H_2O}$	-237000	-238812.12	-240376.26	-242028.23
$G^o(T)_{H^+}$	0	0	0	0
$G^o(T)_{Fe_2O_3}$	-742000	-744278	-746275.6	-748419.9
$G^o(T)_{reaction}$	31000	26443.58	22548.51	18470.796
E^o	-0.054	-0.046	-0.039	-0.032
$E = RT\ln(a_{Fe^{2+}})/zF$	0	0	0	0
Free parameter	-0.054	-0.046	-0.039	-0.032
pH parameter	-0.059	-0.064	-0.068	-0.072

Table A.7: Calculation for Line (5) represents the reaction: $2Fe^{3+} + 3H_2O = Fe_2O_3 + 6H^+$.

T, $[K]$	**298**	**323**	**343**	**363**
$G^o(T)_{Fe}$	-10709.8	-4127	656.63	4966.6
$G^o(T)_{H_2O}$	-237000	-238812.12	-240376.26	-242028.23
$G^o(T)_{H^+}$	0	0	0	0
$G^o(T)_{Fe_2O_3}$	-742000	-744278	-746275.6	-748419.9
$G^o(T)_{reaction}$	-9580.34	-19587.48	-26460.08	-32268.39
$G^o(T)_{reaction}/(2.303RT)$	-0.839	-1.583	-2.014	-2.321
pH parameter	1.72	1.47	1.33	1.23

Table A.8: The equations of boundary lines between the passive and dissolution regions see Figure A.1.

Line	Temperature [K]	Equation
Line 1	298	E= -0.618
	323	E= -0.617
	343	E= -0.618
	363	E= -0.620
Line 2	298	E= 0.771
	323	E= 0.814
	343	E= 0.848
	363	E= 0.879
Line 3	298	E= 1.076 - 0.177 pH
	323	E= 1.097 - 0.192 pH
	343	E= 1.119 - 0.204 pH
	363	E= 1.144 - 0.216 pH
Line 4	298	E= -0.054 - 0.059 pH
	323	E= -0.046 - 0.064 pH
	343	E= -0.039 - 0.068 pH
	363	E= -0.032 - 0.072 pH
Line 5	298	pH = 1.72
	323	pH = 1.47
	343	pH = 1.33
	363	pH = 1.23

Appendix B

CFD Simulation Run Configuration

B.1 General

This appendix summarise the CFD runs configuration that have been commenced for the first case study; (Enayet et al. [115]), and the second case study; (Wood et al. [72]). The summery is the output file from the FLUENT software after the simulation is done.

B.2 First case study (Enayet et al.)

B.2.1 Model Settings

Space: 3D.

Time: Steady .

Viscous: Standard k-epsilon turbulence model.

Wall: Treatment: Standard Wall Functions.

B.2.2 Boundary conditions

Outlet: Outflow.

Inlet: Velocity-inlet.

Outer-wall: Wall.

Inner-wall: Wall.

Default-interior: Interior.

B.2.2.1 Inlet boundary

Velocity-Magnitude-(m/s): 0.92000002

X-Component-of-Flow-Direction: 1.

Y-Component-of-Flow-Direction: 0.

Z-Component-of-Flow-Direction: 0.

X-Coordinate-of-Axis-Origin-(m): 0.

Y-Coordinate-of-Axis-Origin-(m): 0.

Z-Coordinate-of-Axis-of-Axis-Origin-(m): 0.

Turbulent-Intensity(%): 0.099999994.

Hydraulic-Diameter-(m): 0.047999999.

B.2.2.2 Outlet boundary

Outflow-ratio(%): 100.

B.2.3 Solver control

Relaxation: default.

Pressure-Velocity-Coupling: SIMPLE.

Discretisation-Scheme:

- Pressure: Standard.

- Momentum: Second Order Upwind.
- Turbulent Kinetic Energy: Second Order Upwind.
- Turbulent Dissipation Rate: Second Order Upwind.

B.2.4 Material properties

Material: water-liquid (fluid).

Density kg/m3 constant 1000.

Cp (Specific Heat) j/kg-k constant 4182.

Viscosity kg/m-s constant 0.001027.

B.3 Second case study (Wood et al.)

B.3.1 Model Settings

Space: 3D.

Time: Steady .

Viscous: Standard k-epsilon turbulence model.

Wall: Treatment: Standard Wall Functions.

B.3.2 Boundary conditions

Outlet: Outflow.

Inlet: Velocity-inlet.

Outer-wall: Wall.

Inner-wall: Wall.

Default-interior: Interior.

B.3.2.1 Inlet boundary

Velocity-Magnitude-(m/s): 3.0.

X-Component-of-Flow-Direction: 1.

Y-Component-of-Flow-Direction: 0.

Z-Component-of-Flow-Direction: 0.

X-Coordinate-of-Axis-Origin-(m): 0.

Y-Coordinate-of-Axis-Origin-(m): 0.

Z-Coordinate-of-Axis-of-Axis-Origin-(m): 0.

Turbulent-Intensity(%): 0.099999994.

Hydraulic-Diameter-(m): 0.078.

B.3.2.2 Outlet boundary

Outflow-ratio(%): 100.

B.3.3 Solver control

Relaxation: default.

Pressure-Velocity-Coupling: SIMPLE.

Discretisation-Scheme:

- Pressure: Standard.
- Momentum: Second Order Upwind.
- Turbulent Kinetic Energy: Second Order Upwind.
- Turbulent Dissipation Rate: Second Order Upwind.

B.3.4 Material properties

Material:	water-liquid (fluid)
Density	kg/m3 constant 998.2.
Cp	(Specific Heat) j/kg-k constant 4182.
Viscosity	kg/m-s constant 0.001003.

Appendix C

List of Published Papers

Conference papers:

(i) Stack, M. M. and Abdelrahman, S. M., (2010), "Some reflections on a model to predict the erosion rate of the passive film on pure metals", In: 13^{th} International Conference on Aerospace Science and Aviation Technology, ASAT 2009, 26-28 May 2009, Cairo, Egypt.

(ii) Stack, M. M., Abdelrahman, S. M. and Jana, B. D., (2009), "A map and a pipe: a new approach to characterizing erosion-corrosion regimes of Fe in three dimensions using CFD modelling", In: EuroCorr 2009, 6-10 September 2009, Nice, France.

(iii) Stack, M. M. and Abdelrahman, M. S., (2010), "CFD modelling of erosion-corrosion of steel in aqueous environments - particle concentration effects on the regime boundaries", In: 14^{th} Nordic Conference on Tribology, NordTrib 2010, 8-11 June 2010, Luleå, Sweden, (In Press).

Journal paper:

(i) Stack, M. M., Abdelrahman, S. M., and Jana, B.D., (2010), "A new methodology for modelling erosion-corrosion regimes on real surfaces: gliding down the galvanic series for a range of metal-corrosion systems", WEAR, 268 (3-4). pp. 533-542.

Some reflections on a model to predict the erosion rate of the passive film on pure metals

Paper: ASAT-13-MS-16

13th International Conference on
AEROSPACE SCIENCES & AVIATION TECHNOLOGY,
ASAT- 13, May 26 – 28, 2009, E-Mail: asat@mtc.edu.eg
Military Technical College, Kobry Elkobbah, Cairo, Egypt
Tel : +(202) 24025292 – 24036138, Fax: +(202) 22621908

Some Reflections on a Model to Predict the Erosion Rate of the PassiveFilm on Pure Metals

M. M. Stack* and S. Abdelrahman†

Abstract: A model to predict the erosion rates on the passive films of metals is proposed. The model investigates the effect of eroded particles on metals on which a passive (oxide) film has formed. To date, many of the existing erosion models concentrated in the normal angle erosion of the oxide layer. This new approach considers the effect of oblique impacts on the oxide layer and the effect of its thickness on the amount of metal and oxide layer removal. The model is then tested by comparison to previous experimental work.

Keywords: erosion, corrosion, passive layer wear, oblique impact.

1. Introduction

Wastage as a result of the combined effects of the erosion-corrosion by solid particles is a major factor in many industrial situations such as mineral processing and oil and gas exploration. The synergistic effect of both erosion and corrosion may cause rapid metal wastage of components in such environments. In many cases, the surface material forms a passive film during the erosion-corrosion process. However, the removal process involving the transition from erosion of oxide films to the underlying metal is not well understood.

In the literature, Tirupataiah et al. [1] investigated the nature of the elastic rebound on ductile materials when impacted by spherical particles. In this work, an expression was developed for predicting the size of the crater diameter, by equating the kinetic energy of the particle impacting the surface with the energy needed to remove a crater volume from the oxide layer. The model assumed that all the energy of the impact is consumed in the erosion process and the particle was spherical. The basic assumption on which this model is based is that all the relaxation of the crater shape occurs in the direction of the impacting particle.

Later, Roy et. al. [2] investigated the transition effect of the oxide erosion to substrate erosion and developed a similar expression for the crater diameter but for sharp edged or conical particles and for an oxide layer based on the same first assumption of Tirupataiah. The derivation was applicable for both the substrate (ductile) and the oxide brittle layer. However, the model only considers normal impact and the assumption of the complete consumption of the particle energy in the erosion process ignores any energy expended in elastic work.

† Research student, University of Strathclyde, s.m.abdelrahman@strath.ac.uk.
* Professor, University of Strathclyde, margaret.stack@strath.ac.uk

Based on the work of Tirupataiah, previous work involving the current investigators [3] introduced an erosion model for passive layers of metals. The basic assumption was that the rebound velocity is explicitly small compared to the impact velocity and the impact angle is normal. This erosion model was necessary in constructing the erosion-corrosion mapping for various ranges of pure metals and low carbon steel. However, these assumptions constrain the model applicability in dynamic slurry flow motions, as in such environments, the target material is generally exposed to oblique impacts and the rebound characteristics of the impacting particles are considerable. Thus, it is necessary to adapt the model to account for oblique impacts and to account for elastic rebound effects. In addition the model considers the important transition when the eroding particles penetrate an oxide film during the impact process.

2. Model Assessment

Starting with the approach of Tirupataiah[1], it is assumed that the energy involved in the erosion process is the difference between the initial impact energy and the energy that causes the particle to rebound namely energy remaining after rebound. It is also assumed that the erosion process is adiabatic, thus discounting the amount of energy consumed during the erosion process due to friction and local melting of the material.

Thus, equating the energy difference by the energy required to form a crater gives:

$$\frac{m_p}{2}\left[V_1^{\,2} - V_2^{\,2}\right] = H\,U \tag{1}$$

where m_p is the particle mass, V is particle velocity, H is the material hardness, U is the crater volume and the subscripts *1,2* are for the impact and rebound process respectively. Assuming that the surface shear stresses due to oblique impact may be neglected in case of brittle materials, Finnie[4] stated that the crater diameter of ring crack d is related to the vertical component of the velocity. Then, by default the energy balance in equation (1) will be:

$$\frac{m_p}{2}\left[V_1^{\,2}\sin^2\alpha_1 - V_2^{\,2}\sin^2\alpha_2\right] = H\,U \tag{2}$$

where α_1 and α_2 are the impact and rebound angles respectively.

By definition, the normal impact velocity component is related to the normal rebound velocity component by the coefficient of restitution e, thus and by rearranging:

$$\frac{m_p}{2}\left[V_1^{\,2}\sin^2\alpha_1\right]\left(1-e^2\right) = H\,U \tag{3}$$

Assuming that the particle is a sphere and the crater depth is comparably smaller than the particle diameter, i.e. at low particle velocities, the shape of the crater on the passive film (oxide) surface can be assumed as part of a sphere and U can be related to the crater diameter W by [1]:

$$U = \frac{\pi W^{\,4}}{32\,d_p} \tag{4}$$

Where d_p is the particle diameter. Applying equation (4) into (3) gives:

$$W = 1.5023 \left[\frac{m_p \, d_p \left(1 - e^2\right)}{H} \right]^{0.25} \left(V_1 \sin \alpha_1\right)^{0.5} \tag{5}$$

The crater depth d is related to crater diameter using the same assumption above by:

$$d = \frac{W^2}{4 d_p} \tag{6}$$

From Jana [3], the mass of passivating oxides film removed per impact is given as:

$$M_t = \pi \, k_2 \, d_p \, d \, h \, \rho_f \tag{7}$$

Where k_2 is constant depending on the substrate material and is given for different pure metals in table.1 taken from [3], h is the passive layer thickness and ρ_f is the passive layer density. Substituting equation (5) into (6) and apply to (7) then we finally get:

$$M_t = 1.7726 \, k_2 \, h \, \rho_f \left[\frac{m_p \, d_p \left(1 - e^2\right)}{H} \right]^{0.5} \left(V_1 \sin \alpha_1\right) \tag{8}$$

Further simplification to the above equation can be made if we put ($m_p = \frac{\pi \, d_p{}^3 \rho_p}{6}$), leads to:

$$M_t = \pi \, k_2 \, h \, \rho_f \, d_p{}^2 \left[\frac{\rho_p \left(1 - e^2\right)}{6 \, H} \right]^{0.5} \left(V_1 \sin \alpha_1\right) \tag{9}$$

The unit given for the erosion model by equation (9) is *[g impact^{-1}]*. To convert to a useful unit *[kg m^{-2}s^{-1}]* for example, one should multiply equation (9) by the particle impact frequency. This can be varied according to the application under investigation. For example, if the flow is homogeneous (constant particle concentration) then particle impact frequency may be given as [5]:

$$I_p = \frac{c \, V_1 \sin \alpha_1}{m_p} \tag{10}$$

Table.1: **Properties for some pure metals and their passive films taken from [3]**

Metal Properties	Fe	Fe_2O_3	Ni	NiO	Cu	Cu_2O	Al	Al_2O_3	Silica particles
ρ [kg/m^3]	7800	5240	8900	6720	8930	6400	2700	3970	2670
$2k_2$	1398.9	—	1571.7	—	1597.7	—	1058.5	—	—
E[GPa]	211		200		130		71	380	94
ν	0.293		0.312		0.343		0.345	0.22	0.3
H [MPa]	820	5246.7	862	6560.9	495	2736.2	260	2088.9	—

And c is the particle concentration by mass $[kg\ m^{-3}]$. The coefficient of restitution was developed elsewhere [6] and is defined as the ratio between the normal component of the particle rebound velocity to that of the impact velocity:

$$e = \frac{1.36\,H^{0.625}}{E_e^{0.5}\,\rho_p^{0.125}\,V_1^{0.25}} \tag{11}$$

Equation (9) is a simple expression for estimating the erosion rates for the oxide or passive layers on a substrate. The equation is valid only for the brittle oxide materials where the deformation even in the oblique impact has an approximate ring shape. The equation is useful for CFD applications since it accounts for the effect of the impact angle in erosion-corrosion evaluation or mapping techniques.

3. Model Validation

To validate equation (9), experimental work in previous investigations was used to test the validity of the model. Oka et al.[7] investigated the erosion of the aluminium oxide scale at various impact angles. Later, Griffin et al.[8] used his experimental results to validate the results of a three dimensional finite element erosion model of alumina scale on MA956 alloy substrate. Figure 1 shows the experimental results of Oka as reported by Griffin and the prediction by equation (9) after multiplying by $[1/(m_P * \rho_f)]$ for unit consistency. The experiment involved the impact of quartz particles with 325 $[\mu m]$ mean diameter and an impact velocity of 100 $[m\ s^{-1}]$ on an Al_2O_3 scale.

The predicted line here is a function of the scale thickness layer and thus the model agrees well with the experimental results. Although this agreement is sufficient for validating the model, the authors consider more validation through a set of experimental work necessary to investigate the effect of the oxide layer thickness on the model application.

It is possible that very different results may be obtained for erosion of passive films of different density. To date, this has not been considered. In addition, the size of the erosion footprint at various impact angles may have a very significant on the erosion process as it dictates the volume of material removed. Hence, future work will concentrate on the verification of this model through a series of laboratory tests and addressing the above issues.

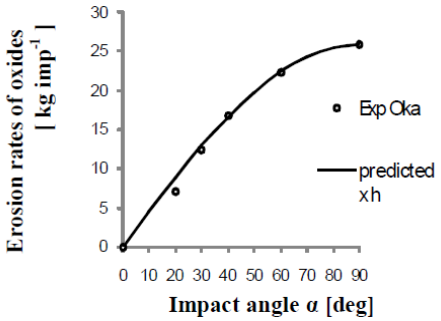

Fig.1: Comparison with the experiment results by Oka et al. [7]

4. Conclusions:

(i) A theoretical model has been presented to predict the erosion rates of the passive film which forms on a material instantaneously during exposure to erosioncorrosion environments.

(ii) The model has potential applications to CFD modeling of erosion-corrosion of materials in aqueous slurries.

(iii) Future direction for the research will involve further validation and testing of the model for various metal oxide systems and at different impact angles.

5. Acknowledgement:

The authors are grateful for the financial support of the Egyptian Government for sponsorship of this PhD.

5. References

[1] Tirupataiah, Y., Venkataraman, B. and Sundararajan, G. (1990) The nature of the elastic rebound of a hard ball impacting on ductile metallic gtarget materials. *Materials Science and Engineering a-Structural Materials Properties Microstructure and Processing*. **124**(2) 133-140.

[2] Roy, M., Ray, K. K. and Sundararajan, G. (1998) An analysis of the transition from metal erosion to oxide erosion. *Wear*. **217**(2) 312-320.

[3] Stack, M. M. and Jana, B. D. (2004) Modelling particulate erosion-corrosion in aqueous slurries: some views on the construction of erosion-corrosion maps for a range of pure metals. *Wear*. **256**(9-10) 986-1004.

[4] Finnie, I. (1960) Erosion of surfaces by solid particles. *Wear*. **3** 87-103.

[5] B.T. Lu, J. L. L. (2008) Correlation between repassivation kinetics and corrosion rate over a passive surface in flowing slurry. *Electrochimica Acta*. **53**(23) 7022-7031.

[6] Stack, M. M., Corlett, N. and Zhou, S. (1998) Some thoughts on the effect of elastic rebounds on the boundaries of the aqueous erosion-corrosion map. *Wear*. **214**(2) 175-185.

[7] Oka, Y. I., Ohnogi, H., Hosokawa, T. and Matsumura, M. (1997) The impact angle dependence of erosion damage caused by solid particle impact. *Wear*. **203** 573-579.

[8] Griffin, D., Daadbin, A. and Datta, S. (2004) The development of a three-dimensional finite element model for solid particle erosion on an alumina scale/MA956 substrate. *Wear*. **256**(9-10) 900-906.

A map and a pipe: a new approach to characterizing erosion-corrosion regimes of Fe in three dimensions using CFD modelling

A map and a pipe: a new approach to characterizing erosion-corrosion regimes of Fe in three dimensions using CFD modelling

M.M. Stack[1], S.M. Abdelrahman[2] and B.D. Jana[3]

University of Strathclyde,
James Weir Building
75 Montrose St.,
Glasgow, G1 1XJ, UK

[1]*Corresponding author*

[1]*University of Strathclyde, UK E-mail: margaret.stack@strath.ac.uk*
[2]*University of Strathclyde, UK, s.m.abdelrahman@strath.ac.uk*
[3]*University of Strathclyde, UK, buddhadev.jana@corusgroup.com*

Abstract

In studies of erosion-corrosion, much work has been carried out in recent years to identify regimes of behaviour. Such regimes describe the transition between the erosion and corrosion dominated mechanisms. They can also be used, by assigning various criteria, to identify other regimes of behaviour such as extent of "synergy/antagonism" in the process, so-called "additive" behaviour and the extent of wastage.

Despite this work, there has been very little effort to combine the concept of the two dimensional erosion-corrosion map with CFD modelling approaches, in which the characteristics of the fluid are accounted for in the regime description. This means that extrapolation of such maps in two dimensions to a three dimensional real surface presents some difficulties. However, it is these surfaces that corrosion engineers are required to tailor, either through modification of the material composition, the surface or the process parameters, for optimum erosion-corrosion resistance.

In this paper, a methodology is generated to combine the concepts of CFD modelling, and the erosion-corrosion regime map for a specific geometry and for pure Fe. The changes in regimes are presented as a function of variation in the erosion and corrosion variables i.e. particle size, hardness and solution pH. Erosion-corrosion regimes are presented based on the model results, showing the wide range of mechanistic and wastage mechanisms possible over the component surface.

Keywords: Erosion-Corrosion, CFD Modelling, Regimes, Maps

1. Introduction

There have been several attempts at characterizing erosion-corrosion interactions reported in the literature in recent years [1-5]. These include theoretical and experimental methodologies to describe the erosion-corrosion interactions. Various regimes descriptions have been employed in order to distinguish between the relative contributions of erosion and corrosion and, whether the effect of corrosion on erosion enhances the overall wastage rate in a so-called "synergistic" manner, or impede it in an antagonistic manner [1-4].

Several recent studies have used CFD (Computational Fluid Dynamics) simulation to predict erosive wear in "real life" components [5]. Other work [6] has used pre-determined experimental data [7] to test the predictions of the latter model for the erosion-corrosion on the inner surfaces of a pipe. A further approach [8, 9] has used CFD to predict wear due to erosion-corrosion on other real-life systems.

In dry conditions, erosion-corrosion simulations were carried out [10] to model the erosion of an alumina oxide scale on an aluminum alloy substrate and to investigate the multiple impacts of particles on a single site. This revealed that the crack formation due to tensile failure and shear stress could be simulated and predicted. A further erosion-corrosion study in aqueous conditions involved a finite difference method [11] to estimate the corrosion rates using knowledge of the concentration of ions in the near wall area. This revealed that changes in oxygen concentration will also increase the pH level and thus the amount of Fe ions released from the pipe surface.

CFD [12] was used to investigate the relationship between shear stress of the oblique impact flow and the dissolution of the aluminium oxide layer. Other work [13] has found experimental agreement with model predictions for erosion-corrosion of 304L steel alloy in aqueous conditions. Hence, there has been significant activity in CFD modelling of erosion-corrosion, both in dry and aqueous conditions in the past five years.

Despite such studies, there has been no work carried out to combine the erosion-corrosion mapping approach with CFD simulations of the wastage process. This paper addresses this issue by combining various erosion models in a CFD analysis with those for aqueous corrosion. Furthermore, these models are incorporated in a simulation of a multiphase flow environment using the Dispersed Particle Method (DPM) techniques for solid particle tracking. The results for "mapping the pipe" present a new technique for characterizing erosion-corrosion on real pipes, thereby introducing an important step-change in the interpretation and use of erosion-corrosion mapping approaches to date.

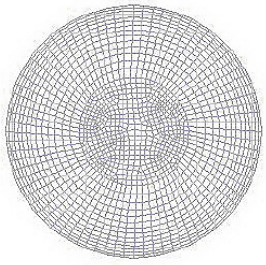

Figure 1: Diagram of front view of mesh generated at inlet of component.

2. Methodology

2.1. Slurry Flow Modelling

The following are the various steps in the model development.

(i) A dilute slurry flow of water-alumina sand particles, of size 10^{-3}[m] and volume fraction of 0.1, was ingested through a pipe bend inlet with bore diameter D equal to 0.078 [m] and $R_c\ D^{-1}$ ratio of 1.2.

(ii) The CFD simulations were generated by FLUENT ver.6.3 [14], which uses a finite element based finite volume method to solve the flow governing equations. Table 1 summarizes the equations and operating and boundary conditions used in this study while table 2 lists the mechanical and physical properties for the slurry and target material. Figure 1 illustrates the mesh at the inlet which was generated and used for the study.

(iii) A structured grid was generated in the near wall region together with a unstructured grid in the bulk flow region. The imbalance between the mass flow rate in the exit boundary compared to that in the inlet was computed (to ensure mass continuity) and found to be 1.144×10^{-5}[kg s^{-1}] which indicates very good accuracy of the simulation.

(iv) To validate the CFD analysis, a comparison with the case study [15] was carried out as shown in table 3. The validation exercise was carried out for SS304L stainless steel alloy using the Forder erosion model [16].

(v) The results in the current work were simulated for mild steel using Sundararajan's second model [17].

Table 1: CFD modelling equations, operating and boundary conditions.

Model parameter	**Water**	**Alumina sand**
Solver equations	Navier-Stokes	DPM
Turbulence	Standard k-ε	
Wall treatment	Standard wall function	
Coupling		Two-way coupling
Operating conditions	Ambient	
Inlet velocity [m s^{-1}]	3.0	3.0

Table 2: Physical and mechanical properties for the slurry and target material.

Model parameter	**Fluid (Water)**	**Sand (alumina)**	**Target (mild steel)**
Density [kg m^{-3}]	998	2650	7850
Particle size [m]		10^{-3}	
Mass flow rate [kg s^{-1}]	14.3	3.827	

Table 3: Comaparison between the current study and experimental and simulation of other workers [15]

Model parameter	**Experimental [15]**	**Simulation [15]**	**Current study (SS304L)**
Erosion rates [μm^3 $impact^{-1}$]	2.2-5.5	5.5	5.48

2.2. Erosion models

As stated above, the models used include that of Forder's erosion model [16] given as:

where

$$\dot{W} = \frac{100 r_p^3}{2\sqrt{29}} \left(\frac{V_p}{C_k} \right)^{n_f} \sin(2\alpha) \sqrt{\sin\alpha} + \frac{m_p}{2E_f} \left(V \sin\alpha - D_k \right)^2 \tag{1}$$

and

$$C_k = \sqrt{3\sigma \frac{R_f^{0.6}}{\rho_p}} \tag{2}$$

$$D_k = \frac{\pi^2}{2\sqrt{10}} \left(1.59Y \right)^{2.5} \left(\frac{R_f}{\rho_t} \right)^{0.5} \left[\frac{\left(1-\nu_p^2\right)}{E_t} + \frac{\left(1-\nu_t^2\right)}{E_p} \right]^2 \tag{3}$$

The second model of Sundararajan [17] is divided into two expressions, one for localised deformation at the impact point, while the other accounts for the ductile cutting mechanism during the impact [17] i.e.

$$Er_{def} = \frac{5.5\times10^{-2}}{\left(T_m - 436\right)^{0.75}} \frac{2^{n_c} f_t V^2 \sin^2\alpha \left(1-e_n^{\,2}\right)}{n_c C_p} \tag{4}$$

$$Er_{cut} = \frac{5.5\times10^{-2}}{\left(T_m - 436\right)^{0.75}} \frac{\left(n_c+1\right)\left(\frac{\mu_f}{\mu_{fc}}\right)\left(2-\frac{\mu_f}{\mu_{fc}}\right) V^2 \cos^2\alpha}{\left(1+\lambda\right) 2^{(2-n_c)}\, n_c\, C_p} \tag{5}$$

where:

$$\mu_{fc} = \frac{1}{\left(1+\lambda\right)\left(1+e_n\right)\tan\alpha} \tag{6}$$

The coefficient of restitution *e* can be estimated either by relating the energy dissipated during the impact with the mechanical properties of the target and impact velocity [18]. This is valid only for normal impact.

$$e_n = \frac{1.36\, H_s^{0.625}}{E_e^{0.5}\, \rho_p^{0.125}\, V^{0.25}} \tag{7}$$

or it can be related to the impact angle through a semi-empirical relation [16]:

$$e_n = 0.988 - 0.78\alpha + 0.19\alpha^2 - 0.024\alpha^3 + 0.027\alpha^4 \quad (8)$$

$$e_t = 1.0 - 0.78\alpha + 0.84\alpha^2 - 0.21\alpha^3 + 0.028\alpha^4 - 0.022\alpha^5 \quad (9)$$

For consistency with corrosion rate calculations, erosion rates are converted to [kg m^{-2} s^{-1}].

2.3. Corrosion models

2.3.1. Active corrosion model

Assuming that the corrosion reaction is activation controlled, the dissolution current density is given by the Butler-Volmer equation [19]:

$$i = i_o \left[\exp\left(\frac{2.303\,\Delta E}{b_a} \right) - \exp\left(\frac{-2.303\,\Delta E}{b_c} \right) \right] \quad (10)$$

where the over-potential is defined as:

$$\Delta E = E_{ap} - E_{rev} \quad (11)$$

the corrosion rate is therefore given by

$$K_c = \frac{M_{Fe}\, i}{z_m\, F} \quad (12)$$

2.3.2. Repassivation model

An expression for the corrosion rate under passivation condition has been introduced [20] and is currently modified to include the effect of the oblique impact [21].

$$M_t = \pi k_2\, h\, \rho_f d_p^2 \left[\frac{\rho_p \left(1 - e^2\right)}{6H_s} \right]^{0.5} \left(V \sin\alpha \right) \quad (13)$$

where h can be assumed to be related to the over-potential of the passivation [22]:

$$h = h_o + 3\times10^{-9} \left(E_{ap} - E_{pas} \right) \quad (14)$$

2.3.3. Determination of passivation potential on the simplified Pourbaix diagram [23]

Figure 2 shows the Pourbaix diagram for pure Fe. The passivation potential E_{pas} can be determined from the intersection of the operating pH with the line representing the following precipitation electrochemical reaction

$$2Fe + 3H_2O \rightarrow Fe_2O_3 + 6H^+ + 6e^- \quad (15)$$

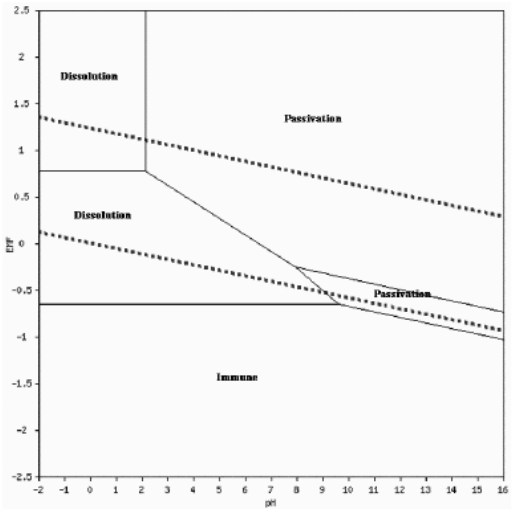

Figure 2: Pourbaix diagram for Fe.

The equation of this line can be given at 298 [K] by [24].

$$E_{pas} = 1.08 - 0.177\,pH - 0.245 \quad (16)$$

The passivation potential is expressed in [V] with respect to standard calomel electrode (SCE).

2.4. Erosion-corrosion mapping

The total wear can be estimated as the sum of the erosion and corrosion rates i.e.

$$K_t = K_e + K_c \quad (17)$$

where

$$K_e = K_{eo} + \Delta K_e \quad (18)$$

and

$$K_c = K_{co} + \Delta K_c \quad (19)$$

In the active region, the erosion enhanced corrosion ΔK_c and corrosion enhanced erosion ΔK_e are neglected while in passive region, the pure corrosion is much lower than the erosion enhanced corrosion. Hence, in the active region, the total wear is given by:

$$K_t = K_{eo} + K_{co} \quad (20)$$

and in passive region

$$K_t = K_{eo} + \Delta K_c \quad (21)$$

The regime boundaries needed for constructing the regime maps on the interior surfaces of the pipe are defined by the ratio K_c/K_e and are used to determine the transition regimes at a given applied pH and applied potential.

$$\frac{K_c}{K_e} < 0.1 \quad \text{(Erosion dominated)} \quad (17)$$

$$0.1 \le \frac{K_c}{K_e} < 1 \quad \text{(Erosion-Corrosion dominated)} \quad (18)$$

$$1 \le \frac{K_c}{K_e} < 10 \quad \text{(Corrosion-Erosion dominated)} \quad (19)$$

$$\frac{K_c}{K_e} \ge 10 \quad \text{(Corrosion- dominated)} \quad (20)$$

The wastage maps boundaries are set to give the transition regions between low, medium and high wastage. These are set as low wastage i.e. less or equal to 1 [mm year^{-1}], medium wastage ie. between 1-10 [mm year^{-1}] and high wastage i.e. greater or equal to 10 [mm year^{-1}]. (Units are converted from [kg m^{-2}s^{-1}] to [mm year^{-1}] in the model).

3. Results

The simulation commenced by using a single phase CFD run using FLUENT software and then injecting the particles uniformly at the inlet by using DPM method. A sample of 1655 particles of 10^{-3} [m] diameter was injected. Each impact with the walls of the pipe triggers a UDF (User Defined Function) to calculate the erosion and corrosion rates. All figures incorporate a blue area

indicating that there was no erosion occurring on this section of the component in order to distinguish it from the areas of the component where impacts are observed.

3.1. Effect of pH on the erosion-corrosion map

The results, Fig. 3, showed that at pH 5 and 7, the erosion-corrosion regime pattern for Fe consisted mainly of dissolution and dissolution – erosion dominated behaviour. However, at pH 9, there was a change in the pattern of wastage, with the predominant erosion-corrosion regime for the component being erosion-passivation. This can be compared to the Pourbaix diagram for Fe, Fig. 2, with Fe passivating at high pH values.

3.2. Effect of applied potential on the erosion-corrosion transition boundaries.

Changes in applied potential in the positive direction, Fig. 4 (a-b), from -0.75 V (SCE), to -0.5 V (SCE), indicated there was very little evidence of corrosion affecting the process at the lower potentials. Increase in applied potential, to -0.5 V (SCE) however, effected a significant change in the erosion-corrosion regime, with the component now being dominated by dissolution. At the higher potentials, by contrast, the erosion-corrosion regime was mainly erosion-passivation, Fig.4 (c)

3.3. Wastage maps generated by simulation results at various pH values

The wastage maps, Fig. 5(a-b), indicated, consistent with the regime maps, Fig. 3(a-b), that there were similar wastage regimes predominating at pH 5 and 7. The high wastage rates over the component were attributed to the dissolution dominated regime which predominated. At higher pH values, Fig. 5 (c), at pH 9, there was a change in wastage mechanism with the high wastage regime mainly predominating over the middle of the component where a very high impact frequency is encountered.

4. Discussion

It is clear from the results that the stability regimes for Fe as identified on the Pourbaix diagrams, Fig. 2, determine the erosion-corrosion regimes, Fig. 3-5. The change in regime from dissolution affected behaviour at pH 5 and 7 to in turn passivation affected behaviour at pH 9, is consistent with the changes in the corrosion stability region on the Pourbaix diagram, Fig. 2. Moreover, the variation in distribution of particle impacts and velocities over the surface also have an effect on the erosion-corrosion regime, particularly in the passive region of the Pourbaix diagram, where particle repassivation rates between impacts will result in high wastage rates, Fig. 3(c), Fig. 4(c).

The change in electrochemical potential in the positive direction, Fig. 4, shows significant shifts in the erosion-corrosion regimes over the surface. Increases in the potential in a positive direction can modify the corrosion regime and in so doing change the erosion response as, in the passive region, this will be greater than in the active region due to re-passivation, as indicated above.

For the purpose of the model, a blue area has been incorporated to distinguish the location of the component where no erosion is taking place. Depending on the corrosion conditions, this may be subject to corrosion. However, in this work, it was though important to highlight this region independently in the CFD simulation.

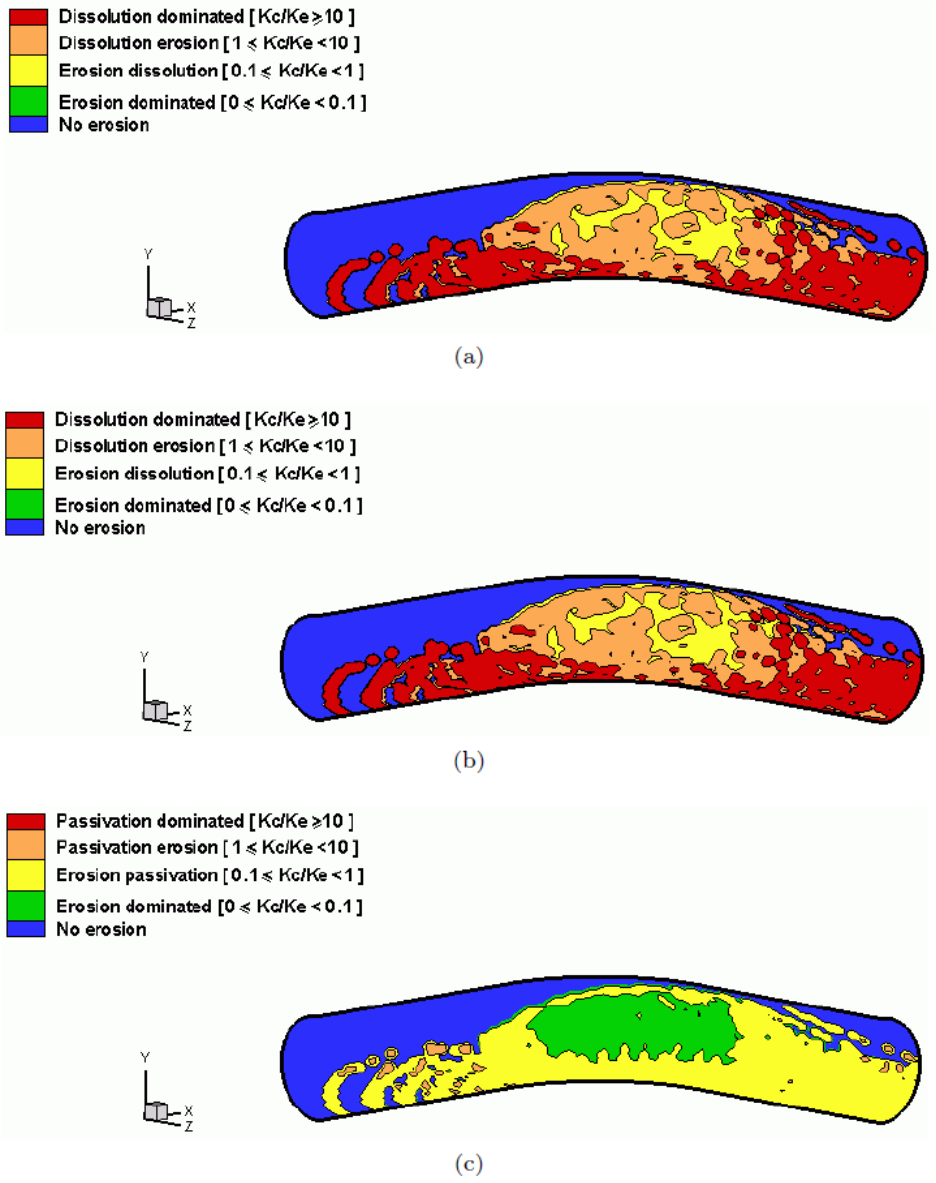

Figure 3: Erosion-corrosion maps for Fe component at V= -0.6 V [SCE] and pH: (a) 5 (b) 7 (c) 9.

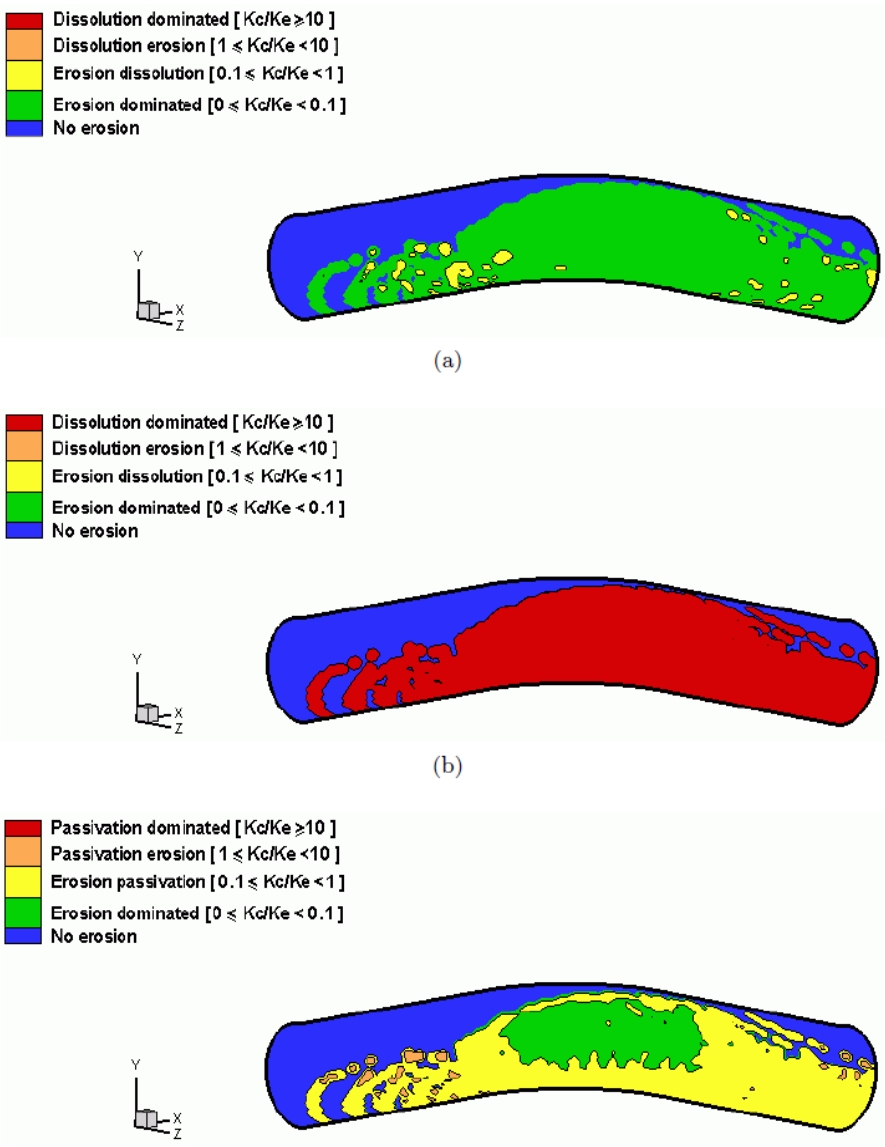

Figure 4: Erosion-corrosion maps for Fe component at pH = 7 and applied potential [V][SCE]: (a) -0.75 (b) -0.5 (c) -0.25.

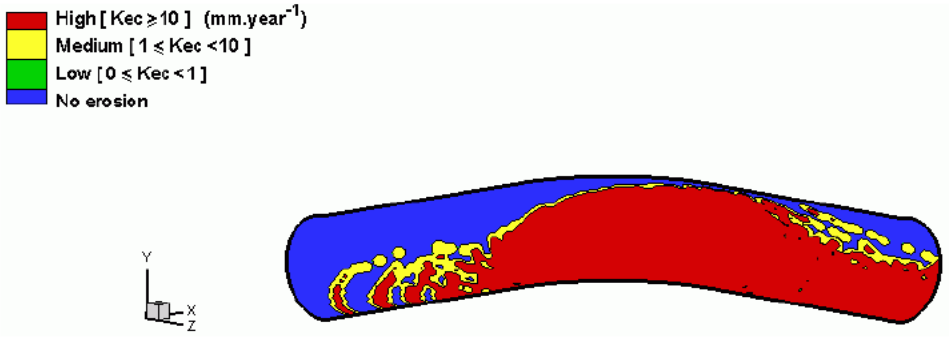

(a)

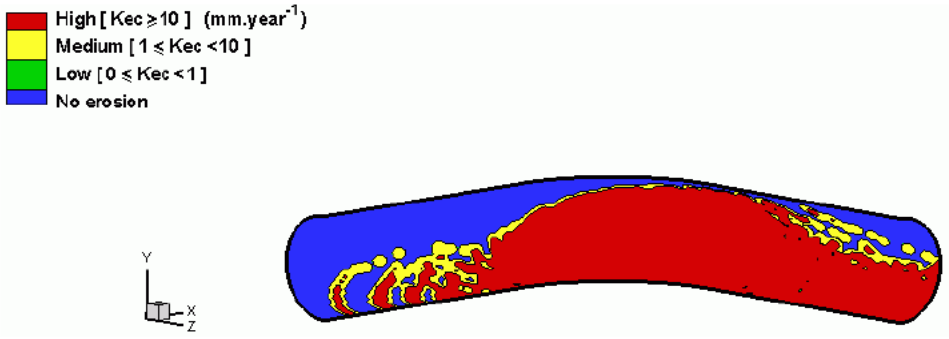

(b)

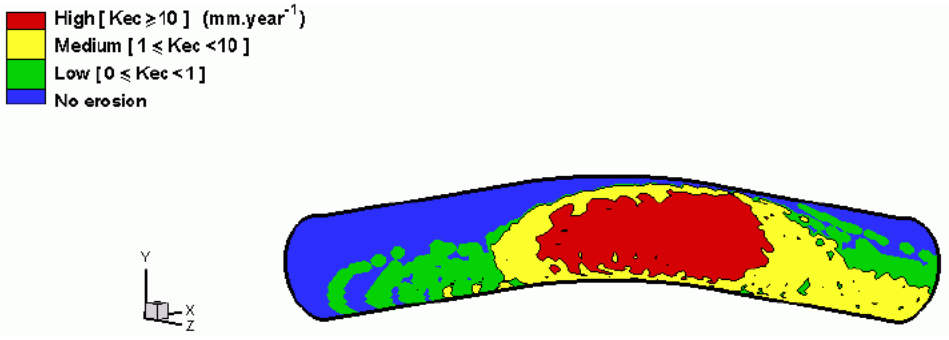

(c)

Figure 5: Wastage maps for Fe component at V= -0.6 V[SCE] and pH: (a) 5 (b) 7 (c) 9.

Various developments in mapping methodologies in two dimensions [24-28] have concentrated on assessing the changes in erosion-corrosion regime according to the position on the galvanic series, and considering the erosion-corrosion regimes for composite materials where synergistic erosion-corrosion effects may be high. Other work has assessed the effect of oxygen concentration on the erosion-corrosion behaviour [29]. At present the effect of corrosion on the mechanical properties of the material is not considered for simplicity in the existing model although it is acknowledged that this may be a very significant in the overall wastage rate. Further work will be to consider these factors in the three dimensional CFD simulations.

Hence, the results indicate that it is possible to superimpose erosion-corrosion regimes on three dimensional component surfaces such as pipes. This is a new development in research in erosion-corrosion mapping and three dimensional modelling should enable more precise prediction of erosion-corrosion rates according to various geometries. Many important applications of this approach are envisaged over the wider tribo-corrosion area.

5. Conclusions

(i)A method to superimpose the erosion-corrosion maps on the surfaces of Fe components has been developed using CFD analysis.

(ii)The results have shown that it is possible to identify erosion-corrosion regimes in 3-dimensional applications.

(iii) Such a technique offers great promise in transferring the existing tribo-corrosion mapping methodologies to many other processes where tribology interacts with corrosion.

6. References

[1] Stack, M. M., Corlett, N. and Zhou, S. (1997) A methodology for the construction of the erosion-corrosion map in aqueous environments. *Wear*. **203** 474-488.

[2] Stack, M. M. and Pungwiwat, N. (2002) Particulate erosion-corrosion of Al in aqueous conditions: some perspectives on pH effects on the erosion-corrosion map. *Tribology International*. **35** 651-660.

[3] Jana, B. D. and Stack, M. M. (2005) Modelling impact angle effects on erosion-corrosion of pure metals: Construction of materials performance maps. *Wear*. **259**(1-6) 243-255.

[4] Stack, M. M. and Abd El Badia, T. M. (2006) On the construction of erosion-corrosion maps for WC/Co-Cr-based coatings in aqueous conditions. *Wear*. **261**(11-12) 1181-1190.

[5] Keating, A. and Nesic, S. (1999) Prediction of Two-phase Erosion-corrosion in Bends. Second International Conference on CFD in the Minerals and Process Industries, CSIRO pp. 229-236.

[6] Davis, C. and Frawley, P. (2009) Modelling of erosion-corrosion in practical geometries. *Corrosion Science*. **51**(4) 769-775.

[7] Founti, M. and Klipfel, A. (1998) Experimental and computational investigations of nearly dense two-phase sudden expansion flows. *Experimental Thermal and Fluid Science*. **17**(1-2) 27-36.

[8] Ferng, Y. M., Ma, Y. P., Ma, K. T. and Chung, N. M. (1999) A new approach for investigation of erosion-corrosion using local flow models. *Corrosion*. **55**(4) 332-342.

[9] Ferng, Y. M., Ma, Y. P. and Chung, N. M. (2000) Application of local flow models in predicting distributions of erosion-corrosion locations. *Corrosion*. **56**(2) 116-126.

[10] Griffin, D., Daadbin, A. and Datta, S. (2004) The development of a three-dimensional finite element model for solid particle erosion on an alumina scale/MA956 substrate. *Wear*. **256**(9-10) 900-906.

[11] Naser, G. and Karney, B. (2007) A 2-d transient multicomponent simulation model: Application to pipe wall corrosion. *Journal of Hydro-Environment Research*. **1** 56-69.

[12] Xu, L. Y. and Cheng, Y. F. (2008) Electrochemical characterization and CFD simulation of flow-assisted corrosion of aluminum alloy in ethylene glycol-water solution. *Corrosion Science*. **50**(7) 2094-2100.

[13] Wood, R. J. K., Jones, T. F., Ganeshalingam, J. and Miles, N. J. (2004) Comparison of predicted and experimental erosion estimates in slurry ducts. *Wear*. **256**(9-10) 937-947.

[14] FLUENT, I. (2006) Ttile., Lebanon, NH, USA.

[15] Wood, R. J. K. and Jones, T. F. (2003) Investigations of sand-water induced erosive wear of AISI 304L stainless steel pipes by pilot-scale and laboratory-scale testing. *Wear*. **255** 206-218.

[16] Forder, A., Thew, M. and Harrison, D. (1998) A numerical investigation of solid particle erosion experienced within oilfield control valves. *Wear*. **216**(2) 184-193.

[17] Sundararajan, G. (1991)A comprehensive model for the solid particle erosion of ductile materials, *Wear*. **149**(1-2) 111-127.

[18] Stack, M. M., Corlett, N. and Zhou, S. (1998) Some thoughts on the effect of elastic rebounds on the boundaries of the aqueous erosion-corrosion map. *Wear*. **214**(2) 175-185.

[19] Marcus, P. (2002) Corrosion Mechanisms in Theory and Practice Marcel Dekker, Inc., New York.

[20] Stack, M. M., Corlett, N. and Zhou, S. (1996) Construction of erosion-corrosion maps for erosion in aqueous slurries. *Materials Science and Technology*. **12**(8) 662-672.

[21] Abdelrahman, S. M. and Stack, M. M. (2009) Some reflections on a model to predict the erosion rate of the passive film on pure materials. Thirteenth International Conference on Aerospace Science and Aviation Technology, ASAT pp. In press.

[22] Graham, M. J., Bardwell, J. A., Sproule, G. I., Mitchell, D. F. and Macdougall, B. R. (1993), The growth and stability of passive films. *Corrosion Science*. **35**(1-4) 13-18.

[23] Pourbaix, M. (1966) Atlas of Electrochemical Equilibria in Aqueous Solutions Pergamon Press, Oxford, New York.

[24] Stack, M. M. and Jana, B. D. (2004) Modelling particulate erosion-corrosion in aqueous slurries: some views on the construction of erosion-corrosion maps for a range of pure metals. *Wear*. **256**(9-10) 986-1004.

[25] Stack, M. M. and Bray, L. (1995) Interpretation of wastage mechanisms of materials exposed to elevated temperature erosion using erosion-corrosion maps and computer graphics, *Wear*. **186**(1) 273-283.

[26] Stack, M. M., Corlett, N. and Turgoose, S. (1999) Some recent advances in the development of theoretical approaches for the construction of erosion-corrosion maps in aqueous conditions. *Wear*. **233** 535-541.

[27] Stack, M. M. and El-Badia, T. M. A. (2008) Some comments on mapping the combined effects of slurry concentration, impact velocity and electrochemical potential on the erosion-corrosion of WC/Co-Cr coatings. *Wear*. **264**(9-10) 826-837.

[28] Stack, M. M., Antonov, M. M. and Hussainova, I. (2006) Some views on the erosion-corrosion response of bulk chromium carbide based cermets. *Journal of Physics D-Applied Physics*. **39**(15) 3165-3174.

[29] Liu, J. J., Lin, Y. Z. and Li, X. Y. (2008) Numerical simulation for carbon steel flow-induced corrosion in hiqh-velocity flow seawater. *Anti-Corrosion Methods and Materials*. **55**(2) 66-72.

Appendix1. Nomenclature

b_a Anodic Tafel slope. [V decade^{-1}] (0.05)
b_c Cathodic Tafel slope. [V decade^{-1}] (0.05)
C_k Cutting characteristic velocity. [m s^{-1}]
C_p Specific heat capacity. [J kg^{-1} K^{-1}] (439)
c_p Particle concentration. [kg m^{-3}]
D Diameter of a pipe bore. [m]
D_k Deformation characteristic velocity. [m s^{-1}]
d_p Particle diameter. [m] (0.001)
ΔE Over potential. [V]
E_{ap} Applied potential. [V]
E_e Elastic modulus of collision. [Pa]
E_f Deformation erosion factor. [J m^{-3}] (1.9×10^{10})
e_n normal coefficient of restitution
E_p Particle Young's modulus. [Pa] (94×10^9)
E_{pas} Passivation potential. [V]
Er_{cut} Cutting Erosion rate. [dimensionless]
Er_d Plastic deformation erosion rate. [dimensionless]
E_{rev} Reversible equilibrium potential. [V] (-0.44)
E_t Target Young's modulus. [Pa] (211×10^9)
e_t tangential coefficient of restitution.
F Faraday number. [C mol^{-1}] (96485)
f_t Numerical constant. (0.025)
h Oxide layer thickness. [m]
h_o Thickness of passive layer at passive potential. [m](10^{-9})
H_s Hardness of material. [Pa](8.2×10^8)
i Dissolution current density. [A m^{-2}]
i_o Exchange current density. [A m^{-2}] (10^{-8})
k_2 Material constant. (699.9) [24]
K_c Corrosion rate. [kg m^{-2} s^{-1}]
ΔK_c Additive effect of erosion influencing the corrosion rate. [k gm^{-2}s^{-1}]
K_{co} Pure corrosion rate. [kg m^{-2}s^{-1}]
ΔK_e Synergistic effect of corrosion influencing the erosion rate. [kg m^{-2}s^{-1}]
K_{eo} Pure erosion rate. [kg m^{-2}s^{-1}]
K_t Total wear. [kg m^{-2}s^{-1}]
M_{Fe} Relative atomic mass for Fe. [kg] (0.05585)
m_p Particle mass. [kg]
n_c Strain hardening coefficient. (0.3)
n_f Velocity ratio exponent. (2.54)
R_c Radius of the curvature of a pipe. [m]
R_f Roundness factor for the particle. (0.5)
r_p Particle radius. [m] (0.0005)
T_m Target material melting temperature. [K] (1808)
V_p Particle impact velocity. [m s^{-1}]
Y Yield stress of the target material. [Pa] (3.2×10^8)
z_m Number of electrons involved in the dissolution reaction. (2)
α Particle impact angle. [rad]
λ Particle shape factor. (0.0 for point mass)
μ_f Coefficient of friction. (0.3)
μ_{fc} Critical coefficient of friction.

v_p Particle Poisson ratio. (0. 3)
v_t Target Poisson ratio. (0.293)
ρ_f Density of oxide layer. [kg m^{-3}] (5240)
ρ_p Density of the particle. [kg m^{-3}] (2650)
ρ_t Density of target. [kg m^{-3}] (7850)
σ Plastic flow stress of the target material. [Pa] (1×10^9)

CFD modelling of erosion-corrosion of steel in aqueous environments - particle concentration effects on the regime boundaries

CFD Modelling of Erosion-corrosion of Steels in Aqueous Environments: Particle Concentration Effects on the Regime Boundaries.

M. M. Stack[*] and S. M. Abdelrahman

University of Strathclyde,

Department of Mechanical Engineering
75 Montrose Street,
Glasgow, G1 1XJ, UK.

[*]Corresponding author: margaret.stack@strath.ac.uk

Abstract:

In this study, a new methodology is used to model the effects of particle concentration on the inner surfaces of a circular pipe 90^o bend, assuming applied potential controlled aqueous slurry flow at room temperature. This enables the regimes of the component to be mapped according to the intensity of erosion and corrosion contributions. The results show that for a constant inlet particle concentration, it is shown how transitions between erosion-corrosion regimes are observed around the pipe For increases in particle concentration, significant variation of the erosion-corrosion regimes are observed, with a reduction of the corrosion dominated regime. geometry. The results are interpreted in the terms of the changes in local erosion conditions along the component in the flowing environments. Typical results from the model are shown illustrating how this new mapping method can be used effectively to optimize process conditions and materials in such environments.

Key words: Erosion-Corrosion maps, CFD Modelling, mild steel.

1. NOTATION AND UNITS

Latin letters:

A_{in}	Pipe inlet area.	$[m^2]$
c	Particle concentration	$[g\ cm^{-3}]$
C_p	Specific heat capacity	$[J\ kg^{-1}\ K^{-1}]$
d	Diameter of the pipe.	$[m]$
E	Applied potential.	$[V]$ (SCE)
e_n	Normal coeff. of restitution.	
F	Faraday constant. (96485)	$[C\ mol^{-1}]$
f_t	Numerical constant. (0.025)	
H_s	Hardness of the substrate.	$[Pa]$
h	Thickness of the oxide layer.	$[m]$
h_o	Initial thickness of the oxide.	$[m]$
I_p	Impact frequency.	$[imp\ cm^{-2}\ s^{-1}]$
i_{anet}	Net anodic current density.	$[A\ m^{-2}]$
i_o	Exchange current density.	$[A\ m^{-2}]$
K_c	Pure corrosion rate.	$[g\ m^{-2}\ s^{-1}]$
K_{ec}	Total wastage rate.	$[g\ m^{-2}\ s^{-1}]$

K_e	Pure erosion rate.		$[g\ m^{-2}\ s^{-1}]$
k	Material constant.	(0.699)	
k_2	Material constant.	(1.398)	
M_t	Amount of mass removal per impact.		$[g\ impact^{-1}]$
m_p	Mass of impacting particle.		$[kg]$
n_c	Strain hardening coefficient.	(0.3)	
RAM	Relative atomic mass of Fe.	(55.8)	$[g\ mol^{-1}]$
T_m	Melting point of the Fe.	(1808)	$[K]$
V_p	Particle velocity.		$[m\ s^{-1}]$
v_f	Volume fraction of particles		
W_C	Erosion by cutting.		$[kg\ kg^{-1}]$
W_D	Erosion by deformation.		$[kg\ kg^{-1}]$
z_m	Number of electrons.	(2)	

Greek letters:

α_p	impact angle		$[deg]$
λ	Particle shape factor	(0.0)	
μ	Frictional coefficient	(0.1)	
μ_f	Critical friction coefficient (Sundararajan)		
π	Pi ratio	(3.142)	
ρ_f	Density of the oxide layer.	(5240)	$[kg\ m^{-3}]$
ρ_p	Density of the particle	(2650)	$[kg\ m^{-3}]$

Subscripts:

ap	Applied potential.
rev	Reversible equilibrium potential.

2. INTRODUCTION

In studies of modelling erosion-corrosion, both finite element (FE) [1] and computational fluid dynamics (CFD) [2-4] techniques have been used to investigate mass loss of materials and to evaluate the effect of various parameters controlling the erosion and corrosion process. However, the majority of these investigations do not introduce a full definition for erosion-corrosion regimes resulting from the interaction between erosion and corrosion. These regimes are very useful in identifying the synergistic, additive, and antagonistic behaviour of this phenomenon in addition to identifying the mechanism of degradation [5].

An approach to identify the transition regimes for the erosion-corrosion process and also to monitor the effects of various parameters was developed by Stack et al. [5] as an extension of earlier work on erosion-corrosion mapping [6-8]. Although 2D mapping is capable of capturing the influence of any particular parameter on erosion-corrosion regime boundaries, it does not give any indication of the combined effect of all the parameters on these boundaries, nor the metal degradation in a 3D space.

A new methodology was introduced in previous work [9] to study the integrated effect of these parameters together (namely those related to the particle, fluid flow, and environment), on the boundaries of the erosion-corrosion regime and wastage maps by combining the concept of CFD with the erosion-corrosion mapping techniques. Such approach enables us to map the surfaces of any 3D component that are exposed to aqueous slurry flow. Furthermore, it provides a powerful predictive tool for estimating the predominance of various erosion-corrosion regimes.

In this study, a 3D mapping technique is used to investigate the effect of the particle concentration and on the construction of erosion-corrosion mechanism and wastage maps. The effects of particle concentration are evaluated on the regime boundaries. The results are discussed in terms of the applications of this technique to erosion-corrosion in slurry flows in addition to addressing some current limitations.

3. METHODOLOGY

A dilute slurry flow of water-alumina particles of size $10^{-3}[m]$ and four volume fractions i.e. 0.025, 0.05, 0.075, and 0.1 is ingested through a pipe bend inlet with bore diameter (D) equal to 0.078 $[m]$ and ($R\ D^{-1}$) ratio of 1.2.

The CFD simulation generated by FLUENT ver.6.3 [10] uses a finite element based finite volume method to solve the flow governing equations. Table 1 summarizes the equations used, operating and boundary conditions used in this study while Table 2 lists the mechanical and physical properties for the slurry and target material.

Validation of the erosion results is carried out in [9] by comparison to previous experimental work

as described elsewhere [11], and is summarised in Table 3. The simulation validation was carried out for a SS304L stainless steel alloy using Forder's erosion model [12] as in the case study, and the results were simulated for mild steel using Sundararajan's second model [13].

Table 1. CFD modeling equations, operating and boundary conditions

Model parameter	Water	Sand Particles
Solver equations	Navier-Stokes	DPM
Turbulence model	Standard *k-ε*	
Wall treatment	Standard wall function- no slip	
Coupling		One way
Operating cond.	ambient	
Inlet velocity [$m\ s^{-1}$]	3.0	3.0

Table 2. Physical and mechanical properties for the slurry and target material

	Fluid (water)	Particles (alumina)	Target (mild steel)
density [$kg\ m^{-3}$]	998	2670	7850
particle size [m]		10^{-3}	
Flow rate [$kg\ s^{-1}$]	14.3	variable	
k_2 [14]			1.398

Table 3. Comparison between the current study and Experimental and simulation work of Wood et al. [11]

	Experimental [11]	Simulation [11]	current study
Erosion rates [$mm^3\ imp^{-1}$]	2.2-5.5	5.5	5.45

3.1. Erosion modelling

The second model of Sundararajan is divided into two expressions; one accounts for the localised deformation at the impact point, whilst the other addresses the ductile cutting mechanism during the impact. The total erosion rate is the summation of these two mechanisms. The formulation is as follows [13]:

$$\dot{W}_D = \frac{5.5\times10^{-2}}{(T_m - 436)^{0.75}} \frac{2^{n_c} \bar{f}_t V^2 \sin^2\alpha\,(1-e_n{}^2)}{n_c C_p} \quad (1)$$

$$\dot{W}_C = \frac{5.5\times10^{-2}}{(T_m - 436)^{0.75}} \frac{(n_c+1)\left(\frac{\mu}{\mu_f}\right)\left(2-\frac{\mu}{\mu_f}\right) V^2 \cos^2\alpha}{(1+\lambda)\,2^{2-n_c}\, n_c\, C_p} \quad (2)$$

where

$$\mu_f = \frac{1}{(1+\lambda)(1+e)\tan\alpha} \quad (3)$$

and e_n is the normal restitution ratio [12] :

$$e_n = 0.988 - 0.78\alpha + 0.19\alpha^2 - 0.024\alpha^3 + 0.027\alpha^4 \quad (4)$$

For unit consistency, erosion rates should be converted to [$kg\ m^{-2}\ s^{-1}$] in line with the calculated corrosion rates below.

3.2. Corrosion rates

3.2.1. Active corrosion model

In the active region, it is assumed that the total corrosion is estimated from knowledge of the dissolution current density from the Butler-Volmer equation:

$$i_{anet} = i_o \left[\exp\left(\frac{\beta\, z_m\, Fr\, \Delta E}{R_o\, T}\right) - \exp\left(\frac{-(1-\beta)\, z_m\, Fr\, \Delta E}{R_o\, T}\right) \right] \quad (5)$$

where the over-potential ΔE is defined as:

$$\Delta E = E_{ap} - E_{rev} \quad (6)$$

The corrosion rate is therefore given by:

$$K_c = K_{co} = \frac{RAM\ i_{anet}}{z_m\ F} \quad (7)$$

3.2.2. Repassivation model

For the passivation mechanism, we assume that pure corrosion (K_{co}) rate is sufficiently low as to be negligible and the corrosion rate is the additive effect of corrosion enhanced by erosion (ΔK_c) [14]. An expression for the corrosion rate in passivation conditions has been introduced [5] and is currently modified to include the effect of the oblique impact [9, 15].

$$M_t = \pi k\ h\ \rho_f d_p^2 \left[\frac{\rho_p \left(1-e_n^{\ 2}\right)}{6H_s}\right]^{0.5} \left(V_p \sin\alpha_1\right) \quad (8)$$

The constant k is defined as the mass ratio between the metal and the oxide created during the corrosion reaction, multiplied by the number of moles of metal involved in the reaction and is related to k_2 in [14] by definition as ($k = k_2/2$). The thickness of the passive layer h can be assumed to vary with the potential difference and may be given from [16] assuming a linear relationship between the over-potential and passive layer thickness:

$$h = h_o + 3\times10^{-9}\left(E_{ap} - E_{pas}\right) \quad (9)$$

and: h_o=1×10^{-9} [m].

The unit given by equation (8) is [$kg\ impact^{-1}$]. To convert to [$kg\ m^{-2}\ s^{-1}$], it is multiplied by particle impact flux as outlined in [14]. This can be varied according to the application under investigation. For example, if the flow is homogeneous then particle impact frequency may be used and is given as [17]:

$$K_c = \Delta K_c = \frac{M_t\ c\ V_p \sin\alpha}{m_p} \quad (10)$$

3.2.3. Erosion-corrosion boundaries

The regime boundaries are determined in terms of the ratio K_c/K_e as

$$\frac{K_c}{K_e} < 0.1 \quad \text{(Erosion dominated)} \quad (11)$$

$$0.1 \le \frac{K_c}{K_e} < 1 \quad \text{(Erosion-Corrosion dominated)} \quad (12)$$

$$1 \le \frac{K_c}{K_e} < 10 \quad \text{(Corrosion-Erosion dominated)} \quad (13)$$

$$\frac{K_c}{K_e} \ge 10 \quad \text{(Corrosion- dominated)} \quad (14)$$

The transition boundaries for the wastage maps are given as follows:

$$K_{ec} < 1 \ \ [mm\ year^{-1}] \quad \text{(low wastage)} \quad (15)$$

$$1 \le K_{ec} < 10 \ \ [mm\ year^{-1}] \quad \text{(medium wastage)} \quad (16)$$

$$K_{ec} \ge 10 \ [mm\ year^{-1}] \quad \text{(high wastage)} \quad (17)$$

4. RESULTS

Figure 1 illustrates the Pourbaix diagram for Fe at $T=298$ [K] and identifies the possible corrosion mechanisms (i.e. immunity, dissolution and passivation mechanisms) for various values of temperature, pH and applied potential.

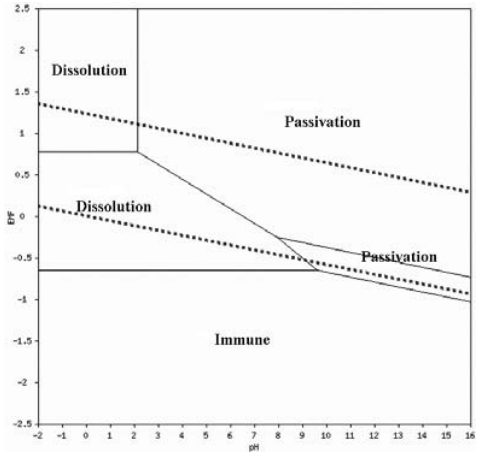

Figure 1: Simplified Pourbaix diagram for Fe at T=298 [K].

To investigate the particle concentration effect, a homogeneous particle distribution in the pipe inlet is assumed and the particle concentration is thus related to the particle mass flow rate according to the relation:

$$\dot{m}_p = \alpha_p \ \rho_p V_p \ A_{in} \qquad (18)$$

The simulation was thus run at various particle mass flow rates; namely 0.957, 1.9169, 2.87 and 3.8276 [$kg\ s^{-1}$] which are equivalent to particle inlet volume fractions of 0.025, 0.05, 0.075 and 0.0909 respectively.

Figure 2 shows the regime maps at the inner surfaces of the pipe bend at pH=7 and applied potential E=-0.6 [V] (SCE), illustrating the changes in erosion-corrosion regimes with increasing the particle volume fraction. As the particle volume fraction increases, the erosion rates increases linearly and as a result, the erosion-dissolution and erosion dominated regimes are enlarged. In addition, the dissolution dominated regime reduces with increasing particle volume fraction. This indicates the importance of the volume fraction (or particle concentration) as a factor affecting the erosion-corrosion regimes.

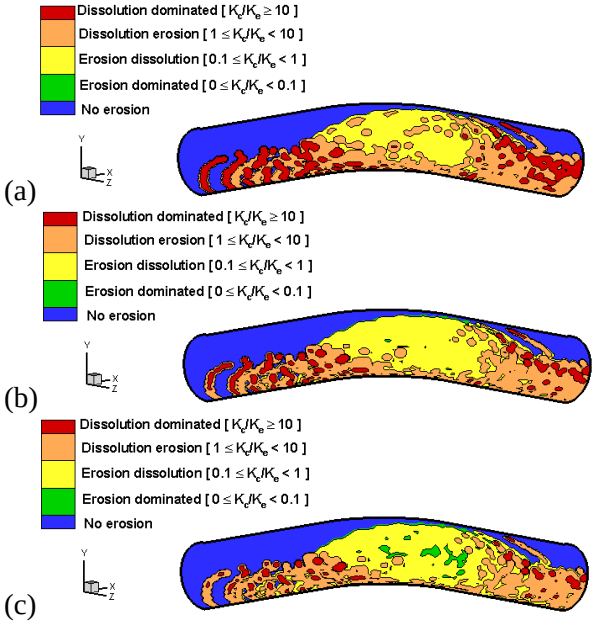

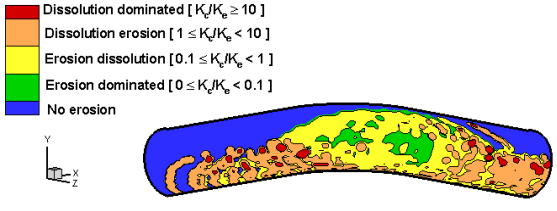

Figure 2: Regime maps on the outer surface of Fe pipe bend at pH=7 and E= -0.6 [V] (SCE) for particle mass flow rates: (a) 0.957 (b) 1.9169 (c) 2.87 (d) 3.8276 [kg s^{-1}].

Figure 3 illustrates the wastage maps for pH=7 and at applied potential E=-0.6 [V] (SCE) for the same particle mass flow rates listed above as in figure 2. Again the high wastage regime area (red colour region) is increased as the particle mass flow rate increases.

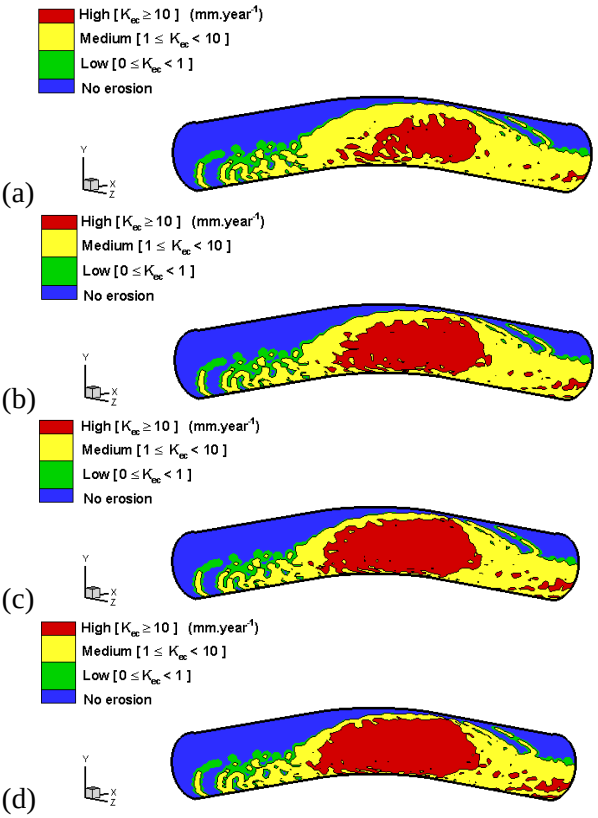

Figure 3: Wastage maps on the outer surface of Fe pipe bend at pH=7 and E= -0.6 [V] (SCE) for particle mass flow rates: (a) 0.957 (b) 1.9169 (c) 2.87 (d) 3.8276 [kg s-1].

5. DISCUSSION

The results indicate that particle volume fraction effects play a significant role in changing the erosion-corrosion regime in 3-D, Figs. 2-3. In the 3-D case, various regimes are observed over the surface, Fig. 2. With increasing volume fraction, the erosion-dominated regime is enhanced. This is due to the increase in erosion rate with increasing particle concentration, shifting the corrosion affected regimes towards those dominated by erosion.

The above trends in the variation of erosion-corrosion regimes on the pipe bend are also observed in earlier work by the current authors [9]. In this work, the significant changes in particle concentration and velocity for the component are identified, resulting in a variation of erosion intensity on the surface. In addition, the local impact angle also changes. Hence, the erosion-corrosion regime variation on the component can be attributed to these factors.

Nonetheless, it should be noted that the variation of the erosion-corrosion regimes only occurs at the pipe bend only and the remaining parts (i.e. entrance and exit straight pipes) exhibit no erosion-corrosion regime change (results not shown). This indicates that the erosion rates at these regions remain unaffected during the simulation. For the wastage maps, the pipe exit exhibits a minor variation from the medium to the high wastage regime as the particle concentration increases. Hence, the erosion-corrosion mapping technique is a potentially sensitive method of detecting any change in the erosion-corrosion behavior in such environments where changes in component geometry are anticipated.

For the present study, additive erosion-corrosion behaviour is assumed i.e. erosion enhanced corrosion and the effect of corrosion on erosion is negligible. The latter effect, the so-called "synergistic/antagonistic" interaction has been attributed to a number of possible mechanisms relating to the material microstructure [18, 19] and it is acknowledged that this is a simplistic assumption. Hence, initial work on mapping the component for the materials above has made such assumptions but future work will address such issues in more detail by assessing materials with composite structures.

The erosion and corrosion rates are assumed to be constant with time, i.e. both processes are independent of time. The time interval between impacts is very important factor in the erosion-corrosion process, as in the passive region, it determines the film thickness and growth kinetics. However, for this study, as the thickness of the passive film is assumed to be in the order of nanometers, significant increase in film thickness is not considered for long intervals between impacts, as defined for low concentrations of particles here. This will be considered in further work.

Hence, 3D erosion-corrosion maps provide a useful tool for predicting and identification the erosion-corrosion regimes and wastage regions for in-service conditions. The results have indicated significant changes in regimes along the geometry of the component and as a function of increasing particle volume concentration in the pipe. Further work will be to model the effects of other parameters such as oxygen concentration and temperature in addition to extending the range of materials in the model and the synergism /antagonism between the processes.

6. CONCLUSIONS

- CFD methods, involving fluid dynamics and multiphase flow parameters, have been used to model the erosion-corrosion behaviour of Fe at range of particle concentration values for a 3-D space.
- The results indicate changes in erosion-corrosion regimes over the component geometry.
- Increases in particle concentration have a significant effect on the boundaries on the erosion-corrosion

regime maps, reducing the corrosion affected regimes in favour of those dominated by erosion.

7. REFERENCES

[1] Griffin, D., Daadbin A., and Datta S., 2004, "The development of a three-dimensional finite element model for solid particle erosion on an alumina scale/MA956 substrate," Wear, 256(9-10), pp. 900-906.

[2] Keating A., and Nesic S., 1999, "Prediction of Two-phase Erosion-corrosion in Bends," Second International Conference on CFD in the Minerals and Process Industries, CSIROMelbourne, Australia, pp. 229-236.

[3] Davis C., and Frawley P., 2009, "Modelling of erosion-corrosion in practical geometries," Corrosion Science, 51(4), pp. 769-775.

[4] Ferng Y., Ma Y., and Chung N., 2000, "Application of local flow models in predicting distributions of erosion-corrosion locations," Corrosion, 56(2), pp. 116-126.

[5] Stack M., Corlett N., and Zhou S., 1996, "Construction of erosion-corrosion maps for erosion in aqueous slurries," Materials Science and Technology, 12(8), pp. 662-672.

[6] Stack M., Corlett N., and Zhou S., 1997, "A methodology for the construction of the erosion-corrosion map in aqueous environments," Wear, 203, pp. 474-488.

[7] Stack M., and Pungwiwat N., 2004, "Erosion-corrosion mapping of Fe in aqueous slurries: some views on a new rationale for defining the erosion-corrosion interaction," Wear, 256(5), pp. 565-576.

[8] Stack M., and Abd El Badia, T., 2006, "On the construction of erosion-corrosion maps for WC/Co-Cr-based coatings in aqueous conditions," Wear, 261(11-12), pp. 1181-1190.

[9] Stack M., Abdelrahman S., and Jana B., 2010, "A new methodology for modelling erosion-corrosion regimes on real surfaces: Gliding down the galvanic series for a range of metal-corrosion systems," Wear, 268(3-4), pp 533-542.

[10] FLUENT Inc., 2006, "FLUENT user's guide, Version 6.3,"Lebanon, NH, USA.

[11] Wood R. J. K., Jones, T., Ganeshalingam J., and Miles N., 2004, "Comparison of predicted and experimental erosion estimates in slurry ducts," Wear, 256(9-10), pp. 937-947.

[12] Forder A., Thew M., and Harrison D., 1998, "A numerical investigation of solid particle erosion experienced within oilfield control valves," Wear, 216(2), pp. 184-193.

[13] Sundararajan G., 1991, "A Comprehensive Model for the Solid Particle Erosion of Ductile Materials," Wear, 149(1-2), pp. 111-127.

[14] Stack M., and Jana, B., 2004, "Modelling particulate erosion-corrosion in aqueous slurries: some views on the construction of erosion-corrosion maps for a range of pure metals," Wear, 256(9-10), pp. 986-1004.

[15] Abdelrahman, S., and Stack, M., 2009, "Some reflictions on a model to predict the erosion rate of the passive film on pure materials," 13th Int. Conf. on Aerospace Science and Aviation Technology, ASAT-2009, Cairo, Egypt.

[16] Graham M., Bardwell J., Sproule G., Mitchell D., and Macdougall, B., 1993, "The Growth and Stability of Passive Films", Corrosion Science, 35(1-4), pp. 13-18.

[17] Lu B., Lue J., 2008, "Correlation between repassivation kinetics and corrosion rate over a passive surface in flowing slurry," Electrochimica Acta, 53(23), pp. 7022-7031.

[18] Stack M., Corlett N., and Turgoose S., 2003, "Some thoughts on modelling the effects of oxygen and particle concentration on the erosion-corrosion of steels in aqueous slurries," Wear, 255, pp. 225-236.

[19] Stack M., Antonov M., and Hussainova I., 2006, "Some views on the erosion-corrosion response of bulk chromium carbide based cermets," J. of Physics: D-Applied Physics, 39(15),pp3165-3174.

A new methodology for modelling erosion-corrosion regimes on real surfaces: gliding down the galvanic series for a range of metal-corrosion systems

Wear 268 (2010) 533–542

Contents lists available at ScienceDirect

Wear

journal homepage: www.elsevier.com/locate/wear

A new methodology for modelling erosion–corrosion regimes on real surfaces: Gliding down the galvanic series for a range of metal-corrosion systems

M.M. Stack*, S.M. Abdelrahman, B.D. Jana

Department of Mechanical Engineering, University of Strathclyde, 75 Montrose St., Glasgow, G1 1XJ, UK

ARTICLE INFO

Article history:
Received 1 April 2009
Received in revised form 31 August 2009
Accepted 22 September 2009
Available online 1 October 2009

Keywords:
CFD Modelling
Erosion-Corrosion Regimes
3-D Maps
Pure Metals

ABSTRACT

Erosion–corrosion of materials in aqueous environments is a complex phenomenon involving a very large number of variables. In such cases, characteristics of the target, particle and the environment affect the degradation mechanism. Predicting material behaviour may sometimes be a "black art" due to the parameter size which is involved in such processes.

In studies of erosion–corrosion, there have been significant advances in the modelling of such processes in recent years. Various methodologies employed include quasi-static modelling, using CFD modelling and erosion–corrosion mapping. In such cases, the output of the various models can differ significantly.

In this work, a methodology combining CFD modelling and erosion–corrosion mapping has been developed to model the erosion–corrosion behaviour of pure metals, which variously passivate and dissolve under a range of simulated conditions. This provides a means of mapping the component undergoing erosion–corrosion and thus is a step change on previous modelling work in this area as it enables superimposition of the erosion–corrosion map on real surfaces. The relative advantages and limitations of this approach are discussed in this paper.

1. Introduction

Particulate erosion–corrosion in aqueous conditions has been the subject of much research in recent years concentrating on a very wide range of materials and conditions [1–5]. Erosion–corrosion is a process which is still the subject of much investigation mechanistically. Nonetheless, various modelling approaches have been developed concentrating on many different kinds of output data.

An advance in studying the effects of chemical degradation, caused by corrosion, and mechanical degradation caused by solid particle erosion has been the development of mechanistic maps showing the regime of degradation, the mechanism of wastage and providing a basis for materials selection decisions in a range of conditions [1–5]. Such maps have been developed using predictive models of erosion–corrosion. However, a limitation of their application to erosion in flowing conditions is that they do not incorporate a parameter relating to fluid flow.

Aqueous fluid flow simulation can be divided into various categories. In the Lagrangian–Eulerian methodology, the Navier–Stokes equations are numerically used to simulate fluid flow processes and the effects of the particles dispersed in the flow are simulated using particle tracking and erosion model techniques. In the Eulerian–Eulerian approach, the fluid and particles are treated essentially as fluids. The first method is thus generally used for dilute multiphase flows where the particle trajectory can be tracked and modelled. For dense flows, where particle–particle interactions may be significant, the two phases can be interpreted and modelled as interacting continuous media [6].

In studies of erosion–corrosion there are no models available which attempt to combine the effects of particle erosion, corrosion and fluid flow with mapping tribo-corrosion methodologies. This has limited the characterization of tribo-corrosion phenomena in real life environments to date.

In this work, various models of solid particle erosion are combined with those for aqueous corrosion. In addition, these models are incorporated in a simulated flowing environment using CFD techniques. The results present a new technique for mapping erosion–corrosion on real pipes, thereby introducing an important step-change in the interpretation of erosion–corrosion mapping techniques to date.

2. Methodology

The initial work involved evaluation of several erosion models against some laboratory erosion results [7]. A methodology was then developed to predict the combined effect of the erosion and corrosion wastage using the model of Sundararajan [8] to predict the erosion rates and a range of corrosion models to predict the

* Corresponding author. Tel.: +00 44 141 548 3754; fax: +00 44 141 552 5105.
E-mail address: margaret.stack@strath.ac.uk (M.M. Stack).

0043-1648/$ – see front matter © 2009 Elsevier B.V. All rights reserved.
doi:10.1016/j.wear.2009.09.013

Nomenclature

Latin letters:

A_i	area of the surface cell [m^2]
b_a	anode Tafel slope [V decade^{-1}]
b_c	cathode Tafel slope [V decade^{-1}]
C_f	non-dimensional constant (Finnie) (0.5)
C_k	cutting characteristic velocity (Forder) [m s^{-1}]
C_p	specific heat capacity [J kg^{-1} K^{-1}]
c	particle concentration [g cm^{-3}]
D, D_c	diameter of the pipe roundness, crater diameter [m]
D_k	deformation characteristic velocity (Forder) [m s^{-1}]
d	pipe diameter, crater depth [m]
E	applied potential, relative to saturated calomel electrode, modulus of elasticity of the material. V(SCE), [Pa]
E_e	reduced Young's modulus of elasticity (modulus of collision) [Pa]
e	coefficient of restitution
Fr	Faraday's constant (96485) [C mol^{-1}]
$f(\alpha)$	function depends on the impact angle
f_t	numerical constant (0.025)
H	hardness [Pa]
h	thickness of the oxide layer [m]
h_0	initial thickness of the oxide layer [m]
I_p	impact frequency [imp cm^{-2} s^{-1}]
i_{anet}	net anodic current density [A m^{-2}]
i_0	exchange current density [A m^{-2}]
K_c	corrosion rate [kg m^{-2} s^{-1}]
K_{ec}	total wastage rate [kg m^{-2} s^{-1}]
K_e	erosion rate [kg m^{-2} s^{-1}]
k	ratio of vertical to horizontal forces (Finnie) (2)
k_2	metal to its oxide molecular mass ratio [8]
M_t	total erosion rate by single impact particle [kg impact^{-1}]
m_p	mass of impacting particle [kg]
n	empirical constant (Neilson–Gilchrist)
n_f	velocity ratio exponent (Forder) (2.54)
n_c	strain hardening coefficient (0.3)
P_H	eroding surface flow stress related to hardness (Finnie) [Pa]
RAM	relative atomic mass
R_f	particle roundness factor (Forder) (0.5)
r_p	radius of impacting particle [m]
T_m	melting temperature point of the metal [K]
U	Crater volume [m^3]
V	Velocity [m s^{-1}]
v_f	Volume fraction of particles
W	erosion rates [m^3 impact^{-1}]
W_C	erosion by cutting [kg kg^{-1}]
W_D	erosion by deformation [kg kg^{-1}]
W_t	total erosion (Sundararajan) [kg kg^{-1}]
w_{av}	area weighted average wastage of metal [kg m^{-2} s^{-1}]
w_i	wastage of metal at centre node on the eroded surface cell [kg m^{-2} s^{-1}]
Y	yield stress of the target material (Forder) [Pa]
z_m	number of electrons

Greek letters:

α	impact angle [deg]
ε	deformation wear factor (Neilson–Gilchrist)
λ	particle shape factor (0.0)
μ	frictional coefficient (0.1)
μ_f	critical friction coefficient (Sundararajan)
ν	Poisson's ratio
π	Pi ratio (3.1416)
ρ	density [kg m^{-3}]
ρ_p	density of the particle (2650) [kg m^{-3}]
Φ	cutting wear factor (Neilson–Gilchrist)
Ψ	ratio of depth of contact to depth of cut (Finnie) (2)

Subscripts:

p	particle
pas	passivation
s	substrate
o	initial, reversible equilibrium potential
f	friction, oxide film
t	total, target
i	node
c	corrosion, crater
e	erosion, reduced elasticity
m	melting
1	impact
2	rebound
ap	applied potential
av	average
ce	total wastage due to erosion and corrosion
K	threshold, deformation(N–G)
tp	threshold, cutting (N–G)

corrosion rates. The total wastage was estimated by combining the erosion and corrosion rates.

The modelling processes thus involved several steps i.e.:

(i) A single elbow-pipe with diameter ratio RD^{-1} of 1.2 with a bore diameter of 0.078 [m] was used for the simulation.
(ii) A standard k–ε model was employed with standard wall function and zero roughness to model the turbulence [9].
(iii) A Lagrangian–Eulerian simulation was used to model the multi-phase flow of the particles trajectories to evaluate the erosion rate using the Discrete Phase Modelling (DPM) method [6]. The DPM method is based on the Lagrangian tracking of every particle using several discritizing methods for tracing the ingested particles (the method used here is Runge–Kutta method).
(iv) A user defined function (UDF) was developed in the above algorithms to evaluate the erosion rate based on the models of Forder et al. [10], Finnie (first model) [11], Neilson and Gilchrist [12], and Sundararajan (second model) [8]. These are outlined in Eqs. (2)–(5).
(v) A further UDF file was developed to calculate the corrosion and erosion rates at every impact site (according to the original erosion–corrosion mapping methodology generated in 2D [15]).
(vi) For evaluation of the erosion–corrosion rates, Sundararajan's model [8] below was used to calculate the erosion components. The impact angles computed ranged between 7.5 and 10° and this is why this model was used as it accounts for impact angle effects.

The simulation commenced by using a single phase CFD run using FLUENT software and then injecting the particles uniformly at the inlet by using DPM method. A sample of 1655 particles of 10^{-3} [m] diameter was injected with total mass flow rate equal 3.8 [kg s^{-1}] to represent 22.88% particle concentration which corresponds to particle volume fraction of 0.09.

(The work on 3D maps in this paper was based on earlier studies carried out by Stack and Jana [15], where 2D erosion–corrosion maps for 1 mm diameter particle sizes were generated. A particle size of 1 mm was thus chosen to be comparable with results in this earlier study. In ref. [15], a value of 25.29% by mass (volume fraction = 0.101) was used. This value is marginally above the allowed limit for dilute slurries i.e. 0.1. Thus, a value of 22.88% was chosen which corresponds to a volume fraction of 0.091. This means that the value chosen is within the limit of using DPM in the FLUENT simulation.).

The walls were chosen as "no slip boundary conditions" and the initial flow velocity was 3 [m s^{-1}]. The erosion rates were evaluated in terms of volume loss per impact. The total erosion rate over the surface was estimated by calculating the weighted average of all erosion rates on the outer surfaces per unit area i.e. $\dot{W}$ [14]

$$\dot{w}_{av} = \frac{\sum_{node_i} \dot{w}_i A_i}{\sum_{node_i} A_i} \tag{1}$$

2.1. Erosion models for impact by solid particles

For the various models, the erosion rates $\dot{W}$ are given as follows: (all mathematical terms are given in the list of nomenclature).

(1) Finnie's erosion model [11]:

$$\dot{W} = C_f \frac{V^2}{P_H \psi k} f(\alpha) \tag{2.a}$$

$$f(\alpha) = \begin{cases} \sin(2a) - 4\sin^2\alpha & \alpha \le 14.04^\circ \\ \dfrac{1}{4}\cos^2\alpha & \alpha > 14.04^\circ \end{cases} \tag{2.b}$$

Finnie recommended a value of 0.1, 2 and 2 for C_f, ψ, and k respectively.

(2) Neilson–Gilchrest model [12]:

$$\dot{W} = \begin{cases} \dfrac{1}{2}\dfrac{(V^2\cos^2\alpha - V_{tp}^2)}{\phi} + \dfrac{1}{2}\dfrac{(V\sin\alpha - V_K)^2}{\varepsilon} & \alpha \le \dfrac{\pi}{2n} \\ \dfrac{1}{2}\left[\dfrac{V^2\cos^2\alpha}{\phi} + \dfrac{(V\sin\alpha - V_K)^2}{\varepsilon}\right] & \alpha > \dfrac{\pi}{2n} \end{cases} \tag{3.a}$$

and

$$V_{tp} = V^2\cos^2\alpha[\sin(n\alpha) - 1] \tag{3.b}$$

(3) Sundararajan's second model [8]:

$$\dot{W}_D = \frac{5.5\times10^{-2}}{(T_m - 436)^{0.75}} \frac{2^{n_c}\bar{f}_t V^2 \sin^2\alpha(1-e^2)}{n_c C_p} \tag{4.a}$$

$$\dot{W}_D = \frac{5.5\times10^{-2}}{(T_m - 436)^{0.75}} \frac{(n_c+1)(\mu/\mu_f)(2-\mu/\mu_f)V^2\cos^2\alpha}{(1+\lambda)2^{2-n_c}n_c C_p} \tag{4.b}$$

and

$$\dot{W}_t = \dot{W}_D + \dot{W}_c \tag{4.c}$$

where

$$\mu_f = \frac{1}{(1+\lambda)(1+e)\tan\alpha} \tag{4.d}$$

$$e = \frac{1.36H_s^{0.625}}{E_e^{0.5}\rho_p^{0.125}V^{0.25}} \tag{4.e}$$

$$E_e = \frac{E_t E_p}{[E_p(1-\nu_t^2) + E_t(1-\nu_p^2)]} \tag{4.f}$$

(4) Forder's model [10]:

$$\dot{W} = \frac{100 r_p^3}{2\sqrt{29}}\left(\frac{V}{C_k}\right)^{n_f}\sin(2\alpha)\sqrt{\sin\alpha} + \frac{m_p}{2E_e}(V\sin\alpha - D_k)^2 \tag{5.a}$$

$$C_k = \sqrt{3\sigma\frac{R_f^{0.6}}{\rho_p}} \tag{5.b}$$

$$D_k = \frac{\pi^2}{2\sqrt{10}}(1.59Y)^{2.5}\left(\frac{R_f}{\rho_t}\right)^{0.5}\left[\frac{(1-\nu_p^2)}{E_t} + \frac{(1-\nu_t^2)}{E_p}\right]^2 \tag{5.c}$$

2.2. Corrosion and erosion–corrosion methodologies

The corrosion rate in the dissolution regime and full details of corrosion reactions anticipated for the pure metals are given elsewhere as generated for the earlier work on two-dimensional erosion–corrosion maps for the pure metals studied in this paper [15]. The corrosion rate in the dissolution regime is given by:

$$K_c = \frac{RAMi_{anet}}{z_m F r} \tag{6.a}$$

where

$$i_{anet} = i_0\left[\exp\left(\frac{2.303(E_{ap}-E_0)}{b_a}\right) - \exp\left(\frac{-2.303(E_{ap}-E_0)}{b_c}\right)\right] \tag{6.b}$$

In the passive region, the corrosion rates estimated for normal impact are given elsewhere [16], based on the work of Tirupataiah et al. [17] for determining a crater diameter for normal impact. To account for the effect of impact angle, we have to modify this approach.

Assuming that the energy involved in the erosion process is the difference between the initial and rebound impact energy and that the erosion process is adiabatic, the energy required to form a crater can be written as:

$$\frac{m_p}{2}(V_1^2 - V_2^2) = H_s U \tag{7}$$

where m_p is the particle mass, V is particle velocity, H_s is the material hardness, U is the crater volume and the subscripts 1 and 2 are for the impact and rebound process respectively. Assuming that the surface shear stresses due to oblique impact may be neglected for erosion of brittle materials, Finnie [11] stated that the crater diameter of ring crack d is related to the vertical component of the velocity. Hence, the energy balance in equation (7) is:

$$\frac{m_p}{2}(V_1^2\sin^2\alpha_1 - V_2^2\sin^2\alpha_2) = H_s U \tag{8}$$

where α_1 and α_2 are the impact and rebound angles respectively. By definition, the normal impact velocity component is related to the normal rebound velocity component by the coefficient of restitution e, thus and by rearranging:

$$\frac{m_p}{2}V^2\sin^2\alpha_1(1-e^2) = H_s U \tag{9}$$

Assuming that the particle is a sphere and the crater depth is comparably smaller than the particle diameter i.e. at low particle velocities, the shape of the crater on the passive film surface can be assumed as part of a sphere and U can be related to the crater diameter D_c by:

$$U = \frac{\pi D_c^4}{32 d_p} \tag{10}$$

Substitution of equation (10) into (9) gives:

$$D_c = 1.5023\left[\frac{m_p d_p(1-e^2)}{H_s}\right]^{0.25}(V\sin\alpha_1)^{0.5} \tag{11}$$

Table 1
Properties for pure metals selected and their passive films.

Metal properties	Fe	Fe_2O_3	Ni	NiO	Cu	Cu_2O	Al	Al_2O_3	Solid particles
ρ [kg m^{-3}]	7800	5240	8900	6720	8930	6400	2700	3970	2670
k_2	1398.9	–	1571.7	–	1597.7	–	1058.5	–	–
E [GPa]	211		200		130		71	380	94
v	0.293		0.312	T	0.343		0.345	0.22	0.3
H [GPa]	0.82	8.012	0.862	6.561	0.495	2.7362	0.260	20	–

The crater depth d is related to crater diameter using the same assumption above by:

$$d = \frac{D_c^2}{4d_p} \tag{12}$$

From [15], the mass of passive film removed per impact is given as:

$$M_t = \pi k_2 d_p d h \rho_f \tag{13}$$

Substituting equation (11) into (12) and apply to (13):

$$M_t = \pi k_2 h \rho_f d_p^2 \left[\frac{\rho_p(1-e^2)}{6H_s}\right]^{0.5} (V \sin\alpha_1) \tag{14}$$

The unit given for the erosion model by equation (14) is [g impact^{-1}]. To convert to K_e [kg m^{-2} s^{-1}], this can be varied according to the application under investigation. For example, if the flow is homogeneous (constant particle concentration) then particle impact frequency may be given as:

$$I_p = \frac{cV \sin\alpha}{m_p} \tag{15}$$

and c is the particle concentration by mass [kg m^{-3}]. The erosion rate from Eq. (4)(a–c) can be multiplied by particle impact flux as outlined in [15].

For evaluation of properties of the pure metals and their passive films, the mechanical properties for Fe, Ni, Cu and Al are given below, in Table 1. The constant k_2 is defined as the mass ratio between the metal and its oxide created during the corrosion reaction multiplied by the number of moles of metal involved in the reaction [15].

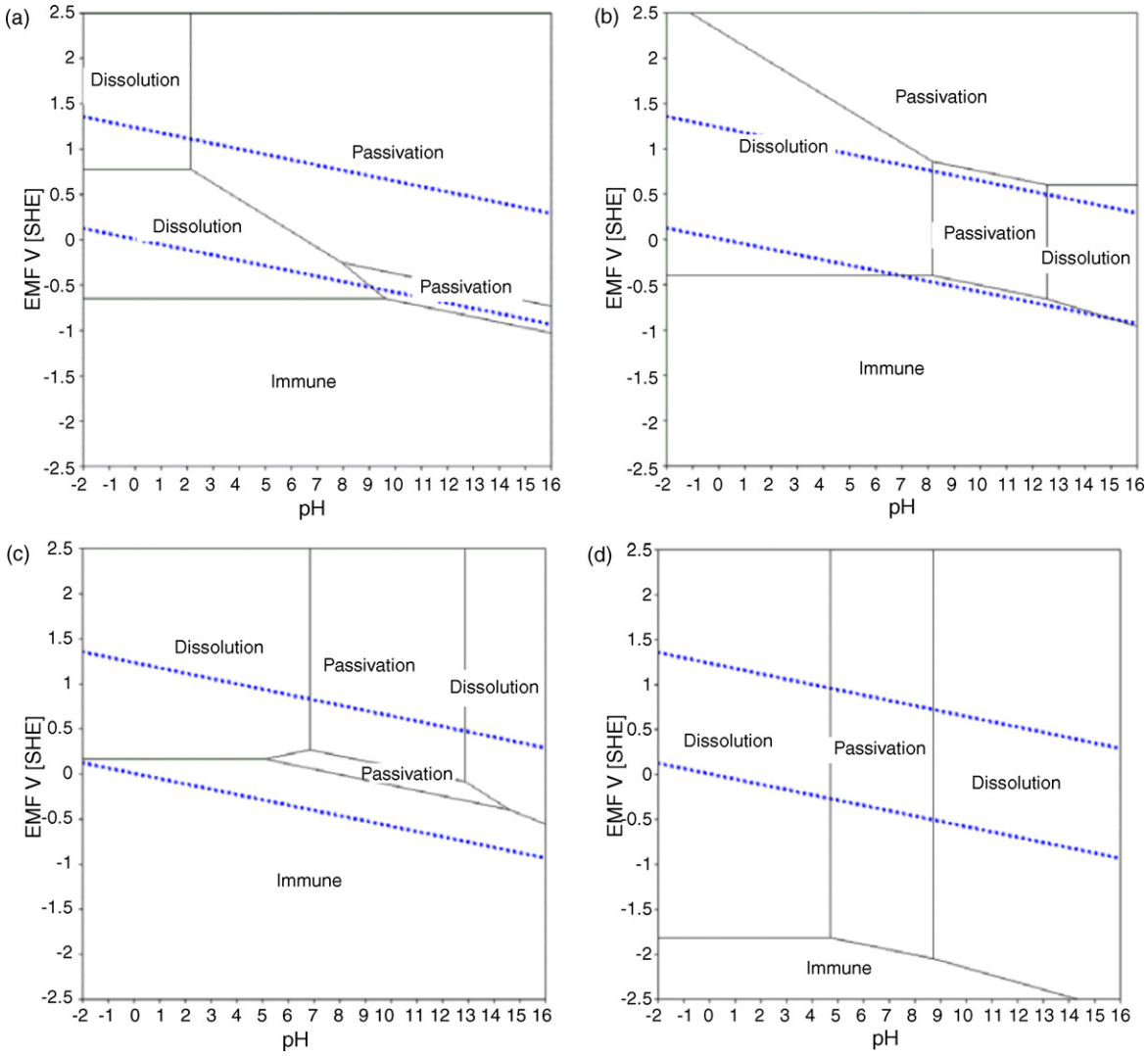

Fig. 1. Pourbaix diagrams for: (a) Fe, (b) Ni, (c) Cu, and (d) Al. [13].

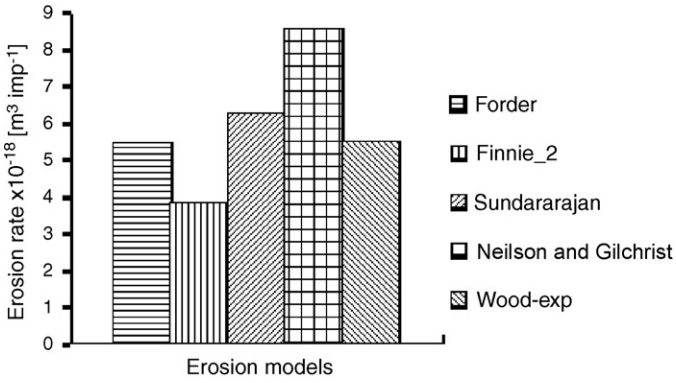

Fig. 2. Prediction of erosion models [8,10–12] and comparison with experimental results [7].

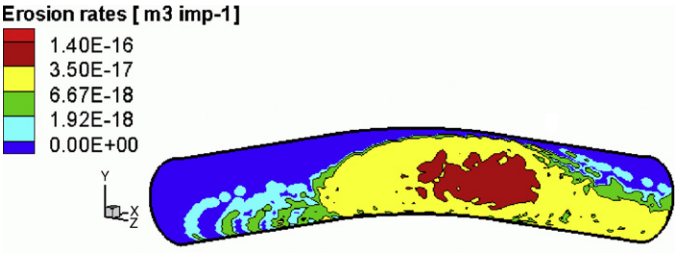

Fig. 3. Erosion rates contours on the outer surface predicted by (DPM) Discrete Particle Method.

The thickness of the passive layer h can be assumed to be varied with the potential difference and may be given from [15]:

$$h = h_0 + 3 \times 10^{-9}(E_{ap} - E_{pas}) \quad (16)$$

and: $h_0 = 1 \times 10^{-9}$ [m].

All corrosion rates must be calculated in [gm cm^{-2} s^{-1}]. The erosion rates from Sundararajan's model [8] must be converted from [kg$_{target}$ kg$_{particle}^{-1}$] accordingly as indicated above.

Eq. (14) is a simple expression for estimating the erosion rates for the passive film on a substrate. It is valid only for the impact of passive film formed during the erosion–corrosion process where the erosion footprint (i.e. the deformed surface) has a ring shape approximately (this is also assumed at oblique impact angles). The equation is useful for CFD applications in which erosion occurs at a range of impact angles. Should the particle fully penetrate the passive film and erode the substrate, another approach is considered i.e. the use of a model for erosion of ductile materials [8].

The calculation of K_{ec}, the total erosion–corrosion rate is outlined below.

2.3. Erosion–corrosion mapping boundaries

The regime boundaries are defined in terms of the ratio K_c/K_e. Therefore, by combining and rearranging the above expression for

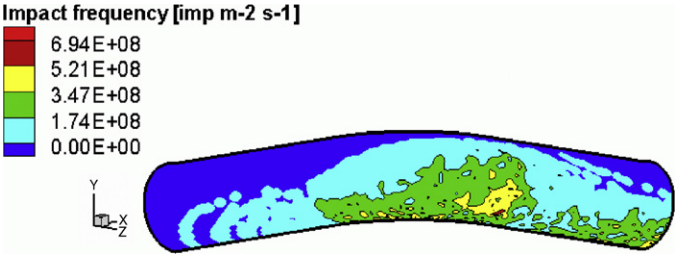

Fig. 4. Impact frequency by (DPM) Discrete Particle Method.

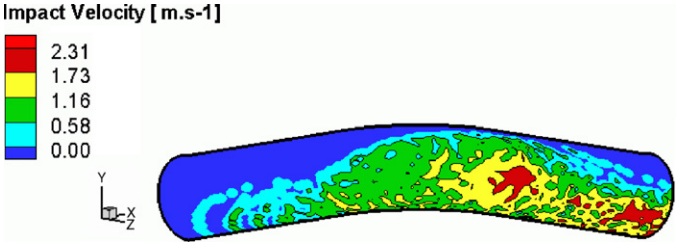

Fig. 5. Impact velocity profile on the surface of the elbow-pipe.

K_c, and K_e, the boundaries for the erosion–corrosion regime maps at a given applied potential can be determined as [15]:

$$\frac{K_c}{K_e} < 0.1 \quad \text{(Erosion dominated)} \quad (17)$$

$$0.1 \leq \frac{K_c}{K_e} < 1 \quad \text{(Erosion–Corrosion dominated)} \quad (18)$$

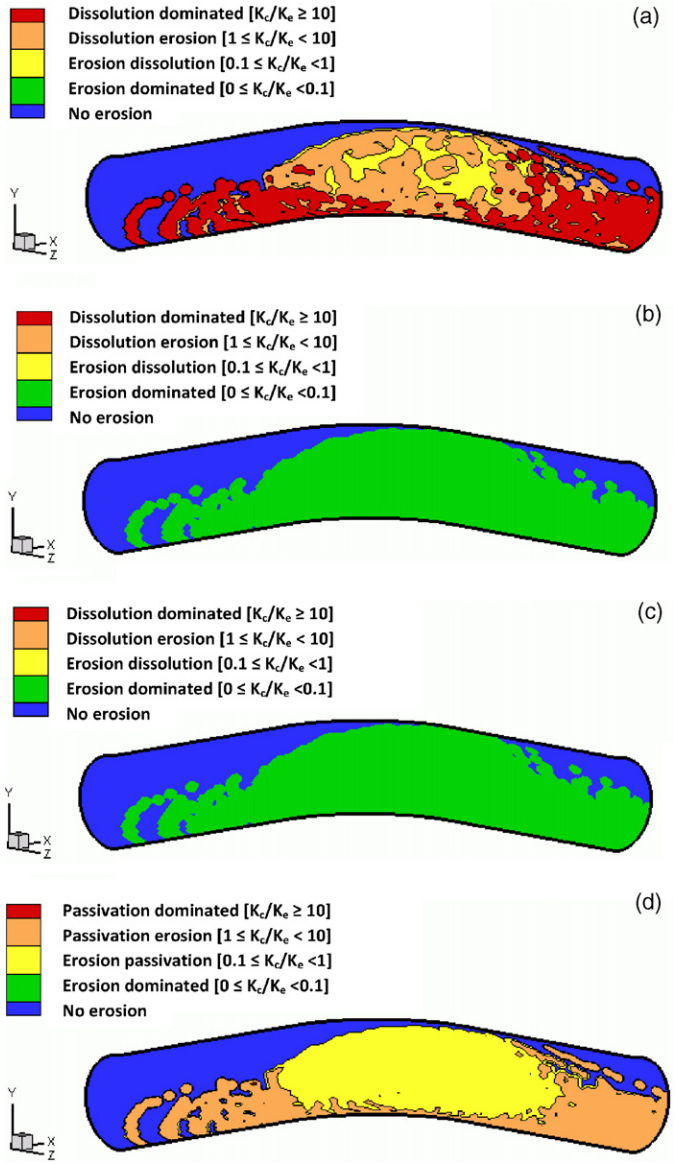

Fig. 6. Erosion–corrosion maps for the outer surface of elbow-pipe at pH 5, E_{ap} = −0.6 V(SCE), particle size = 1000 [μm] and concentration = 22.88% (vf = 0.1) for: (a) Fe. (b) Ni. (c) Cu. (d) Al.

$$1 \leq \frac{K_c}{K_e} < 10 \quad \text{(Corrosion – Erosion dominated)} \tag{19}$$

$$\frac{K_c}{K_e} \geq 10 \quad \text{(Corrosion-dominated)} \tag{20}$$

where in the dissolution region, K_c can be determined from Eq. (6)a and b. In the passive region, the corrosion rate is equal to the additive effect of the erosion on corrosion (i.e. erosion controlled corrosion or simply repassivation) which can be given directly from equation (14). (The Pourbaix diagrams, Fig. 1, indicate whether corrosion process involved in the erosion–corrosion interaction will be erosion–dissolution or erosion–passivation as a function of the pH and potential The ratios of the corrosion to the erosion contributions above identify which process dominates i.e. If the corrosion rate is 10 times the erosion rate then the surface is corrosion dominated and if the Pourbaix diagram, Fig. 1, indicates that dissolution can only take place, then the process is dissolution dominated).

In order to present the erosion–corrosion regime on the pipe surface, the K_c/K_e ratios at each node in the pipe surface are evaluated and contour plots are generated to generate transition boundaries of the erosion–corrosion regimes above.

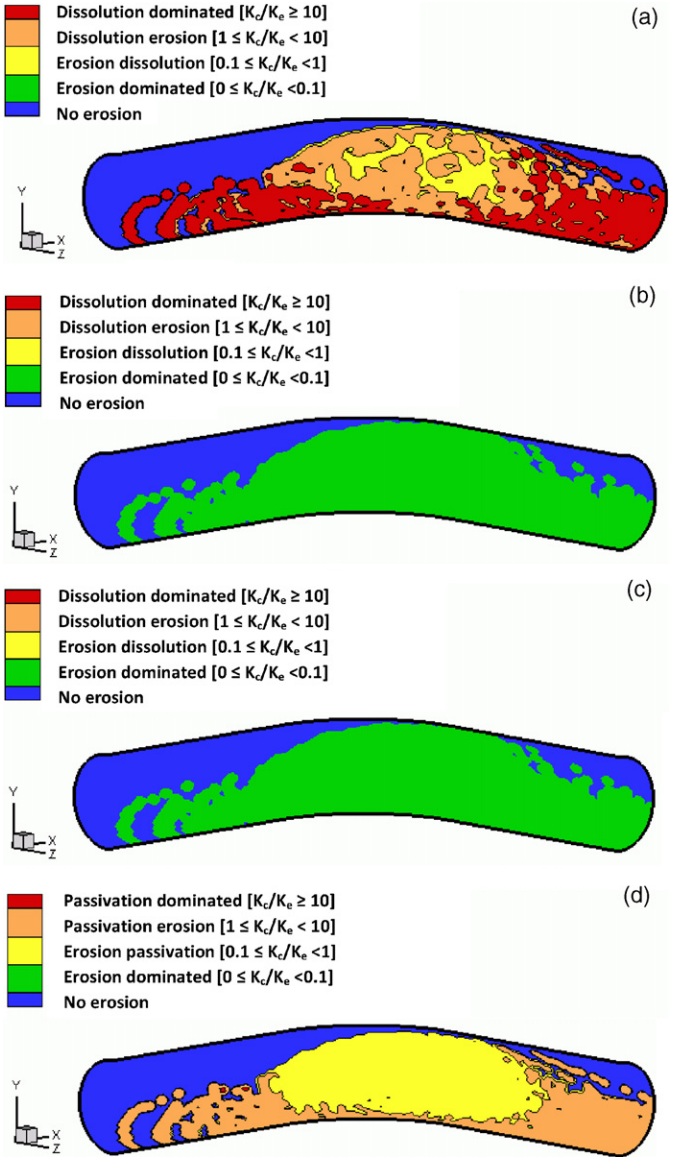

Fig. 7. Erosion–corrosion maps for the outer surface of elbow-pipe at pH 7, E_{ap} = −0.6 V(SCE), particle size = 1000 [μm] and concentration = 22.88% (vf = 0.1) for: (a) Fe. (b) Ni. (c) Cu. (d) Al.

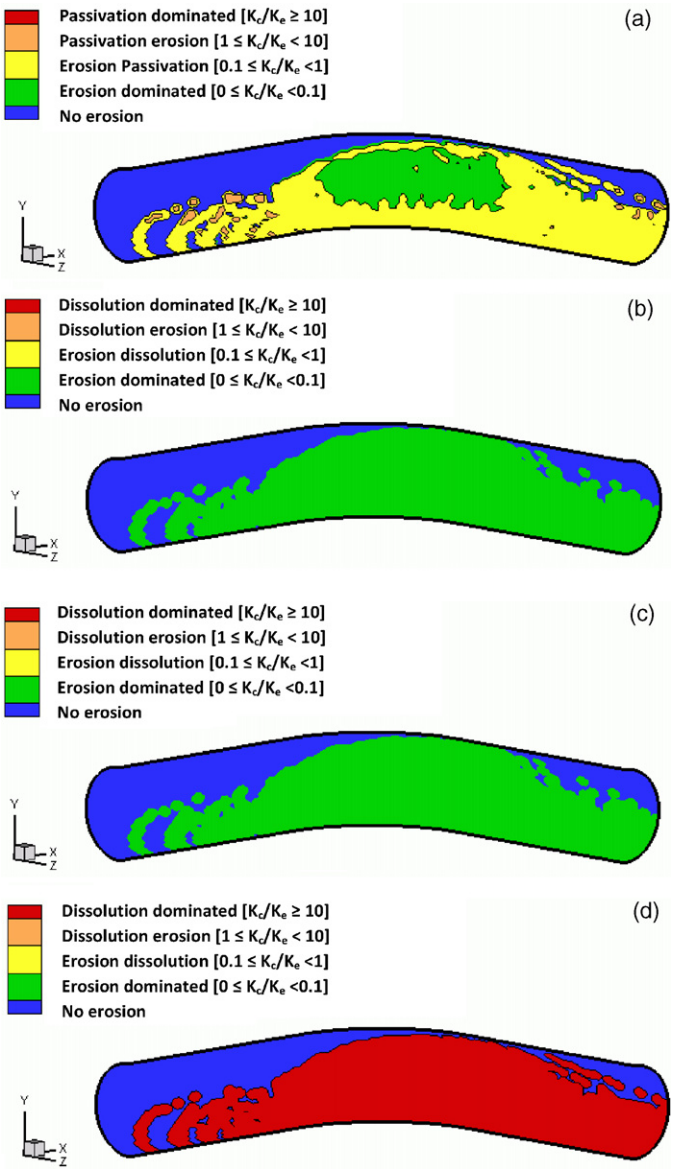

Fig. 8. Erosion–corrosion maps for the outer surface of elbow-pipe at pH 9, E_{ap} = −0.6 V(SCE), particle size = 1000 [μm] and concentration = 22.88% (vf = 0.1) for: (a) Fe. (b) Ni. (c) Cu. (d) Al.

The total wastage in the active and passive regimes can be given by:

$$K_{ec} = K_c + K_e \tag{21}$$

The transition boundaries for the wastage maps:

$$K_{ec} < 1 \quad [\text{mm year}^{-1}]\,(\text{low wastage}) \tag{22}$$

$$1 \leq K_{ec} < 10 \quad [\text{mm year}^{-1}]\,(\text{medium wastage}) \tag{23}$$

$$K_{ec} \geq 10 \quad [\text{mm year}^{-1}]\,(\text{high wastage}) \tag{24}$$

Plots of these regimes at each node in the pipe were generated for the wastage maps below. The erosion–corrosion maps constructed in this work are based on the pure metals data, electrochemical reactions, and pH values used in [15] and are considered an extension from 2D to 3D mappings taking into consideration the effect of the fluid flow properties on the erosion–corrosion mappings, assuming potential controlled corrosion.

3. Results

To clarify the dissolution and passive regions of influence for every pure material selected in this study, Fig. 1 illustrates the Pourbaix diagrams for Fe, Ni, Cu, and Al respectively. These diagrams are the basis for constructing the erosion–corrosion maps below as they determine the corrosion regimes which predominate for each of the pure metals (i.e. dissolution, passivation and immunity). As is shown from the figures, significant differences in the stability regimes are observed for the pure metals as a function of pH and potential which, in the context of the erosion–corrosion maps, will be discussed further below.

3.1. Erosion model predictions

Fig. 2 indicates the various predictions of the erosion models and it can be seen that there are similarities between the erosion rates calculated and evaluated in earlier work [7] when the values in the earlier study were used and hence this was a useful calibration exercise. The predictions on real surfaces are indicated in Fig. 3 where the highest erosion rates were observed at the bend in the pipe. Analysis of the impact frequency; Fig. 4 and the impact velocity profile. Fig. 5 indicates the area around the bend experienced the highest impact frequency and velocities.

3.2. Effect of pH on the erosion–corrosion regime mapping for pure metals

The erosion–corrosion mapping results Fig. 6 (a–d) show the change in erosion–corrosion regimes for the various pure metals at pH 5 and −0.6 V(SCE). It is clear that there were a number of erosion–corrosion regimes operating on the component, under nominally the same initial simulation conditions. Here, it was shown that there were significant differences between the regimes of erosion–corrosion behaviour observed, with dissolution and dissolution–erosion being dominant for Fe, Fig. 6(a), a transition to erosion-dominated behaviour for Ni and Cu, Fig. 6(b and c) and to erosion–passivation for Al, Fig. 6 (d). At pH 7, Fig. 7, as was observed at pH 5, Fig. 6, only Fe, Fig. 7(a), was affected by dissolution. All the other metals were in the erosion-dominated or in the case of Al, Fig. 7(d), passivation affected regimes. At pH 9, Fig. 8, there was a transition to erosion-passivation and erosion-dominated behaviour for the Fe, Fig. 8(a) which contrasted with the behaviour at lower pH values; Figs. 6(a) and 7(a); in which dissolution affected the process. For the Ni and Cu, the erosion–corrosion processes were again characterized by erosion-dominated behaviour, Fig. 8(b and c). For Al; Fig. 8(d) there was a transition to a new corrosion affected regime, dissolution dominated behaviour, which contrasted with the passivation dominated processes observed at the lower pH values, Figs. 6(d) and Fig. 77(d).

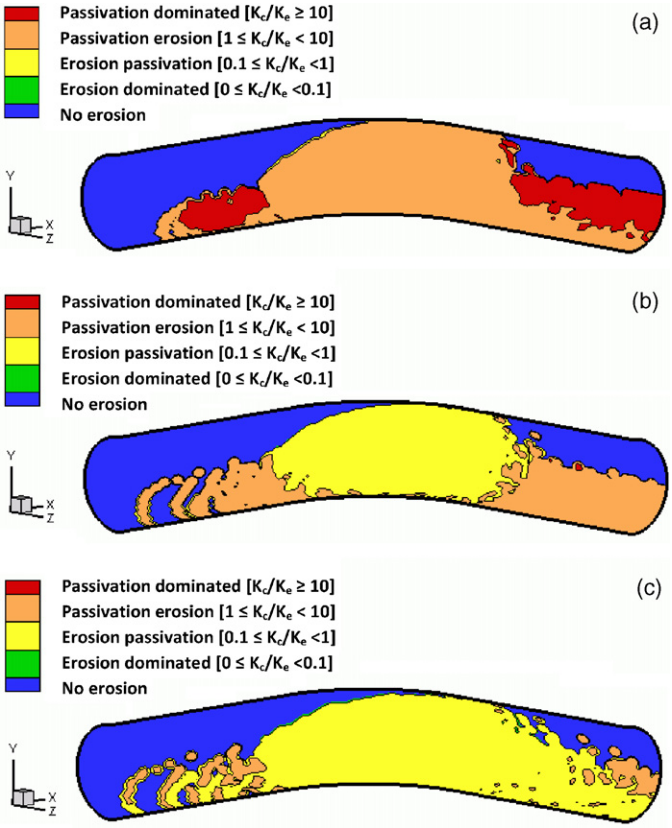

Fig. 9. Erosion–corrosion maps for the outer surface of (Fe) elbow-pipe at pH 9, E_{ap} = −0.6 V(SCE) and concentration = 22.88% (vf = 0.1) for particle size: (a) 250 [μm]. (b) 500 [μm]. (c) 750 [μm].

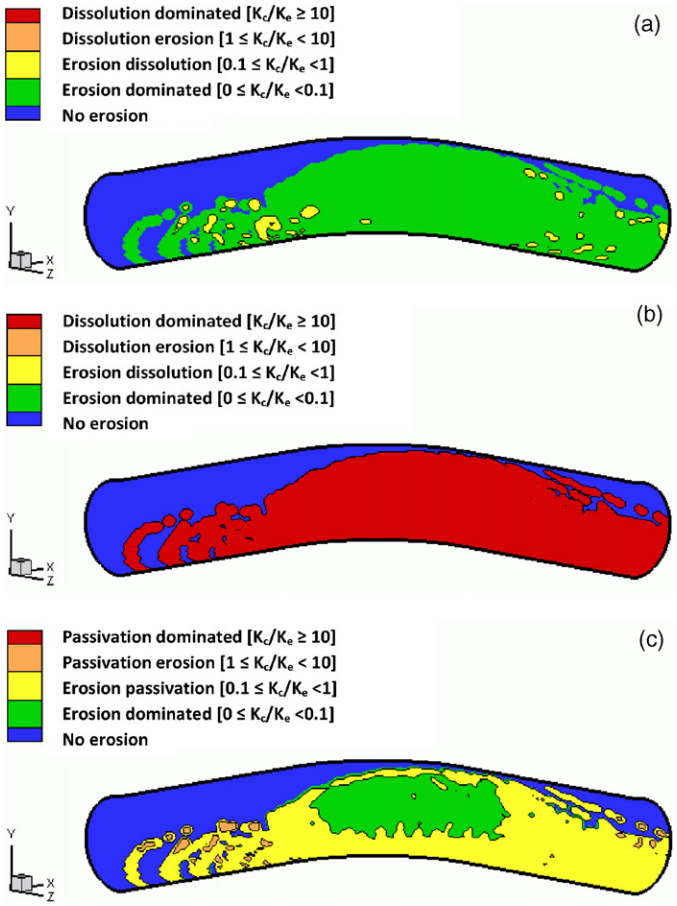

Fig. 10. Erosion–corrosion maps for the outer surface of (Fe) elbow-pipe at pH 7, particle size = 1000 [μm] and concentration = 22.88% (vf = 0.1) for E_{ap}: (a) −0.75, (b) −0.5 and (c) −0.25 V(SCE).

3.3. Effect of particle size and applied potential on erosion–corrosion mapping of Fe

For the effect of particle size on Fe at pH 9 and −0.6 V(SCE), Fig. 9, increases in particle size by a factor of three, Fig. 9(a–c) changed the erosion–corrosion processes from passivation dominated and passivation–erosion dominated behaviour to a situation

where erosion–passivation was the dominant degradation process, with the extent of this regime prevailing being greater at the higher potentials, Fig. 9(b and c). Increases in applied potential, however, Fig. 10 for Fe at pH 7 showed various significant transitions from mainly erosion dominated behaviour at −0.75 V(SCE), Fig. 8(a) to dissolution and mainly erosion–passivation dominated behaviour as the potential was increased from t −0.5 to −0.25 V, Fig. 10(b and c).

3.4. Comparison between erosion–corrosion wastage maps at the various pH values

The results on erosion–corrosion wastage maps, Figs. 11–13, indicate very significant differences for the pure metals at the various pHs. As in the case for the results above, a number of wastage regimes predominated on the component. At pH 5, the highest wastage was observed for the Fe, Fig. 11(a), with the wastage decreasing for Ni and Cu, Fig. 11(b and c). The high wastage regime had a greater presence for Al, Fig. 11(d) than for the latter metals, Fig. 11 (b and c). As the pH was increased to 7, the wastage profiles were similar for all metals, Fig. 12(a–d) as had been the case at pH 5, Fig. 11. However, at pH 9, there was a change in the behaviour, Fig. 13(a–d) with the high wastage regime predominant for the Al, Fig. 13(d), to a greater extent than for the other metals.

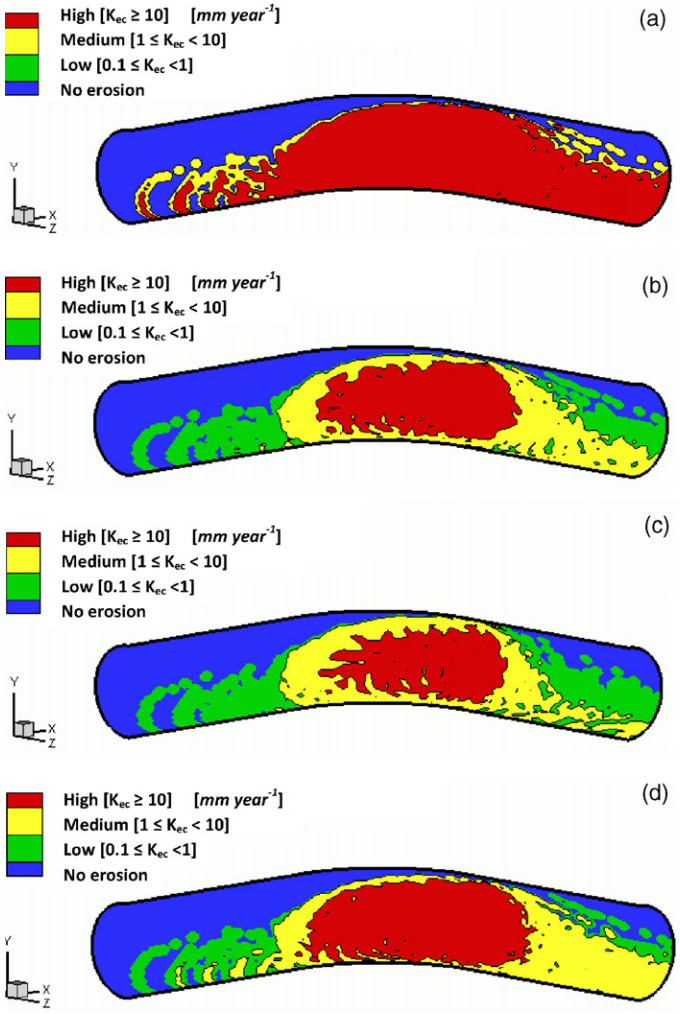

Fig. 11. Erosion–corrosion wastage maps for the outer surface of elbow-pipe at pH 5, E_{ap} = −0.6 V(SCE), particle size = 1000 [μm] and concentration = 22.88% (vf = 0.1) for: (a) Fe. (b) Ni. (c) Cu. (d) Al.

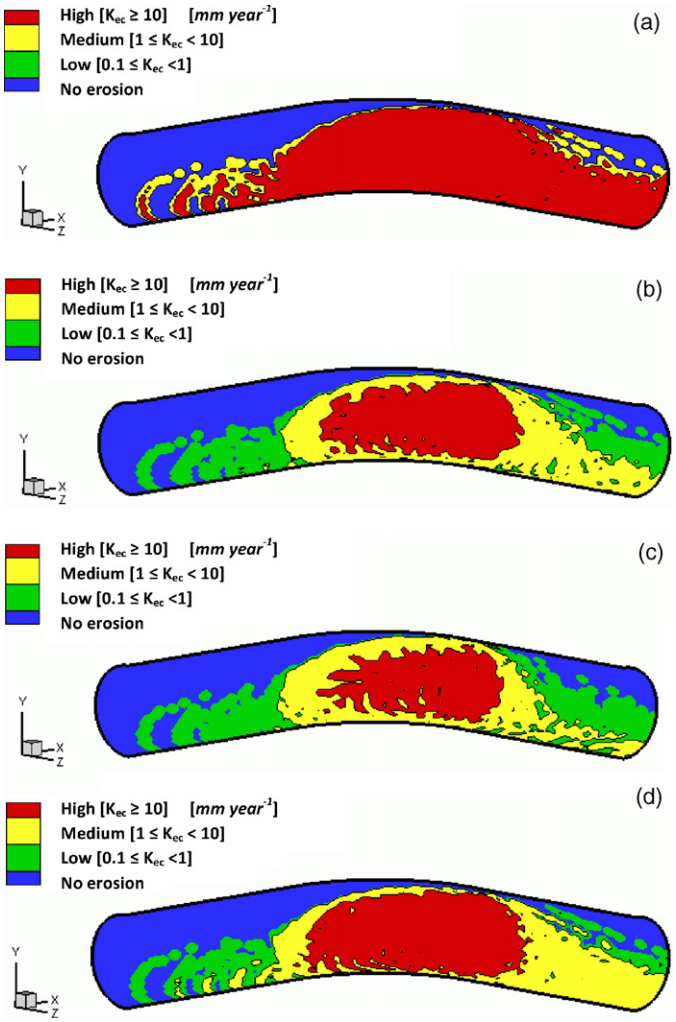

Fig. 12. Erosion–corrosion wastage maps for the outer surface of elbow-pipe at pH 7, E_{ap} = −0.6 V(SCE), particle size = 1000 [μm] and concentration = 22.88% (vf = 0.1) for: (a) Fe. (b) Ni. (c) Cu. (d) Al.

4. Discussion

The results indicate that it is possible to simulate the erosion–corrosion mapping process on real components using such an approach. It is shown that a number of mechanistic regimes are possible, under nominally the same initial tribo-corrosion conditions, Figs. 6–13, and that this may be in part related to the difference in impact frequencies and velocities, Figs. 4–5 observed on the component. This means that designing materials and processes for optimum erosion–corrosion resistance is a complex problem with more than one erosion–corrosion regime possible on a single component.

It is interesting that, as in the two dimensional simulations for erosion–corrosion of pure metals [15], significant differences are found in the three-dimensional simulation between the regimes dominating for the metals, with Cu and Ni being more immune and less likely to be dominated by corrosion than Fe and Al, under the window of conditions employed in the model, Figs. 6–8. However, it should be emphasized that if the conditions differ the results will change significantly. Moreover, it is important to note that various metals will exhibit different erosion–corrosion behaviour and because of the changes of velocity and particle frequency of impact over the component, Figs. 4 and 5, a variety of erosion–corrosion regimes are experienced on the surface of the component.

It is clear that a significant area of the component modelled will not experience any erosion or impact of flowing particles, Figs. 6–13. In practice, the un-eroded surfaces may experience corrosion through dissolution or passivation. Moreover, the corrosion process may be controlled by the flow parameters (flow controlled corrosion) such as fluid temperature and the oxygen concentration in the bulk flow [18,19]. The effect of these parameters will be addressed in further work.

The transition from passivation to dissolution dominated behaviour for Al, is illustrated in Figs. 6(d) and 8(d). Here, at higher pH values, the Al dissolves, in contrast to that which occurs for the other pure metals at such pHs, Fig. 8. This is a characteristic of Al which makes it unsuitable for use at such pH values.

Increases in particle size by a factor of three, Fig. 9, for the Fe, not surprisingly, reduces the passivation affected regimes on the component. The increase in erosion footprint results from the higher impact energy involved in the process. The three-dimensional results highlight the important influence that particle size has on the erosion–corrosion regime.

The effect of changing applied potential in the positive direction, i.e. from −0.75 to −0.25 V(SCE), Fig. 10(a–c), has a very significant effect on the erosion–corrosion degradation mode for the Fe. Here, the regime is changed from dissolution to predominately passivation affected behaviour over the component. This illustrates the importance of electrochemical potential on the stability of the corrosion regime as identified by the Pourbaix diagrams for the various pure metals and their influence on the erosion–corrosion two-dimensional maps [15].

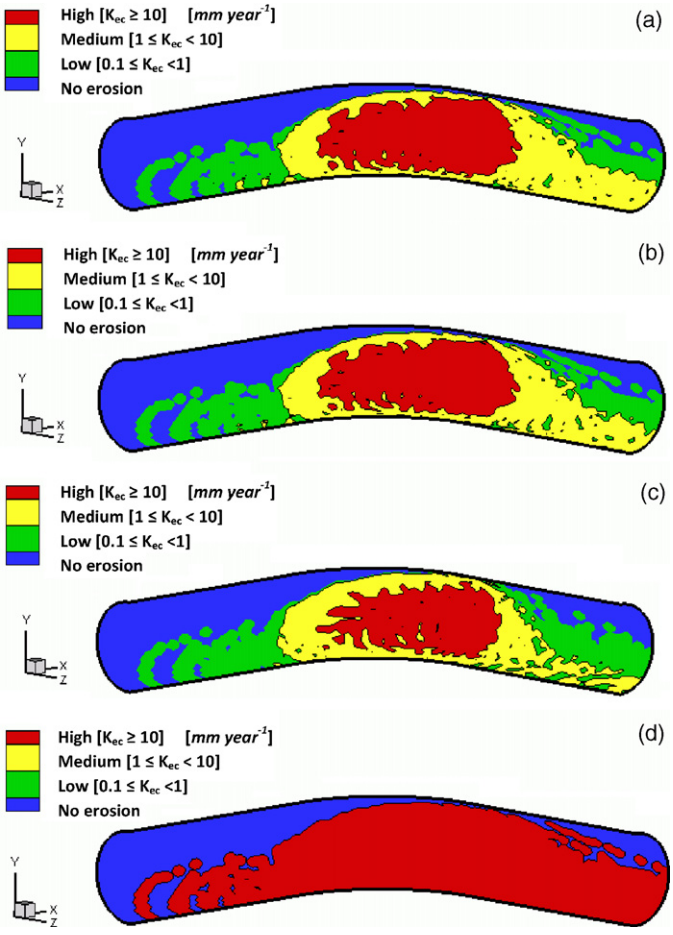

Fig. 13. Erosion–corrosion wastage maps for the outer surface of elbow-pipe at pH 9, E_{ap} = −0.6 V(SCE), particle size = 1000 [μm] and concentration = 22.88% (vf = 0.1) for: (a) Fe. (b) Ni. (c) Cu. (d) Al.

The wastage regime maps for the pure metals, Figs. 11–13, show very little differences between the pure metals at pH 5 and 7, at −0.6 V(SCE) which is surprising. However, at the higher pH values, the wastage is significantly greater for the Al, Fig. 13(d) than at lower pH values, possibly due to the high dissolution rate of this material.

A limitation of the model developed to date is that it assumes no interaction between erosion and corrosion i.e. no synergy or antagonism during the processes. However, the reasons for such effects are not well understood and can be material specific [5,19,20]. This is why the initial work on mapping the component for the materials above has made such assumptions. Further work will be to incorporate such effects in the model, particularly in the case where they can be directly related to material properties i.e. for the erosion–corrosion of composites both in bulk and in coating form [5,21].

It is acknowledged that in situations where re-passsivation cannot take place due to a very short duration between impacts, a transition to erosion affected dissolution behaviour may occur as identified in other tribo-corrosion studies in aqueous environments [22]. This is a potentially complex situation which has not been considered to date in the above approach. Further work will be to consider the more complex interactions in erosion–corrosion as discussed above.

Hence, the model developed provides a new tool for representing the transitions between erosion–corrosion regimes on real surfaces. The results indicate the variety of regimes possible over one single component. Further work will be to investigate a range of other variables in the model, such as temperature and oxygen concentration, in addition to the above issues together with identifying how materials and process parameters may be optimized for erosion–corrosion resistance using such an approach.

5. Conclusions

(i) CFD methods which involve fluid dynamics and multiphase flow parameters have been used to model the erosion–corrosion behaviour of a range of metal-corrosion systems.
(ii) The results indicate that it is possible to identify erosion–corrosion mechanistic regimes on real components under nominally similar fluid flow conditions.
(iii) The effects of erosion and corrosion parameters such as particle size and applied potential show significant differences on the three-dimensional erosion–corrosion regimes indicating the important effects of erosion–corrosion variables on the stability of such regimes observed on real life components.

References

[1] M.M. Stack, F.H. Stott, An approach to modeling erosion–corrosion of alloys using erosion–corrosion maps, Corrosion Science 35 (1993) 1027–1034.
[2] M.M. Stack, S. Lekatos, F.H. Stott, Erosion–corrosion regimes: number, nomenclature and justification? Tribology International 28 (1995) 445–451.
[3] M.M. Stack, N. Corlett, S. Zhou, Construction of erosion–corrosion maps for erosion in aqueous slurries, Materials Science and Technology 12 (1996) 662–672.
[4] M.M. Stack, Some issues relating to the construction of materials selection maps for resistance to elevated temperature erosion, Tribology International 30 (1997) 435–444.
[5] M.M. Stack, T.M. Abd El-Badia, Some comments on mapping the combined effects of slurry concentration, impact velocity and electrochemical potential on the erosion–corrosion of WC/Co–Cr coatings, Wear 264 (2008) 826–837.
[6] N.I. Kolev, Multiphase Flow Dynamics 1: Fundamentals, second ed., Springer Berlin Heidelberg, New York, 2004.
[7] R.J.K. Wood, T.F. Jones, J. Ganeshalingam, N.J. Miles, Comparison of predicted and experimental erosion estimates in slurry ducts, Wear 256 (2004) 937–947.
[8] G. Sundararajan, A comprehensive model for the solid particle erosion of ductile materials, Wear 149 (1991) 111–127.
[9] B.E. Launder, Lectures in Mathematical Models of Turbulence, Academic Press, London, 1972.

[10] A. Forder, M. Thew, D. Harrison, A numerical investigation of solid particle erosion experienced within oilfield control valves, Wear 216 (1998) 184–193.
[11] I. Finnie, Erosion of surfaces by solid particles, Wear 3 (1960) 87–103.
[12] J.H. Neilson, A. Gilchrist, Erosion by a stream of solid particles, Wear 11 (1968) 111–143.
[13] M. Pourbaix, Atlas of Electrochemical Equilibria in Aqueous Solutions, Pergamon Press, Oxford, New York, 1966.
[14] FLUENT Inc.: Fluent user's guide, version 6.3, Lebanon, NH, USA, 2006.
[15] M.M. Stack, B.D. Jana, Modelling particulate erosion–corrosion in aqueous slurries: some views on the construction of erosion–corrosion maps for a range of pure metals, Wear 256 (2004) 986–1004.
[16] B.D. Jana, M.M. Stack, Modelling impact angle effects on erosion-corrosion of pure metals: construction of materials performance maps, Wear 259 (2005) 243–255.
[17] Y. Tirupataiah, B. Venkataraman, G. Sundararajan, The nature of the elastic rebound of a hard ball impacting on ductile, metallic target materials, Materials Science and Engineering A-Structural Materials Properties Microstructure and Processing 124 (1990) 133–140.
[18] F.H. Stott, M.P. Jordan, S. Lekatos, M.M. Stack, G.C. Wood, The erosion-corrosion of alloys under oxidizing-sulfidizing conditions at high-temperature, Wear 186 (1995) 291–298.
[19] M.M. Stack, N. Corlett, S. Turgoose, Some thoughts on modelling the effects of oxygen and particle concentration on the erosion-corrosion of steels in aqueous slurries, Wear 255 (2003) 225–236.
[20] M.M. Stack, M. Antonov, I. Hussainova, some views on the erosion-corrosion response of bulk chromium carbide cermets, Journal of Physics D: Applied Physics 39 (2006) 3165–3174.
[21] M.M. Stack, T.M. Abd El-Badia, Mapping erosion-corrosion of WC/Co-Cr based composite coatings: particle velocity and applied potential effects, Surface and Coatings Technology 201 (3–4) (2006) 1335–1347.
[22] M.M. Stack, K. Chi, Mapping sliding wear of steels in aqueous conditions, Wear 255 (2003) 456–465.